Dynamics and Mechanics of Associating Polymer Networks

Shengchang Tang

B.Eng. Polymer Materials and Engineering, Tsinghua University, 2010
M.S. Chemical Engineering Practice, Massachusetts Institute of Technology, 2014

Submitted to the Department of Chemical Engineering
in partial fulfillment of the requirements for the degree of

Doctor of Philosophy

at the

Massachusetts Institute of Technology

September 2016

Signature of Author: Signature redacted

Department of Chemical Engineering
July, 2016

Certified by: Signature redacted

Bradley D. Olsen
Paul M. Cook Career Development
Associate Professor of Chemical Engineering
Thesis Supervisor

Accepted by: Signature redacted

Daniel Blankschtein
Herman P. Meissner (1929) Professor of Chemical Engineering
Chairman, Committee for Graduate Students

Dynamics and Mechanics of Associating Polymer Networks

Shengchang Tang

Submitted to the Department of Chemical Engineering on July 29, 2016
in partial fulfillment of the requirements of the degree of
Doctor of Philosophy in Chemical Engineering

Abstract

Associating polymers have attracted much interest in a variety of applications such as self-healing materials, biomaterials, rheological modifiers, and actuators. The interplay of polymer topology and sticker chemistry presents significant challenges in understanding the physics of associating polymers across a wide range of time and length scales. This thesis aims to provide new insights into the structure-dynamics-mechanics relationships of associating polymer networks.

This thesis first examines diffusion of various types of associating polymers in the gel state through a combination of experiment and theory. By using forced Rayleigh scattering (FRS), phenomenological super-diffusion is revealed as a general feature in associating networks. Experimental findings are quantitatively explained by a simple two-state model that accounts for the interplay of chain diffusion and the dynamic association-dissociation equilibrium of polymer chains with surrounding network. Furthermore, hindered self-diffusion is shown to directly correlate with a deviation from the Maxwellian behavior in materials rheological response on the long time scale. To further understand how sticker dynamics affects the network mechanical properties, a new method referred to as "sticker diffusion and dissociation spectrometry" is developed to quantify the dissociation rate of stickers in the network junctions. It is demonstrated that sticker dissociation is a prerequisite step for sticker exchange that leads to macroscopic stress relaxation. Finally, this thesis explores the use of fluorescence recovery after photobleaching (FRAP) to measure self-diffusion of associating polymers, and a mathematical framework is established.

The second part of this thesis focuses on the development of new methods of controlling the mechanical properties of associating networks through engineering the molecular structure of polymer chains. Specifically, topological entanglement is introduced into the network through extending the polymer chains to reach beyond their entanglement threshold. This strategy drastically enhances material's toughness, extensibility, creep resistance and stability in solutions. Various types of coupling chemistries are then explored to fine tune the extent of entanglement. The entanglement effect and the long-time relaxation of materials can be further controlled by introducing branching points into the macromolecules.

Thesis supervisor: Bradley D. Olsen, Paul M. Cook Career Development Associate Professor of Chemical Engineering

Acknowledgments

My graduate studies at MIT have been challenging and rewarding. I would like to acknowledge the people who have been with me along this journey.

First and foremost, I would like to express my sincere thanks to my thesis advisor Professor Bradley Olsen for his encouragement and support throughout my time in his lab. My thesis began with many failed attempts in several different projects, but Brad was patient enough to guide me through and watch me make progress day by day. Under his mentorship, I have grown up from a textbook-problem solver to someone that can be independent and fearless to tackle challenging research. Brad has given me a lot of freedom to explore the research topics that are of my personal interest, yet keeping me focus on the most important fundamental problems. His endless pursuit for the best quality of science has left a profound influence on me, which I will strive to carry on to my future career. I am particularly thankful for Brad's help with my academic job research near the end of my PhD, and I hope to become a successful scientist like him one day.

I also want to take this opportunity to thank my thesis committee members, Professors Patrick Doyle, Jeremiah Johnson, Krystyn Van Vliet and a former member Dr. Simona Socrate. Pat always sparked interesting discussions about polymer physics during my committee meetings. Krystyn has been very supportive for my independent career. I enjoyed the monthly ISN update meetings that Krystyn organized, where I could get feedback on my research and learn very different research topics. Jeremiah always had creative chemistry ideas to share during the meetings. I am very grateful to him for allowing me to use his instruments in many situations, and I learnt a lot from reading his papers and interacting with his students and postdocs. Simona taught me many lessons in solid mechanics. I would never forget the afternoons and nights we spent

together doing compression and tension tests on the "magic" hydrogels. Her positive attitude and passion towards science have been inspirational.

Most of my time during graduate school has been spent within the Olsen group, where I have met so many talented colleagues and good friends in the past several years. Muzhou Wang never fails to provide critical feedback on science. Without his knowledge and mentorship, all the studies on polymer diffusion in this thesis would not have been possible. I also want to thank him for his help during my job search, and I look forward to interacting with him in the future. Matthew Glassman introduced me to the research on physical gels before I joined the group. I am grateful for him sharing the protein genes that I used for several studies in this thesis. Outside the lab, Matt has been a very caring friend. My trip with him to New York and Princeton has left me one of the fondest memories. Christopher Lam helped me numerous times inside and outside the lab. He has been my teacher of language and culture for quite a while. His kindness constantly inspired me to be a better person. Yan Xia taught me many things in chemistry, from the most recent research development to lab skills, and I pretty much enjoyed the time working with him. Yin Fan became a good friend of mine since she joined the lab. I thank her for listening to all my complaints and giving me alternative perspectives to look at the problems. Reginal Avery, Charlotte Stewart-Sloan and Dongsook Chang have been great and amusing night-working companions. I know there are always someone to talk to when things are not going well. Michelle Sing has been a remarkable social chair and good cook. I will certainly miss her secret egg dish. Allie Obermeyer always has contagious optimism and enthusiasm to share. I thank her for answering my many questions on bioconjugation and proteins even before she officially started working in the lab. Shuaili Li helped me with some experiments in the thesis and provided me many surprising meals

when I forgot to eat. Thanks also go to other group members for taking care of many things in the lab and making the lab an enjoyable environment to work in.

I am fortunate enough to work with four talented undergraduates, Rujia Zha, Ricardo Paez, June Park and Chelsea Edwards. My experience with them greatly enriched my education and helped me realize my strengths and weaknesses in mentoring.

I also want to thank Professor Sebastian Seiffert and Axel Habicht, now at the Johannes Gutenberg University of Mainz. The collaborative work with them made me think more deeply about my research.

I enjoyed the friendships with many people in the ChemE Chinese community. Being with them always made me feel home at Boston. Xianwen Mao has been a great friend since we first met in the Huang Lab. I followed his footsteps coming to the Chemical Engineering Department at MIT. Talking to him after those frustrating moments makes me feel refreshed. His tasty food always brings joy to life. Mingjiang Zhong gave me many useful advice in job search and shared with me his wisdom in chemistry. Li Tan has been a good friend literally since before graduate school. He has helped me adapt to the cultural environment since my first day in the US. His stories added much fun to the research routines, and I benefit greatly from his advice in life. Yuran Wang has been my classmate for a decade since undergraduate. She has been very kind to continue celebrating the Boys' Day every November even though we are not long in Tsinghua. I also owe her a lot for the chemicals that she offered to share in many occasions.

The four months spent in practice school will have a unique place in my memory. I really enjoyed the opportunities of working in industrial companies and traveling to many different places. I especially would like to thank the station director Dr. Bob Fisher and several amazing

teammates Clarence Yue, Justin Kleingartner, Kaja Kaastrup, Jouha Min, Mark Molaro for making this experience special.

Thanks also go to Professors Karen Gleason and Hadley Sikes, Zhilong Zhu and Stephen Morton for making teaching 10.213 very enjoyable.

Toni Robinson has become a great mentor of mine and helped me tremendously in many of my difficult times in graduate school. Her encouragement and advice made me power through those difficult periods.

I also want to thank my brother-like friend Andy Ho for being there with me whenever I need help, even though we are separated from each other thousands of miles away.

Last but not least, I would like to thank my family for their unconditional love. They have given me the freedom to pursue my personal career and have been supportive for all the decisions that I have made. I feel greatly indebted to their sacrifice. Any of my achievements would not have been possible without them being the scene. I wish to dedicate this thesis to them.

Table of Contents

List of Figures

List of Schemes

List of Tables

Chapter 1 Introduction

1.1. Associating Polymers and Associating Networks: Definition, Properties and Applications

Associating polymers are a family of macromolecular architectures with bonds as pendant side groups or at the chain ends that undergo reversible association and dissociation. These bonds are primarily based on physical interactions such as hydrogen bonding[1-5], electrostatic interactions[6-8], metal-ligand coordination[9, 10], host-guest complexation[11, 12], π-π stacking[13], hydrophobic interactions[14] or a combination of various interactions[15-17]. Alternatively, these bonds can be formed by reversible chemical reactions such as transesterification[18] and formation of disulfide[19, 20], hindered urea[21], oxime[22, 23] or hydrazone[24] bonds. All of these associative motifs are colloquially referred to as "stickers" in the literature, and this nomenclature is adopted throughout the following sections. The internal energy of these associating domains is usually on the order of 1–10 k_BT.[25-27] The low energy barrier permits associative bonds to break and reform at appreciable rates due to thermal fluctuation or when triggered by mild stimuli.[28]

Associating polymers can form a network when the polymer concentration is above a certain threshold, normally referred to as the gelation concentration.[29] Compared to networks where all junctions are built from permanent covalent bonds, associating networks have junctions that are transient, undergoing dissociation and recombination. As a result of the dynamic nature of the bonds, the constituent macromolecular building blocks are allowed to diffuse within the networks on length scales greater than the radius of gyration of the strand. These two features provide a molecular basis for dynamic rearrangement of the network structure, as well as more pronounced responsiveness to external stimuli compared to the permanent covalent network.

Associating polymers have a wide variety of applications across many disciplines, all of which exploit the dynamic properties arising from the reversible formation of junctions.[30, 31] For example, associating networks have shown intrinsic self-healing properties.[9, 10, 21, 23, 32] A small-feature damage can be autonomously repaired within a short duration of time under ambient conditions or when triggered by external stimuli.[33] Associating networks have also gained increasing popularity in biomedical areas. Compared to covalent networks where the small-strain mechanical responses are often time-independent, associating networks show significant stress relaxation.[34] This phenomenon is also found in soft biological tissues such as brain[35] and liver[36]. This mechanical similarity promotes the use of associating networks as synthetic extracellular matrices for tissue engineering applications and for understanding the fundamentals of cell-matrix interactions.[24, 32, 37-39] In particular, associating networks can be used as injectable biomaterials promising for minimally invasive surgery applications.[40-42] The injectability takes advantages of the force-activated junction dissociation, typically shown as shear thinning, and the rapid reformation of network junctions and recovery of network properties after removal of shear.[43-45] Compared to other injectable hydrogels based on *in situ* multicomponent polymerization reactions, this shear-thinning injection mechanism achieves faster gelation[43, 46], eliminates the risks of using potential toxic compounds and leaking of gelation components in the liquid state,[43, 46-48] and allows better control over the *in vivo* properties of the gels from *ex vivo* characterizations[45]. Current research in this area has been focused on engineering junction stability and yield stress to improve the materials performance to meet application demands.[44, 49]

Precise control over the properties of associating networks requires a deep fundamental understanding of their structure-property relationships. First, one should always consider if an associating network reaches an equilibrium state or it is somehow kinetically trapped during phase

separation[50-56]. Second, from a dynamics perspective, junction dissociation and reassociation might affect the time scales associated with relaxation of polymer chains on the submolecular, the molecular, and even the supramolecular level.[57-64] Third, the mechanical properties of associating networks can be extremely time sensitive. The viscoelasticity of associating polymer networks can be drastically changed compared to the bare polymers without any associating groups.[58, 65-67] Flow properties under force activation is another complication that invokes the knowledge of thermodynamics and dynamics of associative junctions.[43, 68-77] Overall, the effect of junction properties on the thermodynamics, dynamics and mechanics of associating networks becomes even more complicated and technically challenging due to non-trivial differences between intra- and inter-molecular associations, which may strongly depend on polymer concentrations and molecular structure.[58-61, 78-81] In addition, one should consider structural, dynamic and mechanical inhomogeneities[55, 61, 81-89] on varying length scales within the networks.

1.2. Gelation of Associating Polymers

Investigation of the structure-property relationships of associating networks is only meaningful when associating polymers form a single gel phase. Therefore, it is important to understand the physics governing the sol-gel transition of associating polymers. This section summarizes the theoretical approaches for studying reversible gelation of associating polymers in the single phase regime. Two main questions are addressed in this section. First, how does one accurately determine the physical gelation point? Second, what is the physical origin of gelation?

In the strong association regime where the associative bond energy is larger than k_BT, one would expect that associating networks behave similarly to the ones formed by permanent covalent bonds on time scales shorter than the bond lifetime. Therefore, the sol-gel transition of associating

polymers can be estimated by the well-known mean-field Flory-Stockmayer gel point[90], which was first developed to evaluate the gelation point in irreversible polycondensation reactions that involve multifunctional crosslinkers. Note that the original theoretical formulations from Flory[91] and Stockmayer[92] are different in the treatment of intramolecular cyclization in the post gel regime. The Flory-Stockmayer approach assumes that a percolated network has infinite size and yields estimates of the gel point depending on the junction functionality and stoichiometry of different functionalities. However, this estimation is only strictly valid for end-associating polymers that are above the overlap concentration, since the Flory-Stockmayer gel point does not consider the influence of the polymeric backbone and the sticker position. Additionally, this theory neglects the formation of intramolecular loops, which introduces inaccuracy in further dissecting the structure-property relationship of associating polymer networks.

Gelation of polymers with pendant associating side groups can be described by the theory developed by Semenov and Rubinstein[59]. Their approach accounts for the connectivity between stickers by polymer chains, and it generalizes the mean-field approach by considering the excluded volume interactions due to polymer swelling and the formation of intramolecular association. This theory suggests that physical gelation occurs at a much lower polymer concentration with increasing sticker association energy (when the chain excluded volume interaction is sufficiently strong) and with increasing number density of stickers. Many experimental findings[93-95] have shown qualitative agreement with the theory, but quantitative validation of the theory has not yet been achieved, largely due to the difficulty to measure the parameter of effective bond volume[59] for calculating the gel point.

In the weak association regime where the sticker association energy becomes comparable to the thermal energy k_BT, percolation may not necessarily lead to gelation. Kumar and Douglas[96]

argue that the gel point for weakly associating polymers should better be determined by the abrupt change in dynamic properties such as the sticker lifetime and chain diffusivity. Such a definition of the gel point is similar to the method by which it is usually measured experimentally. In their phase diagram generated by Monte Carlo simulation, the thermoreversible gelation is described by a "clustering line" that captures the onset of chain clusters connecting with each other. At a given reduced temperature, the calculated clustering line separates far from the geometric percolation line with increasing polymer volume fraction, suggesting that geometric percolation is necessary but not sufficient for true gelation. The observations by Kumar and Douglas have been partially supported by a limited number of experimental studies[97, 98], and systematic investigations are needed to further distinguish definitions of gel point from the structural and mechanical perspectives.

Finally, it should be pointed out that the theories and simulation results mentioned above to understand and estimate gel points are primarily focused on associating polymers with stickers being placed along the backbone or at the chain ends. Physical gelation of associating polymers of other molecular architectures should be explained by theories specifically formulated for the type of molecular architecture and mesoscale network structure. For instance, diblock polymers in a concentrated solution can form gels with different ordered nanostructures. Here, the gel point is determined by the packing geometry and is largely governed by thermodynamics that drives microphase separation.[16, 99] The gelation mechanisms for biopolymers such as gelatin, agarose, collagen or artificially engineered polypeptides are even more complicated, which usually invoke theories of spinodal decomposition and nucleation.[53, 100-102] In these cases, guidelines for quantitative estimation of gel point are not available.

1.3. Dynamics of Associating Polymer Networks

There are two main theoretical frameworks for understanding dynamics of associating polymer networks, one developed by Leibler, Semonov, Rubinstein and Colby[57-61], and the other formulated by Cates and Candau[62, 63]. Both of the two theories are built upon the classical polymer theories on dynamics[67], such as the Rouse and Zimm relaxtion for unentangled polymers and reptation for entangled polymers.

The sticky Rouse and reptation theories developed by Leibler, Semonov, Rubinstein and Colby use scaling analysis to consider the effect of associative stickers on polymer dynamics by extending the classic Rouse and reptation theories on polymers without any stickers.[57-61] The original theoretical formulation is focused on modeling linear polymers with many pendant divalent associating side groups that are regularly spaced along the polymer chain. There are multiple key predictions from the theories. First, the fraction of intermolecular bonds increases with polymer concentration. Second, the the lifetime of junction is prolonged in the polymer networks especially at high concentration because dissociated stickers cannot easily find another open partner for exchange and most likely end up reassociating with the original sticker partners. Note that the theories assume that junction breakage is caused by the self-dissociation of the two stickers. Third, the presence of the stickers yields a very strong dependence of dynamic properties on polymer molecular weight, polymer concentration (or volume fraction) and sticker density. The scaling exponents in these relationships are much larger than the ones in ordinary, non-associating polymers. The full spectrum of predicted scaling regimes for the junction relaxation time τ, the zero-shear-rate viscosity η_0 and the chain diffusivity D by the sticky Rouse and reptation theories are summarized in Table 1-1 to 1-3, where the numerical values of scaling exponents in the last columns of the tables are calculated based on good solvent condition. If the polymer volume

fraction is below the entanglement threshold (φ_e), the sticky Rouse theory should be used; otherwise the sticky reptation theory should be employed. It should also be pointed that the sticky Rouse and reptation theories are formulated separately. One should be cautious when considering the transition from the sticky Rouse to the sticky reptation regime.

Some experimental investigations have shown qualitative agreement with the scaling relations on junction relaxation time and zero-shear-rate viscosity that are predicted by the sticky Rouse/reptation theories.[65, 103-105] Quantitative differences between theories and experiments are attributed to the details in molecular characteristics of associating polymers, such as mobility of the junctions (especially for metal-ligand coordination bonds)[65, 103], dispersity of the polymer building blocks[65], and irregular spacing between stickers[65]. Experimental validation of the entire spectrum of scaling regimes shown in Table 1-1 to 1-3 might be technically intractable due to the difficulty in synthesis of polymers with extract same characteristics formulated in theories (large number of stickers and high degree of polymerization between stickers) and the narrow widths of the scaling regimes found in nearly all existing experiments.

The theory developed by Cates and Candau focuses on living polymers from end-associating telechelic polymers that can undergo reversible linear chain extension or from assembled tubular micelles.[62, 63] When the molar mass of the linearly polymerized polymers is above the entanglement threshold, relaxation of the supra-macromolecules is affected by the interplay of reptation of polymers and the kinetics of junction breakage and recombination. More specifically, if the junction lifetime is shorter than the reptation time, junction breakage can significantly affect the relaxtion process of the associative networks before the polymers fully explore the tube. For polymers well above the entanglement threshold, the Cates-Candau theory predicts the following scaling laws under good solvent condition:

(1) terminal relaxation time $\tau \sim \varphi^{1.5}$;

(2) chain diffusivity $D \sim \varphi^{-1.67}$;

(3) zero-shear-rate viscosity $\eta_0 \sim \varphi^{3.6\text{-}3.8}$;

where φ is the volume fraction of the living polymers. Experimental studies on systems from end-associating polymers to wormlike surfactant micelles agree well with the theory.[63, 106-108]

Existing experimental examinations on the dynamic properties of associating networks have been mostly focused on the junction relaxation time and the zero-shear-rate viscosity; both properties are often probed by shear rheology. Fewer have systematically investigated self-diffusion of polymers chains within the networks.[63, 65, 66, 109, 110] Previous works have employed either fluorescence recovery after photobleaching (FRAP) or pulse field gradient nuclear magnetic resonance (PFG-NMR) to measure self-diffusion. In these measurements, the diffusivities are typically larger than 10^{-14} m^2/s, and slower diffusion processes have not been reported. Additionally, self-diffusive behavior can be rather complicated because of its intrinsic dependence of diffusion length scales. This also adds challenges to experimental measurements to access a wide range of length scales.

Table 1-1. Scaling exponents of the sticker lifetime τ as a function of polymer volume fraction φ in transient networks. Adapted from reference 65.

Concentration range	Description	Scaling exponent	Value
Sticky Rouse Model			
$\varphi < \varphi_{ren}$	Unrenormalized bond lifetime; transfer of intra- to intermolecular association	$(2 + 2z) / (3\nu - 1)$	3.2
$\varphi_{ren} < \varphi < \varphi_s$	Renormalized bond lifetime; transfer of intra- to intermolecular association	$(6 + 7z) / (6\nu - 2)$	4.96
$\varphi_s < \varphi < \varphi_e$	Renormalized bond lifetime; mostly intermolecular association	$z / (6\nu - 2)$	0.17
Sticky Reptation Model			
$\varphi_e < \varphi < \varphi_{ren}$	Unrenormalized bond lifetime; mostly intramolecular association	$(3 + 2z) / (3\nu - 1)$	2.9
$\varphi_{ren} < \varphi < \varphi_s$	Renormalized bond lifetime; transfer of intra-to intermolecular association	$(4 + 3.5z) / (6\nu - 2)$	3.13
$\varphi_s < \varphi < \varphi_{te}$	Renormalized bond lifetime; mostly intermolecular association	$(1 + 0.5z) / (3\nu - 1)$	1.46
$\varphi_{te} < \varphi < 1$	Renormalized bond lifetime; entangled strands between stickers	$(1.75 + 0.5z) / (3\nu - 1)$	2.44

Note: φ_{ren} is the critical volume fraction at which stickers transition from intra- to intermolecular association, φ_s is the overlap volume fraction of the polymer segments between stickers, φ_e is the polymer entanglement volume fraction, and φ_{te} is the entanglement of polymer segments between two stickers. ν is the Flory exponent, and its value at good solvent condition is 0.588. z is the parameter quantifying the excluded volume effect, and $z \approx 0.225$ at good solvent limit. The notations are the same for Table 1-2 and 1-3.

Table 1-2. Scaling exponents of the zero-shear-rate viscosity η_0 as a function of polymer volume fraction φ in transient networks. Adapted from reference 65.

Concentration range	Description	Scaling exponent	Value
Sticky Rouse Model			
$\varphi < \varphi_{ren}$	Unrenormalized bond lifetime; transfer of intra- to intermolecular association	$1 + (2 + 2z) / (3\nu - 1)$	4.2
$\varphi_{ren} < \varphi < \varphi_s$	Renormalized bond lifetime; transfer of intra- to intermolecular association	$1 + (6 + 7z) / (6\nu - 2)$	5.96
$\varphi_s < \varphi < \varphi_e$	Renormalized bond lifetime; mostly intermolecular association	$1 + z / (6\nu - 2)$	1.17
Sticky Reptation Model			
$\varphi_e < \varphi < \varphi_{ren}$	Unrenormalized bond lifetime; mostly intramolecular assciation	$(3 + 3\nu + 2z) / (3\nu - 1)$	6.8
$\varphi_{ren} < \varphi < \varphi_s$	Renormalized bond lifetime; transfer of intra- to intermolecular association	$(4 + 3\nu + 3.5z) / (3\nu - 1)$	8.58
$\varphi_s < \varphi < \varphi_{le}$	Renormalized bond lifetime; mostly intermolecular association	$(1 + 3\nu + 0.5z) / (3\nu - 1)$	3.77
$\varphi_{le} < \varphi < 1$	Renormalized bond lifetime; entangled strands between stickers	$(1.75 + 3\nu + 0.5z) / (3\nu - 1)$	4.75

Table 1-3. Scaling exponents of the chain diffusivity D as a function of polymer volume fraction φ in transient networks. Adapted from reference 65.

Concentration range	Description	Scaling exponent	Value
Sticky Rouse Model			
$\varphi < \varphi_{ren}$	Unrenormalized bond lifetime; transfer of intra- to intermolecular association	$-(2\nu + 2z + 1) / (3\nu - 1)$	–3.44
$\varphi_{ren} < \varphi < \varphi_s$	Renormalized bond lifetime; transfer of intra- to intermolecular association	$-(2\nu + 3.5z + 2) / (3\nu - 1)$	–5.19
$\varphi_s < \varphi < \varphi_e$	Renormalized bond lifetime; mostly intermolecular association	$-(2\nu + 0.5z + 1) / (3\nu - 1)$	–3
Sticky Reptation Model			
$\varphi_e < \varphi < \varphi_{ren}$	Unrenormalized bond lifetime; mostly intramolecular association	$-(2\nu + 2z + 2) / (3\nu - 1)$	–4.75
$\varphi_{ren} < \varphi < \varphi_s$	Renormalized bond lifetime; transfer of intra- to intermolecular association	$-(2\nu + 1.75z + 1) / (3\nu - 1)$	–3.36
$\varphi_s < \varphi < \varphi_{le}$	Renormalized bond lifetime; mostly intermolecular association	$-(2\nu + 0.5z) / (3\nu - 1)$	–1.69
$\varphi_{le} < \varphi < 1$	Renormalized bond lifetime; entangled strands between stickers	$-(2\nu + 0.5z + 0.75) / (3\nu - 1)$	–2.67

1.4. Mechanics of Associating Polymer Networks

Theoretical studies on mechanics of transient networks date back to the year of 1946 when Green and Tobolsky[111] formulated the first transient network theory. They hypothesize that the network junctions break and reform at equal rates and assume affine network deformation originally formulated in the theory of rubbery elasticity. The Green-Tobolsky theory shows for the first time that the junction dynamics directly plays an important role in continuum network mechanics. Specifically, the equation of motion in a shear process reduces to the well-known Maxwell model and the zero-shear-rate viscosity becomes the plateau modulus divided by the junction exchange rate. However, the Green-Tobolsky theory oversimplifies the junction exchange dynamics and neglects the influence of chain Rouse/reptation time on junction dynamics.

Tanaka and Edwards[68-70, 112] later generalized the Green-Tobolsky theory by considering a more realistic molecular picture where the junction destruction and recreation rates are two different functions of the end-to-end distance of a network strand. Junction breakage is induced by an exerted tension within the network strand or by an instantaneous tension raised by Brownian motion, whereas junction recombination depends on the chain end-to-end distance distribution and the recombination probability. When junction reformation is slower than dissociation, dangling chains should exist in the transient networks. Additionally, they reason that dangling chains should not be responsible for stress relaxation since chains completely relax before rejoining a new network junction and friction arising from chain movement is negligibly small compared to the energy dissipated by the breakage of junctions. The Tanaka-Edwards theory also predicts a breakdown of the Cox-Merz rule, suggesting that associating polymer networks might be rheologically complex. Finally, the Tanaka-Edwards theory allows forces to transmit from one junction to another, which represents a significant advancement for recognizing the interactions

between network junctions. This theory, however, does not distinguish the intramolecular bonds from the intermolecular ones, which usually underestimates the concentration effect on many rheological properties. Moreover, the assumption that dangling chains do not contribute to network mechanics might not hold. Many other theoretical and experimental works[73, 74, 80] have explicitly shown that dangling chains have an effect on network mechanics.

To account for the effect of chain topology on network mechanics, Annable et al.[113] explicitly consider chains in different states including a bridged chain with both ends attached to different micelles, a looped chain with both ends attached to the same micelle, a dangling chain, a free chain, and a free loop. This topological variability also allows molecular building blocks to form complex architectures such as superbridges and superloops. By considering the transformation of chain topology as a function of polymer concentration, their theory and simulation are able to capture the concentration effect on network mechanics and show good consistency with experiments. In addition, these authors examine the relaxation of a network composed of polymers with different end associating groups. They find that different junctions relax independently because Rouse relaxation of network strands precedes reformation of network junctions. However, it should be noted that their implementation of Monte Carlo simulation is based on some simplified or even inaccurate assumptions. For instance, their sampling methods are biased towards to configurations with closed stickers, and the sticker positions are fixed in space.

Later, Tripathi et al. construct constitutive models to describe linear and nonlinear rheological properties of associating networks from telechelic associating polymers. To calculate the stress response in shear and extensional flows, they account for contributions from both bridged and dangling chains and the finite extensibility of the network strands. By further refining the

assumptions of the Tanaka-Edwards theory, they reason that the energy landscape between the associative and dangling states is significantly altered by an imposed stress, thus resulting in nonlinear chain association and dissociation rates that depend on junction association energy and chain deformation. Their molecular picture leads to successful predictions of the zero-shear-rate viscosity, small-amplitude oscillatory shear response, and nonlinear features such as shear thickening followed by shear thinning, which all quantitatively agree with experimental measurements on hydrophobically modified ethoxylate-urethane (HEUR) polymers at varying concentrations. However, it should be noted that their models do not include the effect of looped chains. Even though the models show success in capturing mechanical properties of the polymer networks in the semi-dilute unentangled regime, it is expected to cause non-negligible deviation in the dilute limit.

Recently, Sing et al.[74] adopt a different theoretical approach to examine dynamics of telechelic associating polymers in networks using a set of Smoluchowski reaction-diffusion equations. They numerically evaluate the end-to-end distance distribution of finite extensible dumbbells to extract the fractions of bridged, looped and dangling chains in the networks at the quiescent state and under shear flows. A non-monotonic shear stress profile is observed as a function of shear rates in the slow dissociation regime where the end group dissociation rate is nearly two orders of magnitude smaller than the Rouse time of the polymer chains. At high shear, chain tumbling is observed for the first time, which promotes the reformation of bridges, suppresses loop formation and leads to a steady state plateau modulus in the large strain-rate regime. Chain tumbling is also responsible for the stress overshoot in start-up shear experiments. This investigation considers interconversion of bridged, loops and dangling chains under shear, providing new methods to interrogate the structural origin of rheological response of transient

networks. However, this single-chain approach has an inherent limitation because it does not consider higher order chain architectures and their effect on network mechanics; this scope of research might be better explored by simulation methods such as Brownian dynamics[71, 72], molecular dynamics[89, 114] or Monte Carlo (sometime in conjunction with molecular dynamics) [113, 115, 116].

The transient network theories described above provide insight into associating network mechanics. First, network relaxation is largely affected by the exchange rate of junctions, but the actual relaxation process can be complicated by the chain relaxation motions and thus may not be captured by the simple Maxwell model. Second, network modulus depends on the chain microstructure and can be highly sensitive to polymer concentrations. Third, the structure-mechanics relationship of associating networks is altered substantially under external mechanical forces. While these theories are able to qualitatively explain and even predict changes of network mechanical properties according to molecular parameters, quantitative descriptions remain true challenges.

The linear mechanical properties of transient networks over a large time or frequency window are often experimentally measured by small-amplitude oscillatory shear experiments.[45, 113] Three important features are usually observed for rheological response of transient networks, the high-frequency plateau modulus, the crossover between elastic and loss moduli, and the terminal relaxation (see representative data in Figure 1-1).[4, 9, 24, 43, 64, 66, 79, 103, 113] Consistent with the theoretical descriptions, multiple relaxation modes are seen in some cases, and constitutive modeling of the rheological response requires more than one Maxwell element or more complicated models.[24, 43, 64, 66, 117, 118] Deviations from the Maxwell model are often observed in the high-frequency and the low-frequency limits, but they have distinct physical origins. In the

low frequency limit, associative interaction between stickers can delay the relaxation of Rouse segments of low relaxation modes, which introduces another relaxation mechanism and manifests as a new elastic plateau.[4, 64, 104] Experimental observations of this kind are referred to as the sticky Rouse relaxation.[4, 64] In the high frequency limit, motion of the junction point itself or the Rouse relaxation of individual polymer chains may also introduce an additional relaxation mechanism, which is often seen as a separate peak in the loss modulus.[73, 117] However, this is only rationalized in the micellar networks, and generalizations to other systems have not yet been achieved.[43, 66, 117]

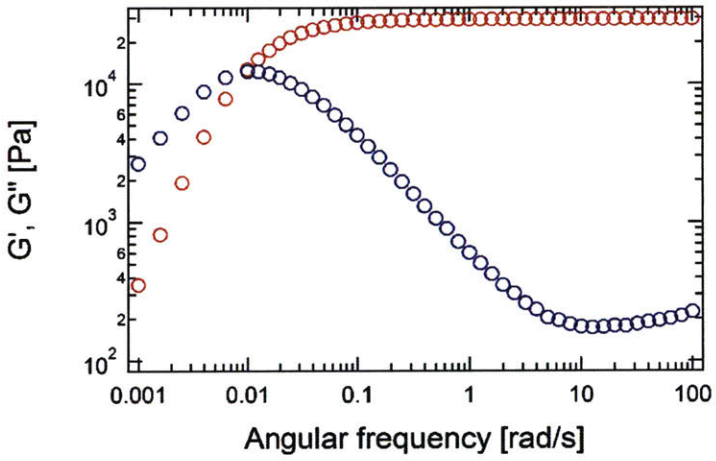

Figure 1-1. Representative small-amplitude oscillatory shear response of associating networks. Data was taken on telechelic coiled-coil protein gels.

The elastic modulus of associating networks is arguably the most important property and dictates their applications. However, it is still very difficult to predict network modulus based on structural information of associating networks. Current methods of correlating network modulus with chain topologies still largely rely on the affine and phantom network theories,[44, 76, 86, 103, 119, 120] which are still unproven despite being widely used. An alternate approach is to construct

simplified models designed for particular systems based on the thermodynamics and other characteristics of the network junctions[79, 80]. In most cases, these two methods can only yield estimates on the number of elastically effect chains, but such estimations are difficult to justify. Although experimental methods[121-125] have been developed to quantify the network defects such as primary loops and dangling chains in covalent networks, to the best of the author's knowledge, direct measurements of network imperfections in associating networks have not been realized. Furthermore, when the networks stands do not behave as Gaussian chains, the structure-modulus relationship can be even more complicated.[126, 127]

Much experimental effort has also been devoted to correlating the isolated junction exchange dynamics (microscopic properties) to network relaxation (macroscopic properties). The exchange rates of different isolated, associative bonds in dilute solution have been measured by nuclear magnetic resonance[18, 128] (such as exchange spectroscopy or coalescence experiments) or by fluorescence quenching[129]. These measured junction exchange rates are found to directly correlate with the longest relaxation time of the network[129] or yield a master flow curve by renormalizing the shear rate dependent network viscosity[128, 130]. However, quantitative relationships have not yet emerged. All of these experiments support the argument that junction dynamics greatly controls materials relaxation. However, it should be emphasized that the majority of the existing measurements on junction kinetics are performed in dilute solutions where the effects of the connectivity of stickers to the macromolecular architecture and crowding are not considered. In theory, the exchange rate constant should not exhibit any concentration dependence, but network relaxtion has been shown to be concentration dependent[60, 63, 65, 66, 80]. Therefore, all of these measurements cannot explain the concentration effect on network relaxation, and direct measurement of the exchange rates between junctions is still lacking.

1.5. Thesis Aims and Overview

This thesis aims to advance our understanding of the structure-property relationships of associating polymer networks and to develop new methods to increase the mechanical tunability of associating networks. The remaining parts of this thesis are organized as follows. First, Chapter 2 describes model associating polymers used in this thesis and summarizes key experimental methods for their synthesis and characterization. Chapter 3 provides the first experimental measurement of self-diffusion of unentangled linear artificial proteins in gels over multiple length scales by forced Rayleigh scattering (FRS), and the observation of anomalous diffusion is correlated to the macroscopic sticky-Rouse-like rheological response of the gels. Chapter 4 demonstrates the generality of anomalous diffusion through studying a new model network formed by star-shaped poly(ethylene glycol) polymers transiently linked to Zn^{2+} in a polar organic solvent. Quantitative comparisons between self-diffusion and tracer diffusion are discussed in detail from analysis with a proposed two-state model. Chapter 5 shows a new type of anomalous self-diffusion in a new model transient network formed by linear poly(*N*,*N*-dimethylacrylamide) polymers with pendant histidine side groups complexed to Ni^{2+} in aqueous buffer. This chapter also provides a new method termed as diffusion spectroscopy to directly measure junction dissociation in gels. Chapter 6 describes initial efforts in measuring self-diffusion of associating polymers using fluorescence recovery after photobleaching (FRAP). A new mathematical framework in analyzing diffusion data using the two-state model is developed to fully utilize the spatio-temporal information in FRAP measurements. Preliminary comparison between FRAP and FRS is also given. Chapters 3-6 together provide new insights into the emergent phenomenon of self-diffusion of associating polymers. Chapter 7 develops a new method to control the mechanical properties of artificially engineered protein hydrogels. Specifically, topological entanglement is introduced

to the coiled-coil protein gels to effectively modulate the low-frequency elastic modulus, creep and recovery, toughness, extensibility and surface erosion. Experimental results are discussed in light of the sticky reptation theory. Chapter 8 systematically compares the performance of four different chain extension chemistries targeting cysteine residues on the proteins. Entangled, branched proteins are also synthesized, and the effect of branching on the mechanical properties of networks is discussed. The studies in Chapters 7-8 together demonstrate a new concept of controlling the network mechanics by manipulating polymer chain architectures. Last, Chapter 9 summarizes entire thesis and presents new directions in further understanding and controlling the structure-property relationships in associating polymer networks.

1.6. References

1. Guo, M.; Pitet, L. M.; Wyss, H. M.; Vos, M.; Dankers, P. Y. W.; Meijer, E. W. Tough Stimuli-Responsive Supramolecular Hydrogels with Hydrogen-Bonding Network Junctions. *Journal of the American Chemical Society* 2014, 136, 6969-6977.

2. Albertazzi, L.; van der Zwaag, D.; Leenders, C. M. A.; Fitzner, R.; van der Hofstad, R. W.; Meijer, E. W. Probing Exchange Pathways in One-Dimensional Aggregates with Super-Resolution Microscopy. *Science* 2014, 344, 491-495.

3. Cordier, P.; Tournilhac, F.; Soulie-Ziakovic, C.; Leibler, L. Self-Healing and Thermoreversible Rubber from Supramolecular Assembly. *Nature* 2008, 451, 977-980.

4. Lewis, C. L.; Stewart, K.; Anthamatten, M. The Influence of Hydrogen Bonding Side-Groups on Viscoelastic Behavior of Linear and Network Polymers. *Macromolecules* 2014, 47, 729-740.

5. Brinke, G.; Ruokolainen, J.; Ikkala, O. Supramolecular Materials Based on Hydrogen-Bonded Polymers. In *Hydrogen Bonded Polymers*, Binder, W., Ed. Springer Berlin Heidelberg: Berlin, Heidelberg, 2007; pp 113-177.

6. Hunt, J. N.; Feldman, K. E.; Lynd, N. A.; Deek, J.; Campos, L. M.; Spruell, J. M.; Hernandez, B. M.; Kramer, E. J.; Hawker, C. J. Tunable, High Modulus Hydrogels Driven by Ionic Coacervation. *Advanced Materials* 2011, 23, 2327-2331.

7. Lemmers, M.; Sprakel, J.; Voets, I. K.; van der Gucht, J.; Cohen Stuart, M. A. Multiresponsive Reversible Gels Based on Charge-Driven Assembly. *Angewandte Chemie International Edition* 2010, 49, 708-711.

8. Sun, T. L.; Kurokawa, T.; Kuroda, S.; Ihsan, A. B.; Akasaki, T.; Sato, K.; Haque, M. A.; Nakajima, T.; Gong, J. P. Physical Hydrogels Composed of Polyampholytes Demonstrate High Toughness and Viscoelasticity. *Nat Mater* 2013, 12, 932-937.

9. Holten-Andersen, N.; Harrington, M. J.; Birkedal, H.; Lee, B. P.; Messersmith, P. B.; Lee, K. Y. C.; Waite, J. H. Ph-Induced Metal-Ligand Cross-Links Inspired by Mussel Yield Self-Healing Polymer Networks with near-Covalent Elastic Moduli. *Proceedings of the National Academy of Sciences* 2011, 108, 2651-2655.

10. Bode, S.; Zedler, L.; Schacher, F. H.; Dietzek, B.; Schmitt, M.; Popp, J.; Hager, M. D.; Schubert, U. S. Self-Healing Polymer Coatings Based on Crosslinked Metallosupramolecular Copolymers. *Advanced Materials (Deerfield Beach, Fla.)* 2013, 25, 1634-1638.

11. Harada, A.; Kobayashi, R.; Takashima, Y.; Hashidzume, A.; Yamaguchi, H. Macroscopic Self-Assembly through Molecular Recognition. *Nat Chem* 2011, 3, 34-37.

12. Appel, E. A.; del Barrio, J.; Loh, X. J.; Scherman, O. A. Supramolecular Polymeric Hydrogels. *Chemical Society Reviews* 2012, 41, 6195-6214.

13. Parkinson, P.; Müller, C.; Stingelin, N.; Johnston, M. B.; Herz, L. M. Role of Ultrafast Torsional Relaxation in the Emission from Polythiophene Aggregates. *The Journal of Physical Chemistry Letters* 2010, 1, 2788-2792.

14. Su, Y.-l.; Wang, J.; Liu, H.-z. Ftir Spectroscopic Investigation of Effects of Temperature and Concentration on Peo−Ppo−Peo Block Copolymer Properties in Aqueous Solutions. *Macromolecules* 2002, 35, 6426-6431.

15. Petka, W. A.; Harden, J. L.; McGrath, K. P.; Wirtz, D.; Tirrell, D. A. Reversible Hydrogels from Self-Assembling Artificial Proteins. *Science* 1998, 281, 389-392.

16. Nowak, A. P.; Breedveld, V.; Pakstis, L.; Ozbas, B.; Pine, D. J.; Pochan, D.; Deming, T. J. Rapidly Recovering Hydrogel Scaffolds from Self-Assembling Diblock Copolypeptide Amphiphiles. *Nature* 2002, 417, 424-428.

17. Xu, C.; Breedveld, V.; Kopeček, J. Reversible Hydrogels from Self-Assembling Genetically Engineered Protein Block Copolymers. *Biomacromolecules* 2005, 6, 1739-1749.

18. Cromwell, O. R.; Chung, J.; Guan, Z. Malleable and Self-Healing Covalent Polymer Networks through Tunable Dynamic Boronic Ester Bonds. *Journal of the American Chemical Society* 2015, 137, 6492-6495.

19. Barcan, G. A.; Zhang, X.; Waymouth, R. M. Structurally Dynamic Hydrogels Derived from 1,2-Dithiolanes. *Journal of the American Chemical Society* 2015, 137, 5650-5653.

20. Sun, Y.; Huang, Y. Disulfide-Crosslinked Albumin Hydrogels. *Journal of Materials Chemistry B* 2016.

21. Ying, H.; Zhang, Y.; Cheng, J. Dynamic Urea Bond for the Design of Reversible and Self-Healing Polymers. *Nat Commun* 2014, 5.

22. Lin, F.; Yu, J.; Tang, W.; Zheng, J.; Defante, A.; Guo, K.; Wesdemiotis, C.; Becker, M. L. Peptide-Functionalized Oxime Hydrogels with Tunable Mechanical Properties and Gelation Behavior. *Biomacromolecules* 2013, 14, 3749-3758.

23. Mukherjee, S.; Hill, M. R.; Sumerlin, B. S. Self-Healing Hydrogels Containing Reversible Oxime Crosslinks. *Soft Matter* 2015, 11, 6152-6161.

24. McKinnon, D. D.; Domaille, D. W.; Cha, J. N.; Anseth, K. S. Biophysically Defined and Cytocompatible Covalently Adaptable Networks as Viscoelastic 3d Cell Culture Systems. *Advanced Materials* 2014, 26, 865-872.

25. Israelachvili, J. N. *Intermolecular and Surface Forces*. 3rd ed.; Academic Press: Burlington, Mass., 2011; p xxx, 674 p.

26. Rossow, T.; Seiffert, S. Supramolecular Polymer Networks: Preparation, Properties, and Potential. In *Supramolecular Polymer Networks and Gels*, Seiffert, S., Ed. Springer International Publishing: Cham, 2015; pp 1-46.

27. Biedermann, F.; Schneider, H.-J. Experimental Binding Energies in Supramolecular Complexes. *Chemical Reviews* 2016.

28. Wojtecki, R. J.; Meador, M. A.; Rowan, S. J. Using the Dynamic Bond to Access Macroscopically Responsive Structurally Dynamic Polymers. *Nat Mater* 2011, 10, 14-27.

29. Rubinstein, M.; Dobrynin, A. V. Associations Leading to Formation of Reversible Networks and Gels. *Current Opinion in Colloid & Interface Science* 1999, 4, 83-87.

30. Aida, T.; Meijer, E. W.; Stupp, S. I. Functional Supramolecular Polymers. *Science* 2012, 335, 813-817.

31. Liu, K.; Kang, Y.; Wang, Z.; Zhang, X. 25th Anniversary Article: Reversible and Adaptive Functional Supramolecular Materials: "Noncovalent Interaction" Matters. *Advanced Materials (Deerfield Beach, Fla.)* 2013, 25, 5530-5548.

32. Webber, M. J.; Appel, E. A.; Meijer, E. W.; Langer, R. Supramolecular Biomaterials. *Nat Mater* 2016, 15, 13-26.

33. Blaiszik, B. J.; Kramer, S. L. B.; Olugebefola, S. C.; Moore, J. S.; Sottos, N. R.; White, S. R. Self-Healing Polymers and Composites. *Annual Review of Materials Research* 2010, 40, 179-211.

34. Zhao, X.; Huebsch, N.; Mooney, D. J.; Suo, Z. Stress-Relaxation Behavior in Gels with Ionic and Covalent Crosslinks. *Journal of Applied Physics* 2010, 107, 063509.

35. Levental, I.; Georges, P. C.; Janmey, P. A. Soft Biological Materials and Their Impact on Cell Function. *Soft Matter* 2007, 3, 299-306.

36. Liu, Z.; Bilston, L. On the Viscoelastic Character of Liver Tissue: Experiments and Modelling of the Linear Behaviour. *Biorheology* 2000, 37, 191-201.

37. Chaudhuri, O.; Gu, L.; Darnell, M.; Klumpers, D.; Bencherif, S. A.; Weaver, J. C.; Huebsch, N.; Mooney, D. J. Substrate Stress Relaxation Regulates Cell Spreading. *Nat Commun* 2015, 6.

38. Chaudhuri, O.; Gu, L.; Klumpers, D.; Darnell, M.; Bencherif, S. A.; Weaver, J. C.; Huebsch, N.; Lee, H.-p.; Lippens, E.; Duda, G. N., *et al.* Hydrogels with Tunable Stress Relaxation Regulate Stem Cell Fate and Activity. *Nat Mater* 2016, 15, 326-334.

39. Rosales, A. M.; Anseth, K. S. The Design of Reversible Hydrogels to Capture Extracellular Matrix Dynamics. *Nature Reviews Materials* 2016, 1, 15012.

40. Parisi-Amon, A.; Mulyasasmita, W.; Chung, C.; Heilshorn, S. C. Protein-Engineered Injectable Hydrogel to Improve Retention of Transplanted Adipose-Derived Stem Cells. *Advanced Healthcare Materials* 2013, 2, 428-432.

41. Guvendiren, M.; Lu, H. D.; Burdick, J. A. Shear-Thinning Hydrogels for Biomedical Applications. *Soft Matter* 2012, 8, 260-272.

42. Lu, H. D.; Charati, M. B.; Kim, I. L.; Burdick, J. A. Injectable Shear-Thinning Hydrogels Engineered with a Self-Assembling Dock-and-Lock Mechanism. *Biomaterials* 2012, 33, 2145-2153.

43. Olsen, B. D.; Kornfield, J. A.; Tirrell, D. A. Yielding Behavior in Injectable Hydrogels from Telechelic Proteins. *Macromolecules* 2010, 43, 9094-9099.

44. Glassman, M. J.; Chan, J.; Olsen, B. D. Reinforcement of Shear Thinning Protein Hydrogels by Responsive Block Copolymer Self-Assembly. *Advanced Functional Materials* 2013, 23, 1182-1193.

45. Yan, C.; Pochan, D. J. Rheological Properties of Peptide-Based Hydrogels for Biomedical and Other Applications. *Chemical Society Reviews* 2010, 39, 3528-3540.

46. Tao, Y.; Tong, X.; Zhang, Y.; Lai, J.; Huang, Y.; Jiang, Y.-R.; Guo, B.-H. Evaluation of an in Situ Chemically Crosslinked Hydrogel as a Long-Term Vitreous Substitute Material. *Acta Biomaterialia* 2013, 9, 5022-5030.

47. Van Tomme, S. R.; Storm, G.; Hennink, W. E. In Situ Gelling Hydrogels for Pharmaceutical and Biomedical Applications. *International Journal of Pharmaceutics* 2008, 355, 1-18.

48. Silva, G. A.; Czeisler, C.; Niece, K. L.; Beniash, E.; Harrington, D. A.; Kessler, J. A.; Stupp, S. I. Selective Differentiation of Neural Progenitor Cells by High-Epitope Density Nanofibers. *Science* 2004, 303, 1352-1355.

49. Glassman, M. J.; Olsen, B. D. Structure and Mechanical Response of Protein Hydrogels Reinforced by Block Copolymer Self-Assembly. *Soft Matter* 2013, 9, 6814-6823.

50. Heymann, E. Studies on Sol-Gel Transformations. I. The Inverse Sol-Gel Transformation of Methylcellulose in Water. *Transactions of the Faraday Society* 1935, 31, 846-864.

51. Kobayashi, K.; Huang, C.-i.; Lodge, T. P. Thermoreversible Gelation of Aqueous Methylcellulose Solutions. *Macromolecules* 1999, 32, 7070-7077.

52. Cardinaux, F.; Gibaud, T.; Stradner, A.; Schurtenberger, P. Interplay between Spinodal Decomposition and Glass Formation in Proteins Exhibiting Short-Range Attractions. *Physical Review Letters* 2007, 99, 118301.

53. Glassman, M. J.; Olsen, B. D. Arrested Phase Separation of Elastin-Like Polypeptide Solutions Yields Stiff, Thermoresponsive Gels. *Biomacromolecules* 2015, 16, 3762-3773.

54. Kumar, D. K.; Steed, J. W. Supramolecular Gel Phase Crystallization: Orthogonal Self-Assembly under Non-Equilibrium Conditions. *Chemical Society Reviews* 2014, 43, 2080-2088.

55. Gkikas, M.; Avery, R. K.; Olsen, B. D. Thermoresponsive and Mechanical Properties of Poly(L-Proline) Gels. *Biomacromolecules* 2016, 17, 399-406.

56. Teunissen, A. J. P.; Nieuwenhuizen, M. M. L.; Rodríguez-Llansola, F.; Palmans, A. R. A.; Meijer, E. W. Mechanically Induced Gelation of a Kinetically Trapped Supramolecular Polymer. *Macromolecules* 2014, 47, 8429-8436.

57. Leibler, L.; Rubinstein, M.; Colby, R. H. Dynamics of Reversible Networks. *Macromolecules* 1991, 24, 4701-4707.

58. Rubinstein, M.; Semenov, A. N. Thermoreversible Gelation in Solutions of Associating Polymers. 2. Linear Dynamics. *Macromolecules* 1998, 31, 1386-1397.

59. Semenov, A. N.; Rubinstein, M. Thermoreversible Gelation in Solutions of Associative Polymers. 1. Statics. *Macromolecules* 1998, 31, 1373-1385.

60. Rubinstein, M.; Semenov, A. N. Dynamics of Entangled Solutions of Associating Polymers. *Macromolecules* 2001, 34, 1058-1068.

61. Semenov, A. N.; Rubinstein, M. Dynamics of Entangled Associating Polymers with Large Aggregates. *Macromolecules* 2002, 35, 4821-4837.

62. Cates, M. E. Reptation of Living Polymers: Dynamics of Entangled Polymers in the Presence of Reversible Chain-Scission Reactions. *Macromolecules* 1987, 20, 2289-2296.

63. Cates, M. E.; Candau, S. J. Statics and Dynamics of Worm-Like Surfactant Micelles. *Journal of Physics: Condensed Matter* 1990, 2, 6869.

64. Chen, Q.; Tudryn, G. J.; Colby, R. H. Ionomer Dynamics and the Sticky Rouse Modela). *Journal of Rheology* 2013, 57, 1441-1462.

65. Hackelbusch, S.; Rossow, T.; van Assenbergh, P.; Seiffert, S. Chain Dynamics in Supramolecular Polymer Networks. *Macromolecules* 2013, 46, 6273-6286.

66. Rossow, T.; Habicht, A.; Seiffert, S. Relaxation and Dynamics in Transient Polymer Model Networks. *Macromolecules* 2014, 47, 6473-6482.

67. Rubinstein, M.; Colby, R. H. *Polymer Physics*. Oxford University Press: Oxford ; New York, 2003; p xi, 440 p.

68. Tanaka, F.; Edwards, S. F. Viscoelastic Properties of Physically Crosslinked Networks: Part 1. Non-Linear Stationary Viscoelasticity. *Journal of Non-Newtonian Fluid Mechanics* 1992, 43, 247-271.

69. Tanaka, F.; Edwards, S. F. Viscoelastic Properties of Physically Crosslinked Networks: Part 2. Dynamic Mechanical Moduli. *Journal of Non-Newtonian Fluid Mechanics* 1992, 43, 273-288.

70. Tanaka, F.; Edwards, S. F. Viscoelastic Properties of Physically Crosslinked Networks. *Journal of Non-Newtonian Fluid Mechanics* 1992, 43, 289-309.

71. van den Brule, B. H. A. A.; Hoogerbrugge, P. J. Brownian Dynamics Simulation of Reversible Polymeric Networks. *Journal of Non-Newtonian Fluid Mechanics* 1995, 60, 303-334.

72. Hernández Cifre, J. G.; Barenbrug, T. M. A. O. M.; Schieber, J. D.; van den Brule, B. H. A. A. Brownian Dynamics Simulation of Reversible Polymer Networks under Shear Using a Non-Interacting Dumbbell Model. *Journal of Non-Newtonian Fluid Mechanics* 2003, 113, 73-96.

73. Tripathi, A.; Tam, K. C.; McKinley, G. H. Rheology and Dynamics of Associative Polymers in Shear and Extension: Theory and Experiments. *Macromolecules* 2006, 39, 1981-1999.

74. Sing, M. K.; Wang, Z.-G.; McKinley, G. H.; Olsen, B. D. Celebrating Soft Matter's 10th Anniversary: Chain Configuration and Rate-Dependent Mechanical Properties in Transient Networks. *Soft Matter* 2015, 11, 2085-2096.

75. Xu, D.; Hawk, J. L.; Loveless, D. M.; Jeon, S. L.; Craig, S. L. Mechanism of Shear Thickening in Reversibly Cross-Linked Supramolecular Polymer Networks. *Macromolecules* 2010, 43, 3556-3565.

76. Xu, D.; Liu, C.-Y.; Craig, S. L. Divergent Shear Thinning and Shear Thickening Behavior of Supramolecular Polymer Networks in Semidilute Entangled Polymer Solutions. *Macromolecules* 2011, 44, 2343-2353.

77. Xu, D.; Craig, S. L. Strain Hardening and Strain Softening of Reversibly Cross-Linked Supramolecular Polymer Networks. *Macromolecules* 2011, 44, 7478-7488.

78. Shen, W.; Kornfield, J. A.; Tirrell, D. A. Structure and Mechanical Properties of Artificial Protein Hydrogels Assembled through Aggregation of Leucine Zipper Peptide Domains. *Soft Matter* 2007, 3, 99-107.

79. Shen, W.; Zhang, K.; Kornfield, J. A.; Tirrell, D. A. Tuning the Erosion Rate of Artificial Protein Hydrogels through Control of Network Topology. *Nat Mater* 2006, 5, 153-158.

80. Skrzeszewska, P. J.; de Wolf, F. A.; Werten, M. W. T.; Moers, A. P. H. A.; Cohen Stuart, M. A.; van der Gucht, J. Physical Gels of Telechelic Triblock Copolymers with Precisely Defined Junction Multiplicity. *Soft Matter* 2009, 5, 2057-2062.

81. Kumar, S. K.; Panagiotopoulos, A. Z. Thermodynamics of Reversibly Associating Polymer Solutions. *Physical Review Letters* 1999, 82, 5060-5063.

82. Hecht, A. M.; Duplessix, R.; Geissler, E. Structural Inhomogeneities in the Range 2.5-2500 .Ang. In Polyacrylamide Gels. *Macromolecules* 1985, 18, 2167-2173.

83. Hirokawa, Y.; Jinnai, H.; Nishikawa, Y.; Okamoto, T.; Hashimoto, T. Direct Observation of Internal Structures in Poly(N-Isopropylacrylamide) Chemical Gels. *Macromolecules* 1999, 32, 7093-7099.

84. Shibayama, M.; Tsujimoto, M.; Ikkai, F. Static Inhomogeneities in Physical Gels: Comparison of Temperature-Induced and Concentration-Induced Sol−Gel Transition. *Macromolecules* 2000, 33, 7868-7876.

85. Loppinet, B.; Stiakakis, E.; Vlassopoulos, D.; Fytas, G.; Roovers, J. Reversible Thermal Gelation in Star Polymers: An Alternative Route to Jamming of Soft Matter. *Macromolecules* 2001, 34, 8216-8223.

86. Rossow, T.; Seiffert, S. Supramolecular Polymer Gels with Potential Model-Network Structure. *Polymer Chemistry* 2014, 5, 3018-3029.

87. Malo de Molina, P.; Lad, S.; Helgeson, M. E. Heterogeneity and Its Influence on the Properties of Difunctional Poly(Ethylene Glycol) Hydrogels: Structure and Mechanics. *Macromolecules* 2015, 48, 5402-5411.

88. Di Lorenzo, F.; Seiffert, S. Nanostructural Heterogeneity in Polymer Networks and Gels. *Polymer Chemistry* 2015, 6, 5515-5528.

89. Bedrov, D.; Smith, G. D.; Douglas, J. F. Influence of Self-Assembly on Dynamical and Viscoelastic Properties of Telechelic Polymer Solutions. *EPL (Europhysics Letters)* 2002, 59, 384.

90. Odian, G. G. *Principles of Polymerization.* 4th ed.; Wiley-Interscience: Hoboken, N.J., 2004; p xxiv, 812 p.

91. Flory, P. J. Molecular Size Distribution in Three Dimensional Polymers. I. Gelation1. *Journal of the American Chemical Society* 1941, 63, 3083-3090.

92. Stockmayer, W. H. Theory of Molecular Size Distribution and Gel Formation in Branched - Chain Polymers. *The Journal of Chemical Physics* 1943, 11, 45-55.

93. Kujawa, P.; Audibert-Hayet, A.; Selb, J.; Candau, F. Rheological Properties of Multisticker Associative Polyelectrolytes in Semidilute Aqueous Solutions. *Journal of Polymer Science Part B: Polymer Physics* 2004, 42, 1640-1655.

94. Bokias, G.; Hourdet, D.; Iliopoulos, I. Positively Charged Amphiphilic Polymers Based on Poly(N-Isopropylacrylamide): Phase Behavior and Shear-Induced Thickening in Aqueous Solution. *Macromolecules* 2000, 33, 2929-2935.

95. Wong Po Foo, C. T. S.; Lee, J. S.; Mulyasasmita, W.; Parisi-Amon, A.; Heilshorn, S. C. Two-Component Protein-Engineered Physical Hydrogels for Cell Encapsulation. *Proceedings of the National Academy of Sciences* 2009, 106, 22067-22072.

96. Kumar, S. K.; Douglas, J. F. Gelation in Physically Associating Polymer Solutions. *Physical Review Letters* 2001, 87, 188301.

97. Liu, Y.; Lloyd, A.; Guzman, G.; Cavicchi, K. A. Polyelectrolyte–Surfactant Complexes as Thermoreversible Organogelators. *Macromolecules* 2011, 44, 8622-8630.

98. Zhou, X.; Wu, X.; Wang, H.; Liu, C.; Zhu, Z. Phase Diagram of the Pluronic L64\Char21{}H${}_{2}$O Micellar System from Mechanical Spectroscopy. *Physical Review E* 2011, 83, 041801.

99. Hamley, I. Concentrated Solutions. In *Block Copolymers in Solution: Fundamentals and Applications*, John Wiley & Sons, Ltd: 2005; pp 105-172.

100. Xiong, J.-Y.; Narayanan, J.; Liu, X.-Y.; Chong, T. K.; Chen, S. B.; Chung, T.-S. Topology Evolution and Gelation Mechanism of Agarose Gel. *The Journal of Physical Chemistry B* 2005, 109, 5638-5643.

101. Comper, W. D.; Veis, A. The Mechanism of Nucleation for in Vitro Collagen Fibril Formation. *Biopolymers* 1977, 16, 2113-2131.

102. Djabourov, M. Architecture of Gelatin Gels. *Contemporary Physics* 1988, 29, 273-297.

103. Xu, D.; Craig, S. L. Scaling Laws in Supramolecular Polymer Networks. *Macromolecules* 2011, 44, 5465-5472.

104. Feldman, K. E.; Kade, M. J.; Meijer, E. W.; Hawker, C. J.; Kramer, E. J. Model Transient Networks from Strongly Hydrogen-Bonded Polymers. *Macromolecules* 2009, 42, 9072-9081.

105. Kujawa, P.; Audibert-Hayet, A.; Selb, J.; Candau, F. Effect of Ionic Strength on the Rheological Properties of Multisticker Associative Polyelectrolytes. *Macromolecules* 2006, 39, 384-392.

106. Sijbesma, R. P.; Beijer, F. H.; Brunsveld, L.; Folmer, B. J. B.; Hirschberg, J. H. K. K.; Lange, R. F. M.; Lowe, J. K. L.; Meijer, E. W. Reversible Polymers Formed from Self-Complementary Monomers Using Quadruple Hydrogen Bonding. *Science* 1997, 278, 1601-1604.

107. Hirschberg, J. H. K. K.; Beijer, F. H.; van Aert, H. A.; Magusin, P. C. M. M.; Sijbesma, R. P.; Meijer, E. W. Supramolecular Polymers from Linear Telechelic Siloxanes with Quadruple-Hydrogen-Bonded Units. *Macromolecules* 1999, 32, 2696-2705.

108. Xu, J.; Fogleman, E. A.; Craig, S. L. Structure and Properties of DNA-Based Reversible Polymers. *Macromolecules* 2004, 37, 1863-1870.

109. Rao, B.; Uemura, Y.; Dyke, L.; Macdonald, P. M. Self-Diffusion Coefficients of Hydrophobic Ethoxylated Urethane Associating Polymers Using Pulsed-Gradient Spin-Echo Nuclear Magnetic Resonance. *Macromolecules* 1995, 28, 531-538.

110. Joabsson, F.; Nydén, M.; Thuresson, K. Temperature-Induced Fractionation of a Quasi-Binary Self-Associating Polymer Solution. A Phase Behavior and Polymer Self-Diffusion Investigation. *Macromolecules* 2000, 33, 6772-6779.

111. Green, M. S.; Tobolsky, A. V. A New Approach to the Theory of Relaxing Polymeric Media. *The Journal of Chemical Physics* 1946, 14, 80-92.

112. Tanaka, F.; Edwards, S. F. Viscoelastic Properties of Physically Crosslinked Networks. 1. Transient Network Theory. *Macromolecules* 1992, 25, 1516-1523.

113. Annable, T.; Buscall, R.; Ettelaie, R.; Whittlestone, D. The Rheology of Solutions of Associating Polymers: Comparison of Experimental Behavior with Transient Network Theory. *Journal of Rheology* 1993, 37, 695-726.

114. Guo, L.; Luijten, E. Reversible Gel Formation of Triblock Copolymers Studied by Molecular Dynamics Simulation. *Journal of Polymer Science Part B: Polymer Physics* 2005, 43, 959-969.

115. Groot, R. D.; Agterof, W. G. M. Dynamic Viscoelastic Modulus of Associative Polymer Networks: Off-Lattice Simulations, Theory and Comparison to Experiments. *Macromolecules* 1995, 28, 6284-6295.

116. Hoy, R. S.; Fredrickson, G. H. Thermoreversible Associating Polymer Networks. I. Interplay of Thermodynamics, Chemical Kinetics, and Polymer Physics. *The Journal of Chemical Physics* 2009, 131, 224902.

117. Ng, W. K.; Tam, K. C.; Jenkins, R. D. Lifetime and Network Relaxation Time of a Heur-C20 Associative Polymer System. *Journal of Rheology* 2000, 44, 137-147.

118. Uneyama, T.; Suzuki, S.; Watanabe, H. Concentration Dependence of Rheological Properties of Telechelic Associative Polymer Solutions. *Physical Review E* 2012, 86, 031802.

119. Zhao, Y.; Beck, J. B.; Rowan, S. J.; Jamieson, A. M. Rheological Behavior of Shear-Responsive Metallo-Supramolecular Gels. *Macromolecules* 2004, 37, 3529-3531.

120. Kim, M.; Tang, S.; Olsen, B. D. Physics of Engineered Protein Hydrogels. *Journal of Polymer Science Part B: Polymer Physics* 2013, 51, 587-601.

121. Zhou, H.; Woo, J.; Cok, A. M.; Wang, M.; Olsen, B. D.; Johnson, J. A. Counting Primary Loops in Polymer Gels. *Proceedings of the National Academy of Sciences* 2012, 109, 19119-19124.

122. Zhou, H.; Schön, E.-M.; Wang, M.; Glassman, M. J.; Liu, J.; Zhong, M.; Díaz Díaz, D.; Olsen, B. D.; Johnson, J. A. Crossover Experiments Applied to Network Formation Reactions: Improved Strategies for Counting Elastically Inactive Molecular Defects in Peg Gels and Hyperbranched Polymers. *Journal of the American Chemical Society* 2014, 136, 9464-9470.

123. Kawamoto, K.; Zhong, M.; Wang, R.; Olsen, B. D.; Johnson, J. A. Loops Versus Branch Functionality in Model Click Hydrogels. *Macromolecules* 2015, 48, 8980-8988.

124. Lange, F.; Schwenke, K.; Kurakazu, M.; Akagi, Y.; Chung, U.-i.; Lang, M.; Sommer, J.-U.; Sakai, T.; Saalwächter, K. Connectivity and Structural Defects in Model Hydrogels: A Combined Proton Nmr and Monte Carlo Simulation Study. *Macromolecules* 2011, 44, 9666-9674.

125. Samiullah, M. H.; Reichert, D.; Zinkevich, T.; Kressler, J. Nmr Characterization of Peg Networks Synthesized by Cuaac Using Reactive Oligomers. *Macromolecules* 2013, 46, 6922-6930.

126. Head, D. A.; Levine, A. J.; MacKintosh, F. C. Deformation of Cross-Linked Semiflexible Polymer Networks. *Physical Review Letters* 2003, 91, 108102.

127. Storm, C.; Pastore, J. J.; MacKintosh, F. C.; Lubensky, T. C.; Janmey, P. A. Nonlinear Elasticity in Biological Gels. *Nature* 2005, 435, 191-194.

128. Yount, W. C.; Loveless, D. M.; Craig, S. L. Small-Molecule Dynamics and Mechanisms Underlying the Macroscopic Mechanical Properties of Coordinatively Cross-Linked Polymer Networks. *Journal of the American Chemical Society* 2005, 127, 14488-14496.

129. Shen, W.; Kornfield, J. A.; Tirrell, D. A. Dynamic Properties of Artificial Protein Hydrogels Assembled through Aggregation of Leucine Zipper Peptide Domains. *Macromolecules* 2007, 40, 689-692.

130. Yount, W. C.; Loveless, D. M.; Craig, S. L. Strong Means Slow: Dynamic Contributions to the Bulk Mechanical Properties of Supramolecular Networks. *Angewandte Chemie International Edition* 2005, 44, 2746-2748.

Chapter 2 Methods

Some parts of the following sections are reproduced with permission from the following publications: (1) S. Tang et al., *Macromolecules* **2014**, 1130; (2) S. Tang et al., *Front. Chem.* **2014**, 2:23; (3) S. Tang et al., *J. Am. Chem. Soc.* **2015**, 3946.

2.1. Expression and purification of coiled-coil proteins

2.1.1. Protein structure and genetic information

Three artificially engineered proteins with associative coiled-coil domains are used in this thesis, which are named as Cys-P_4-Cys, Cys-P_4 and P_4 (Figure 2-1). These protein polymers share the same backbone structure, but differ from each other by the number of cysteine residues near the C- and N- termini. The protein sequences were created by Dr. Matthew Glassman. The genetic codes and amino acid sequences can be found as referenced[1-3], and they are shown below for completeness. The genes encoding the proteins of intereste were flanked with *Bam*HI and *Hin*dIII restriction sites and incorporated into the pQE9 plasmid (Qiagen) after a double digestion and ligation. All of the genes have an N-terminal 6×His-tag. The constructed plasmids were transformed into the SG13009 strain of *Escherichia coli* for protein expression.

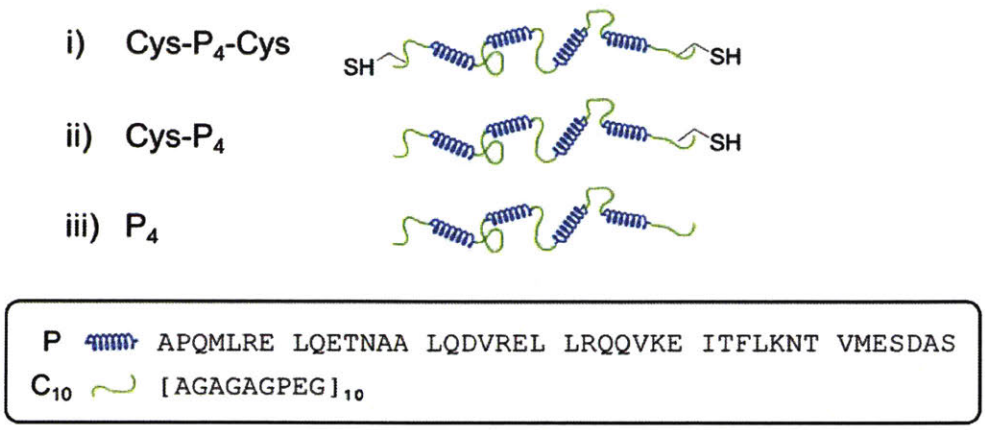

Figure 2-1. Structure and sequence of the associative coiled-coil proteins used in this thesis. (i) Cys-P_4-Cys, (ii) Cys-P_4 and (iii) P_4.

(i) Cys-P_4-Cys

Complete plasmid sequence (the genes encoding Cys-P_4-Cys highlighted in blue text)

CTCGAGAAATCATAAAAAATTTATTTGCTTTGTGAGCGGATAACAATTATAATAGATTCAATTGTGAG
CGGATAACAATTTCACACAGAATTCATTAAAGAGGAGAAATTAACTATGAGAGGATCGCATCACCATC
ACCATCACGGATCCGATGACGATGACAAATGTACTAGCTATCGCGATCCGATGGGTGCCGGCGCTGGT
GCGGGCCCGGAAGGTGCAGGCGCTGGTGCGGGCCCGGAAGGTGCCGGCGCTGGTGCGGGCCCGGAAG
GTGCAGGCGCTGGTGCGGGCCCGGAAGGTGCCGGCGCTGGTGCGGGCCCGGAAGGTGCAGGCGCTGG
TGCGGGCCCGGAAGGTGCCGGCGCTGGTGCGGGCCCGGAAGGTGCAGGCGCTGGTGCGGGCCCGGAA
GGTGCCGGCGCTGGTGCGGGCCCGGAAGGTGCAGGCGCTGGTGCGGGCCCGGAAGGTGCCCGCATGC
CGACTAGCGCGCCGCAGATGCTGCGTGAACTGCAGGAAACCAACGCGGCGCTGCAGGACGTTCGTGA
ACTGCTGCGTCAGCAGGTTAAAGAAATCACCTTCCTGAAAAACACCGTTATGGAATCTGACGCGTCTG
GTACTAGCTATCGCGATCCGATGGGTGCCGGCGCTGGTGCGGGCCCGGAAGGTGCAGGCGCTGGTGCG
GGCCCGGAAGGTGCCGGCGCTGGTGCGGGCCCGGAAGGTGCAGGCGCTGGTGCGGGCCCGGAAGGTG
CCGGCGCTGGTGCGGGCCCGGAAGGTGCAGGCGCTGGTGCGGGCCCGGAAGGTGCCGGCGCTGGTGC
GGGCCCGGAAGGTGCAGGCGCTGGTGCGGGCCCGGAAGGTGCCGGCGCTGGTGCGGGCCCGGAAGGT
GCAGGCGCTGGTGCGGGCCCGGAAGGTGCCCGCATGCCGACTAGCGCGCCGCAGATGCTGCGTGAAC
TGCAGGAAACCAACGCGGCGCTGCAGGACGTTCGTGAACTGCTGCGTCAGCAGGTTAAAGAAATCAC
CTTCCTGAAAAACACCGTTATGGAATCTGACGCGTCTGGTACTAGCTATCGCGATCCGATGGGTGCCG
GCGCTGGTGCGGGCCCGGAAGGTGCAGGCGCTGGTGCGGGCCCGGAAGGTGCCGGCGCTGGTGCGGG
CCCGGAAGGTGCAGGCGCTGGTGCGGGCCCGGAAGGTGCCGGCGCTGGTGCGGGCCCGGAAGGTGCA
GGCGCTGGTGCGGGCCCGGAAGGTGCCGGCGCTGGTGCGGGCCCGGAAGGTGCAGGCGCTGGTGCGG
GCCCGGAAGGTGCCGGCGCTGGTGCGGGCCCGGAAGGTGCAGGCGCTGGTGCGGGCCCGGAAGGTGC
CCGCATGCCGACTAGCGCGCCGCAGATGCTGCGTGAACTGCAGGAAACCAACGCGGCGCTGCAGGAC
GTTCGTGAACTGCTGCGTCAGCAGGTTAAAGAAATCACCTTCCTGAAAAACACCGTTATGGAATCTGA
CGCGTCTGGTACTAGCTATCGCGATCCGATGGGTGCCGGCGCTGGTGCGGGCCCGGAAGGTGCAGGCG
CTGGTGCGGGCCCGGAAGGTGCCGGCGCTGGTGCGGGCCCGGAAGGTGCAGGCGCTGGTGCGGGCCC
GGAAGGTGCCGGCGCTGGTGCGGGCCCGGAAGGTGCAGGCGCTGGTGCGGGCCCGGAAGGTGCCGGC

GCTGGTGCGGGCCCGGAAGGTGCAGGCGCTGGTGCGGGCCCGGAAGGTGCCGGCGCTGGTGCGGGCC
CGGAAGGTGCAGGCGCTGGTGCGGGCCCGGAAGGTGCCCGCATGCCGACTAGCGCGCCGCAGATGCT
GCGTGAACTGCAGGAAACCAACGCGGCGCTGCAGGACGTTCGTGAACTGCTGCGTCAGCAGGTTAAA
GAAATCACCTTCCTGAAAAACACCGTTATGGAATCTGACGCGTCTGGTACTAGCTATCGCGATCCGAT
GGGTGCCGGCGCTGGTGCGGGCCCGGAAGGTGCAGGCGCTGGTGCGGGCCCGGAAGGTGCCGGCGCT
GGTGCGGGCCCGGAAGGTGCAGGCGCTGGTGCGGGCCCGGAAGGTGCCGGCGCTGGTGCGGGCCCGG
AAGGTGCAGGCGCTGGTGCGGGCCCGGAAGGTGCCGGCGCTGGTGCGGGCCCGGAAGGTGCAGGCGC
TGGTGCGGGCCCGGAAGGTGCCGGCGCTGGTGCGGGCCCGGAAGGTGCAGGCGCTGGTGCGGGCCCG
GAAGGTGCCCGCATGCCGACTAGTTGTAAGCTTAATTAGCTGAGCTTGGACTCCTGTTGATAGATCCA
GTAATGACCTCAGAACTCCATCTGGATTTGTTCAGAACGCTCGGTTGCCGCCGGGCGTTTTTTATTGGT
GAGAATCCAAGCTAGCTTGGCGAGATTTTCAGGAGCTAAGGAAGCTAAAATGGAGAAAAAAATCACT
GGATATACCACCGTTGATATATCCCAATGGCATCGTAAAGAACATTTTGAGGCATTTCAGTCAGTTGCT
CAATGTACCTATAACCAGACCGTTCAGCTGGATATTACGGCCTTTTTAAAGACCGTAAAGAAAAATAA
GCACAAGTTTTATCCGGCCTTTATTCACATTCTTGCCCGCCTGATGAATGCTCATCCGGAATTTCGTAT
GGCAATGAAAGACGGTGAGCTGGTGATATGGGATAGTGTTCACCCTTGTTACACCGTTTTCCATGAGC
AAACTGAAACGTTTTCATCGCTCTGGAGTGAATACCACGACGATTTCCGGCAGTTTCTACACATATATT
CGCAAGATGTGGCGTGTTACGGTGAAAACCTGGCCTATTTCCCTAAAGGGTTTATTGAGAATATGTTTT
TCGTCTCAGCCAATCCCTGGGTGAGTTTCACCAGTTTTGATTTAAACGTGGCCAATATGGACAACTTCT
TCGCCCCCGTTTTCACCATGGGCAAATATTATACGCAAGGCGACAAGGTGCTGATGCCGCTGGCGATT
CAGGTTCATCATGCCGTTTGTGATGGCTTCCATGTCGGCAGAATGCTTAATGAATTACAACAGTACTGC
GATGAGTGGCAGGGCGGGGCGTAATTTTTTTAAGGCAGTTATTGGTGCCCTTAAACGCCTGGGGTAAT
GACTCTCTAGCTTGAGGCATCAAATAAAACGAAAGGCTCAGTCGAAAGACTGGGCCTTTCGTTTTATC
TGTTGTTTGTCGGTGAACGCTCTCCTGAGTAGGACAAATCCGCCCTCTAGAGCTGCCTCGCGCGTTTCG
GTGATGACGGTGAAAACCTCTGACACATGCAGCTCCCGGAGACGGTCACAGCTTGTCTGTAAGCGGAT
GCCGGGAGCAGACAAGCCCGTCAGGGCGCGTCAGCGGGTGTTGGCGGGTGTCGGGGCGCAGCCATGA
CCCAGTCACGTAGCGATAGCGGAGTGTATACTGGCTTAACTATGCGGCATCAGAGCAGATTGTACTGA
GAGTGCACCATATGCGGTGTGAAATACCGCACAGATGCGTAAGGAGAAAATACCGCATCAGGCGCTC
TTCCGCTTCCTCGCTCACTGACTCGCTGCGCTCGGTCGTTCGGCTGCGGCGAGCGGTATCAGCTCACTC
AAAGGCGGTAATACGGTTATCCACAGAATCAGGGGATAACGCAGGAAAGAACATGTGAGCAAAAGGC
CAGCAAAAGGCCAGGAACCGTAAAAAGGCCGCGTTGCTGGCGTTTTTCCATAGGCTCCGCCCCCCTGA
CGAGCATCACAAAAATCGACGCTCAAGTCAGAGGTGGCGAAACCCGACAGGACTATAAAGATACCAG
GCGTTTCCCCCTGGAAGCTCCCTCGTGCGCTCTCCTGTTCCGACCCTGCCGCTTACCGGATACCTGTCC
GCCTTTCTCCCTTCGGGAAGCGTGGCGCTTTCTCATAGCTCACGCTGTAGGTATCTCAGTTCGGTGTAG
GTCGTTCGCTCCAAGCTGGGCTGTGTGCACGAACCCCCCGTTCAGCCCGACCGCTGCGCCTTATCCGGT
AACTATCGTCTTGAGTCCAACCCGGTAAGACACGACTTATCGCCACTGGCAGCAGCCACTGGTAACAG
GATTAGCAGAGCGAGGTATGTAGGCGGTGCTACAGAGTTCTTGAAGTGGTGGCCTAACTACGGCTACA
CTAGAAGGACAGTATTTGGTATCTGCGCTCTGCTGAAGCCAGTTACCTTCGGAAAAAGAGTTGGTAGC
TCTTGATCCGGCAAACAAACCACCGCTGGTAGCGGTGGTTTTTTTGTTTGCAAGCAGCAGATTACGCGC
AGAAAAAAAGGATCTCAAGAAGATCCTTTGATCTTTTCTACGGGGTCTGACGCTCAGTGGAACGAAAA
CTCACGTTAAGGGATTTTGGTCATGAGATTATCAAAAAGGATCTTCACCTAGATCCTTTTAAATTAAAA
ATGAAGTTTTAAATCAATCTAAAGTATATATGAGTAAACTTGGTCTGACAGTTACCAATGCTTAATCAG
TGAGGCACCTATCTCAGCGATCTGTCTATTTCGTTCATCCATAGTTGCCTGACTCCCCGTCGTGTAGAT
AACTACGATACGGGAGGGCTTACCATCTGGCCCCAGTGCTGCAATGATACCGCGAGACCCACGCTCAC
CGGCTCCAGATTTATCAGCAATAAACCAGCCAGCCGGAAGGGCCGAGCGCAGAAGTGGTCCTGCAAC
TTTATCCGCCTCCATCCAGTCTATTAATTGTTGCCGGGAAGCTAGAGTAAGTAGTTCGCCAGTTAATAG
TTTGCGCAACGTTGTTGCCATTGCTACAGGCATCGTGGTGTCACGCTCGTCGTTTGGTATGGCTTCATT
CAGCTCCGGTTCCCAACGATCAAGGCGAGTTACATGATCCCCCATGTTGTGCAAAAAAGCGGTTAGCT
CCTTCGGTCCTCCGATCGTTGTCAGAAGTAAGTTGGCCGCAGTGTTATCACTCATGGTTATGGCAGCAC
TGCATAATTCTCTTACTGTCATGCCATCCGTAAGATGCTTTTCTGTGACTGGTGAGTACTCAACCAAGT
CATTCTGAGAATAGTGTATGCGGCGACCGAGTTGCTCTTGCCCGGCGTCAATACGGGATAATACCGCG
CCACATAGCAGAACTTTAAAAGTGCTCATCATTGGAAAACGTTCTTCGGGGCGAAAACTCTCAAGGAT
CTTACCGCTGTTGAGATCCAGTTCGATGTAACCCACTCGTGCACCCAACTGATCTTCAGCATCTTTTAC
TTTCACCAGCGTTTCTGGGTGAGCAAAAACAGGAAGGCAAAATGCCGCAAAAAAGGGAATAAGGGCG
ACACGGAAATGTTGAATACTCATACTCTTCCTTTTTCAATATTATTGAAGCATTTATCAGGGTTATTGTC
TCATGAGCGGATACATATTTGAATGTATTTAGAAAAATAAACAAATAGGGGTTCCGCGCACATTTCCC

CGAAAAGTGCCACCTGACGTCTAAGAAACCATTATTATCATGACATTAACCTATAAAAATAGGCGTAT
CACGAGGCCCTTTCGTCTTCAC

Amino acid sequence

MRGSHHHHHHGSDDDDKCTSYRDPMGAGAGAGPEGAGAGAGPEGAGAGAGPEGAG

AGAGPEGAGAGAGPEGAGAGAGPEGAGAGAGPEGAGAGAGPEGAGAGAGPEGAGAG

AGPEGARMPTSAPQMLRELQETNAALQDVRELLRQQVKEITFLKNTVMESDASGTSYR

DPMGAGAGAGPEGAGAGAGPEGAGAGAGPEGAGAGAGPEGAGAGAGPEGAGAGAGP

EGAGAGAGPEGAGAGAGPEGAGAGAGPEGAGAGAGPEGARMPTSAPQMLRELQETN

AALQDVRELLRQQVKEITFLKNTVMESDASGTSYRDPMGAGAGAGPEGAGAGAGPEG

AGAGAGPEGAGAGAGPEGAGAGAGPEGAGAGAGPEGAGAGAGPEGAGAGAGPEGAG

AGAGPEGAGAGAGPEGARMPTSAPQMLRELQETNAALQDVRELLRQQVKEITFLKNTV

MESDASGTSYRDPMGAGAGAGPEGAGAGAGPEGAGAGAGPEGAGAGAGPEGAGAGA

GPEGAGAGAGPEGAGAGAGPEGAGAGAGPEGAGAGAGPEGAGAGAGPEGARMPTSA

PQMLRELQETNAALQDVRELLRQQVKEITFLKNTVMESDASGTSYRDPMGAGAGAGPE

GAGAGAGPEGAGAGAGPEGAGAGAGPEGAGAGAGPEGAGAGAGPEGAGAGAGPEGA

GAGAGPEGAGAGAGPEGAGAGAGPEGARMPTSCKLN*

(ii) Cys-P_4

Complete plasmid sequence (the genes encoding Cys-P_4 highlighted in blue text)

CTCGAGAAATCATAAAAAATTTATTTGCTTTGTGAGCGGATAACAATTATAATAGATTCAATTGTGAG
CGGATAACAATTTCACACAGAATTCATTAAAGAGGAGAAATTAACTATGAGAGGATCGCATCACCATC
ACCATCACGGATCCGATGACGATGACAAAACTAGCTATCGCGATCCGATGGGTGCCGGCGCTGGTGCG
GGCCCGGAAGGTGCAGGCGCTGGTGCGGGCCCGGAAGGTGCCGGCGCTGGTGCGGGCCCGGAAGGTG
CAGGCGCTGGTGCGGGCCCGGAAGGTGCCGGCGCTGGTGCGGGCCCGGAAGGTGCAGGCGCTGGTGC
GGGCCCGGAAGGTGCCGGCGCTGGTGCGGGCCCGGAAGGTGCAGGCGCTGGTGCGGGCCCGGAAGGT
GCCGGCGCTGGTGCGGGCCCGGAAGGTGCAGGCGCTGGTGCGGGCCCGGAAGGTGCCCGCATGCCGA
CTAGCGCGCCGCAGATGCTGCGTGAACTGCAGGAAACCAACGCGGCGCTGCAGGACGTTCGTGAACT
GCTGCGTCAGCAGGTTAAAGAAATCACCTTCCTGAAAAACACCGTTATGGAATCTGACGCGTCTGGTA
CTAGCTATCGCGATCCGATGGGTGCCGGCGCTGGTGCGGGCCCGGAAGGTGCAGGCGCTGGTGCGGG

CCCGGAAGGTGCCGGCGCTGGTGCGGGCCCGGAAGGTGCAGGCGCTGGTGCGGGCCCGGAAGGTGCC
GGCGCTGGTGCGGGCCCGGAAGGTGCAGGCGCTGGTGCGGGCCCGGAAGGTGCCGGCGCTGGTGCGG
GCCCGGAAGGTGCAGGCGCTGGTGCGGGCCCGGAAGGTGCCGGCGCTGGTGCGGGCCCGGAAGGTGC
AGGCGCTGGTGCGGGCCCGGAAGGTGCCCGCATGCCGACTAGCGCGCCGCAGATGCTGCGTGAACTG
CAGGAAACCAACGCGGCGCTGCAGGACGTTCGTGAACTGCTGCGTCAGCAGGTTAAAGAAATCACCTT
CCTGAAAAACACCGTTATGGAATCTGACGCGTCTGGTACTAGCTATCGCGATCCGATGGGTGCCGGCG
CTGGTGCGGGCCCGGAAGGTGCAGGCGCTGGTGCGGGCCCGGAAGGTGCCGGCGCTGGTGCGGGCCC
GGAAGGTGCAGGCGCTGGTGCGGGCCCGGAAGGTGCCGGCGCTGGTGCGGGCCCGGAAGGTGCAGGC
GCTGGTGCGGGCCCGGAAGGTGCCGGCGCTGGTGCGGGCCCGGAAGGTGCAGGCGCTGGTGCGGGCC
CGGAAGGTGCCGGCGCTGGTGCGGGCCCGGAAGGTGCAGGCGCTGGTGCGGGCCCGGAAGGTGCCCG
CATGCCGACTAGCGCGCCGCAGATGCTGCGTGAACTGCAGGAAACCAACGCGGCGCTGCAGGACGTT
CGTGAACTGCTGCGTCAGCAGGTTAAAGAAATCACCTTCCTGAAAAACACCGTTATGGAATCTGACGC
GTCTGGTACTAGCTATCGCGATCCGATGGGTGCCGGCGCTGGTGCGGGCCCGGAAGGTGCAGGCGCTG
GTGCGGGCCCGGAAGGTGCCGGCGCTGGTGCGGGCCCGGAAGGTGCAGGCGCTGGTGCGGGCCCGGA
AGGTGCCGGCGCTGGTGCGGGCCCGGAAGGTGCAGGCGCTGGTGCGGGCCCGGAAGGTGCCGGCGCT
GGTGCGGGCCCGGAAGGTGCAGGCGCTGGTGCGGGCCCGGAAGGTGCCGGCGCTGGTGCGGGCCCGG
AAGGTGCAGGCGCTGGTGCGGGCCCGGAAGGTGCCCGCATGCCGACTAGCGCGCCGCAGATGCTGCG
TGAACTGCAGGAAACCAACGCGGCGCTGCAGGACGTTCGTGAACTGCTGCGTCAGCAGGTTAAAGAA
ATCACCTTCCTGAAAAACACCGTTATGGAATCTGACGCGTCTGGTACTAGCTATCGCGATCCGATGGG
TGCCGGCGCTGGTGCGGGCCCGGAAGGTGCAGGCGCTGGTGCGGGCCCGGAAGGTGCCGGCGCTGGT
GCGGGCCCGGAAGGTGCAGGCGCTGGTGCGGGCCCGGAAGGTGCCGGCGCTGGTGCGGGCCCGGAAG
GTGCAGGCGCTGGTGCGGGCCCGGAAGGTGCCGGCGCTGGTGCGGGCCCGGAAGGTGCAGGCGCTGG
TGCGGGCCCGGAAGGTGCCGGCGCTGGTGCGGGCCCGGAAGGTGCAGGCGCTGGTGCGGGCCCGGAA
GGTGCCCGCATGCCGACTAGTTGTAAGCTTAATTAGCTGAGCTTGGACTCCTGTTGATAGATCCAGTAA
TGACCTCAGAACTCCATCTGGATTTGTTCAGAACGCTCGGTTGCCGCCGGGCGTTTTTTATTGGTGAGA
ATCCAAGCTAGCTTGGCGAGATTTTCAGGAGCTAAGGAAGCTAAAATGGAGAAAAAAATCACTGGAT
ATACCACCGTTGATATATCCCAATGGCATCGTAAAGAACATTTTGAGGCATTTCAGTCAGTTGCTCAAT
GTACCTATAACCAGACCGTTCAGCTGGATATTACGGCCTTTTTAAAGACCGTAAAGAAAAATAAGCAC
AAGTTTTATCCGGCCTTTATTCACATTCTTGCCCGCCTGATGAATGCTCATCCGGAATTTCGTATGGCA
ATGAAAGACGGTGAGCTGGTGATATGGGATAGTGTTCACCCTTGTTACACCGTTTTCCATGAGCAAAC
TGAAACGTTTTCATCGCTCTGGAGTGAATACCACGACGATTTCCGGCAGTTTCTACACATATATTCGCA
AGATGTGGCGTGTTACGGTGAAAACCTGGCCTATTTCCCTAAAGGGTTTATTGAGAATATGTTTTTCGT
CTCAGCCAATCCCTGGGTGAGTTTCACCAGTTTTGATTTAAACGTGGCCAATATGGACAACTTCTTCGC
CCCCGTTTTCACCATGGGCAAATATTATACGCAAGGCGACAAGGTGCTGATGCCGCTGGCGATTCAGG
TTCATCATGCCGTTTGTGATGGCTTCCATGTCGGCAGAATGCTTAATGAATTACAACAGTACTGCGATG
AGTGGCAGGGCGGGGCGTAATTTTTTTAAGGCAGTTATTGGTGCCCTTAAACGCCTGGGGTAATGACT
CTCTAGCTTGAGGCATCAAATAAAACGAAAGGCTCAGTCGAAAGACTGGGCCTTTCGTTTTATCTGTT
GTTTGTCGGTGAACGCTCTCCTGAGTAGGACAAATCCGCCCTCTAGAGCTGCCTCGCGCGTTTCGGTGA
TGACGGTGAAAACCTCTGACACATGCAGCTCCCGGAGACGGTCACAGCTTGTCTGTAAGCGGATGCCG
GGAGCAGACAAGCCCGTCAGGGCGCGTCAGCGGGTGTTGGCGGGTGTCGGGGCGCAGCCATGACCCA
GTCACGTAGCGATAGCGGAGTGTATACTGGCTTAACTATGCGGCATCAGAGCAGATTGTACTGAGAGT
GCACCATATGCGGTGTGAAATACCGCACAGATGCGTAAGGAGAAAATACCGCATCAGGCGCTCTTCCG
CTTCCTCGCTCACTGACTCGCTGCGCTCGGTCGTTCGGCTGCGGCGAGCGGTATCAGCTCACTCAAAGG
CGGTAATACGGTTATCCACAGAATCAGGGGATAACGCAGGAAAGAACATGTGAGCAAAAGGCCAGCA
AAAGGCCAGGAACCGTAAAAAGGCCGCGTTGCTGGCGTTTTTCCATAGGCTCCGCCCCCCTGACGAGC
ATCACAAAAATCGACGCTCAAGTCAGAGGTGGCGAAACCCGACAGGACTATAAAGATACCAGGCGTT
TCCCCCTGGAAGCTCCCTCGTGCGCTCTCCTGTTCCGACCCTGCCGCTTACCGGATACCTGTCCGCCTTT
CTCCCTTCGGGAAGCGTGGCGCTTTCTCATAGCTCACGCTGTAGGTATCTCAGTTCGGTGTAGGTCGTT
CGCTCCAAGCTGGGCTGTGTGCACGAACCCCCCGTTCAGCCCGACCGCTGCGCCTTATCCGGTAACTAT
CGTCTTGAGTCCAACCCGGTAAGACACGACTTATCGCCACTGGCAGCAGCCACTGGTAACAGGATTAG
CAGAGCGAGGTATGTAGGCGGTGCTACAGAGTTCTTGAAGTGGTGGCCTAACTACGGCTACACTAGAA
GGACAGTATTTGGTATCTGCGCTCTGCTGAAGCCAGTTACCTTCGGAAAAAGAGTTGGTAGCTCTTGAT
CCGGCAAACAAACCACCGCTGGTAGCGGTGGTTTTTTTGTTTGCAAGCAGCAGATTACGCGCAGAAAA
AAAGGATCTCAAGAAGATCCTTTGATCTTTTCTACGGGGTCTGACGCTCAGTGGAACGAAAACTCACG
TTAAGGGATTTTGGTCATGAGATTATCAAAAAGGATCTTCACCTAGATCCTTTTAAATTAAAAATGAA
GTTTTAAATCAATCTAAAGTATATATGAGTAAACTTGGTCTGACAGTTACCAATGCTTAATCAGTGAGG

CACCTATCTCAGCGATCTGTCTATTTCGTTCATCCATAGTTGCCTGACTCCCCGTCGTGTAGATAACTAC
GATACGGGAGGGCTTACCATCTGGCCCCAGTGCTGCAATGATACCGCGAGACCCACGCTCACCGGCTC
CAGATTTATCAGCAATAAACCAGCCAGCCGGAAGGGCCGAGCGCAGAAGTGGTCCTGCAACTTTATCC
GCCTCCATCCAGTCTATTAATTGTTGCCGGGAAGCTAGAGTAAGTAGTTCGCCAGTTAATAGTTTGCGC
AACGTTGTTGCCATTGCTACAGGCATCGTGGTGTCACGCTCGTCGTTTGGTATGGCTTCATTCAGCTCC
GGTTCCCAACGATCAAGGCGAGTTACATGATCCCCCATGTTGTGCAAAAAAGCGGTTAGCTCCTTCGG
TCCTCCGATCGTTGTCAGAAGTAAGTTGGCCGCAGTGTTATCACTCATGGTTATGGCAGCACTGCATAA
TTCTCTTACTGTCATGCCATCCGTAAGATGCTTTTCTGTGACTGGTGAGTACTCAACCAAGTCATTCTG
AGAATAGTGTATGCGGCGACCGAGTTGCTCTTGCCCGGCGTCAATACGGGATAATACCGCGCCACATA
GCAGAACTTTAAAAGTGCTCATCATTGGAAAACGTTCTTCGGGGCGAAAACTCTCAAGGATCTTACCG
CTGTTGAGATCCAGTTCGATGTAACCCACTCGTGCACCCAACTGATCTTCAGCATCTTTTACTTTCACC
AGCGTTTCTGGGTGAGCAAAAACAGGAAGGCAAAATGCCGCAAAAAAGGGAATAAGGGCGACACGG
AAATGTTGAATACTCATACTCTTCCTTTTTCAATATTATTGAAGCATTTATCAGGGTTATTGTCTCATGA
GCGGATACATATTTGAATGTATTTAGAAAAATAAACAAATAGGGGTTCCGCGCACATTTCCCCGAAAA
GTGCCACCTGACGTCTAAGAAACCATTATTATCATGACATTAACCTATAAAAATAGGCGTATCACGAG
GCCCTTTCGTCTTCAC

Amino acid sequence

MRGSHHHHHHGSDDDDKTSYRDPMGAGAGAGPEGAGAGAGPEGAGAGAGPEGAGA

GAGPEGAGAGAGPEGAGAGAGPEGAGAGAGPEGAGAGAGPEGAGAGAGPEGAGAGA

GPEGARMPTSAPQMLRELQETNAALQDVRELLRQQVKEITFLKNTVMESDASGTSYRD

PMGAGAGAGPEGAGAGAGPEGAGAGAGPEGAGAGAGPEGAGAGAGPEGAGAGAGPE

GAGAGAGPEGAGAGAGPEGAGAGAGPEGAGAGAGPEGARMetPTSAPQMLRELQETN

AALQDVRELLRQQVKEITFLKNTVMESDASGTSYRDPMGAGAGAGPEGAGAGAGPEG

AGAGAGPEGAGAGAGPEGAGAGAGPEGAGAGAGPEGAGAGAGPEGAGAGAGPEGAG

AGAGPEGAGAGAGPEGARMPTSAPQMLRELQETNAALQDVRELLRQQVKEITFLKNTV

MESDASGTSYRDPMGAGAGAGPEGAGAGAGPEGAGAGAGPEGAGAGAGPEGAGAGA

GPEGAGAGAGPEGAGAGAGPEGAGAGAGPEGAGAGAGPEGAGAGAGPEGARMPTSA

PQMLRELQETNAALQDVRELLRQQVKEITFLKNTVMESDASGTSYRDPMGAGAGAGPE

GAGAGAGPEGAGAGAGPEGAGAGAGPEGAGAGAGPEGAGAGAGPEGAGAGAGPEGA

GAGAGPEGAGAGAGPEGAGAGAGPEGARMPTSCKLNS*

(iii) P_4

Complete plasmid sequence (the genes encoding P_4 highlighted in blue text)

CTCGAGAAATCATAAAAAATTTATTTGCTTTGTGAGCGGATAACAATTATAATAGATTCAATTGTGAG
CGGATAACAATTTCACACAGAATTCATTAAAGAGGAGAAATTAACTATGAGAGGATCGCATCACCATC
ACCATCACGGATCCGATGACGATGACAAAGCTAGCTATCGCGATCCGATGGGTGCCGGCGCTGGTGCG
GGCCCGGAAGGTGCAGGCGCTGGTGCGGGCCCGGAAGGTGCCGGCGCTGGTGCGGGCCCGGAAGGTG
CAGGCGCTGGTGCGGGCCCGGAAGGTGCCGGCGCTGGTGCGGGCCCGGAAGGTGCAGGCGCTGGTGC
GGGCCCGGAAGGTGCCGGCGCTGGTGCGGGCCCGGAAGGTGCAGGCGCTGGTGCGGGCCCGGAAGGT
GCCGGCGCTGGTGCGGGCCCGGAAGGTGCAGGCGCTGGTGCGGGCCCGGAAGGTGCCCGCATGCCGA
CTAGCGCGCCGCAGATGCTGCGTGAACTGCAGGAAACCAACGCGGCGCTGCAGGACGTTCGTGAACT
GCTGCGTCAGCAGGTTAAAGAAATCACCTTCCTGAAAAACACCGTTATGGAATCTGACGCGTCTGGTA
CTAGCTATCGCGATCCGATGGGTGCCGGCGCTGGTGCGGGCCCGGAAGGTGCAGGCGCTGGTGCGGG
CCCGGAAGGTGCCGGCGCTGGTGCGGGCCCGGAAGGTGCAGGCGCTGGTGCGGGCCCGGAAGGTGCC
GGCGCTGGTGCGGGCCCGGAAGGTGCAGGCGCTGGTGCGGGCCCGGAAGGTGCCGGCGCTGGTGCGG
GCCCGGAAGGTGCAGGCGCTGGTGCGGGCCCGGAAGGTGCCGGCGCTGGTGCGGGCCCGGAAGGTGC
AGGCGCTGGTGCGGGCCCGGAAGGTGCCCGCATGCCGACTAGCGCGCCGCAGATGCTGCGTGAACTG
CAGGAAACCAACGCGGCGCTGCAGGACGTTCGTGAACTGCTGCGTCAGCAGGTTAAAGAAATCACCTT
CCTGAAAAACACCGTTATGGAATCTGACGCGTCTGGTACTAGCTATCGCGATCCGATGGGTGCCGGCG
CTGGTGCGGGCCCGGAAGGTGCAGGCGCTGGTGCGGGCCCGGAAGGTGCCGGCGCTGGTGCGGGCCC
GGAAGGTGCAGGCGCTGGTGCGGGCCCGGAAGGTGCCGGCGCTGGTGCGGGCCCGGAAGGTGCAGGC
GCTGGTGCGGGCCCGGAAGGTGCCGGCGCTGGTGCGGGCCCGGAAGGTGCAGGCGCTGGTGCGGGCC
CGGAAGGTGCCGGCGCTGGTGCGGGCCCGGAAGGTGCAGGCGCTGGTGCGGGCCCGGAAGGTGCCCG
CATGCCGACTAGCGCGCCGCAGATGCTGCGTGAACTGCAGGAAACCAACGCGGCGCTGCAGGACGTT
CGTGAACTGCTGCGTCAGCAGGTTAAAGAAATCACCTTCCTGAAAAACACCGTTATGGAATCTGACGC
GTCTGGTACTAGCTATCGCGATCCGATGGGTGCCGGCGCTGGTGCGGGCCCGGAAGGTGCAGGCGCTG
GTGCGGGCCCGGAAGGTGCCGGCGCTGGTGCGGGCCCGGAAGGTGCAGGCGCTGGTGCGGGCCCGGA
AGGTGCCGGCGCTGGTGCGGGCCCGGAAGGTGCAGGCGCTGGTGCGGGCCCGGAAGGTGCCGGCGCT
GGTGCGGGCCCGGAAGGTGCAGGCGCTGGTGCGGGCCCGGAAGGTGCCGGCGCTGGTGCGGGCCCGG
AAGGTGCAGGCGCTGGTGCGGGCCCGGAAGGTGCCCGCATGCCGACTAGCGCGCCGCAGATGCTGCG
TGAACTGCAGGAAACCAACGCGGCGCTGCAGGACGTTCGTGAACTGCTGCGTCAGCAGGTTAAAGAA
ATCACCTTCCTGAAAAACACCGTTATGGAATCTGACGCGTCTGGTACTAGCTATCGCGATCCGATGGG
TGCCGGCGCTGGTGCGGGCCCGGAAGGTGCAGGCGCTGGTGCGGGCCCGGAAGGTGCCGGCGCTGGT
GCGGGCCCGGAAGGTGCAGGCGCTGGTGCGGGCCCGGAAGGTGCCGGCGCTGGTGCGGGCCCGGAAG
GTGCAGGCGCTGGTGCGGGCCCGGAAGGTGCCGGCGCTGGTGCGGGCCCGGAAGGTGCAGGCGCTGG
TGCGGGCCCGGAAGGTGCCGGCGCTGGTGCGGGCCCGGAAGGTGCAGGCGCTGGTGCGGGCCCGGAA
GGTGCCCGCATGCCGACTAGTTGGTAAGGATCCGTCGACCTGCAGCCAAGCTTAATTAGCTGAGCTTG
GACTCCTGTTGATAGATCCAGTAATGACCTCAGAACTCCATCTGGATTTGTTCAGAACGCTCGGTTGCC
GCCGGGCGTTTTTTATTGGTGAGAATCCAAGCTAGCTTGGCGAGATTTTCAGGAGCTAAGGAAGCTAA
AATGGAGAAAAAAATCACTGGATATACCACCGTTGATATATCCCAATGGCATCGTAAAGAACATTTTG
AGGCATTTCAGTCAGTTGCTCAATGTACCTATAACCAGACCGTTCAGCTGGATATTACGGCCTTTTTAA
AGACCGTAAAGAAAAATAAGCACAAGTTTTATCCGGCCTTTATTCACATTCTTGCCCGCCTGATGAAT
GCTCATCCGGAATTTCGTATGGCAATGAAAGACGGTGAGCTGGTGATATGGGATAGTGTTCACCCTTG
TTACACCGTTTTCCATGAGCAAACTGAAACGTTTTCATCGCTCTGGAGTGAATACCACGACGATTTCCG
GCAGTTTCTACACATATATTCGCAAGATGTGGCGTGTTACGGTGAAAACCTGGCCTATTTCCCTAAAGG
GTTTATTGAGAATATGTTTTTCGTCTCAGCCAATCCCTGGGTGAGTTTCACCAGTTTTGATTTAAACGTG
GCCAATATGGACAACTTCTTCGCCCCCGTTTTCACCATGGGCAAATATTATACGCAAGGCGACAAGGT
GCTGATGCCGCTGGCGATTCAGGTTCATCATGCCGTTTGTGATGGCTTCCATGTCGGCAGAATGCTTAA
TGAATTACAACAGTACTGCGATGAGTGGCAGGGCGGGGCGTAATTTTTTTAAGGCAGTTATTGGTGCC
CTTAAACGCCTGGGGTAATGACTCTCTAGCTTGAGGCATCAAATAAAACGAAAGGCTCAGTCGAAAGA
CTGGGCCTTTCGTTTTATCTGTTGTTTGTCGGTGAACGCTCTCCTGAGTAGGACAAATCCGCCCTCTAG
AGCTGCCTCGCGCGTTTCGGTGATGACGGTGAAAACCTCTGACACATGCAGCTCCCGGAGACGGTCAC
AGCTTGTCTGTAAGCGGATGCCGGGAGCAGACAAGCCCGTCAGGGCGCGTCAGCGGGTGTTGGCGGG
TGTCGGGGCGCAGCCATGACCCAGTCACGTAGCGATAGCGGAGTGTATACTGGCTTAACTATGCGGCA
TCAGAGCAGATTGTACTGAGAGTGCACCATATGCGGTGTGAAATACCGCACAGATGCGTAAGGAGAA
AATACCGCATCAGGCGCTCTTCCGCTTCCTCGCTCACTGACTCGCTGCGCTCGGTCGTTCGGCTGCGGC

GAGCGGTATCAGCTCACTCAAAGGCGGTAATACGGTTATCCACAGAATCAGGGGATAACGCAGGAAA
GAACATGTGAGCAAAAGGCCAGCAAAAGGCCAGGAACCGTAAAAAGGCCGCGTTGCTGGCGTTTTTC
CATAGGCTCCGCCCCCCTGACGAGCATCACAAAAATCGACGCTCAAGTCAGAGGTGGCGAAACCCGA
CAGGACTATAAAGATACCAGGCGTTTCCCCCTGGAAGCTCCCTCGTGCGCTCTCCTGTTCCGACCCTGC
CGCTTACCGGATACCTGTCCGCCTTTCTCCCTTCGGGAAGCGTGGCGCTTTCTCATAGCTCACGCTGTA
GGTATCTCAGTTCGGTGTAGGTCGTTCGCTCCAAGCTGGGCTGTGTGCACGAACCCCCCGTTCAGCCCG
ACCGCTGCGCCTTATCCGGTAACTATCGTCTTGAGTCCAACCCGGTAAGACACGACTTATCGCCACTGG
CAGCAGCCACTGGTAACAGGATTAGCAGAGCGAGGTATGTAGGCGGTGCTACAGAGTTCTTGAAGTG
GTGGCCTAACTACGGCTACACTAGAAGGACAGTATTTGGTATCTGCGCTCTGCTGAAGCCAGTTACCTT
CGGAAAAAGAGTTGGTAGCTCTTGATCCGGCAAACAAACCACCGCTGGTAGCGGTGGTTTTTTTGTTT
GCAAGCAGCAGATTACGCGCAGAAAAAAAGGATCTCAAGAAGATCCTTTGATCTTTTCTACGGGGTCT
GACGCTCAGTGGAACGAAAACTCACGTTAAGGGATTTTGGTCATGAGATTATCAAAAAGGATCTTCAC
CTAGATCCTTTTAAATTAAAAATGAAGTTTTAAATCAATCTAAAGTATATATGAGTAAACTTGGTCTGA
CAGTTACCAATGCTTAATCAGTGAGGCACCTATCTCAGCGATCTGTCTATTTCGTTCATCCATAGTTGC
CTGACTCCCCGTCGTGTAGATAACTACGATACGGGAGGGCTTACCATCTGGCCCCAGTGCTGCAATGA
TACCGCGAGACCCACGCTCACCGGCTCCAGATTTATCAGCAATAAACCAGCCAGCCGGAAGGGCCGA
GCGCAGAAGTGGTCCTGCAACTTTATCCGCCTCCATCCAGTCTATTAATTGTTGCCGGGAAGCTAGAGT
AAGTAGTTCGCCAGTTAATAGTTTGCGCAACGTTGTTGCCATTGCTACAGGCATCGTGGTGTCACGCTC
GTCGTTTGGTATGGCTTCATTCAGCTCCGGTTCCCAACGATCAAGGCGAGTTACATGATCCCCCATGTT
GTGCAAAAAAGCGGTTAGCTCCTTCGGTCCTCCGATCGTTGTCAGAAGTAAGTTGGCCGCAGTGTTAT
CACTCATGGTTATGGCAGCACTGCATAATTCTCTTACTGTCATGCCATCCGTAAGATGCTTTTCTGTGA
CTGGTGAGTACTCAACCAAGTCATTCTGAGAATAGTGTATGCGGCGACCGAGTTGCTCTTGCCCGGCG
TCAATACGGGATAATACCGCGCCACATAGCAGAACTTTAAAAGTGCTCATCATTGGAAAACGTTCTTC
GGGGCGAAAACTCTCAAGGATCTTACCGCTGTTGAGATCCAGTTCGATGTAACCCACTCGTGCACCCA
ACTGATCTTCAGCATCTTTTACTTTCACCAGCGTTTCTGGGTGAGCAAAAACAGGAAGGCAAAATGCC
GCAAAAAAGGGAATAAGGGCGACACGGAAATGTTGAATACTCATACTCTTCCTTTTTCAATATTATTG
AAGCATTTATCAGGGTTATTGTCTCATGAGCGGATACATATTTGAATGTATTTAGAAAAATAAACAAA
TAGGGGTTCCGCGCACATTTCCCCGAAAAGTGCCACCTGACGTCTAAGAAACCATTATTATCATGACA
TTAACCTATAAAAATAGGCGTATCACGAGGCCCTTTCGTCTTCAC

Amino acid sequence

MRGSHHHHHHGSDDDDKASYRDPMGAGAGAGPEGAGAGAGPEGAGAGAGPEGAGA

GAGPEGAGAGAGPEGAGAGAGPEGAGAGAGPEGAGAGAGPEGAGAGAGPEGAGAGA

GPEGARMPTSAPQMLRELQETNAALQDVRELLRQQVKEITFLKNTVMESDASGTSYRD

PMGAGAGAGPEGAGAGAGPEGAGAGAGPEGAGAGAGPEGAGAGAGPEGAGAGAGPE

GAGAGAGPEGAGAGAGPEGAGAGAGPEGAGAGAGPEGARMPTSAPQMLRELQETNA

ALQDVRELLRQQVKEITFLKNTVMESDASGTSYRDPMGAGAGAGPEGAGAGAGPEGA

GAGAGPEGAGAGAGPEGAGAGAGPEGAGAGAGPEGAGAGAGPEGAGAGAGPEGAGA

GAGPEGAGAGAGPEGARMPTSAPQMLRELQETNAALQDVRELLRQQVKEITFLKNTVM

ESDASGTSYRDPMGAGAGAGPEGAGAGAGPEGAGAGAGPEGAGAGAGPEGAGAGAG

PEGAGAGAGPEGAGAGAGPEGAGAGAGPEGAGAGAGPEGAGAGAGPEGARMPTSAP
QMLRELQETNAALQDVRELLRQQVKEITFLKNTVMESDASGTSYRDPMGAGAGAGPEG
AGAGAGPEGAGAGAGPEGAGAGAGPEGAGAGAGPEGAGAGAGPEGAGAGAGPEGAG
AGAGPEGAGAGAGPEGAGAGAGPEGARMPTSW*

2.1.2. Protein expression

Proteins were expressed at 37 °C in 1 L terrific broth in a 2.8 L shaker flask, supplemented with ampicillin (200 mg/L) and kanamycin (50 mg/L). When the optical density of the medium at 600 nm reached 0.9–1.0, the expression was induced with 1.0 mM isopropyl β-D-1-thiogalactopyranoside (IPTG). Six hours after induction, the cells had expressed a significant amount of protein, as confirmed by the sodium dodecyl sulfate-polyacrylamide gel electrophoresis (SDS-PAGE) analysis (Figure 2-2). To perform this step, 1 mL of suspended cell culture was pipetted into a 1.7 mL Eppendorf tube, and the suspension was centrifuged at 21,100 ×g at 4 °C for 2 min. The supernatant was decanted, and 200 μL of buffer containing 8 M urea and 100 mM sodium phosphate (pH 8.0) was added to resuspend the cell pellets. The lysis suspension was then analyzed. To harvest cells, the expression media was transferred into 500 mL high-speed centrifuge bottles. Centrifugation was performed at 4 °C and at 6,000 RPM using a Fiberlite™ F10-6×500y fixed-angle rotor for 10 min. Supernatant was then removed by decanting. The cell pellets were stored at –80 °C until protein purification. Typical wet cell mass from 1 L culture was approximately 19 ± 2 g.

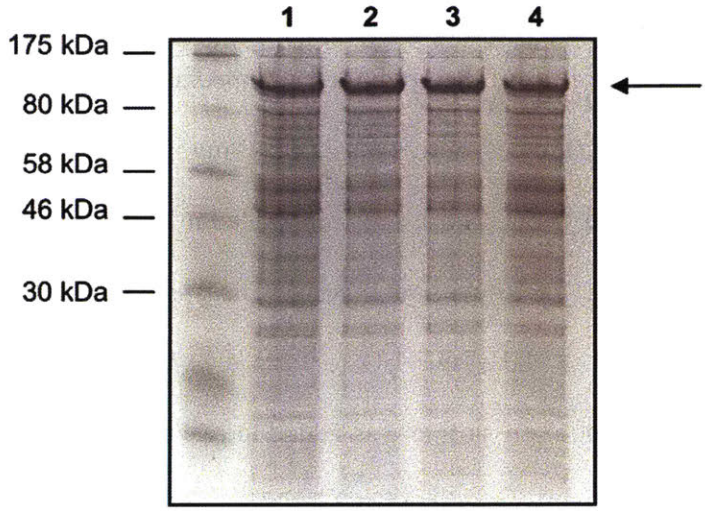

Figure 2-2. SDS-PAGE showing the expression level of desired proteins (indicated by the arrow on the right) six hours after induction. The proteins run on the gel with an apparent molecular weight equal to approximately twice the true molecular weight. This is attributed to a weak binding affinity between the negatively charged C_{10} domains and anionic surfactants SDS, resulting in a reduced effective charge and electrophoretic mobility. A similar effect has been previously observed in structurally similar proteins.[4] Lanes 1–4 were culture withdrawn from four separate flasks but expressed at the same time.

2.1.3. Protein purification

Proteins were first purified by ammonium sulfate precipitation following a procedure developed by Dr. Matthew Glassman.[1] Cell pellets from 1 L expression culture were resuspended in 50 mL lysis buffer (10 mM Tris, 1 mM EDTA, 100 mM NaCl, 5 mM $MgCl_2$, pH 7.5). Lysozyme (100 mg, lyophilized powder from chicken egg white, activity $\geq$ 40,000 U/mg, Sigma) was then added to the suspension. After incubation at 4 °C for 2 h, the mixture was sonicated on ice for 15 min twice at 50% duty cycle at an output power of 5. Since purification was usually done on pellets combined from a large scale of expression, the lysate was combined and transferred into 500 mL high-speed centrifuge bottles. The lysate was clarified by centrifugation at 9,000 RPM

and at 4 °C using a Fiberlite™ F10-6×500y fixed-angle rotor for 30 min. The supernatant was carefully decanted to separate it from the precipitates immediately after centrifugation. DNase I (2 mg, grade II, from bovine pancreas, activity ~ 2,000 U/mg, Roche) and RNase A (2 mg, from bovine pancreas, activity ≥ 60 U/mg, Amresco) were added to 50 mL of clarified lysate, and the mixture was incubated at 37 °C for 2 h without mixing. The lysate was subsequently denatured by adding 42.4 g urea and 1.21 g $NaH_2PO_4 \cdot H_2O$ to form a buffer with 8 M urea and 100 mM phosphate. Then 17.5 g ammonium sulfate was added to reach a 20% (w/v) ammonium sulfate concentration. After the mixture was agitated at 37 °C for 2 h to achieve complete dissolution of all solids, it was centrifuged at 9,500 RPM and at 37 °C using a Fiberlite™ F10-6×500y fixed-angle rotor for 60 min. This long centrifugation time was necessary to completely pellet the precipitates. The pellets with minimal amount of the desired proteins were discarded (see lanes 3 and 4 in Figure 2-3). The supernatant was transferred to a clean high-speed centrifuge bottle, and 8.25 g ammonium sulfate was added to bring the ammonium sulfate concentration to 30% (w/v). The mixture was again agitated at 37 °C for 2 h and then centrifuged at 9,500 RPM and at 37 °C using a Fiberlite™ F10-6×500y fixed-angle rotor for 60 min. Immediately after the centrifugation cycle stopped, the supernatant that did not contain any desired proteins was poured out carefully (see lane 5 in Figure 2-3). The centrifuge bottles with the collected pellets were held upside down for 15 min. The pellets were redissolved in 15–20 mL of buffer containing 6 M urea and 20 mM Tris (pH 8.0). The purity of the crude proteins after two rounds of ammonium sulfate precipitation was usually 70–80% (see lanes 1 and 2 in Figure 2-3).

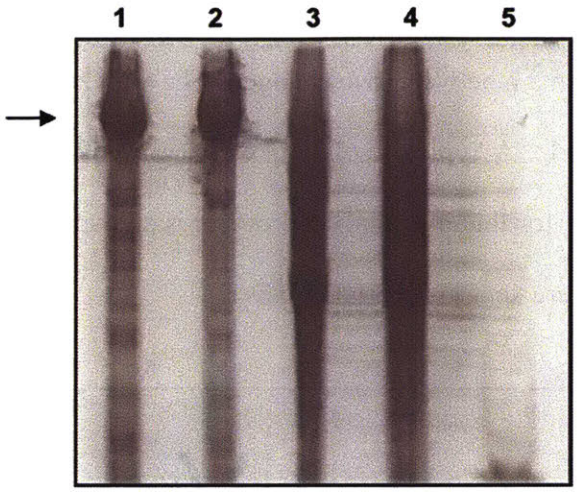

Figure 2-3. SDS-PAGE analysis of the precipitates and supernatant fractions during ammonium sulfate precipitation. Lanes 1 and 2: crude proteins (indicated by the arrow on the left) in the pellets after two rounds of ammonium sulfate precipitation. Lanes 3 and 4: fractions in the pellets after one round of ammonium sulfate precipitation. Lane 5: fractions in the supernatant after the final precipitation step.

Proteins were further purified by anion exchange chromatography using one of the following two procedures. These two protocols were developed in a chronological order. All purifications could be done using the second procedure to increase throughput.

In the first procedure, crude proteins from previous steps were purified using QAE-Sephadex A-50 resin (GE Healthcare). 5 g of resin was first swollen in 250 mL of buffer containing 6 M urea and 20 mM Tris (pH 8.0) for overnight and then packed into an Econo-Column (Bio Rad). Solutions containing crude proteins were loaded slowly on top on the resin to minimize band dispersion prior to separation. The column was washed with 2 × 100 mL buffer with 6 M urea and 20 mM Tris (pH 8.0). Proteins were eluted with 5 × 40 mL buffer with 6 M urea, 20 mM Tris and 1 M NaCl (pH 8.0). Pure fractions were combined and dialyzed extensively against ultrapure water (molecular weight cutoff 3,500 Da). For dialysis, the amount of protein solution

was no more than 200 mL to be dialyzed against 4L ultrapure water. The dialysis was changed 7 times in total with more than 3 h between two changes. The dialyzed solution was lyophilized for 3 d to be completely dried. A typical isolation yield was 150 mg protein per liter culture. Representative SDS-PAGE for this purification protocol is shown in Figure 2-4. For long term storage, protein powders were kept in a −20 °C freezer.

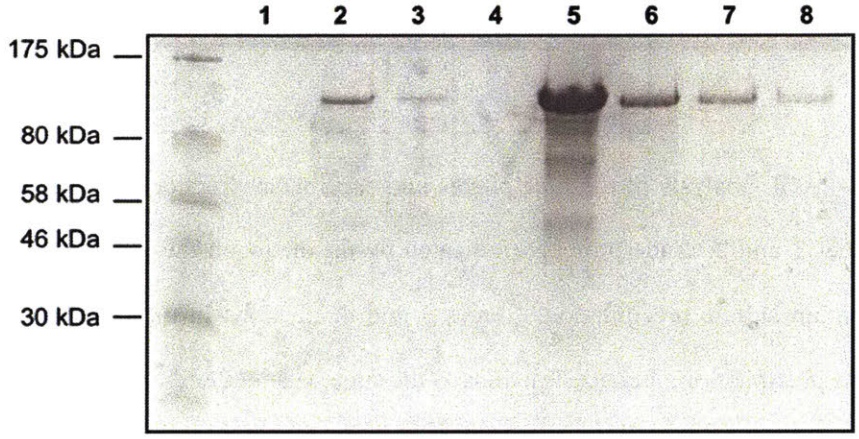

Figure 2-4. Representative denaturing SDS-PAGE showing purification of associative coiled-coil proteins using anion exchange on Sephadex A-50 resin. Proteins were first loaded on the column, and the flow-through (lane 1) was collected. After the column was washed twice (lanes 2–3), proteins were eluted in five fractions (lanes 4–8).

In the second procedure, crude proteins were first dialyzed against deionized water and lyophilized. A typical yield of these crude proteins were 150–250 mg per liter expression culture. The lyophilized powders were then redissolved in a buffer containing 6 M urea and 20 mM Tris (pH 8.0) to reach a protein concentration of 15–20 mg/mL. Complete dissolution might take somewhere from 3 h up to overnight. After proteins were completely dissolved, the solution was transferred into 50 mL conical tubes and centrifuged at 12,500 RPM using a Fiberlite™ F14-14×50cy fixed-angle rotor for 30 min at 4 °C. The clarified supernatant was decanted to separate

from the precipitates. Purification was performed using two HiTrap Q Sepharose HP 5 mL columns (GE healthcare) in series on an automated fast protein liquid chromatography (FPLC, ÄKTA pure, GE healthcare). FPLC was chosen as the purification method because it could remove the impurities in the crude proteins as shown in lane 5 in Figure 2-3. FPLC also offered high throughput purification: a large amount of proteins up to 1 g could be easily purified within 1 day. Purification was performed using the following elution profile at a constant flow rate of 2 mL/min:

(1) Load 15 mL of the sample solution to the column;

(2) Wash the column with 6 column volumes (CVs) of buffer A (6 M urea and 20 mM Tris, pH 8.0);

(3) Elute over a gradient of buffer B (6 M urea, 20 mM Tris and 2 M NaCl, pH 8.0) from 0–10% for 19 CVs, 10–20% for 5 CVs, to 20–50% for 6 CVs.

Fractions were collected into a 96-well plate by an automated fractionator, with the volume of each fraction being 2 mL. A representative elution chromatogram is shown in Figure 2-5 and the corresponding SDS-PAGE analysis is shown in Figure 2-6. A typical isolation yield is 100–120 mg per liter culture, and the protein purity was determined to be >97% pure by SDS-PAGE (Figure 2-6).

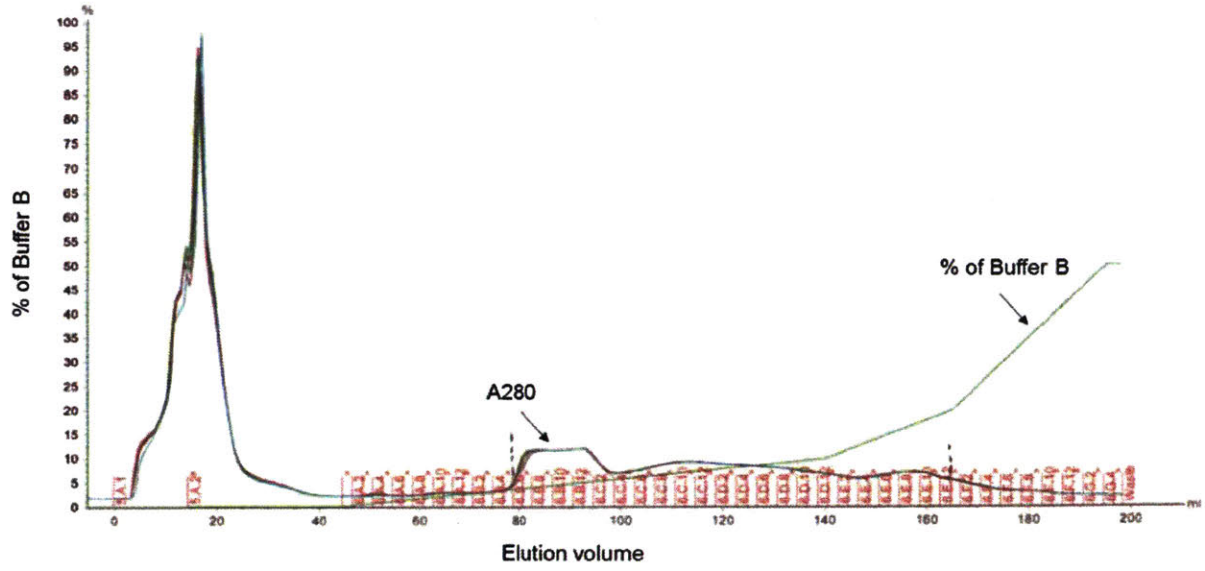

Figure 2-5. Anion exchange chromatograph of purification of Cys-P_4-Cys, showing the absorbance of 280 nm. The green linear line shows the percentage of buffer B used during elution. Chromatograms from four separate purification runs on the same batch crude proteins are overlaid to show good reproducibility.

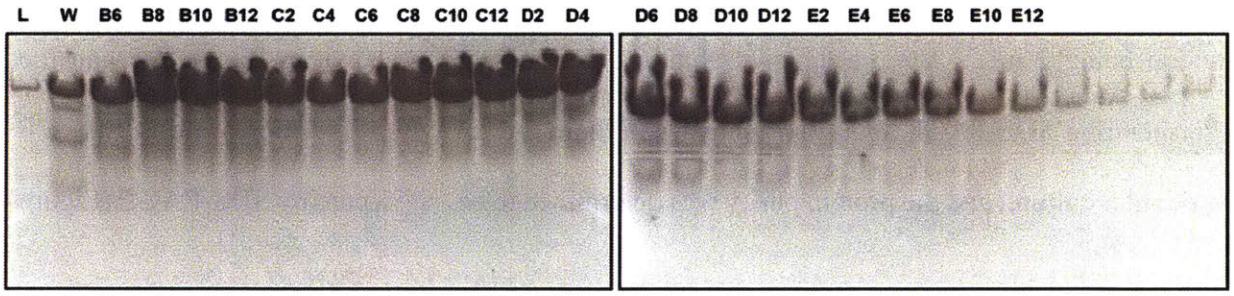

Figure 2-6. SDS-PAGE analysis of protein fraction during anion exchange chromatography. The most intense band was the desired protein product. Fractions B6–E12 had relatively high absorbance at 280 nm shown on the chromatograms and showed relatively intensive bands on the SDS-PAGE. Thus, these fractions were selected as pure fractions. Fractions B6–E12 were combined, dialyzed and lyophilized.

2.2. Chain extension and branching reactions of coiled-coil proteins

To produce linearly chain-extended or branched associative proteins from Cys-P_4-Cys, several bioconjugation methods were explored in this thesis, which are disulfide, thiol-maleimide, thiol-bromomaleimide and thio-ene coupling chemistries (Figure 2-7). Experimental procedures for different chain extension reactions are described in detail below.

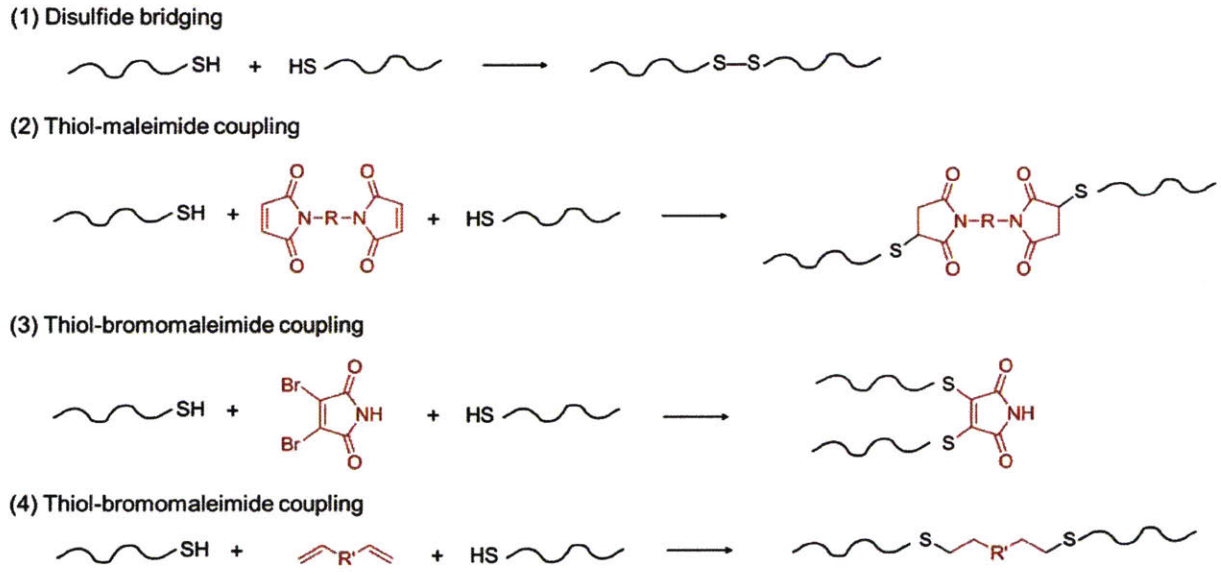

Figure 2-7. Reaction schemes showing the four bioconjugation methods for protein chain extension.

2.2.1. Disulfide bridging

Protein Cys-P_4-Cys was dissolved in a freshly prepared buffer with 6 M urea and 20 mM Tris (pH 8.0) to a final concentration of 10% (w/v), yielding a clear, slightly yellow solution. To reduce the existing disulfide bonds during protein purification, a two-fold molar excess of solid tris(2-carboxyethyl)phosphine hydrochloride (TCEP) relative to the cysteine content was added. The mixture was allowed to stir for a week at 4 °C. The protein solution was then dialyzed extensively against ultrapure water and lyophilized to obtain protein powders.

Two methods were used to evaluate the degree of chain extension. First, frequency sweep measurements were performed on hydrogels formed by the chain-extended proteins (experimental details of the rheology measurements will be discussed in Section 2.4.1). Rheological analysis is of particular interest because an ultimate goal of this research effort is to control the extent of chain extension to manipulate the mechanical properties of hydrogels. Upon chain-extension and preparing the gels at high enough concentration above the entanglement threshold, a low-frequency elastic plateau (entanglement plateau) was seen around an angular frequency of 0.001 rad/s, and storage modulus *G'* remained larger than *G"* in this low-frequency regime (Figure 2-8A). The appearance of the entanglement plateau suggested that proteins were long enough to form topological constraints with others, indicating success of the chain extension reaction. In contrast, for monomeric proteins P_4 that were not capable of chain-extending, a *G'*-*G"* crossover was observed, and there was no entanglement plateau (Figure 2-8B).

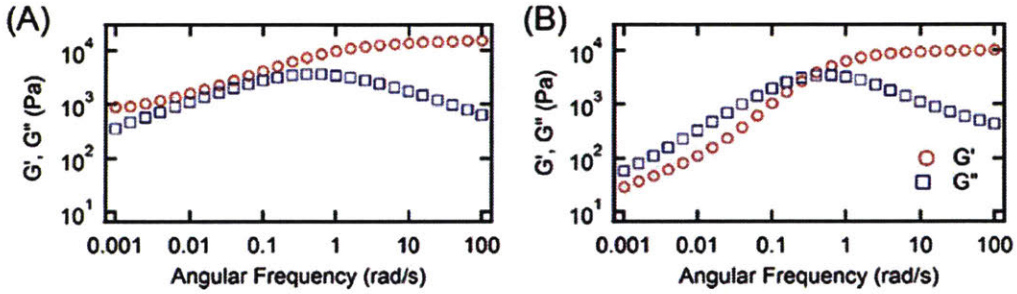

Figure 2-8. Comparison of the frequency sweep spectra from (A) oxidized Cys-P_4-Cys and (B) P_4 only at 15% (w/v) at 25 °C.

The effect of chain extension can be further quantified using the following two metrics, the entanglement plateau modulus, G_e, and the *G'*-*G"* crossover frequency, ω_e. Although G_e of polymers with a small dispersity should not depend on the molecular weight, chain-extended

proteins formed *via* macromolecular condensation reactions are expected to show a very broad molecular weight distribution, with a certain fraction of the protein chains below the critical entanglement length (see examples in the SDS-PAGE analysis in the following parts). These "short" proteins act as macromolecular diluents and lower the effective concentration of the entangled species. Therefore, an increase in the chain molecular weight can lead to an increase in the G_e. In the following section, G_e will be used to compare the performance of different chain coupling chemistries. On the other hand, ω_e is usually taken as the frequency-dependent solid-liquid transition in associating networks, from which a network relaxation time is calculated. A smaller ω_e is normally correlated with a mixture of proteins at a higher average molecular weight (Figure 2-8 and 2-9).

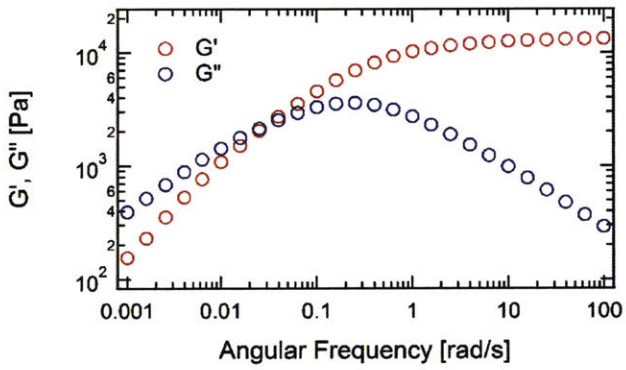

Figure 2-9. An example of hydrogels at 15% (w/v) from chain-extended proteins Cys-P_4-Cys. The degree of chain extension was not high enough such that no entanglement plateau is seen. However, ω_e appears at a lower frequency compared to case in Figure 2-8B, suggesting the presence of chain extension.

The second method to evaluate chain-extension reaction was quantifying the molecular weight distribution of the reaction mixture by SDS-PAGE. The experiments were performed on Mini-PROTEAN TGX™ gradient gels (4–15%, BioRad) under non-reducing condition in buffer

containing 2.5 mM Tris, 19.2 mM glycine and 0.01% SDS (pH 8.3) at 150 V. Note that the buffer did not contain any BME (β-mercaptoethanol). The duration for electrophoresis was somewhere between 120 and 150 min to maximize separation of the high-molecular-weight species. The formation of chain-extended species was shown in the bands above the monomeric starting proteins (see Figure 2-10). The weight fractions of different species were estimated by densitometry using the BioRad Image Lab software. Data analysis will be discussed later in Section 2.2.5.

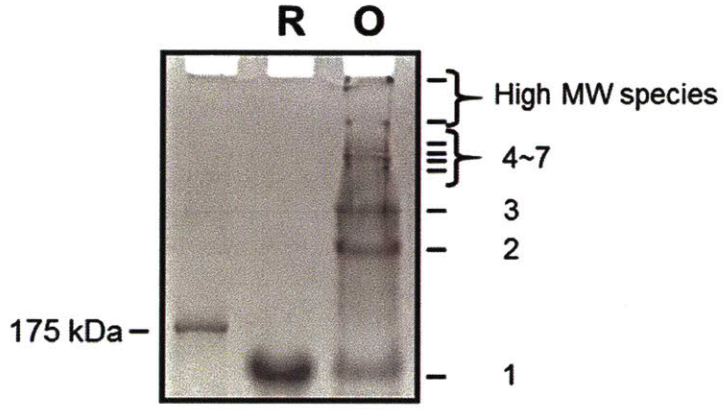

Figure 2-10. Representative SDS-PAGE analysis of chain extension reaction on Cys-P_4-Cys through disulfide bridging. Proteins at the reduced and oxidized states are denoted as R and O, respectively. Notations at the right hand side indicate the degrees of polymerization of the proteins.

It was later discovered that oxidation could be performed in the gel state. Proteins were hydrated in 100 mM sodium phosphate buffer (pH 7.6) at 15% (w/v) and reduced by a five-fold excess TCEP relative to the cysteine content. The gel pH was adjusted back to 7.6 after 1 d by adding 1 M NaOH (a.q.) solution. The hydrogel sample was mechanically agitated with a micro spatula to introduce air and stored at 4 °C. The mixing procedure was repeated every several days.

Compared to oxidation reaction in the solution, oxidation in the gels could take up to 2 months with periodic mixing to reach significant entanglement (Figure 2-11). The slow kinetics was presumably due to slow diffusion rate of proteins in gels.

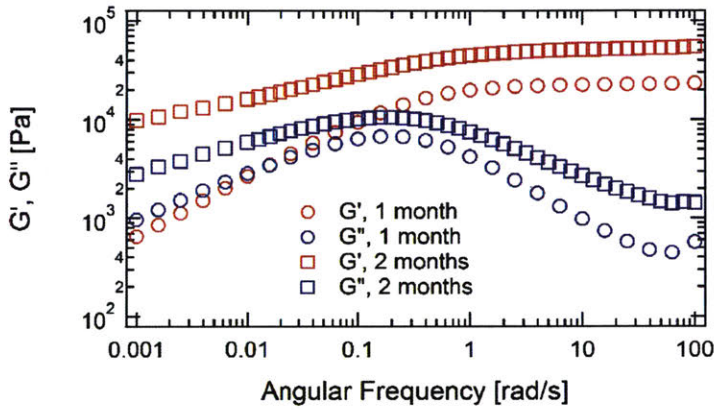

Figure 2-11. Frequency sweeps of gels under varying time periods of chain-extension. Gel concentration: 20% (w/v).

Several considerations should be kept in mind to achieve success in high degree chain extension and entanglement. First, it is very important to maintain the integrity of the cysteine residues to maximize the endgroup conversion. This was achieved by adding 20 mM BME (usually within less than 3 months old after the container was opened) in all purification buffers. However, residual BME could from disulfide linkages with the cysteine residues on the proteins. This undesirably masks the reactive cysteines and can negatively impact the chain extension reactions. Due to the large molar mass of these associative proteins, it was difficult to characterize the integrity of cysteines using methods such as LC-MS or Ellman's assay. In the author's hands, the best chain extension results came from purification using fresh BME. Protein purification completely without BME was also tried. Such procedure also could also yield proteins that were

able to achieve significant chain extension, provided that the entire purification procedure (including dialysis) was finished within 3–4 days. Second, urea buffer must be freshly prepared before each use. Urea buffer after long time storage may generate cyanate that can react with cysteine residues.[5] Third, the oxidation period must be sufficiently long. Low degree of chain extension would results in mechanical properties similar to the one shown in Figure 2-9. Attempts were made to use mild oxidizing agents, such as H_2O_2 solution, to expedite the oxidation process. However, these efforts did not lead to any success. An excess amount of oxidizing agents may cause degradation of proteins.

2.2.2. Thiol-maleimide conjugation

Protein Cys-P_4-Cys was dissolved in a freshly-prepared denaturing buffer (8 M urea and 100 mM sodium phosphate, pH 8.0) to reach a concentration of 10% (w/v). TCEP (20 eq.) was added from a stock solution at 0.5 M, and the solution pH was adjusted to 7.5 by adding 0.1 M NaOH (a.q). In this thesis, two commercially available bismaleimide compounds, bismaleimide diethylene glycol, abbreviated as $BM(PEG)_2$ and bismaleimide with a 1 kDa poly(ethylene glycol) spacer, abbreviated as MAL-PEG-MAL, were used to study the effect of spacer between two maleimide groups. The bismaleimide compounds were first dissolved in HPLC grade DMF at a concentration of 0.2 M. An appropriate amount of the bismaleimide solution (1 eq. to the protein) was then added to the protein solution. The reaction was stirred at room temperature for 3 d, and it was then dialyzed against MilliQ water and lyophilized. The long reaction time was chosen based on experimental results to maximize end group conversion and entanglement in gels. However, it should be noted that minimal effort was made to monitor the reaction kinetics, and a high endgroup conversion might be reached at a time shorter than 3 d. Based on the observation

by others, a higher solution pH at 8.0 or above is not recommended to minimize maleimide hydrolysis.[6] From the SDS-PAGE analysis and rheology characterization (Figure 2-12), the length of the spacer in the bismaleimide compounds did not seem to influence the performance of the chain-extension reaction.

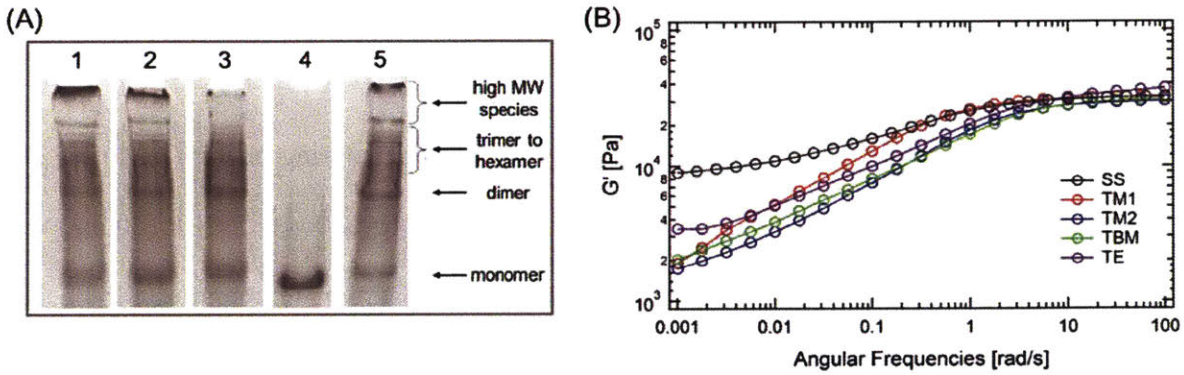

Figure 2-12. (A) SDS-PAGE analysis of chain-extension reactions. Lane 1: thiol-maleimide conjugation using $BM(PEG)_2$ (TM1); lane 2: thiol-maleimide conjugation using MAL-PEG1k-MAL (TM2); lane 3: thiol-bromomaleimide conjugation (TBM); lane 4: proteins reduced by TCEP; and lane 5: thiol-ene coupling (TE). (B) Comparison of frequency sweep spectra of hydrogels produced from different chain extension reactions. Gel concentration: 20% (w/v).

2.2.3. Thiol-bromomaleimide conjugation

Protein Cys-P_4-Cys was dissolved in a freshly-prepared denaturing buffer (8 M urea and 100 mM sodium phosphate, pH 8.0) to reach a concentration of 10% (w/v). TCEP (20 eq.) was added from a stock solution at 0.5 M, and the pH was adjusted to 6.2 using a micro pH meter. This relatively low pH was chosen to suppress maleimide hydrolysis.[6, 7] 2,3-dibromomaleimide was dissolved in dimethyl sulfoxide (DMSO) at a concentration of 10 mg/mL, and 1 eq. was added to the solution. The solution color quickly turned slightly bright yellow. This was an evidence of

fast formation of the fluorescently active dithiomaleimide adduct, a phenomenon that has been reported by others[8]. The reaction was stirred at 4 °C for 7 d, and it was then dialyzed against MilliQ water and lyophilized. Again, the reaction time was not optimized, and future effort might lead to a shorter reaction time successfully producing chain-extended proteins. SDS-PAGE analysis and frequency sweep spectrum is shown in Figure 2-12.

2.2.4. Thiol-ene conjugations

Protein Cys-P_4-Cys was dissolved in a freshly-prepared denaturing buffer (8 M urea and 100 mM sodium phosphate, pH 8.0) to reach a concentration of 10% (w/v). TCEP (20 eq.) was added from a stock solution at 0.5 M. The mixture was left to stir at room temperature for 4 h, and it was then dialyzed against MilliQ water and lyophilized. After this reduction step, >99% of the proteins were in the monomeric state as assessed by SDS-PAGE (lane 4 in Figure 2-12A) where the loading and running buffer did not contain any BME. Reduced proteins were hydrated in 100 mM sodium phosphate buffer (pH 7.6), and mixed with a bifunctional chain extension reagent 3,3'-[Ethylenebis(oxyethyleneoxy)]bis(2-methyl-1-propene) (1 eq.) and VA-044 (0.2 eq.). The final protein concentration was adjusted to 20% (w/v). Hydrogel samples were loaded on the rheometer after hydration for 2 d. The reaction was triggered by heating at 60 °C for 3 h. The dynamic moduli were monitored at 25 °C to ensure that the steady state was reached before further measurements were performed. SDS-PAGE analysis and a frequency sweep spectrum are shown in Figure 2-12.

In branching reactions, a trifunctional crosslinker 2,4,6-triallyloxy-1,3,5-triazine was used partially or completely in place of the bifunctional crosslinkers. The total number of alkene groups was kept at 1:1 molar ratio to thiol groups, while the amount of trifunctional crosslinkers was varied from 0–100% of the total mole fraction of alkene-containing oligomers. The SDS-PAGE

analysis is shown in Figure 2-13A and B. Within the resolution of SDS-PAGE, the fractions of trienes in the mixture did not seem to greatly influence the molecular weight distribution of the proteins. However, varying the content of trienes in the branching reaction led to substantial changes in the rheological properties of hydrogels, especially in the low-frequency regime (Figure 2-13C).

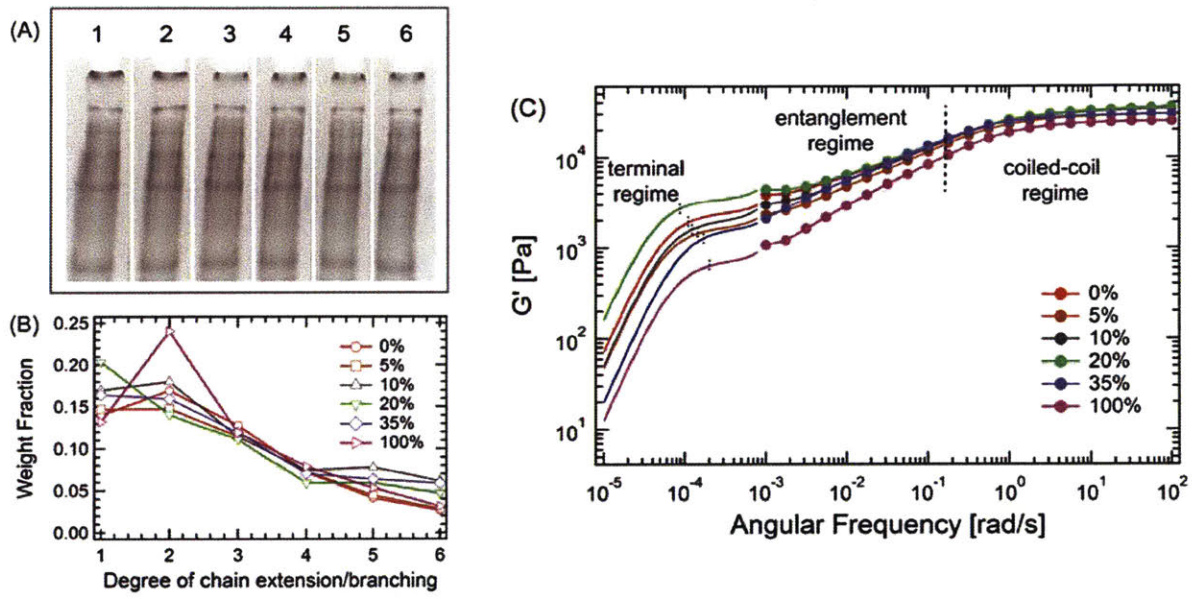

Figure 2-13. (A) SDS-PAGE: the molecular fractions of triene in lanes 1-6 is 0, 5, 10, 20, 35, and 100%, respectively. (B) Weight fractions extracted by densitometry. (C) Rheology characterizations of hydrogels at 20% (w/v).

2.2.5. Analysis of chain extension reactions

The molecular weight distribution of polymerized proteins may be fit to the theoretical Jacobson-Stockmayer distribution[9] using the MATLAB built-in lsqcurvefit algorithm to estimate the extent of end group conversion and the fractions of ring and chain species. Due to the

resolution limitation of SDS-PAGE, the high-molecular-weight species usually cannot be well separated. Therefore, only the weight fractions of unimers to heptamers were used in the calculation. Furthermore, the linear and ring species were assumed to have the same electrophoretic mobility. The theory assumes that the molecular size distribution for the chain fraction of the same form as the distribution in the ring-free case, namely, the Flory-Schulz distribution, the number of n-mer linear chains in the mixture is

$$C_n = Ax^n, \tag{2-1}$$

where A is a normalization constant and x is the fraction of reacted endgroups in the chain fraction. The number of n-mer rings in the mixture is assumed to be

$$R_n = Bx^n n^{-5/2}, \tag{2-2}$$

where B is a constant. Therefore, the weight fraction of n-mer, including chains and rings, is

$$w_n = \frac{n(C_n + R_n)}{\sum n(C_n + R_n)} = \frac{\frac{A}{B}nx^n + x^n n^{-3/2}}{\frac{A}{B}\frac{x}{(1-x)^2} + \sum x^n n^{-3/2}} = \frac{anx^n + x^n n^{-3/2}}{\frac{ax}{(1-x)^2} + \sum x^n n^{-3/2}}. \tag{2-3}$$

The fitting parameters are a (the ratio of A to B) and x. The fits for the SDS-PAGE in Figure 2-10 is shown in Figure 2-14, and the values of a and x from nonlinear regression are 0.574 ± 0.378 and 0.610 ± 0.089, respectively. The error bars in the calculation represent 95 % confidence interval of the fitting parameter, calculated based on the built-in nlparci algorithm.

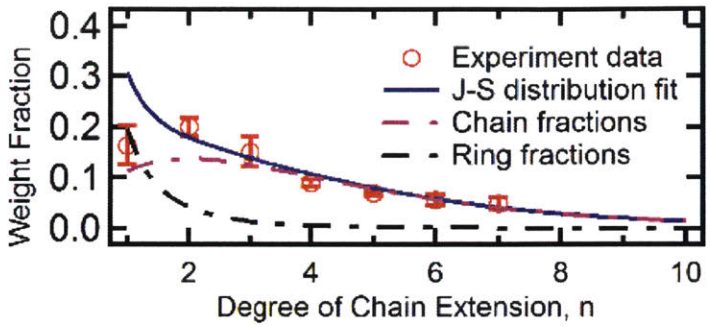

Figure 2-14. The molecular weight distribution of the SDS-PAGE shown in Figure 2-10 is analyzed by densitometry and further fit to the Jacobson–Stockmayer distribution that accounts for intramolecular looping. Error bars represent the standard deviations of three separate experiments.

By using the estimated values of a and x, other quantities can be calculated as follows.

The number and weight fractions of rings in the system are,

$$n_r = \frac{\sum R_n}{\sum (C_n + R_n)} = \frac{\sum x^n n^{-5/2}}{\frac{ax}{(1-x)} + \sum x^n n^{-5/2}}, \tag{2-4}$$

$$w_r = \frac{\sum nR_n}{\sum n(C_n + R_n)} = \frac{\sum x^n n^{-3/2}}{\frac{ax}{(1-x)^2} + \sum x^n n^{-3/2}}. \tag{2-5}$$

The fraction of reacted functional groups in the system is,

$$p = x + (1-x)w_r. \tag{2-6}$$

The number and weight average degrees of polymerization of the chain fraction are,

$$\bar{X}_{cn} = \frac{1}{1-x}, \quad \bar{X}_{cw} = \frac{1+x}{1-x}. \tag{2-7}$$

The number and weight average degrees of polymerization of the ring fraction are,

$$\bar{X}_{rn} = \frac{\sum x^n n^{-3/2}}{\sum x^n n^{-5/2}}, \qquad \bar{X}_{rw} = \frac{\sum x^n n^{-1/2}}{\sum x^n n^{-3/2}}. \tag{2-8}$$

The number and weight average degrees of polymerization of the system are,

$$\bar{X}_n = n_r \bar{X}_{rn} + (1 - n_r)\bar{X}_{cn}, \qquad \bar{X}_w = w_r \bar{X}_{rw} + (1 - w_r)\bar{X}_{cw}. \tag{2-10}$$

Attempts were also made to apply the analysis using the Jacobson-Stockmayer distribution to extract quantitative information about the degree of end group conversion and the fractions of the chain and ring species in the A_2 + B_2 type polycondensation reactions employing thiol-maleimide, thiol-bromomaleimide and thiol-ene coupling chemistries. However, it was found that the fits were not satisfactory in all these cases (Figure 2-15), and the 95% confidence intervals for the parameters of interest were very large (Figure 2-16). There were two major challenges in applying the Stockmayer-Jacobson theory for these A_2 + B_2 type reactions. First, it was difficult to separate the large-molar-mass bands in the SDS-PAGE for these reaction products; the reasons are not well understood. Second, and perhaps more importantly, the aforementioned analysis is based on an important assumption that the functional groups A and B were in perfect stoichiometric balance. However, it was difficult to precisely control the stoichiometry of reagents in small samples due to inherent experimental errors, which in turn may render the analysis not applicable.

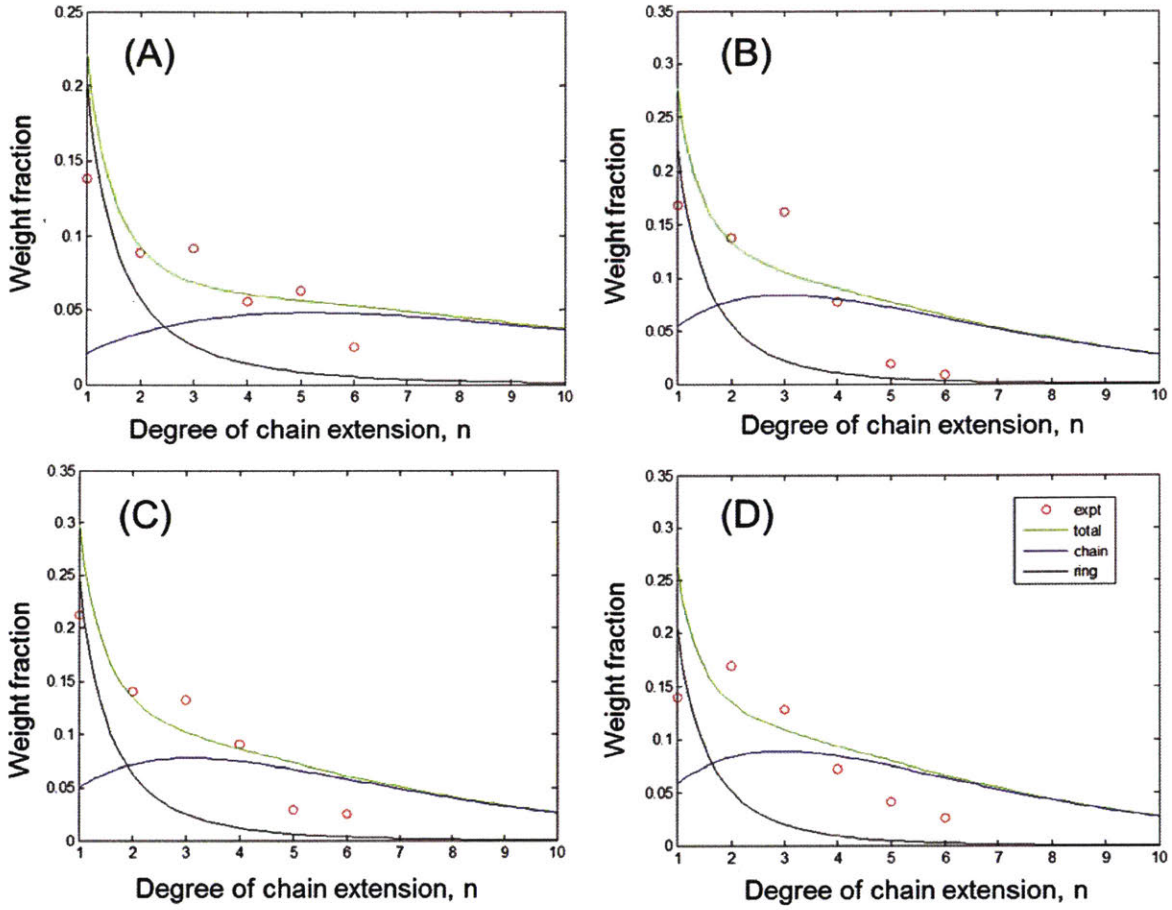

Figure 2-15. Molecular weight distributions of proteins fit to the Jacobson-Stockmayer distribution. Reactions were performed using (A) thiol-maleimide conjugation using $BM(PEG)_2$, (B) thiol-maleimide conjugation using MAL-PEG1k-MAL, (C) thiol-bromomaleimide conjugation, and (D) thiol-ene coupling.

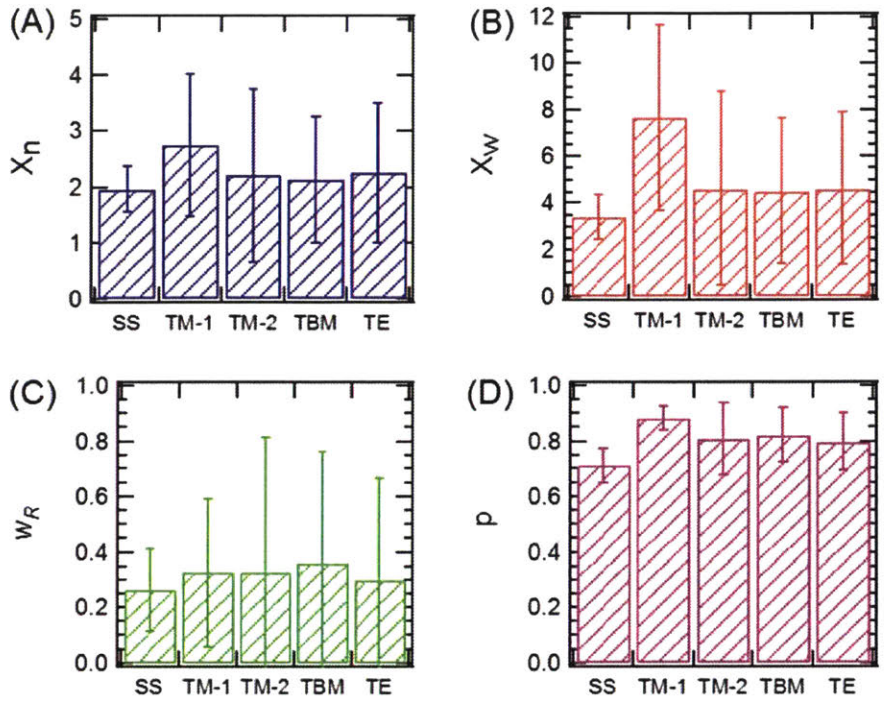

Figure 2-16. Comparison of (A) the total number-average degree of polymerization, (B) the total weight-average degree of polymerization, (C) the weight fractions of rings and (D) the end group conversion across different chain extension chemistries. Abbreviations: SS – disulfide bridging, TM-1 – thiol-maleimide conjugation using $BM(PEG)_2$, TM-2 – thiol-maleimide conjugation using MAL-PEG1k-MAL, TBM – thiol-bromomaleimide conjugation, and TE: thiol-ene coupling.

Finally, it should be noted that the Jacobson-Stockmayer theory does not apply to $A_2 + B_3$ type reactions. Therefore, the molecular weight distributions in these branching reactions were not analyzed with the theory.

2.3. Synthesis of poly(*N*,*N*-dimethylacrylamide) with pendant histidine side groups

2.3.1. Materials

Boc-His(Trt)-OH was purchased from Chem-Impex International Inc. (Wood Dale, IL). *N*-(3-aminopropyl)methacrylamide hydrochloride was purchased from Polysciences Inc. (Warrington, PA). These two chemicals were used as received. *N*,*N*-dimethylacrylamide (DMA) was purified through a basic alumina column to remove the inhibitor monomethyl ether hydroquinone. Azobisisobutylonitrile (AIBN) was recrystallized twice from ethanol. First, 5 g of AIBN was dissolved in ethanol. The solution was carefully heated to 80 °C with stirring and was kept at 80 °C for 3–5 min. The hot solution was filtered to remove any undissolved impurities. The hot filtrate was collected and cooled down to room temperature. Then the filtrate was stored at 4 °C overnight. The crystals were collected by vacuum filtration, washed with cold ethanol twice, and dried under vacuum in the dark.

2.3.2. Synthesis of *N*-Boc-N^{im}-Trityl-*N*-3-methacrylamidopropyl-L-histidinamide (1)

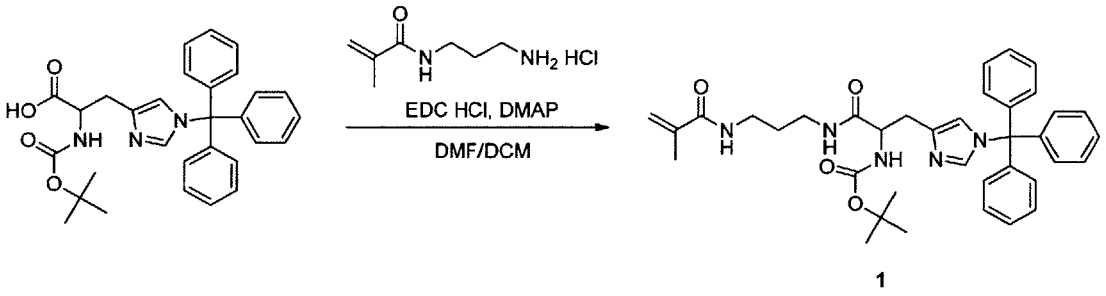

Figure 2-17. Synthesis of **1**.

Boc-His(Trt)-OH (5.00 g, 10.0 mmol), *N*-(3-aminopropyl)methacrylamide hydrochloride (1.79 g, 10.0 mmol) and 4-(dimethylamino)pyridine (2.44 g, 20.0 mmol) were dissolved in 100 mL of DCM/DMF mixture (1:1 v/v). *N*-(3-Dimethylaminopropyl)-*N'*-ethylcarbodiimide

hydrochloride (2.30 g, 12.0 mmol) was added to solution, and the reaction was stirred at room temperature overnight. The reaction mixture was diluted with 50 mL DCM and washed with 50 mL of 0.1 N HCl (a.q.), water, saturated $NaHCO_3$ (a.q.), water and brine. The organic phase was dried over Na_2SO_4, and the solvent was removed under vacuum. The crude product was further purified by silica gel flash chromatography using 0–10% MeOH in DCM to give **1** a white solid (4.80 g, 77.2% yield). ^{1}H NMR (300 MHz, $CDCl_3$) δ 7.42 (s, 1H), 7.36 – 7.29 (m, 9H), 7.17 – 7.02 (m, 8H), 6.85 (s, 1H), 6.43 (s, 1H), 5.78 (s, 1H), 5.30 (m, 1H), 4.44 (s, 1H), 3.32 – 3.18 (m, 3H), 3.17 – 3.02 (m, 2H), 2.99 – 2.92 (m, 1H), 1.96 (s, 3H), 1.64 – 1.55 (m, 2H), 1.42 (s, 9H). LRMS (ESI) m/z calculated for $C_{37}H_{44}N_5O_4$ $[M + H]^+$ 622.3, found 622.4.

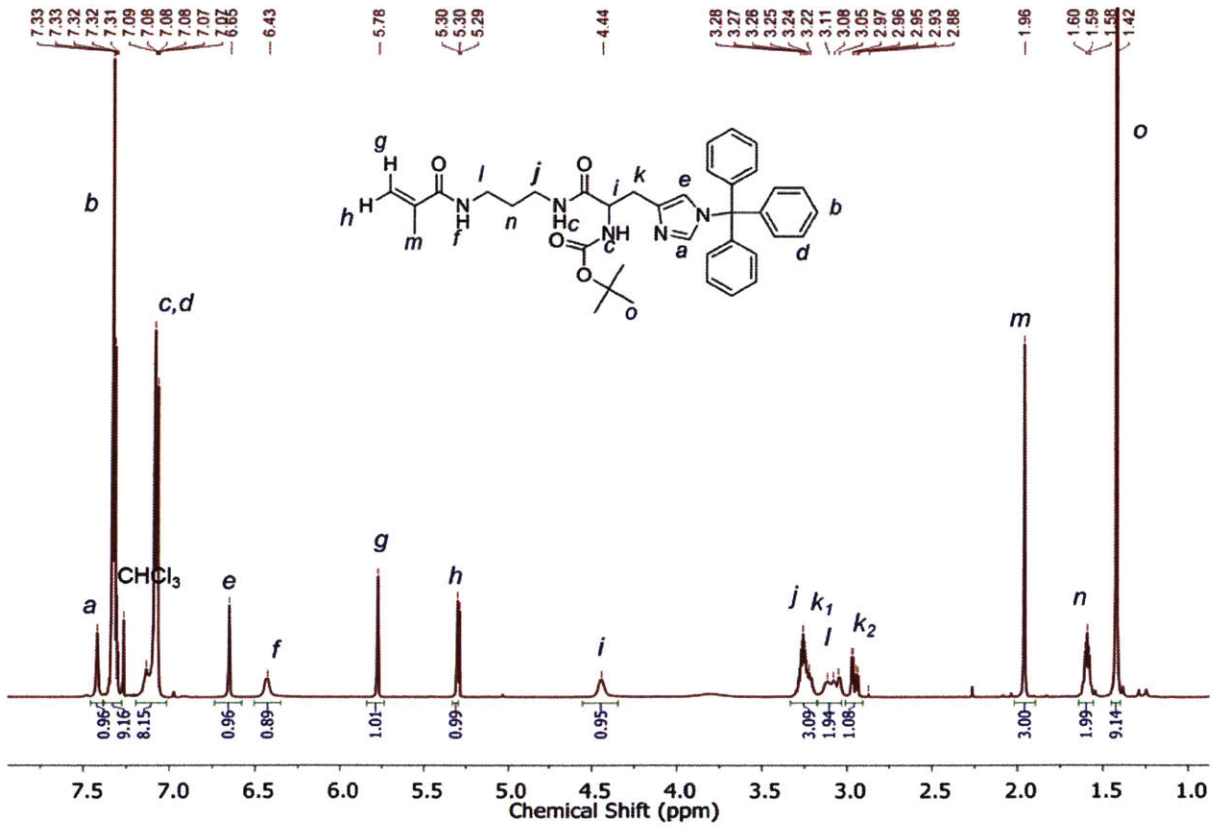

Figure 2-18. ^{1}H NMR spectrum of **1** in $CDCl_3$ (300 MHz).

2.3.3. Polymer synthesis and characterization

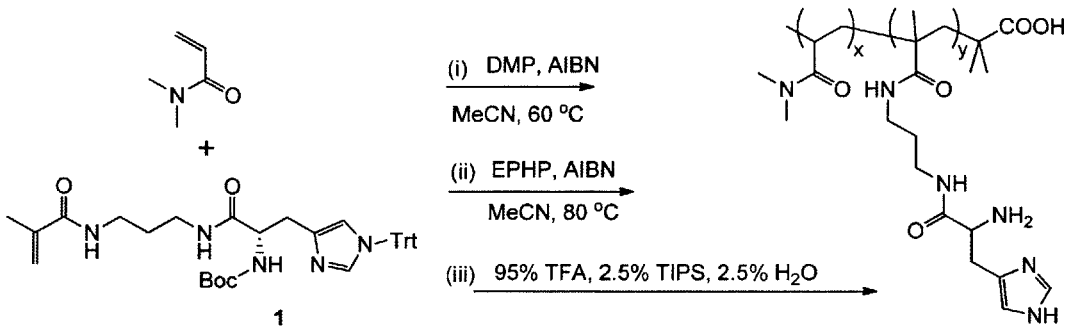

Figure 2-19. Synthesis of PDMA polymers with pendant histidine side groups.

Copolymers from DMA and **1** were synthesized by reversible addition-fragmentation chain transfer (RAFT) polymerization. The total monomer concentration was 2.0 M, and the ratio of DMA/**1**/DMP/AIBN was 342:18:1:0.2. Polymerization was performed in MeCN at 60 °C for 4 h, after which the reaction flask was immersed into liquid nitrogen and exposed to air. Polymers were purified by precipitation into diethylether three times and dried under vacuum. The molecular weight of polymer was 42.5 kg mol^{-1}, characterized by GPC (Figure 2-20). The mole fraction of monomer **1** in the final polymers was 5.3% as determined by ^1H NMR (Figure 2-21).

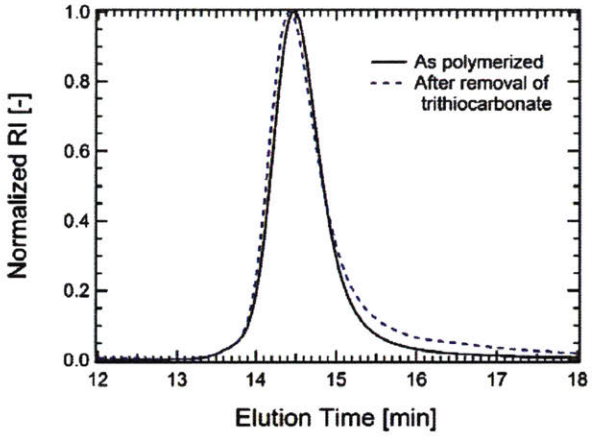

Figure 2-20. GPC characterization of copolymers (a) as polymerized and (b) after removal of trithiocarbonate.

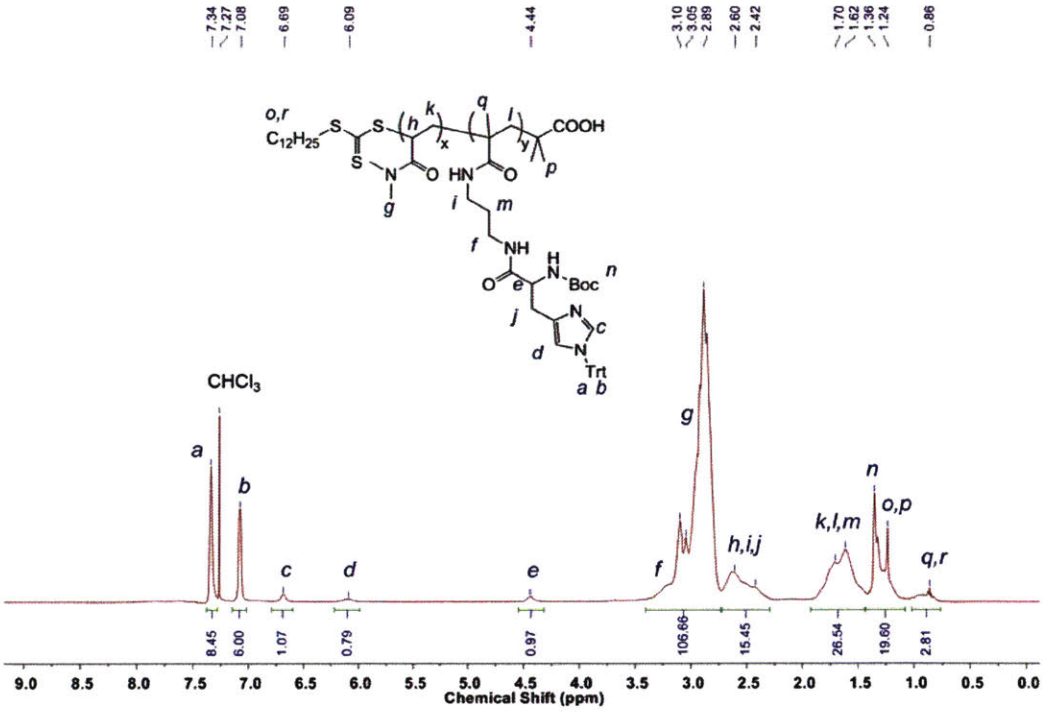

Figure 2-21. ^{1}H NMR characterization of PDMA polymers with protected histidine side groups in $CDCl_3$, 500 MHz. Peaks *b* and *g* assigned in the spectrum, corresponding to the protons in the *ortho-* position in the trityl groups in **1** and the protons of the methyl groups in DMA, are used for calculating the monomer ratio in the polymers.

The trithiocarbonate end group was then removed by radical-induced reduction. To a Schlenk tube was added polymers (500 mg, 11.8 μmol), 1-ethylpiperidine hypophosphite (105 mg, 588 μmol), AIBN (0.97 mg, 5.90 μmol), and MeCN (5 mL). The mixture was degassed by three cycles of freeze-pump-thaw. After the reaction was heated at 85 °C overnight, the solvent was removed under vacuum. The residue was dissolved in DCM (20 mL), and washed with brine (20 mL × 3). The organic phase was dried over Na_2SO_4 and concentrated under vacuum. The polymers were recovered by precipitation into diethylether three times. The resulting polymers maintained their low dispersity as confirmed by GPC (Figure 2-20). Complete removal of the trithiocarbonate end group was evidenced by the disappearance of the absorption peak at 312 nm from UV-vis spectroscopy (Figure 2-22).

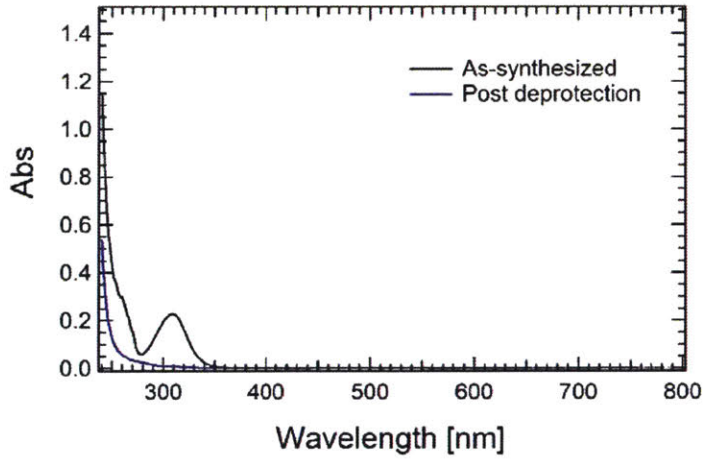

Figure 2-22. UV-vis spectroscopy confirming the removal of trithiocarbonate chain ends. Both polymers were prepared in MeOH at 0.5 mg mL^{-1}.

To remove the Boc and Trt protection groups, the resulting polymers (300 mg) were dissolved in DCM (5 mL). Water (125 μL), triisopropylsilane (TIPS, 125 μL) and trifluoroacetic acid (TFA, 5 mL) was then added sequentially to the solution. The mixture was stirred at room temperature for 2 h. The volatiles were removed under vacuum, and the residue was dissolved in a small amount of DCM.

The polymers were recovered by precipitation into diethylether three times and dried under vacuum. Quantitative deprotection was shown in ^{1}H NMR (Figure 2-23).

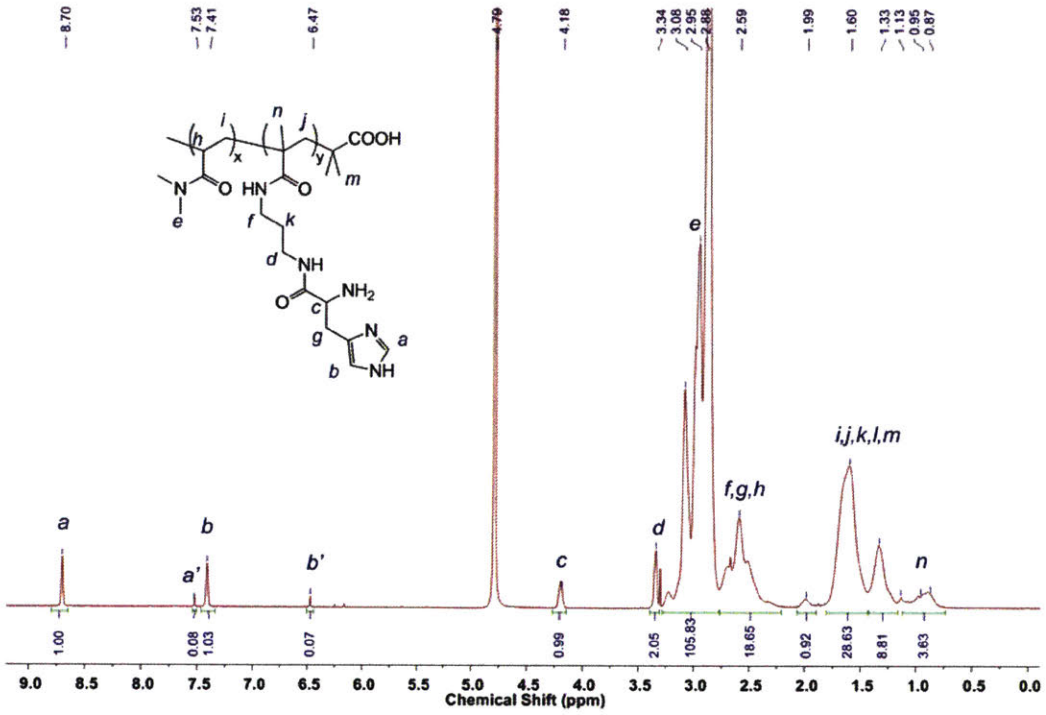

Figure 2-23. ^{1}H NMR characterization of copolymers after removal of trithiocarbonate chain end and the protecting groups (Boc and Trt) in D_2O, 500 MHz. The proton peaks *a* and *b* correspond to the histidine-TFA salt, and the peaks *a'* and *b'* correspond to the free histidine.

2.4. Mechanical tests

In this thesis, mechanical properties of protein or polymer gels were measured by shear rheology and uniaxial compression and tension tests. Experimental procedures for different mechanical tests are summarized below.

2.4.1. Shear rheology

Instrumentation. Shear rheology experiments were performed on Anton Paar rheometers (MCR 301 and MCR 502, stress-controlled but normally operated at the Direct Strain Oscillation mode, or MCR 702, strain-controlled). For consistency, motor adjustment and inertial calibration were performed before each experiment, during which no vibration should be allowed. The adjustment and calibration steps are highly recommended for all measurements and should be performed for measurements at angular frequencies above 100 rad/s or below 0.01 rad/s. When cone measuring tools were used in experiments at varying temperatures, adjustment and calibration were performed at the median temperature if the temperature sweep window was relatively narrow with a temperature difference less than 40 °C. Alternatively, experiments were performed using the TruGap accessories that have built-in sensors to automatically correct the thermal expansion factor and adjust the measuring gap at different temperatures. In all cases, the temperature was controlled by a Peltier device.

The measuring tools (or sometimes referred to as upper geometries) used in this thesis are listed in Table 2-1. Most of the experiments were performed using a 25 mm cone-plate. For testing the linear mechanics of the protein hydrogels and polymers gels studied in this thesis, the surface treatment of the measuring tool was found not to affect the experimental result. However, a sandblasted cone plate CP25-1/S was used for strain sweep measurements that extended to large strains such as 1,000% to suppress slip. A 50 mm cone plate CP50-0.5 was used in some cases to generate torque values 8 times larger than those from CP25. Hence CP50-0.5 was used for measuring soft gels to generate sufficient torques to ensure data accuracy (more detailed discussion will be presented later in this section). The sample volume required for PP10 was the smallest

among all the tools, and nearly 50 μL was sufficient to completely fill the space of a 500 μm measuring gap. Therefore, PP10 was used for measurements under sample volume constraints.

Table 2-1. Measuring tools (upper geometries) used in this thesis for rheology experiments.

Entry	Diameter [mm]	Measuring gap [μm]	Surface treatment	Conversion factor [Pa/mNm]
CP25-1/S	25	48	Sandblasted	244.4625
CP25-1/TG	25	50	TruGap coating	244.4285
CP25-1	25	50	Stainless steel	244.5001
CP50-0.5/TG	50	50	TruGap coating	30.5999
PP-10	10	Adjustable, normally set at 500	Stainless steel	3414.7325

Sample preparation. All gel samples were centrifuged at 21,100 ×g for 10 min to remove bubbles before loading onto the rheometer. To minimize evaporation of water (for hydrogels) or polar organic solvent (for instance, DMF in metallogels), the edge of sample was coated with mineral oil. This practice was necessary for measurements longer than 1 h at room temperature. For hydrogels formed by entangled proteins, samples were first heated from 25 to 90 °C at a ramping rate of 5 °C/min and then immediately cooled to 25 °C at a ramping rate of 5 °C/min (Figure 2-24). This brief thermal treatment unfolded the coiled-coil domains, enabling rapid stress relaxation in the protein network and effectively eliminating thermal and shear history in the sample. This temperature ramp procedure was not used for measuring the metallogels due to their relatively fast stress relaxation.

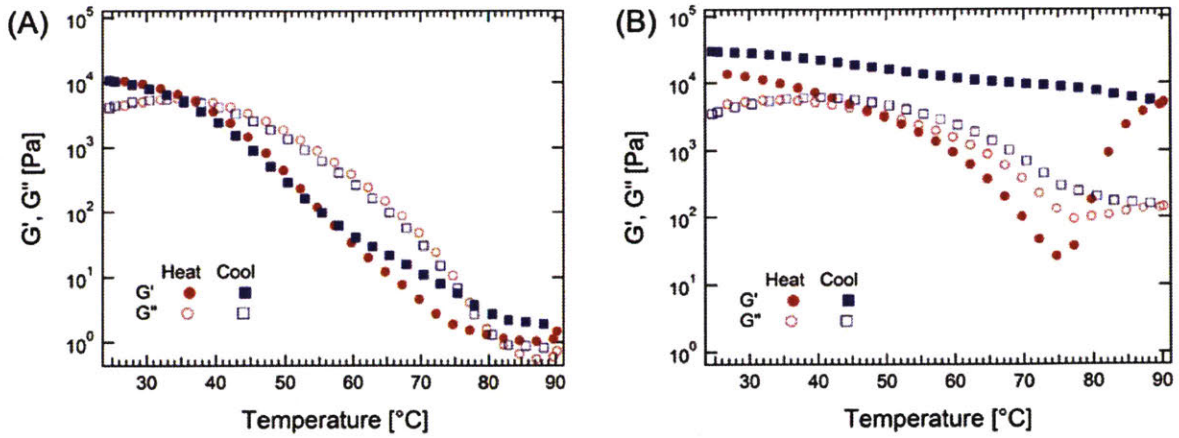

Figure 2-24. Thermal annealing of protein hydrogels (A) P_4 and (B) Cys-P_4-Cys on the rheometer. Both gels were at 20% (w/v). The measurements were taken at 1% strain and 1 rad/s.

Frequency sweep. The linear viscoelastic (LVE) regimes of various gels were first determined by strain sweep measurements from 0.01 or 0.1 to 1,000% strains (Figure 2-25). For gels investigated in this thesis, 1% strain amplitude was typically within the LVE, and this strain amplitude was typically used for frequency sweep measurements.

Frequency sweep experiments were performed from 100 to 0.001 rad/s in the LVE at a data density of at least 5 points per decade on a logarithmic scale. Data with torque values larger than 0.5 μNm, which is two orders of magnitude larger than the minimal torque oscillation (~ 2 nNm for all three rheometers used), were reported. To increase the torque values, a larger upper geometry could be used (Figure 2-26). Even above this minimum acceptable torque cutoff, there were noticeable differences of data obtained by using a larger geometry. In addition, the last cycle of the stress and strain waveforms could be examined to ensure good data quality (Figure 2-27). This information could be useful to examine samples that were mechanically weak or could easily fracture.

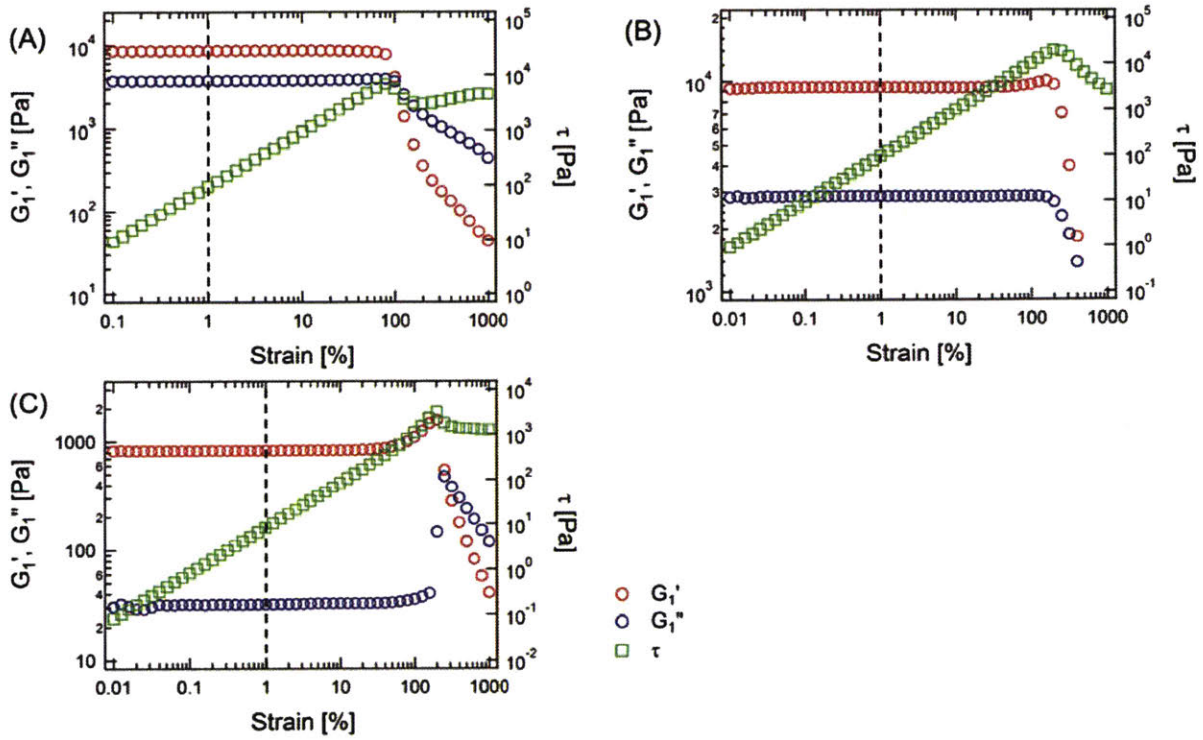

Figure 2-25. Strain sweep experiments on (A) hydrogels P_4 at 15% (w/v), (B) metallogels formed by terpyridine end-functionalized four-arm PEG polymers transiently linked to Zn^{2+} in DMF at 10% (w/v), and (C) metallogels formed by linear PDMA polymers with pendant histidine side groups transiently linked to Ni^{2+} in 100 mM Bis-Tris buffer (pH 7.0) at a polymer concentration of 10% (w/v). The strain amplitude 1% used in the frequency sweep experiments is shown in dashed line in all panels.

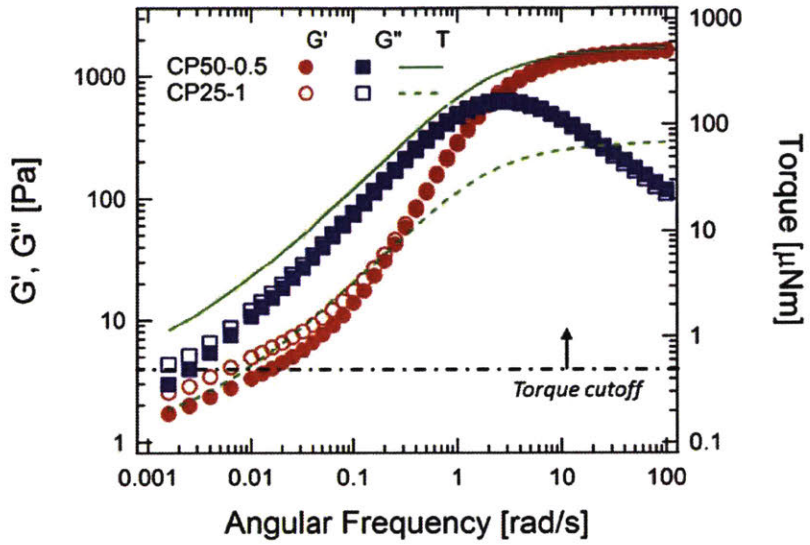

Figure 2-26. Comparison of frequency sweep measurements on hydrogel P_4 at 5% (w/v) using CP25-1 and CP50-0.5. The proposed 0.5 μNm torque cutoff is shown as the dotted dashed line in black.

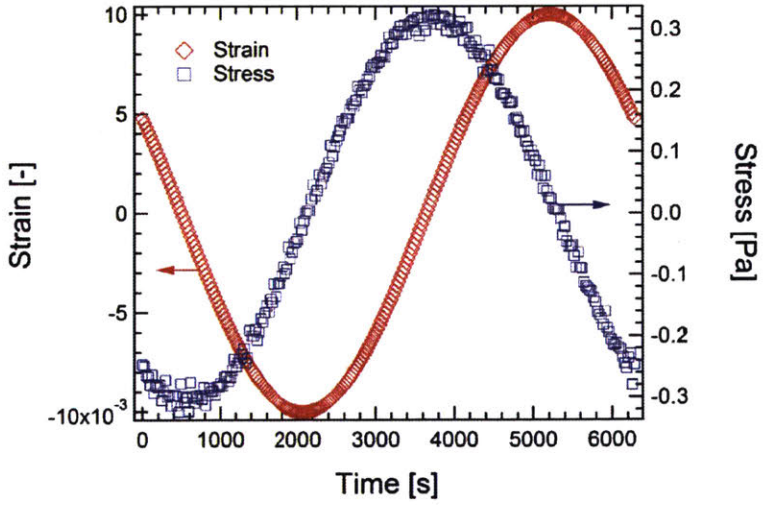

Figure 2-27. Strain and stress waveforms at the last oscillation cycle in a frequency sweep measurement on hydrogel P_4 at 10% (w/v) at 1% strain amplitude and at 0.001 rad/s.

Creep and recovery. In creep experiments, samples were subjected to a constant load for 30 min or up to 2h until a steady-state creep was reached, which manifested as a linear strain-time relationship (Figure 2-28). After then the load was subsequently removed to examine the recovery behavior for the same time period. Three loading conditions with varying stress levels should be tested to ensure that the test was in the linear regime where creep compliance vs time relationship (the ratio of strain to stress, unit: Pa^{-1}) was independent of the stress applied (Figure 2-28).

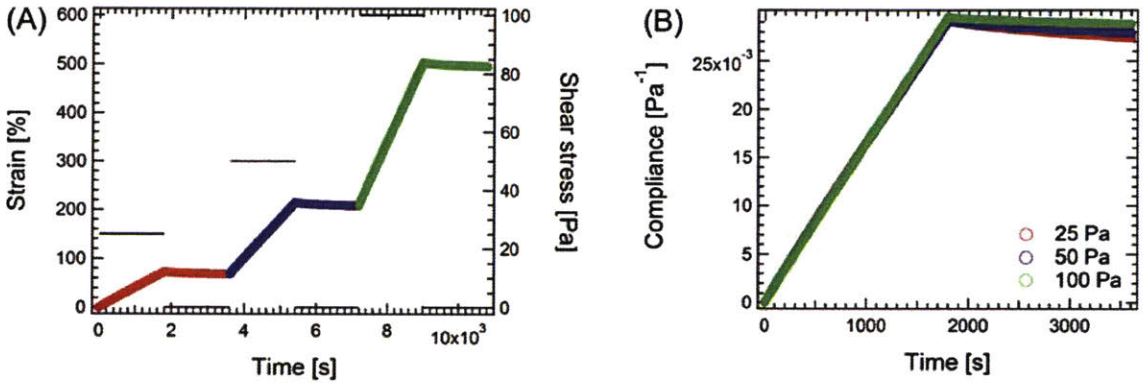

Figure 2-28. Representative creep-recovery data of hydrogel P_4 at 30% (w/v) under three different applied stresses: 25, 50 and 100 Pa. (A) Strain vs. time. (B) Compliance vs. time. The superposition of three compliance-time curves demonstrates that the tests were performed in the linear regime. The steady-state phase of creep was taken from 1500 to 1800 s.

A method of converting creep compliance to dynamic moduli. Typical frequency sweep measurements end at 10^{-3} rad/s because it takes a very long time (more than 15 h) to generate one data point at frequencies below 10^{-3} rad/s; however, it is often desirable to obtain rheological information in the low-frequency regime. In addition, because the measuring torque decreases with frequency, it also becomes more difficult to obtain reliable data in the low-frequency limit. The principle of time-temperature superposition, which is often used to obtain rheological master

curves for conventional polymers over a large frequency window, may not be applicable to associating polymeric solutions, gels or melts because of their thermodynamic complexity. Therefore, in this thesis, the relationship of creep compliance vs. time was transformed into dynamic moduli in order to access information in the very low frequency regime (10^{-4}–10^{-3} rad/s). First, time dependent creep compliance was first transformed into dynamic moduli using the methods described by Ferry.[10]

$$J'(\omega) = J_e^0 - \omega\int_0^\infty \left[J_e^0 - J(t) + t/\eta_0\right]\sin\omega t dt \tag{2-11}$$

$$J''(\omega) = 1/\omega\eta_0 + \omega\int_0^\infty \left[J_e^0 - J(t) + t/\eta_0\right]\cos\omega t dt \tag{2-12}$$

where J_e^0 is the recoverable compliance and η_0 the zero-shear-rate viscosity. They are the intercept and the inverse of the slope from a linear fit in the steady-state of creep, respectively. The extraction of J_e^0 and η_0 are very important to the success of this transformation. The dynamic moduli were then calculated as

$$G' = J'/\left(J'^2 + J''^2\right) \tag{2-13}$$

$$G'' = J''/\left(J'^2 + J''^2\right) \tag{2-14}$$

The data obtained by small-amplitude oscillatory shear and by transformation from the creep data overlap for at least one decade in the frequency domain, confirming the efficacy of the method described here (see an example in Figure 2-29). The MATLAB code for the transformation is provided in the appendix of this chapter (Section 2.7).

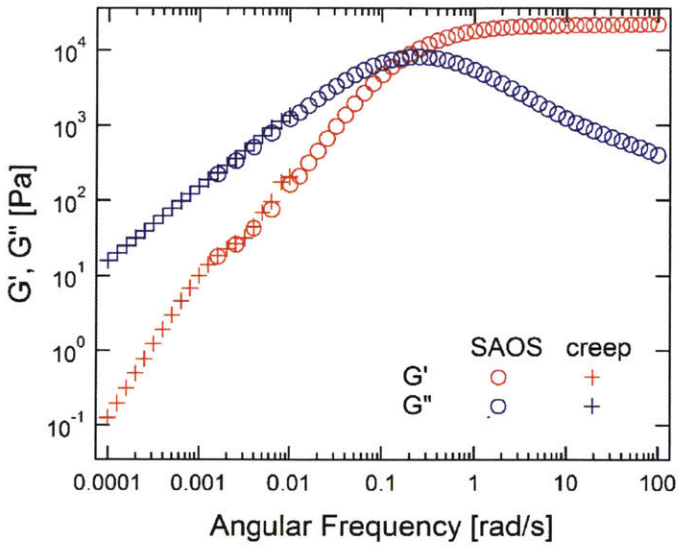

Figure 2-29. Representative dynamic moduli master curves combing small amplitude oscillatory shear (SAOS) and creep data.

2.4.2. Uniaxial Compression and Tension

Instrumentation. Uniaxial tension and compression experiments were performed on a Zwick/Roell Z2.5/TS1S materials testing machine and TestXpert V10.1 master software (Ulm, Germany) with a 20 N load cell. All tests were performed at room temperature, 24 ± 1 °C. All samples tested were free of any visible defects such as bubbles and voids.

Compression. Hydrogel specimens were pressed into cylindrical Teflon molds of 8 mm in diameter and 8 mm in height, with both ends sealed with thick Teflon sheets (Figure 2-30). Samples were annealed in a humidified incubator at 37 °C for 3 h and stored in fridge at 4 °C for 2 d to allow stress relaxation. This time period was at least one order of magnitude larger than the network relaxation time calculation from the *G'-G"* crossover frequency.

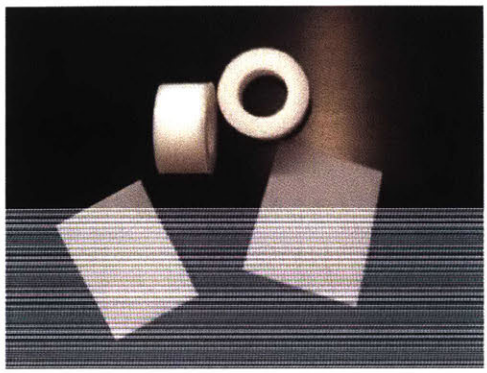

Figure 2-30. A picture showing the Teflon molds for preparing samples for compression test.

To perform the compression test, the specimen was placed on a bottom plate. A thin layer of soapy water (approximately 5% v/v of VWR SoftCIDE extra mild hand soap) was used to provide sufficient lubrication during compression. A preload of 0.005–0.01 N was applied to samples to initiate contact. This amount of preload was large enough to be above the resolution of the load cell (0.001 N) but small enough to minimize deforming the sample before the actual experiments. Two test procedures were used in this thesis. (A) Compression experiments were performed at three different nominal strain rates (0.1, 1 and 10%/s) to a final true strain of 160%, followed by unloading to 0% strain at a nominal strain rate of 10%/s. (B) Interval loading at 1%/s nominal strain rate to 160% true strain, with partial unloading (10%/s nominal strain rate) segments at 40, 80 and 120% to probe the relaxation behavior. Representative compression data from these two procedures is shown in Figure 2-31.

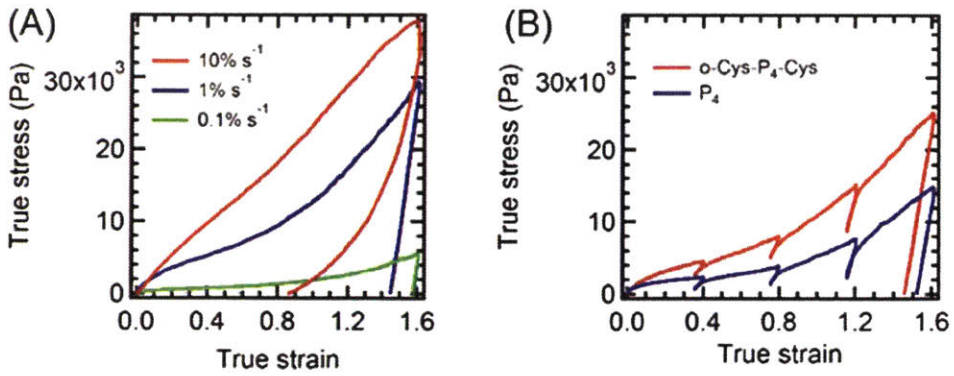

Figure 2-31. (A) Uniaxial compression of chain-extended, entangled hydrogels at 15% (w/v) at different strain rates. (B) Uniaxial compression of chain-extended, entangled protein gel o-Cys-P_4-Cys and unentangled protein gel P_4 at 1% 1/s nominal strain rate to probe the relaxation behavior.

Tension. For better visualization, hydrogels were hydrated in phosphate buffer supplemented with 0.1 mg/mL fluorescein amine (isomer I, Sigma). Hydrogel specimens were prepared in nearly rectangular Teflon molds 20 mm in width, 28 mm in length and 2 mm in thickness (Figure 2-32). Samples were annealed in a humidified chamber at 37 °C for 3 h and stored in fridge at 4 °C for 2 d to allow complete stress relaxation. A custom designed cutter was used to obtain a dogbone shaped tensile specimen with a neck width of 4 mm (Figure 2-32). No visible defects were observed after cutting. Sandpaper (ISO grid designation: P80) was glued to the grips to provide friction and to ensure that the sample did not slip. The ramp-relaxation testing protocol consisted of loading ramps alternating with relaxation intervals of 600 s, until specimen failure. During the loading ramps, the specimens were stretched at an average true strain rate at 0.06 s^{-1} to increasing levels of engineering strain (625, 1,250, 2,500 and 3,750%) until mechanical failure (Figure 2-33). This protocol was developed by accident but was found to be an effective procedure that yielded the most significant stretch. When intermittent holding periods were

shortened to 60 s, the entangled gels were still extensible but could only be stretched up to ca. 1,250% engineering strain (Figure 2-33). It was thus hypothesized that the holding period could stabilize the aligned protein chains. Further studies should be performed to carefully characterize the structural transformation during tensile loading.

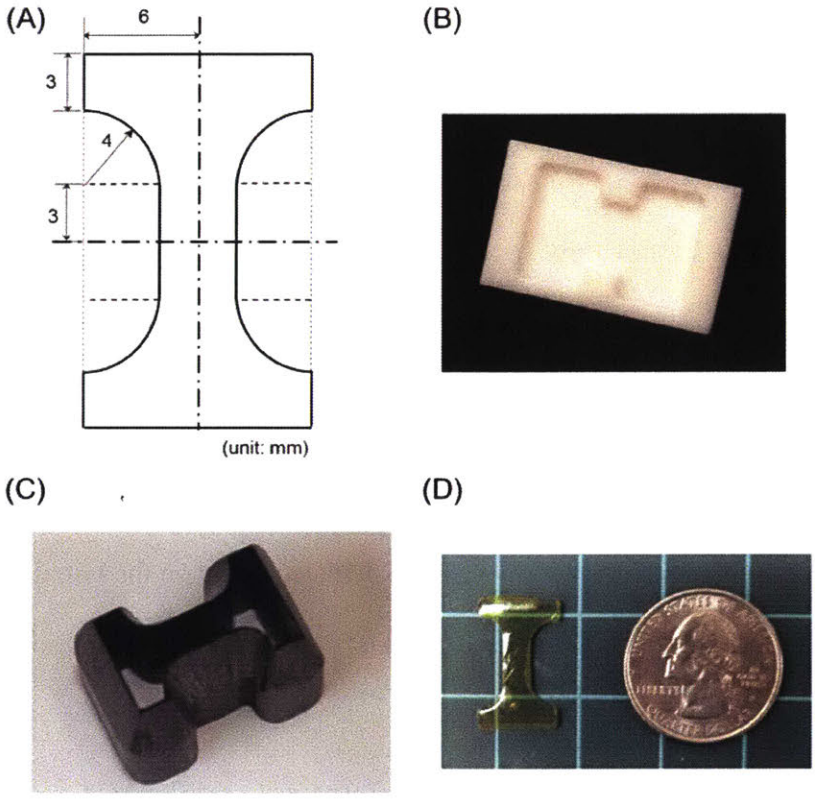

Figure 2-32. (A) An engineering drawing of the dog bone dimension, unit: mm. (B) Teflon mold. (C) The custom designed dog bone cutter. (D) A hydrogel specimen for tensile testing.

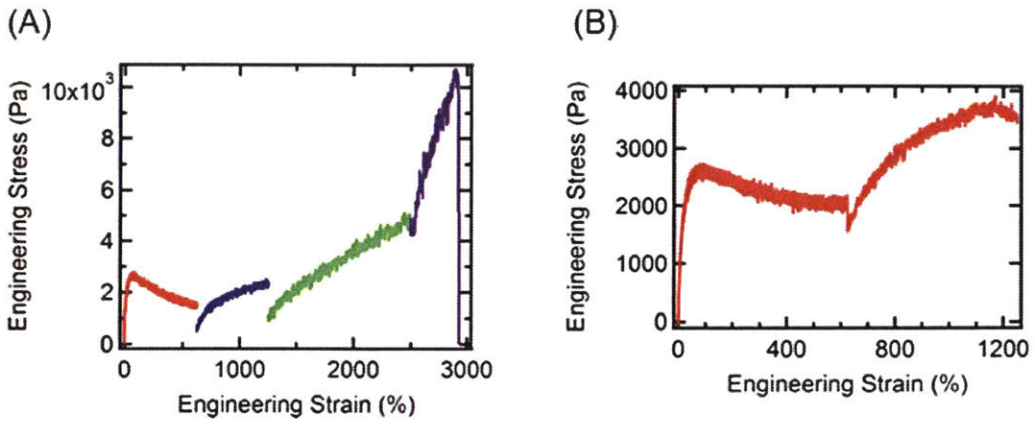

Figure 2-33. Uniaxial tensile experiment on o-Cys-P_4-Cys at 15% (w/v) at 25 °C. The holding time in (A) and (B) were 600 s and 60 s, respectively.

Calculation of stress, strain and toughness. The stress-strain curve is obtained from the raw force-displacement relationship. The engineering stress (σ_E) is calculated based the initial cross-sectional area and engineering strain (ε_E) is calculated based on the initial sample geometry. The true strain (ε_T) and true stress (σ_T) are calculated from the following relations:

$$\varepsilon_T = \ln(1+\varepsilon_E), \tag{2-15}$$

$$\sigma_T = \sigma_E(1+\varepsilon_E). \tag{2-16}$$

Toughness, U, is the energy per unit volume that a sample absorbs before failure. Mathematically, it is calculated as the area underneath the stress-strain curve:

$$U = \int_0^{\varepsilon_f} \sigma d\varepsilon, \tag{2-17}$$

where ε_f is the failure strain.

2.5. Site-specific labeling of artificial proteins or polymers *via* thiol-maleimide coupling

2.5.1. Labeling and purification of P_4-Cys

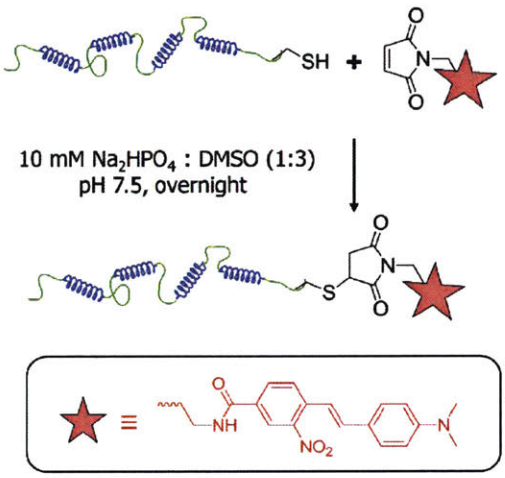

Figure 2-34. Synthesis of ONS-Labeled Proteins P_4 via Thiol-Maleimide Conjugation.

The synthesis of the maleimide-functionalized photochromic 4'-(*N*,*N*'-dimethylamino)-2-nitrostilbene dye (ONS-M) followed a previously published procedure without changes.[11] In a typical conjugation reaction, protein P_4-Cys was first dissolved in a 3:1 (v/v) mixture of DMSO : (10 mM NaH_2PO_4) to a concentration of 1 mg/mL, and the solution was stirred at room temperature for 2 h to ensure complete dissolution of proteins. Next, a 20-fold excess of TCEP was added from a freshly prepared stock solution at 0.5 M. The mixture was then incubated at room temperature for 15 min to reduce pre-formed disulfide bridges. During this time, ONS-M was prepared as a stock solution in DMSO at a concentration of 100 mg/mL. The ONS-M stock solution was then added dropwise to the protein solution, and the pH of the reaction mixture was adjusted to 7.5 using a pH meter. After overnight reaction in the dark, the mixture was dialyzed

against MilliQ water and lyophilized. To partially remove the unreacted free dye, the lyophilized powder was redissolved in a buffer with 6 M urea and 20 mM Tris at pH 8.0 (freshly prepared). After the solution was centrifuged in 50 mL conical tubes at 12,500 RPM using a Fiberlite™ F14-14×50cy fixed-angle rotor for 30 min to remove precipitated dyes, the supernatant was separated from the precipitates and transferred to a spin concentrator (Millipore, MWCO 30kDa). The supernatant was spun at 4,000 ×g and concentrated to ~ 1 mL. The spin-through fraction containing free dyes appeared to be an orange color and was discarded. Urea buffer (~ 14 mL) was added to the spin concentrator. The process was repeated several times until the spin-through was almost colorless, which typically took 5-8 cycles. The product was then purified by anion exchange using HiTrapQ Sepharose HP 5mL columns (GE Healthcare) using the same purification method specified for the same associative proteins. A representative elution profile and corresponding SDS-PAGE analysis are shown in Figure 2-35 and 2-36, respectively. The product was further purified by size exclusion with Sephadex LH-20 resins (GE healthcare) as an orthogonal purification to ensure complete removal of free dyes using a buffer containing 6 M urea and 20 mM Tris (pH 8.0). The conjugation efficiency was determined greater than 99% confirmed by UV/Vis spectroscopy (Figure 2-37) using a previously measured ONS extinction coefficient[12] ε (365 nm) = 18,200 M^{-1} cm^{-1}. The estimation is shown below:

$$\text{dye conjugation efficiency} = \frac{\text{dye conc.}}{\text{protein conc.}} = \frac{0.03718 / \left(18200\left[\text{M}^{-1}\text{cm}^{-1}\right] \times 1[\text{cm}]\right)}{2.0 \times 10^{-6}[\text{M}]} = 102\% \qquad (2\text{-}18)$$

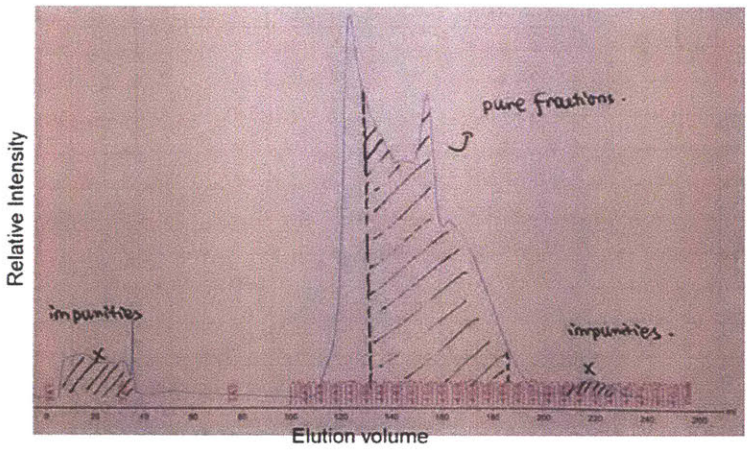

Figure 2-35. Representative elution chromatogram of anion exchange purification of ONS-labeled P_4 proteins.

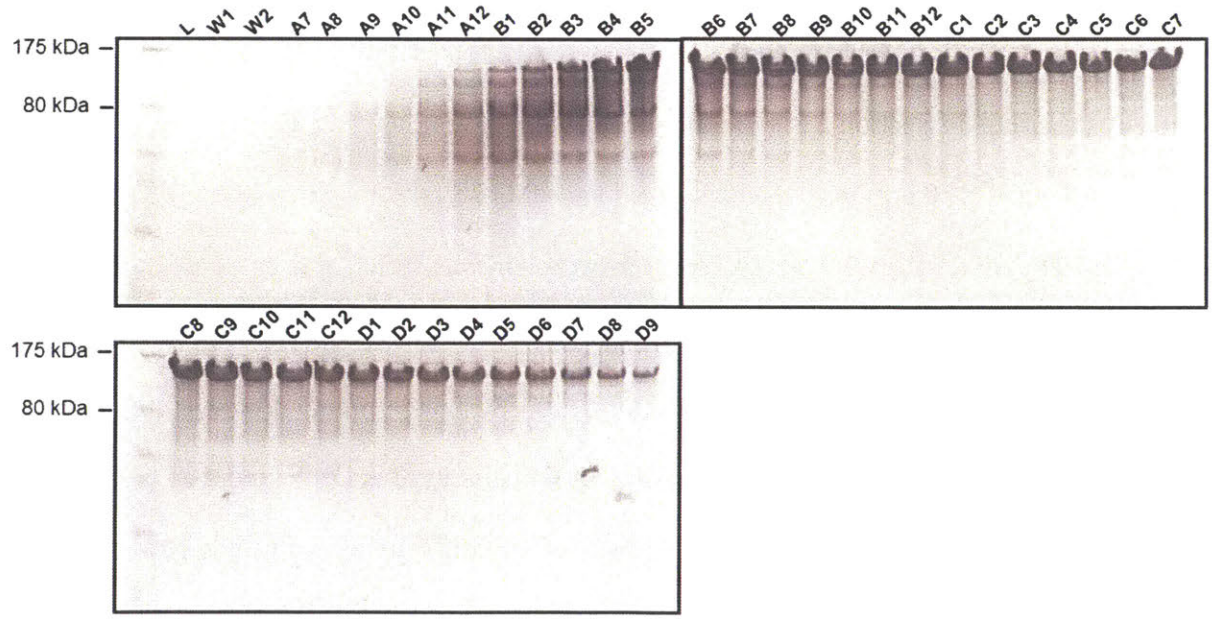

Figure 2-36. SDS-PAGE analysis of eluted fractions. In this example, fractions B5–D6 were combined and used for diffusion studies. The letters L and W represent fraction eluted during the loading and wash steps.

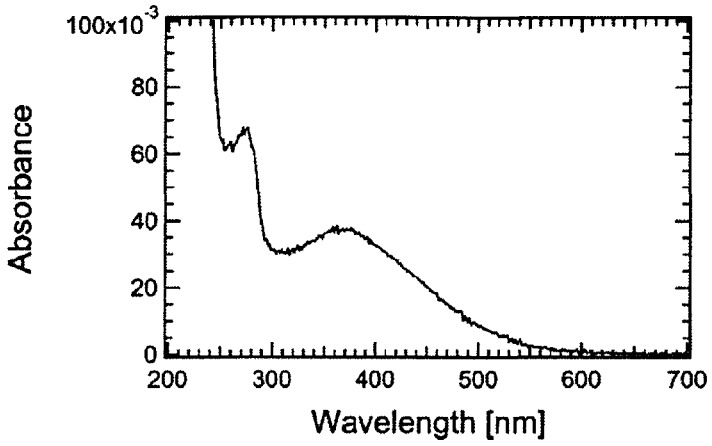

Figure 2-37. UV-vis spectrum of ONS-P_4 at 2 μM in 100 mM phosphate buffer at pH 7.6.

2.5.2. Labeling and purification of PDMA polymers with pendant histidine side groups

Copolymers from DMA and **1** were first polymerized under the same condition as previously described in Section 2.3.3. In the second step for removing the Boc and Trt protecting groups, copolymers (150 mg) were then dissolved in DCM (3.3 mL), to which water (83 μL), TIPS (83 μL), and TFA (3.2 mL) were added. After the reaction was stirred at room temperature for 2 h, volatiles were removed under vacuum. The residue was redissolved in small amount of DCM, and polymers were purified by precipitated into diethylether three times. For dye conjugation, polymers from the previous step (74 mg, 2 μmol) was first dissolved in DMF, and then hexylamine (5.3 μL, 40 μmol) was added. The reaction was stirred overnight under a nitrogen atmosphere to ensure complete aminolysis and to minimize undesirable cysteine oxidation. Then tris(2-carboxyethyl)phosphine hydrochloride (5.7 mg, 2 μmol) and maleimide-functionalized 4′-(*N*,*N*′-dimethylamino)-2-nitrostilbene (8.7 mg in 200 μL DMSO, 40 μmol) were added to the reaction mixture. After the reaction was stirred for 6 h in the dark, the solution was diluted with 30% MeOH in water. The mixture was transferred to a centrifugal filter (10 kDa MWCO), spun at

4,000 ×g for 12 min at room temperature, and more solution of 30% MeOH in water was added. This process was repeated several times until the spin-through fraction was nearly colorless. The resulting polymer solution was further purified over a Sephadex LH-20 resin to ensure complete removal of free dyes. Polymers were recovered after dialysis and lyophilization.

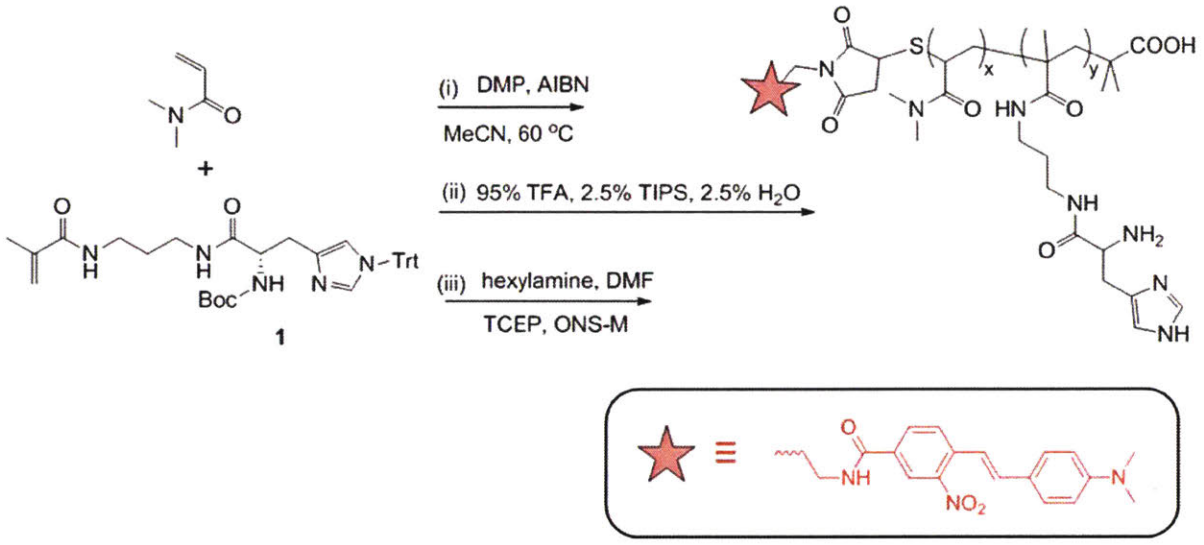

Figure 2-38. Synthesis of ONS-labeled PDMA polymers with histidine side groups.

2.6. Diffusion measurements using forced Rayleigh scattering

2.6.1. Dye options

In this thesis, three different photochromic dyes were used for labeling polymers or proteins for forced Rayleigh scattering (FRS) experiments. These dyes were *ortho*-nitrostilbene (ONS), nitrobenzoxadiazole (NBD, sometimes also referred as nitrobenzofurazan) and fluorescein, and their chemical structures are shown in Figure 2-39. All dyes can be irreversibly bleached by using a cyan laser at 488 nm. In the following paragraphs, the advantages and disadvantages of different dyes are briefly discussed.

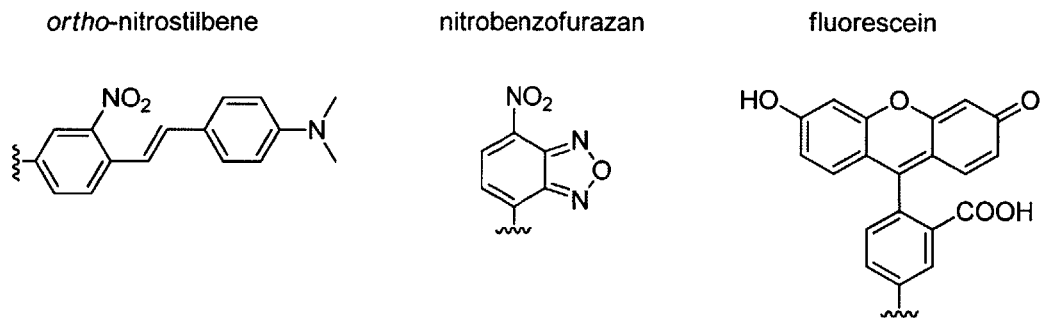

Figure 2-39. Molecular structure of *ortho*-nitrostilbene (ONS), nitrobenzoxadiazole (NBD) and fluorescein.

Among the three dyes, ONS is most frequently used for FRS measurements at different conditions including melt[13, 14], solutions[12] and gels[15]. The photo-induced isomerization reaction of ONS has been well characterized and documented in literature.[16, 17] In addition, ONS is thermally stable up to 200 °C. However, side reactions, mainly oxidation, may occur in the presence of oxygen when the experiment temperature is above 100 °C, which results in abnormal FRS signals.[16, 17] The ONS dye has several disadvantages that can limit its application in FRS experiments. First, the most useful ONS-COOH form for derivation is not commercially available, and its synthesis takes several steps with a low yield.[12] Second, the carboxylic acid group on the ONS molecule has relatively low reactivity. To achieve high degree of labeling, the carboxylic acid is usually converted to acyl chloride[12], or the reaction is run at an elevated temperature for a long time (for example at 50 °C for 2 days)[11, 14]. Third, because ONS is fairly hydrophobic, extra caution should be given when using ONS for labeling small molecules for diffusion measurements in aqueous solutions. Fourth, under some experimental condition, ONS may show a complimentary grating effect, which will be discussed in more detail in Section 2.6.3; however, the physical origin has not been well understood.[14] Last, ONS may not be a good option for

studying fast diffusion processes since the shortest grating writing time is 250 ms using a 100 mW cyan laser from the author's experience.

To the best of the author's knowledge, this thesis demonstrates for the first time that NBD can be used as a photochromic dye in FRS experiments. Previously, NBD has only been used in FRAP measurements, especially in the studies of the mobility of lipids embedded in the membranes.[18-21] However, the photobleaching reaction of NBD is not well characterized. Various forms of derivatizable NBD molecules are commercially available from Sigma-Aldrich, for example, carboxylic acid for esterification, amine for amidation, chloride for nucleophilic substitution[21], and hydrazine that can react with aldehyde or ketones. From the molecular structure, NBD is less hydrophobic compared to ONS and has a weaker tendency to aggregate in an aqueous environment. This is perhaps one of the main reasons that NBD has been extensively used in FRAP experiments in aqueous solutions.[18-20] NBD has also been used in measurements at the glass state[21] or in polar organic solvents[22], and exhibits thermal stability up to 80 °C.[21] For NBD, it takes at least 200 ms to write a holographic grating in FRS experiments using a 100 mM cyan laser in the author's hands. Finally, complementary grating phenomenon has not been observed by the author, but it should be emphasized that only a limited set of experimental conditions has been explored.

Fluorescein is arguably the most widely used dye molecule for labeling in many applications. Fluorescein is usually linked to other molecules *via* isothiocyanate-amine coupling, maleimide-thiol coupling or *N*-hydroxysuccinimide (NHS) ester-amine coupling. All of the corresponding reactive fluorescein molecules are commercially available from Sigma-Aldrich or Thermo Fisher Scientific. Fluorescein is the most hydrophilic dye among the three, and thus it is very suitable for experiments in aqueous buffers. However, it should be noted that the fluorescence

intensity and the absorption spectrum of fluorescein and its derivatives are pH-dependent.[23] Although fluorescein is mainly used in FRAP experiments, it has also been occasionally used in FRS measurements[24-26]. In the author's hands, the shortest time for writing a grating in FRS experiments is 50 ms when fluorescein is used. Complementary grating phenomenon is usually observed from the author's experience.

2.6.2. Sample preparation

The protein gels for diffusion measurement were prepared by hydrating ONS-labeled P_4 and matrix P_4 in 100 mM sodium phosphate buffer at pH 7.6 (filtered through a 0.2 μm filter) to the desired concentrations at 4 °C for 2 days, and the concentration of ONS-P_4 was approximately at 150 μM. The gels were mixed periodically with a micro spatula to ensure homogenous distribution of dye-labeled proteins. After each mixing step, the gels were centrifuged at 21,100 ×g for 5 min at 4 °C to remove bubbles. The gels were finally pressed in between two quartz disks (17 mm in diameter and 1 mm thick, ground and polished, from Technical Glass Product Inc.) with a 0.5 mm Teflon spacer in a brass sample holder. The quartz disks were previously cleaned with ultrapure water and acetone separately for three times, and they were blow dried by compressed air. The quartz disks for forced Rayleigh scattering experiments should be free of visible scratches. The sample thickness (0.5 mm) should be at least an order of magnitude larger than the largest grating spacing (50 μm). Under this condition and when the differences in the refractive index Δn and the absorptivity with amplitudes Δa were small, the diffracted intensity decay I was proportional to the square of Δn and Δa:[27]

$$\frac{I}{I_0} = \exp\left(\frac{-2aB}{\cos(\theta/2)}\right)\left(\sin^2\frac{\pi B\Delta n}{\lambda\cos(\theta/2)} + \sinh^2\frac{B\Delta a}{2\cos(\theta/2)}\right), \tag{2-19}$$

where I_0 is the incident intensity, θ is the angle at which two laser beams intersect, λ is the beam wavelength, and B is the sample thickness. Therefore, the diffractive intensity was a square function of a (stretched) exponential decay function or a sum of (stretched) exponential functions. This is the mathematical basis for the function forms used in data analysis, which will be discussed more extensively in Section 2.6.3.

Preparation of metallogels made from four-arm poly(ethylene glycol) polymer building blocks (made by Professor Sebastian Seiffert's group) for diffusion measurements is described below. First, an appropriate mass of terpyridine end-functionalized 4-arm PEG polymers was dissolved in 500 μL of DMF. Separately, $Zn(NO_3)_2 \cdot 6H_2O$ in a 2:1 stoichiometric concentration to the PEG polymer was dissolved in 500 μL of DMF and vortexed to reach complete dissolution of solids. Equal volumes of the two solutions were then combined in an Eppendorf tube and mixed rigorously with a micro spatula to ensure homogenous mixing. The sample was centrifuged at 21,100 ×g for 10 min to remove bubbles. To prepare samples for self-diffusion measurements, 2 mol% of NBD-labeled four-arm associating PEG polymers was added and dissolved together with the matrix polymers in the first step. For the samples used in tracer-diffusion measurements, the synthesis method introduced ~2 mol% of the NBD labeled tracers in the matrix. Therefore, the concentration of dye labeled polymers was nearly two orders of magnitude lower than the estimated overlap concentration[22] of the star-shaped polymer building block in DMF ($c^* \approx 94$ g L^{-1}). This condition ensures that interactions between tracers could be neglected. Gels were eventually sealed between two quartz disks (17 mm in diameter) separated by a 0.5 mm thick Teflon spacer.

It is important to minimize introduction of dust during the sample preparation procedure, otherwise data acquisition at long times would be greatly affected by a largely fluctuating baseline

(Figure 2-40), especially at large grating spacings. There were several ways to minimize the negative effect of dust. First, the quartz disks and the Teflon spacer should be cleaned by compressed air. After this cleaning step, they should be placed on a clean piece of aluminum foil and covered with another piece of aluminum foil before the subsequent sample preparation steps. Second, the buffer or solvent used for preparing gels should be filtered through a 0.2 μm filter. Third, when applicable, the proteins or polymers should be pre-filtered in the solution state by a 0.45 μm filter to remove particulates or dust before drying by lyophilization or using a rotary evaporator.

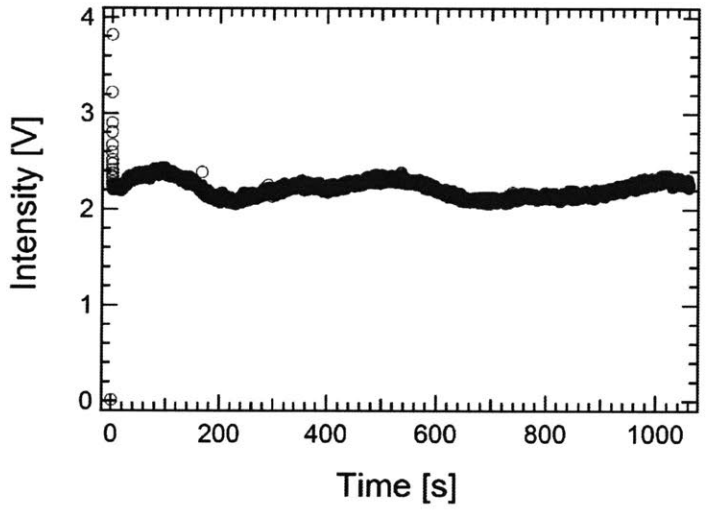

Figure 2-40. An example showing data acquisition at long times with a large baseline fluctuation.

All specimens were stored in the refrigerator at 4 °C overnight in the dark to eliminate shear history from loading and pressing. In forced Rayleigh scattering experiments, the temperature was controlled by a circulating water chiller. Samples were equilibrated at the desired experimental temperature for at least 1 h before further experiments and acquisitions were performed.

2.6.3. Forced Rayleigh scattering measurements

In this thesis, diffusion of proteins or polymers in gels was measured by forced Rayleigh scattering (FRS), a technique widely used in probing slow diffusion of molecules in colloids, micelles, and self-assembled block copolymers.[16] Compared to other popular methods of studying diffusion, such as fluorescence recovery after photobleaching (FRAP) and fluorescence correlation spectroscopy (FCS), FRS has the advantage of accessing smaller length scales that are close to the diffraction limit while measuring over timescales comparable to FRAP and FCS.

The FRS apparatus was modified based on Dr. Muzhou Wang's original design[11, 12] to enable measurement on large length scales up to 50 μm when using a cyan laser at a wavelength at 488 nm (Figure 2-41). This required two coherent laser beams crossing at an angle of 0.638 degrees. To access this very small angle, the most effective way in the author's hands was to move mirrors M2 and M4 closer to each other in the x direction (see Figure 2-41). This was accomplished with the two following major modifications. First, the two mirrors M3 and M4 were offset by one lattice line in the y direction. Second, a D-shaped mirror (1" Broadband Dielectric D-Shaped Mirror, 400-750 nm, Thorlabs, part# BBD1-E02) was fixed on a right-handed kinematic mount (Thorlabs, part# KM100D) to place at the M4 position such that the beam reflected from M2 did not hit the optical elements at the M4 position (Figure 2-42).

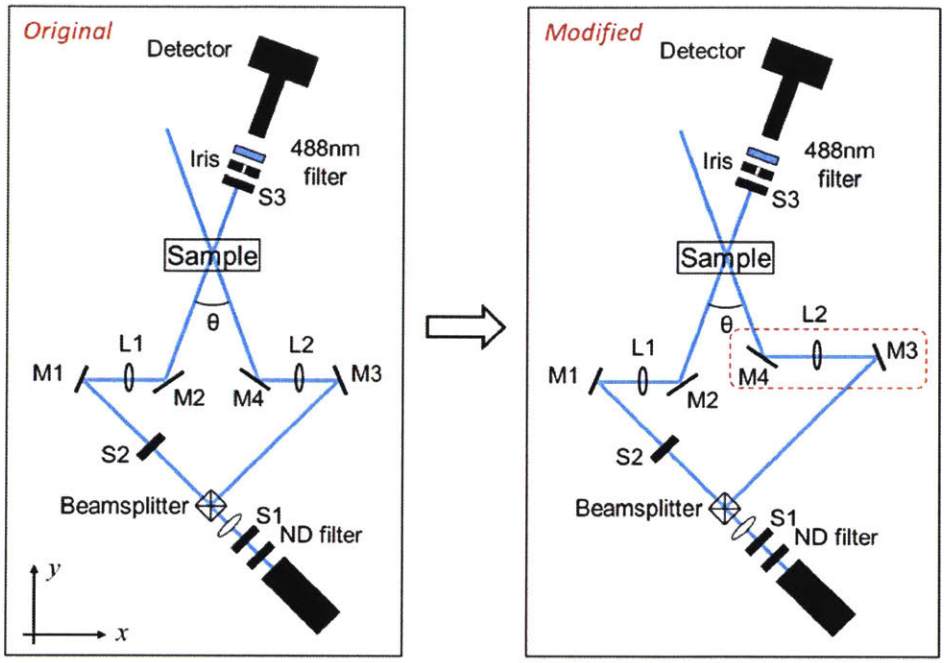

Figure 2-41. Schematic presentation of the modified optics setup (highlighted in a red box) for forced Rayleigh scattering. The following abbreviations are used: mirror (M), shutter (S) and lens (L).

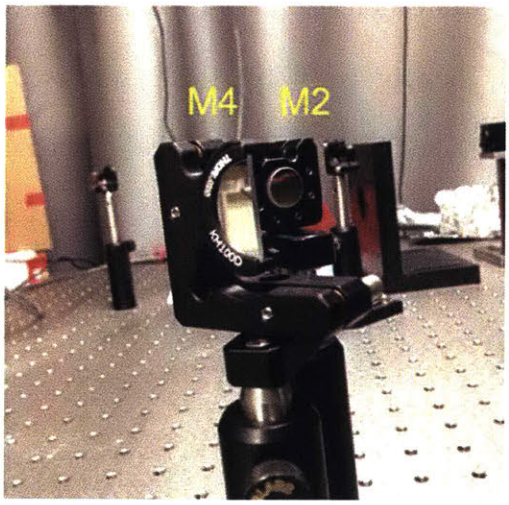

Figure 2-42. A picture showing the mirrors M2 and M4 in the closest *x* direction.

The laser alignment procedure was not affected by the modification of the forced Rayleigh scattering apparatus. To align the laser for data acquisition, an iris was first placed at the lattice point where the sample would eventually sit. The two coherent laser beams from the beam splitter and reflected by M1 and M2 were then forced to intersect at the same point by adjusting the mirrors M2 and M4. Iris was then removed from the sample position, a detector was mounted off lattice, and an iris was placed in front of the detector. The position and the angle to which these the detector and the iris faced were finely adjusted such that the beam reflected from M2 could directly go through the iris and the center of the detector. At the end, the motorized sample stage was put in the sample position.

FRS measurements were performed as previously described.[11] Briefly, a 100 mW continuous wave laser operating in single longitudinal mode at λ = 488 nm was split into two beams, which were individually refocused and intersected at an angle of θ onto the sample. This generated a holographic grating of a characteristic spacing d that is determined by the following equation:

$$d = \frac{\lambda}{2\sin(\theta/2)}. \tag{2-20}$$

By exposing the sample for a certain time period (usually ranging from 250 to 1000 ms depending on the dye concentration and matrix absorptivity), the photochromic dye was irreversibly isomerized in the areas of constructive interference, resulting in an amplitude grating of dye concentration. The evolution of the resulting sinusoidal concentration profile by diffusion was monitored by diffraction of a single reading beam at the same wavelength and angle as one of the writing beams but attenuated by 10^{-4} or 10^{-5} with the use of neutral density filters. The selection of the attenuation factor should be made to optimize the signal-to-noise ratio. A larger attenuation

factor would decrease the gain to avoid signal saturation, but it might require a longer time to write the grating to generate enough signal. It should be noted that the intensity of the reading beam was low enough such that the change of the profile was due only to diffusion, instead of continuous bleaching of the photochromic dye. This claim was supported by the observation of a flat baseline at long times following the initial intensity decay (Figure 2-43).

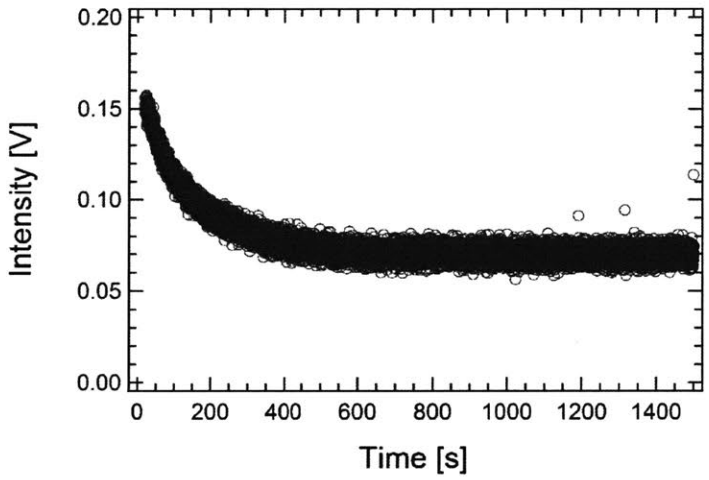

Figure 2-43. Intensity of the diffracted beams vs. time. The data acquisition time was lengthened to confirm the flatness of the baseline at long times.

Additional attention should be paid when performing experiments at small angles with the modified forced Rayleigh scattering setup. Specifically, the accurate value of beam angle becomes sensitive to the distance between M2 and M4 at the x direction, especially at small angles of 2 degrees or below. Therefore, it requires extra attention to precisely place M2 and M4 at the desired spots on the optical rails. At these small angles, background scattering and reflection might raise the baseline. Thus, the signal from the diffracted beam might easily saturate right after the grating writing step. In this case, a neutral density filter can be added inside the flight tube in front of the

detector to further attenuate the reading beam by $10^{-0.5}$ or 10^{-1} and to decrease the detector gain. This adjustment can be accompanied with increasing the grating writing time in order to optimize the signal-to-noise ratio.

There were several functional forms used in this thesis to analyze the diffracted intensity decay to extract average relaxation time constant(s). The fitting was performed in MATLAB using the built-in trust-region algorithm in the optimization toolbox (called by the routine cftool).

(1) A single stretched exponential function

In this case, only one obvious decay was observed from the raw data. Therefore, the signal was fit to a stretched exponential function,

$$I = \left[A \exp\left(-t/\tau\right)^{\beta} \right]^2 + B, \tag{2-21}$$

where I is the intensity, τ is the time constant, β is the stretched exponent ranging from 0 to 1, A is the grating amplitude and B is the incoherent background. The average decay time constant was calculated as the first moment of the stretched exponential

$$\langle \tau \rangle = \frac{\tau_{\mathrm{KWW}}}{\beta} \Gamma\left(\frac{1}{\beta}\right), \tag{2-22}$$

where Γ is the gamma function. The stretched exponent β for artificial proteins was usually 0.75–1.0 and for tetra-arm PEG polymers 0.70–1.0. An example is shown in Figure 2-44.

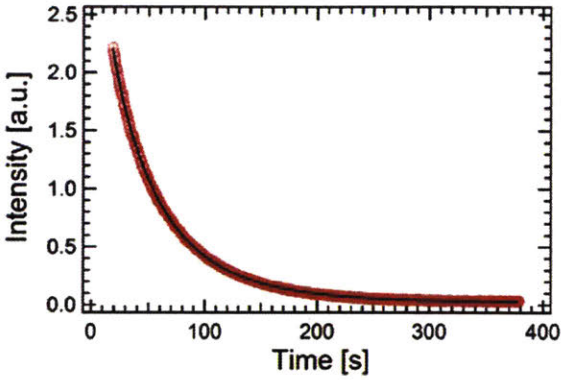

Fitting results:

$A = 2.015 \pm 0.005$

$\tau = 82.5 \pm 0.02$

$\beta = 0.784 \pm 0.003$

$B = 0.0234 \pm 0.0001$

Figure 2-44. An example showing the decay of the diffractive intensity over time (red dots) that is fit to a stretched exponential function (black line). For this curve, the protein gel concentration was 10% (w/v) and the measurement was performed at a beam angle of 20 degrees and temperature of 35 °C.

(2) A sum of two stretched exponential functions with pre-exponential factors of the same sign

In some cases, two decay processes were observed in the time-dependence diffractive intensity. Therefore, the signal was fit to a sum of two stretched exponential functions,

$$I = \left[A_1 \exp\left(-t/\tau_1\right)^{\beta_1} + A_2 \exp\left(-t/\tau_2\right)^{\beta_2} \right]^2 + B, \qquad (2\text{-}23)$$

where A_1 and A_2 are the pre-exponential factors (both of positive signs), τ_1 and τ_2 are the corresponding time constants, β_1 and β_2 are the corresponding stretched exponents, and B is the incoherent background. The existence of two distinct time constants might be explained by the two-state model, which will be described in Chapter 3, or due to two complementary gratings in the measurements. The average decay time constants were then calculated based on eq 2-22. An example is shown in Figure 2-45.

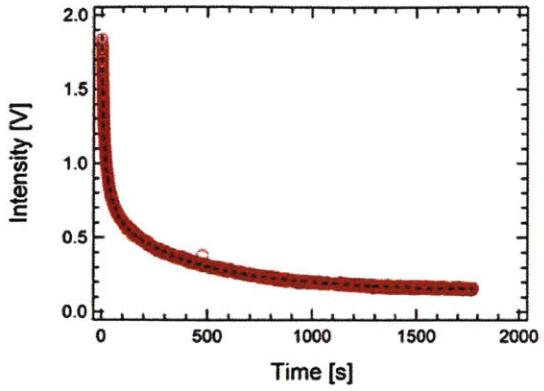

Fitting results:

$A_1 = 0.746 \pm 0.006$ $A_2 = 0.706 \pm 0.005$

$\tau_1 = 16.2 \pm 0.2$ $\tau_2 = 899 \pm 4$

$\beta_1 = 0.566 \pm 0.003$ $\beta_2 = 0.98 \pm 0.01$

$B = 0.1465 \pm 0.0005$

Figure 2-45. An example showing the decay of the diffractive intensity over time (red dots) that is fit to a sum of two stretched exponential functions (black line). For this curve, the polymer concentration in the gels based on nickel-histidine coordination was 10% (w/v) and the measurement was performed at a beam angle of 30 degrees and temperature of 35 °C.

(3) A sum of two exponential functions with pre-exponential factors of the opposite sign

When fluorescein was used as the photochromic dye to label artificial proteins in forced Rayleigh scattering experiments, it was observed that the diffracted intensity often exhibited a decay-growth-decay profile. This phenomenon has been previously reported by others and is explained by the presence of two complementary gratings.[16, 28] Here, the FRS signal was fit to a sum of two exponential functions,

$$I = \left[A_1 \exp(-t/\tau_1) + A_2 \exp(-t/\tau_2) \right]^2 + B, \qquad (2\text{-}24)$$

where A_1 and A_2 are the pre-exponential factors of opposite signs, τ_1 and τ_2 are the corresponding time constants, and B is the incoherent background. Note that stretched exponential functions were not used in the fitting because it was discovered that with stretched exponential functions, the

fitting ended in many local minima and comparison of fitting results across many experiments was difficult. An example of the raw data and fit is shown in Figure 2-46.

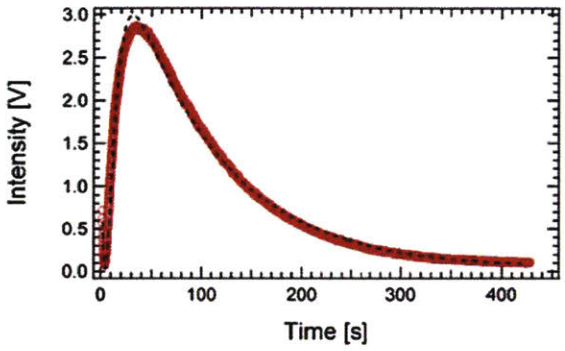

Fitting results:

$A_1 = -2.36 \pm 0.01$

$A_2 = 2.207 \pm 0.004$

$\tau_1 = 11.77 \pm 0.08$

$\tau_2 = 178.5 \pm 0.7$

$B = 0.043 \pm 0.003$

Figure 2-46. An example showing the decay of the diffractive intensity over time (red dots) that is fit to a stretched exponential function (black line). For this curve, the protein concentration in the PE_6P gels was 10% (w/v) and the measurement was performed at a beam angle of 20 degrees and temperature of 25 °C.

2.7. Appendix

MATLAB code for transforming creep compliance data to dynamic moduli.

```
function JG_conversion

clear all; clc; close all;

% estimate slope and the intercept from a linear fit of the
% compliance-temperature data and convert J-t to moduli
% written by Shengchang Tang in 2013

%% data input
data_JT = xlsread(' ');
%%
% Linear fitting to get the slope and the intercept from the fit
tdata = data_JT(:,1);
Jdata = data_JT(:,2);
% time
x = tdata( :end);
% compliance
y = Jdata( :end);
% linear regression, only using the last few data points to get the linear
% fit
```

```
n = length(x);
X = [ones(n,1),x];
[b bint r rint] = regress(y, X);
% rcoplot(r,rint)
% output the parameter for the fit
Je = b(1);  % intercept
inv_eita = b(2);  % slope

%% converting the compliance data to modulus

% spline fit to obtain function J(t)
tt = 0:1:max(tdata);
JJ = spline(tdata,Jdata,tt);
% the parameter in frequency sweep spectrum
omega = logspace( , , );

% using the trapozoid formula to calculate the integral
for n = 1:length(omega)
    % specifiy omega
    w = omega(n);

    % the creep complicance J'(omega)
    J1_part = (Je + tt .* inv_eita - JJ) .* sin(w .* tt);
    J1(n) = Je - w * trapz(tt, J1_part);
    % the creep compliance J" (omega)
    J2_part = (Je + tt .* inv_eita - JJ) .* cos(w .* tt);
    J2(n) = w * trapz(tt, J2_part) + 1/w * inv_eita;

end

% calcualtion
G1 = 100 * J1 ./ (J1.^2 + J2.^2);
G2 = 100 * J2 ./ (J1.^2 + J2.^2);

% loglog(omega, J1, 'r', omega, J2);
figure
loglog(omega, G1, 'r', omega, G2);
```

2.8. References

1. Glassman, M. J.; Chan, J.; Olsen, B. D. Reinforcement of Shear Thinning Protein Hydrogels by Responsive Block Copolymer Self-Assembly. *Advanced Functional Materials* 2013, 23, 1182-1193.

2. Glassman, M. J.; Olsen, B. D. Structure and Mechanical Response of Protein Hydrogels Reinforced by Block Copolymer Self-Assembly. *Soft Matter* 2013, 9, 6814-6823.

3. Glassman, M. J.; Massachusetts Institute of Technology. Department of Chemical Engineering. *Synthesis, Nanostructure, and Mechanics of Thermoresponsively Tough Biomaterials from Artificial Polypeptides*. p 338 pages.

4. McGrath, K. P.; Fournier, M. J.; Mason, T. L.; Tirrell, D. A. Genetically Directed Syntheses of New Polymeric Materials. Expression of Artificial Genes Encoding Proteins with Repeating -(Alagly)3proglugly- Elements. *Journal of the American Chemical Society* 1992, 114, 727-733.

5. Stark, G. R.; Stein, W. H.; Moore, S. Reactions of the Cyanate Present in Aqueous Urea with Amino Acids and Proteins. *Journal of Biological Chemistry* 1960, 235, 3177-3181.

6. Hermanson, G. T. Bioconjugate Techniques. 3rd edition. ed. http://www.sciencedirect.com/science/book/9780123822390.

7. Ryan, C. P.; Smith, M. E. B.; Schumacher, F. F.; Grohmann, D.; Papaioannou, D.; Waksman, G.; Werner, F.; Baker, J. R.; Caddick, S. Tunable Reagents for Multi-Functional Bioconjugation: Reversible or Permanent Chemical Modification of Proteins and Peptides by Control of Maleimide Hydrolysis. *Chemical Communications* 2011, 47, 5452-5454.

8. Robin, M. P.; Wilson, P.; Mabire, A. B.; Kiviaho, J. K.; Raymond, J. E.; Haddleton, D. M.; O'Reilly, R. K. Conjugation-Induced Fluorescent Labeling of Proteins and Polymers Using Dithiomaleimides. *Journal of the American Chemical Society* 2013, 135, 2875-2878.

9. Jacobson, H.; Stockmayer, W. H. Intramolecular Reaction in Polycondensations. I. The Theory of Linear Systems. *The Journal of Chemical Physics* 1950, 18, 1600-1606.

10. Ferry, J. *Viscoelastic Properties of Polymers*. 3d ed.; Wiley: New York, 1980; p xxiv, 641 p.

11. Wang, M.; Timachova, K.; Olsen, B. D. Experimental Measurement of Coil–Rod–Coil Block Copolymer Tracer Diffusion through Entangled Coil Homopolymers. *Macromolecules* 2013, 46, 1651-1658.

12. Wang, M.; Massachusetts Institute of Technology. Department of Chemical Engineering. *Dynamics of Rod-Coil Block Copolymers*. p 300 pages.

13. Eastman, C. E.; Lodge, T. P. Self-Diffusion and Tracer Diffusion in Styrene/2-Vinylpyridine Block Copolymer Melts. *Macromolecules* 1994, 27, 5591-5598.

14. Cavicchi, K. A.; Lodge, T. P. Self-Diffusion and Tracer Diffusion in Sphere-Forming Block Copolymers. *Macromolecules* 2003, 36, 7158-7164.

15. Tang, S.; Wang, M.; Olsen, B. D. Anomalous Self-Diffusion and Sticky Rouse Dynamics in Associative Protein Hydrogels. *Journal of the American Chemical Society* 2015, 137, 3946-3957.

16. Schärtl, W. Forced Rayleigh Scattering – Principles and Application (Self Diffusion of Spherical Nanoparticles and Copolymer Micelles). In *Soft Matter Characterization*, Borsali, R.; Pecora, R., Eds. Springer Netherlands: Dordrecht, 2008; pp 677-703.

17. Sillescu, H.; Ehlich, D. *Applications of Holographic Grating Techniques to the Study of Diffusion Processes in Polymers*. CRC Press Boca Raton,(Florida): 1990; Vol. 3.

18. Yamazaki, V.; Sirenko, O.; Schafer, R. J.; Groves, J. T. Lipid Mobility and Molecular Binding in Fluid Lipid Membranes. *Journal of the American Chemical Society* 2005, 127, 2826-2827.

19. Haldar, S.; Chattopadhyay, A. Application of Nbd-Labeled Lipids in Membrane and Cell Biology. In *Fluorescent Methods to Study Biological Membranes*, Mély, Y.; Duportail, G., Eds. Springer Berlin Heidelberg: Berlin, Heidelberg, 2013; pp 37-50.

20. Wu, E.; Jacobson, K.; Papahadjopoulos, D. Lateral Diffusion in Phospholipid Multibilayers Measured by Fluorescence Recovery after Photobleaching. *Biochemistry* 1977, 16, 3936-3941.

21. Katzenstein, J. M.; Janes, D. W.; Hocker, H. E.; Chandler, J. K.; Ellison, C. J. Nanoconfined Self-Diffusion of Poly(Isobutyl Methacrylate) in Films with a Thickness-Independent Glass Transition. *Macromolecules* 2012, 45, 1544-1552.

22. Rossow, T.; Habicht, A.; Seiffert, S. Relaxation and Dynamics in Transient Polymer Model Networks. *Macromolecules* 2014, 47, 6473-6482.

23. Sjöback, R.; Nygren, J.; Kubista, M. Absorption and Fluorescence Properties of Fluorescein. *Spectrochimica Acta Part A: Molecular and Biomolecular Spectroscopy* 1995, 51, L7-L21.

24. Veniaminov, A. V.; Sillescu, H. Polymer and Dye Probe Diffusion in Poly(Methyl Methacrylate) Below the Glass Transition Studied by Forced Rayleigh Scattering. *Macromolecules* 1999, 32, 1828-1837.

25. Chang, T.; Yu, H. Self-Diffusion of Gelatin by Forced Rayleigh Scattering. *Macromolecules* 1984, 17, 115-117.

26. Schaertl, W.; Tsutsumi, K.; Kimishima, K.; Hashimoto, T. Frs Study of Diffusional Processes in Block Copolymer/Homopolymer Blends Containing Glassy Spherical Micelles. *Macromolecules* 1996, 29, 5297-5305.

27. Goodman, J. W. *Introduction to Fourier Optics*. 3rd ed.; Roberts & Co.: Englewood, Colo., 2005; p xviii, 491 p.

28. Huang, W. J.; Frick, T. S.; Landry, M. R.; Lee, J. A.; Lodge, T. P.; Tirrell, M. Tracer Diffusion Measurement in Polymer Solutions near the Glass Transition by Forced Rayleigh Scattering. *AIChE Journal* 1987, 33, 573-582.

Chapter 3 Anomalous Self-diffusion and Sticky Rouse Dynamics in Associative Protein Hydrogels

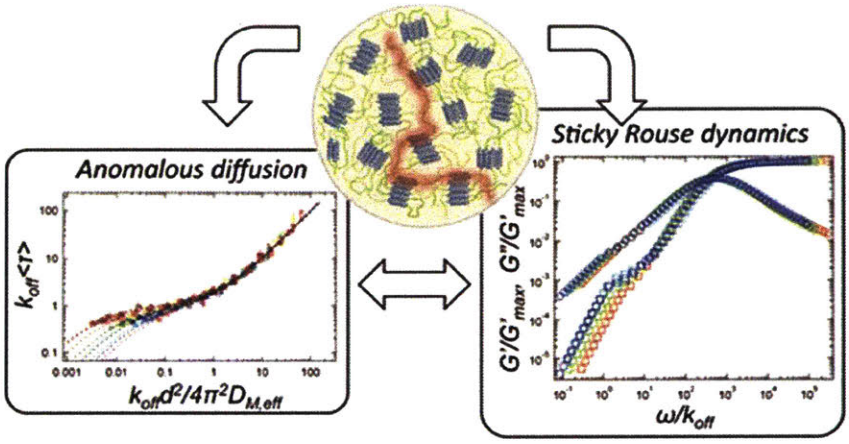

Reproduced with permission from S. Tang et al., *Journal of the American Chemical Society* **2015**, 137 (11), 3946–3957. Copyright © 2015 American Chemical Society.

Natural and synthetic materials based on associating polymers possess diverse mechanical behavior, transport properties and responsiveness to external stimuli. Although much is known about their dynamics on the molecular and macroscopic level, knowledge of self-diffusive dynamics of the network-forming constituents remains limited. Using forced Rayleigh scattering, anomalous self-diffusion is observed in model associating protein hydrogels originating from the interconversion between species that diffuse in both the molecular and associated state. The diffusion can be quantitatively modeled using a two-state model for polymers in the gel, where diffusivity in the associated state is critical to the super diffusive behavior. The dissociation time from bulk rheology measurements was 2–3 orders of magnitude smaller than the one measured by

diffusion, because the former characterizes submolecular dissociation dynamics, whereas the latter depicts single protein molecules completely disengaging from the network. Rheological data also show a sticky Rouse-like relaxation at long times due to collective relaxation of large groups of proteins, suggesting mobility of associated molecules. This study experimentally demonstrates a hierarchy of relaxation processes in associating polymer networks, and it is anticipated that the results can be generalized to other associative systems to better understand the relationship of dynamics among sticky bonds, single molecules, and the entire network.

3.1. Introduction

Natural and synthetic materials based upon associating networks are of longstanding interest across a wide variety of different communities.[1,2] These materials share a common feature that the network junctions are formed by various physical or supramolecular interactions, including hydrogen bonding[3-5], metal-ligand coordination[6-8], ionic interactions (coacervation)[9, 10], hydrophobic interactions[11, 12], host-guest complexation[13, 14], and combinations thereof in intricate self-assembled systems[15-18]. Since the association energies of the physical bonds are typically on the order of a few to tens of k_BT (the thermal energy),[19] these bonds can dissociate and recombine due to thermal fluctuation or when triggered by mild environmental stimuli. This feature distinguishes associating networks from their chemically-crosslinked counterparts and gives rise to many interesting transport and mechanical properties. For example, the nuclear pore complex uses weak associations between proteins to regulate the transport of molecules into the nucleus.[20] Many researchers have incorporated associating bonds into materials to prepare batteries[21], conductive artificial skin[22], elastomers[5, 23, 24], and soft hydrogels[6] with self-healing properties. The associative junctions can also serve as sacrificial bonds for effective energy dissipation in order to

prevent concentrated stress at the early stage of the stretch, enabling soft materials to achieve dramatic enhancements in toughness.[25, 26] Moreover, biocompatible associating gels have shown significant promise as injectable cell-encapsulating materials for medical applications.[27, 28]

Network dynamics are important to control the materials' properties, such as the time scale of self-healing[5], the susceptibility to creep at long time[29, 30], and the influence of relaxation time of synthetic microenvironments on cell response[31]. From a fundamental perspective, the dynamics of an entire network are largely controlled by the dynamics of associating bonds or stickers. This has provided the basis for many theoretical models developed throughout the past seven decades.[32-39] In particular, the sticky Rouse/reptation theories are suitable to describe the dynamics of polymers with associating sidegroups along the backbone.[35] These theories reason that the presence of the stickers introduces additional friction between polymers, and such effect is enhanced drastically with increasing sticker density. As a result, the dynamics (e.g., relaxation time, self-diffusivity, and zero-shear-rate viscosity) of associating polymers strongly depends on the number of stickers per chain, the polymer concentration, and the polymer architecture. This complexity makes it difficult to provide exact correlations between the dynamics of one isolated junction and the dynamics of the entire network.[7]

While the majority of existing studies on dynamics have focused on mechanics, diffusion, especially the self-diffusion of network forming molecules, is less explored. However, diffusion is central to understanding the performance of materials and to rationally designing new materials. For example, the diffusion of polymer chains has been shown to affect the structure of the polyelectrolyte multilayers (PEMs) and to further influence their properties.[40] According to the selective phase model,[20, 41] diffusion of FG-rich proteins should be critical to promote the translocation through the nuclear pore complex. A similar effect is observed for membrane

lipids.[42] Additionally, when cell adhesion epitopes such as RGD are linked to associating polymers inside a synthetic microenvironment, diffusion is expected to alter the spatio-temporal distribution of the cell-binding ligands and thus has an impact on the cell spreading behavior.[31] Diffusion is also relevant for self-healing materials: it is important to know how molecules diffuse across the damaged interface and reform the associative bonds to restore the pristine network structure and mechanical properties.[43] Despite its importance, only a few experimental studies have measured the self-diffusion of polymers in associating networks,[44, 45] and this work mainly focuses on diffusion in the large length scale Fickian limit where an effective diffusivity is obtained. Knowledge about how association kinetics quantitatively affect the diffusion of molecules at various length scales is still lacking.

Biosynthetic hydrogels based upon associating coiled-coil domains are an ideal model system for fundamental investigations of gel physical chemistry due to their mono-disperse backbone molecular weight and sequence-defined sticker positions. These proteins are widely studied and have also shown promise for a myriad of applications, including artificial extracellular matrices (ECMs)[46-48], biocatalysts[49, 50], and drug carriers[51]. These materials can be modularly designed and engineered by taking advantage of the specificity of coiled-coil association. Here, a multi-sticker coiled-coil protein is used as model system to study the relationship between associative molecular diffusion and the linear viscoelasticity of gels. The model coiled-coil protein P_4 has a multiblock architecture, with four coiled-coils on the protein backbone joined by flexible polyelectrolyte linkers C_{10} (Scheme 3-1A and 3-1B). For the first time, self-diffusion of associating proteins in hydrogels is measured over four decades of d^2 (square of the diffractive grating spacing) by forced Rayleigh scattering (FRS) (Scheme 3-1C and 3-1D), revealing

anomalous diffusion below a critical length scale that largely depends upon temperature and concentration in the gels. Linear viscoelastic properties from 10^{-4} to 10^{2} rad/s are obtained from

Scheme 3-1. Self-diffusion of associative proteins in gels probed by forced Rayleigh scattering.(A) Structure of the single protein P_4 that contains four coiled-coil domains on the backbone joined by flexible linkers C_{10}. The chain highlighted with red schematically represents a protein molecule labeled with a single red dye. (B) Schematic of self-diffusion of labeled proteins P_4 in hydrogels made from the same proteins. (C) Forced Rayleigh scattering forms one-dimensional concentration gratings of dye-labeled polymers within a hydrogel when exposed to the full power laser. The blue area within the sample indicates the region of constructive interference, where the photochromic dye was irreversibly isomerized. (D) Diffusion causes decay of the grating. An example showing the decay of the intensity over time (red dots) fit to a stretched exponential function (black line). For this curve, the protein concentration was 10% (w/v) and the measurement was performed at a beam angle of 20 degrees and temperature of 35 °C.

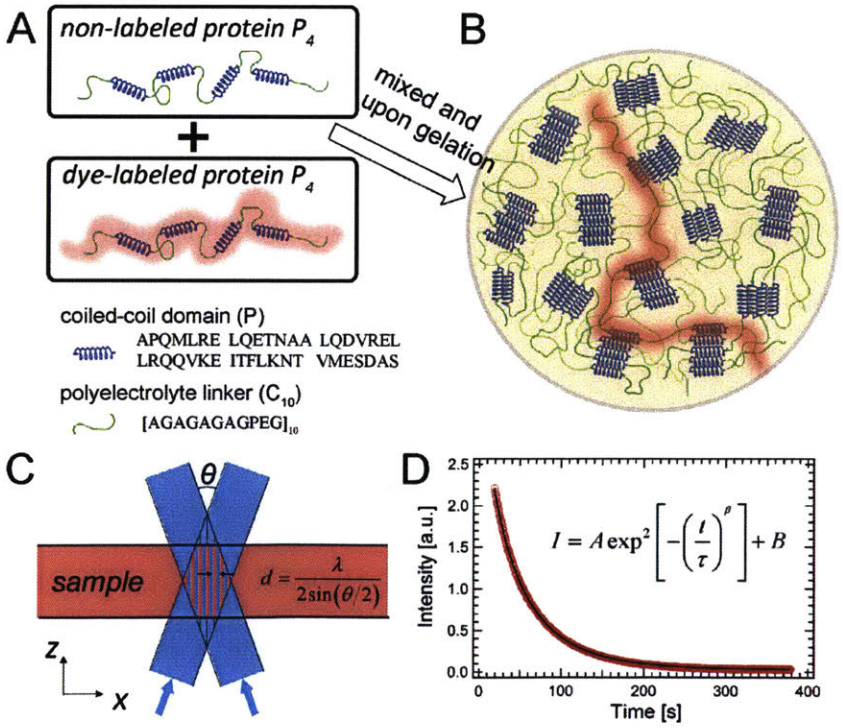

small-amplitude oscillatory shear (SAOS) and creep measurement, and a sticky Rouse relaxation is first identified in associative protein hydrogels, which correlates to the diffusive motions of associative proteins in an aggregated state. The dissociation rate constants from the diffusion studies provide frequency shift factors, enabling a time-concentration-temperature superposition of the rheology data of gels under various experimental conditions, and collapsed dynamic moduli master curves are obtained. These studies provide quantitative insight into the strong couplings between sticker association, molecular diffusion, and material relaxations in associative polymers.

3.2. Results and Discussion

Anomalous Diffusion in Associative Polymers. The self-diffusion of the model associating protein P_4 in hydrogels exhibits two distinct scaling behaviors $\langle\tau\rangle \sim d^{2\mu}$ over a wide range of length scales (Figure 3-1), where d is the characteristic length scale of the grating and $\langle\tau\rangle$ is the corresponding characteristic diffusion time. It is important to point out that the relation $\langle\tau\rangle \sim d^{2\mu}$ is different than classical scaling of mean square displacement over time ($\langle X^2\rangle \sim t^{\alpha}$), and the two power-law exponents are related by $\alpha = 1/\mu$. At large length scales, an exponent of $\mu = 1$ corresponds to a scaling relation of $\langle\tau\rangle \sim d^2$, as is expected for Fickian diffusion. However, an exponent $\mu < 1$ (or equivalently $\alpha > 1$) is observed at short length scales over a wide range of concentrations, indicating a distance vs. time dependence that is stronger than diffusion, i.e., super-diffusion. For example, protein gels at 6.5% (w/v) show a weak power law dependence from ca. 0.05 to 50 μm^2 where the scaling exponent α is 0.304 ± 0.024 (Figure 1). When the concentration of the gel is increased, $\langle\tau\rangle$ increases significantly in the super-diffusive region, from approximately 10 s at a concentration of 6.5% (w/v) to nearly 1000 s at 20% (w/v). The range of d^2 over which the super-diffusive scaling is observed also shifts with increasing concentration;

however, the power law exponent α increases only slightly. Previous studies of diffusion in associating polymers were performed on longer length scales corresponding to the effectively

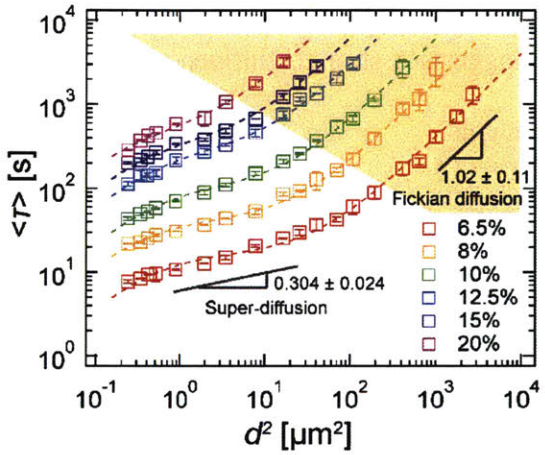

Figure 3-1. Super-diffusion and Fickian diffusion (shaded in light orange) of coiled-coil proteins in hydrogels at various concentrations. All measurements were performed at 35 °C. Error bars represent one standard deviation of measurements performed in triplicate. Dashed lines are fits to the two-state model. For protein gels at 6.5% (w/v), the values of slopes shown in the figure are from fits to power laws, and error bars on the power law exponents represent 95% confidence intervals.

Fickian regime observed here;[44, 45] this is the first time that super-diffusion is observed through studies of diffusion at shorter length scales. Although this observation may appear counter-intuitive at first glance since the presence of associative α-helices reduces the diffusivity of the polymers, the result is reminiscent of the super-diffusion phenomena arising in other self-interacting systems, such as wormlike micelles[52] and *Hydra* cells in aggregates[53]. Although the detailed physics governing these self-interacting systems are substantially different, they share in common that motions of the constituents show spatial and temporal correlations, i.e., movement of one molecule or cell affects the dynamics of others. Therefore, it is hypothesized that the

observed super-diffusive scaling regime in associating protein gels originates from the associative dynamics of the coiled-coil domains. However, the scaling exponent μ in the coiled-coil hydrogels is much smaller than the ones reported in references 52 and 53 (0.75 and 0.81 for their smallest values, respectively), which suggests a stronger influence of the associative interaction on the diffusion process in the protein gels.

As the grating spacing is increased into the large d^2 regime, the expected Fickian diffusion is recovered for gels at all concentrations ($\mu = 1.0$). The transition from the super-diffusive regime to the Fickian regime depends on concentration, and the characteristic d^2 at the transition decreases when concentration increases. The corresponding transition length d occurs on the order of μm. Interestingly, there is also a subtle deviation from the super-diffusive scaling in the small d^2 limit where the slope starts to increase, gradually approaching 1.0. This suggests that there might be a second Fickian diffusion regime on very small length scales, where the smallest d in the experiment is still 488 nm, at least an order of magnitude larger than the radius of gyration (R_g) of an individual protein (Appendix A).

The anomalous diffusion is strongly affected by the temperature (Figure 3-2). The average decay time constant $<\tau>$ at a given grating spacing d^2 increases with decreasing temperature due to the combined effect of a smaller diffusivity of protein molecules and the slower exchange of coiled-coils. In addition, the slope of the power-law regime becomes smaller at lower temperatures; this phenomenon is most pronounced for low concentration gels where both the super-diffusion and Fickian regimes are well developed within the experimentally accessible window. For gels at 6.5% (w/v), the power law exponents are 0.304 ± 0.024, 0.207 ± 0.019, 0.091 ± 0.078 at 35, 25 and 15 °C, respectively. This observation is consistent with the hypothesis that a smaller μ

indicates a stronger association constant for coiled-coils, which is expected with decreasing temperatures.

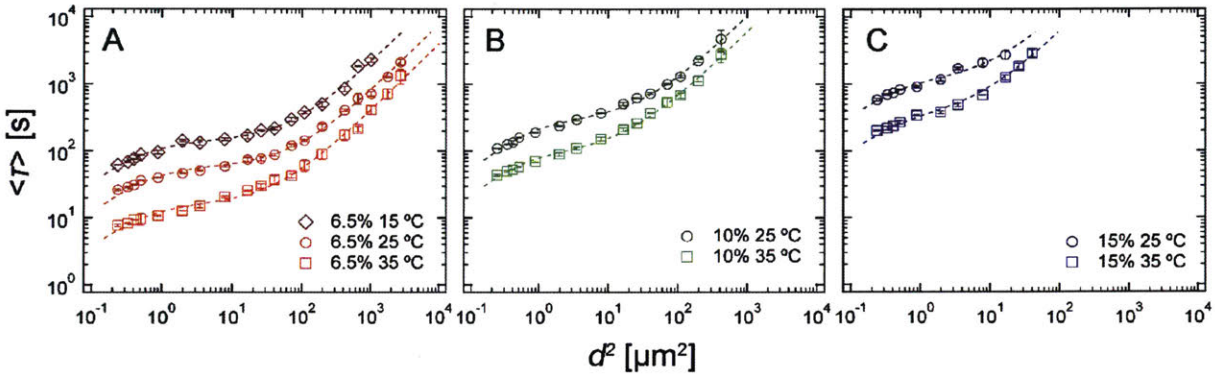

Figure 3-2. Super-diffusion and Fickian diffusion of coiled-coil proteins in hydrogels at various temperatures. The concentrations in panel (A), (B) and (C) are 6.5%, 10% and 15% (w/v), respectively. Error bars represent standard deviations from measurement in triplicate. Dashed lines are fits to the two-state model.

Analysis of Anomalous Diffusion with the Two-State Model. Previous studies in the literature on associating systems have suggested that the apparent super-diffusive scaling may originate from the interplay of diffusive and associative dynamics.[52, 53] In order to quantitatively explore the observed behavior, a two-state model is introduced where a diffusing species is in equilibrium between a molecular state (relatively mobile) and an associated (relatively immobile) state. In the molecular state *M*, proteins behave as free, non-interacting molecules, whereas in the associated state *A*, proteins are associating with each other, but diffuse much more slowly than in the molecular state. Central to this model is the non-zero diffusivity of the associated molecules;

however, the mechanism by which associated species may diffuse is elusive. One possible explanation is that associated proteins "walk" within the network by partially detaching the coiled-coil junctions, although at least one coiled-coil along the protein backbone remains attached to the network at all times. The conversion between states M and A is reversible, and it can be described in the following reaction:

$$M \underset{k_{off}}{\overset{k_{on}}{\rightleftharpoons}} A \tag{3-1}$$

Here, k_{on} and k_{off} characterize the rates at which protein transition between the two states. The change in the concentrations of protein molecules C_M and C_A can be described simply by the following reaction-diffusion equations, which are referred to as the two-state model hereafter:

$$\begin{aligned} \frac{\partial C_M}{\partial t} &= D_M \frac{\partial^2 C_M}{\partial x^2} - k_{on} C_M + k_{off} C_A \\ \frac{\partial C_A}{\partial t} &= D_A \frac{\partial^2 C_A}{\partial x^2} + k_{on} C_M - k_{off} C_A \end{aligned} \tag{3-2}$$

where D_M and D_A are the diffusivities in the molecular and associated states, respectively. The model can be solved analytically using Fourier transform methods with the sinusoidal concentration gradients made during the FRS writing step as an initial condition. The initial condition of C_M and C_A can be calculated from the following two relations: $C_A/C_M = K_{eq}$ (from equilibrium assumption) and $C_A + C_M$ = total protein concentration (by definition). The amplitude of the initial sinusoidal concentration profile decays as a double exponential with short and long time constants that are separated by at least two orders of magnitude and the small time constant is less than 1 s even for gels at high concentrations (see details in Appendix A). Diffracted intensities observed at experimental time scales thus reflect the long relaxation time, which

contains effects from diffusion of both molecular and associated species as well as their exchange kinetics, depending on the length scales probed. A similar model has been applied in a study where fluorescence recovery after photobleaching (FRAP) was used to probe the binding interactions and mobility of the transcription factor inside the nucleus, but the diffusivity of the relatively immobile species was assumed to be zero.[54]

Despite its simplicity, the two-state model is able to qualitatively capture many aspects of the experimental observation and provide insight into the underlying physics (Figures 3-3). In a typical FRS experiment measuring simple Fickian diffusion, the decay time of the diffracted intensity is

$$\tau = \frac{d^2}{4\pi^2 D} \tag{3-3}$$

where D is the diffusion constant of the dye-labeled species, and d is the period of the holographic grating defined by following equation (Scheme 3-1C).

$$d = \frac{\lambda}{2\sin(\theta/2)} \tag{3-4}$$

In this two-state model, the relationship between the observed time constant and diffusivity is significantly more complex. As shown in Figure 3-3, the model predicts the existence of two Fickian regimes at both large and small d^2 with slopes of one in the log-log plot. They are connected by a pseudo power-law regime with a slope less than one, which indicates super-diffusion.

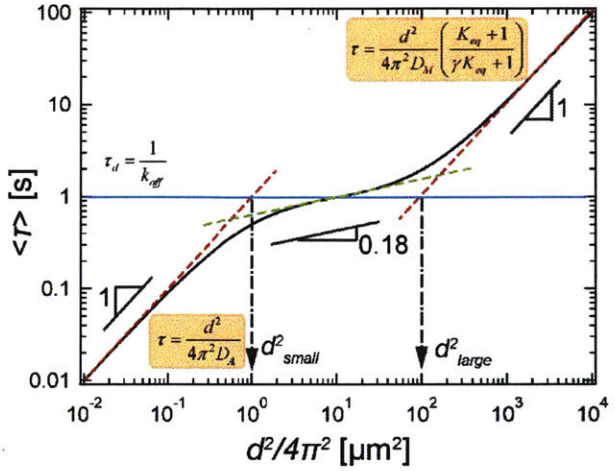

Figure 3-3. Predicted relation $\langle\tau\rangle \sim d^{2\mu}$ from the two-state model (black solid curve) with the parameter values $D_M = 10^{-8}$ m^2/s, $D_A = 10^{-12}$ m^2/s, $k_{on} = 100$ s^{-1}, and $k_{off} = 1$ s^{-1}. The solutions (red dashed line) of the two Fickian regimes with slopes of 1 are shown in rounded rectangles with light yellow background. The super-diffusive regime (green dashed line) has a slope of 0.18. The analytical expression for the slope is $2/[1 + (\gamma K_{eq})^{-1/2}]$. The horizontal line in blue corresponds to the molecular dissociation time $\tau_d = 1/k_{off}$.

These regimes can be explained by considering the physical processes that govern the relaxation of the imposed concentration gradient in the FRS experiment, which can include the diffusion of molecules in both molecular and associated states, and the exchange kinetics between the two states. In all regimes, complete relaxation is only possible after the concentration gradient of the relatively immobile associated proteins has relaxed. At the shortest length scales, the diffusion time scale of associated molecules is sufficiently short that the gradient can relax directly by diffusion, thus

$$\tau = \frac{d^2}{4\pi^2 D_A} \tag{3-5}$$

At the longest length scales, the most rapid relaxation pathway is for proteins to disconnect from the network and diffuse as individual molecules. Therefore, the predicted relaxation time reflects the diffusion of free molecules, slowed down by continuous association/disassociation with the network. The resulting grating relaxation time is

$$\tau = \frac{d^2}{4\pi^2 D_M} \frac{K_{eq} + 1}{\gamma K_{eq} + 1} \tag{3-6}$$

Since the association energy between the coiled-coil domains is large relative to $k_B T$,[55] it is expected that the association rate is much larger than the dissociation rate, i.e., $k_{on} >> k_{off}$, or the equilibrium constant ($K_{eq} = k_{on}/k_{off}$) is large. In the limit when the ratio of associated diffusivity to molecular diffusivity ($\gamma = D_A/D_M$) is small enough such that $\gamma K_{eq} << 1$, the grating relaxation time in the Fickian regime at large d^2 simplifies to

$$\tau = \frac{d^2}{4\pi^2 D_M} K_{eq} \approx \frac{d^2}{4\pi^2 D_{M,\text{eff}}} \tag{3-7}$$

where the effective diffusivity turns out to be the real diffusivity D_M divided by the equilibrium constant K_{eq}. In the strong association limit, the equilibrium constant should be the inverse of the fraction of dissociated chains (f),

$$K_{eq} = \frac{k_{on}}{k_{off}} = \frac{C_{A,eq}}{C_{M,eq}} = \frac{1 - f}{f} \approx \frac{1}{f} \tag{3-8}$$

Therefore, the effective diffusivity can also be expressed as

$$D_{M,\text{eff}} = \frac{D_M}{K_{eq}} = f D_M \tag{3-9}$$

which is the bare diffusivity of the molecular species multiplied by the fraction of dissociated chains. At intermediate lengths, diffusion in the molecular state is still the dominant mechanism, but the grating relaxation time is determined by the conversion rate from the associated state to the molecular state, i.e., k_{off}.

The emergence of the super-diffusive regime can also be explained from a time-scale perspective. The super-diffusive regime is centered around the molecular "off" time, $\tau_d = 1/k_{off}$, which provides a characteristic time scale for proteins to dissociate from the network. For a time period much shorter than τ_d, the dissociation effect is negligible on the timescale over which the grating decays. Therefore, the decay of the FRS grating is due to the diffusive motion of the more abundant but less mobile associated molecules (eqn 3-5). By comparison, for a time period much longer than τ_d, protein molecules dissociate and re-associate with the network several times during the characteristic decay time. The molecules are able to diffuse after disconnecting from the network following Fick's law, but they spend a significant fraction of time associated with the surrounding proteins that effectively slows down the diffusion. Therefore, hindered diffusion of relatively mobile protein molecules is observed (eqns 3-6 to 3-9). The super-diffusive regime arises from the transition between the two Fickian limits, where the association/dissociation dynamics is important. In this regime, the rate of grating decay is limited by the rate of network dissociation, not by the size of the grating. Because most of the coiled-coils have formed pentameric aggregates with each other in the strong association limit and are not available for free molecules to bind, molecules can diffuse a distance larger than the grating period before re-associating with the network. Hence the rate-limiting step is the dissociation of protein molecules and the averaged time constant centers around τ_d. Last, it should be emphasized that a non-zero value of γ or D_A is required to yield a non-zero slope in the power-law region and to observe the

Fickian regime at small length scales. This is a critical difference between the analysis presented here and previous formulations of the two state model where the diffusion of relatively immobile species is neglected.[54]

Fitting the two-state model to experimental data provides quantitative estimates of the rate constants and diffusivities of the two species. While the model does not presuppose any values for the diffusivities or rate constants, the regime relevant to associating polymer gels has $K_{eq} >> 1$ due to strong association of the physical bonds and $\gamma << 1$ arising from a fast and slow species. Fitting is restricted to this regime to obtain physically relevant solutions; within this regime super diffusive behavior emerges when $\gamma K_{eq} << 1$. Because the model predicts that all curves collapse under the experimentally relevant condition when $K_{eq} >> 1$ and $\gamma K_{eq} << 1$ (Appendix A), only three parameters can be independently determined without imposing a specified value of K_{eq}, which are chosen to be the off-rate constant k_{off}, the diffusion coefficient of associated species D_A, and the quantity γK_{eq}. As shown in Figures 1 and 2, the two-state model is able to fit the experimental data with satisfactory agreement under all conditions of temperature and concentration. With the assumption that $K_{eq} >> 1$ and $\gamma K_{eq} << 1$, the effective molecular diffusivity $D_{M,eff}$ simplifies to D_M/K_{eq} and can be calculated from $D_A/\gamma K_{eq}$. As shown in Figure 4A and 4D, $D_{M,eff}$ is estimated to be in the range of $10^{-16} - 10^{-13}$ m^2/s, at least two orders of magnitude smaller than the self-diffusion coefficients of typical polymers in the semi-dilute regime.[56, 57] This observation supports the argument that the association between protein molecules effectively slows down the rate of diffusion. The value of D_A falls into the range of 10^{-18} - 10^{-16} m^2/s (Figure A-5). It is much smaller than D_M given that $K_{eq} >> 1$, but is not negligible. k_{off} has values ranging from 0.1 to 0.001 s^{-1}, and its inverse falls into the time scale in the FRS experiments.

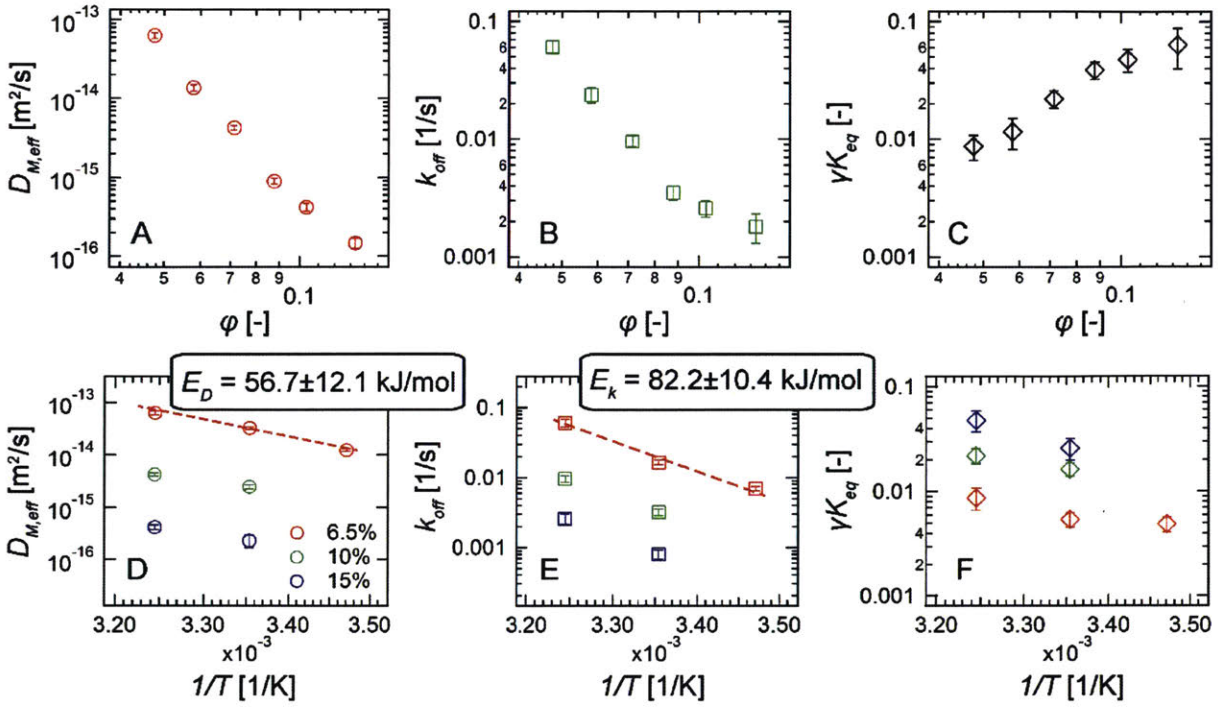

Figure 3-4. Estimated diffusivity $D_{M,eff}$, and rate constant k_{off}, and γK_{eq} as functions of the volume fraction of protein φ (A-C) and the inverse of temperature (D-F). Error bars represent 95% confidence intervals from fits to the two-state model. The values of estimated activation energies are shown in the text box on top of the corresponding panel.

The estimated reaction-diffusion parameters allow quantitative comparisons between observations under different experimental conditions. First, the diffusion coefficients decrease with increasing concentration (Figure 3-4A), as expected. The concentration dependencies are appreciably stronger than what has been reported in literature,[58] but the scaling $D_{M,eff} \sim \varphi^{-5.96 \pm 0.96}$ and $D_A \sim \varphi^{-3.88 \pm 0.68}$ (error bars represent 95% confidence of intervals) are qualitatively consistent with the sticky Rouse predictions.[35] The rate constant k_{off} decreases with increasing concentration (Figure 3-4B), indicating that k_{off} is fundamentally different than the rate constant in classic

biomolecular reactions, which is a function of temperature only. Even though a single coiled-coil could break at a rate independent of concentration, dissociation of a protein molecule, which requires collective dissociation of four coiled-coil domains, may exhibit concentration dependence, possibly due to differences in the fraction of dissociated coiled-coil domains and/or chain connectivity (loops vs. bridges). At equilibrium, the fraction of dissociated coiled-coils decreases with concentration. Therefore, the collective rate for all four coiled-coil domains dissociating from an individual protein goes down. In addition, previous work has demonstrated that the fraction of bridged chains increases with concentration.[30] Dissociation of a bridged chain should be relatively more difficult than a looped chain because it causes changes in the association states of the stickers (closed or open) not only on one bridged chain but also on others connected by intermolecular coiled-coil aggregates. Collectively, it is reasoned that a chain undergoes many failed attempts to disengage from the network before a successful dissociation event takes place. This phenomenon leads to a smaller k_{off} at higher concentrations. The observed concentration-dependent dissociation rate, or dissociation time, is also in agreement with the concept of bond lifetime renormalization in the sticky Rouse theory.[35]

Both diffusivities and k_{off} increase with temperature as a result of enhanced thermal fluctuations, and they follow an empirical Arrhenius behavior over the relatively limited experimental temperature range (Figures 3-4D, 3-4E, and Figure A-6 in Appendix A). The Arrhenius behavior is possibly due to energy barriers required for proteins to dissociate from the network, not the free volume effect in self-diffusion of an unentangled polymer melt[59]. Temperature has a more profound effect on dissociation kinetics than the effective molecular diffusivity, as the activation energy of $D_{M,eff}$ (56.7 ± 12.1 kJ/mol) is smaller than the one of k_{off} (82.2 ± 10.4 kJ/mol). The activation energy of D_A, however, is roughly the same as for k_{off} within

statistical error (Appendix A), suggesting that D_A/k_{off} might be temperature insensitive. The quantity D_A/k_{off} is proportional to the transition d^2 from the small-length-scale Fickian regime to the super-diffusive regime, which can be obtained by setting $\tau = 1/k_{off}$ in eqn (3-4)

$$d^2_{\text{small}} = \frac{4\pi^2 D_A}{k_{off}} \tag{3-10}$$

However, the reason why d^2_{small} does not depend on temperature remains to be determined.

Finally, the product γK_{eq} quantitatively describes the extent of anomalous diffusion, because it is the combined ratio of the two diffusion coefficients and the two rate constants. The non-dimensionalized average time constant and square of the grating spacing are defined as $\tilde{\tau} = k_{off} \langle\tau\rangle$ *and* $\tilde{d}^2 = k_{off} d^2/4\pi^2 D_{M,eff}$ (or equivalently $\gamma K_{eq} k_{off} d^2/4\pi^2 D_A$), respectively, where the symbol ~ indicates dimensionless variables. Figure 3-5 shows that all curves collapse in the Fickian regime at large d^2, and the reduced solution in this regime becomes simply $\tilde{\tau} = \tilde{d}^2$. If $\gamma K_{eq} = 1$, this Fickian regime continues to the smallest the length scale until sub-diffusive motions of polymer segments have to be considered. For all the cases in the current study, where $\gamma K_{eq} << 1$ (Figures 3-4C and 3-4F), a super-diffusion regime starts to develop when $\tilde{d}^2$ or $\tilde{\tau}$ decreases to one. The width of the super-diffusive regime w is defined as the ratios of the two d^2 from the line $1/k_{off}$ intersecting the two Fickian solutions (Figure 3-3),

$$w = \frac{d^2_{\text{large}}}{d^2_{\text{small}}} = \frac{4\pi^2 D_M / \left(K_{eq} k_{off}\right)}{4\pi^2 D_A / k_{off}} = \frac{1}{\gamma K_{eq}} \tag{3-11}$$

Therefore, w increases with decreasing γK_{eq}, as observed for gels at low concentrations or at low temperatures (Figures 3-1, 3-2, and 3-5). As shown in the Appendix A, the slope of the super-diffusive regime is

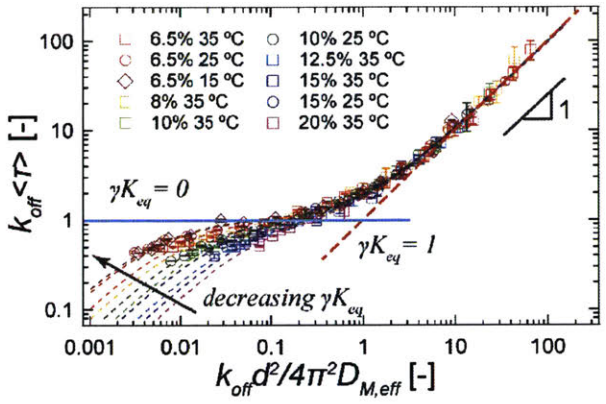

Figure 3-5. Anomalous diffusion plotted in reduced parameter space. The dotted lines are normalized fits to the two-state model. The red dashed line represents the reduced asymptotic solution in the large d^2 Fickian regime. The navy blue line represents the limiting case where $\gamma K_{eq} = 0$.

$$\left.\frac{d\log\tau}{d\log d^2}\right|_{\text{inflection}} \approx \frac{2}{1+\sqrt{w}} = \frac{2}{1+\left(\gamma K_{eq}\right)^{-1/2}} \tag{3-12}$$

which is also a function of γK_{eq} only. When γK_{eq} is non-zero, the slope or the power-law exponent can take any value from zero to one. From eqn (12), it is clear that a smaller value of γK_{eq} yields a smaller slope in the super-diffusive regime (Figures 3-1, 3-2, and 3-5). In the limiting case where $\gamma K_{eq} = 0$, when either associated species are completely immobile or the re-association rate is zero, the super-diffusive regime with a slope of zero is predicted to persist to the smallest length scale. However, for nonzero γK_{eq}, all curves enter a second Fickian regime below the length scale of the super-diffusive regime, where the reduced solution is $\tilde{\tau} = \tilde{d}^2/\gamma K_{eq}$. Therefore, the dimensionless transition $\tilde{d}^2$ from the power-law regime to this small-length-scale Fickian regime is γK_{eq}, from 0.004 to 0.06 in the experiment, as shown in the collapsed data in Figure 5. It is important to point out that both Fickian regimes cannot be superimposed simultaneously because curves with

different values of γK_{eq} have different shapes. If $\tilde{d}^2$ is defined as $k_{off} d^2/4\pi^2 D_A$, the curves will collapsed in the small-length-scale Fickian regime.

The Rheological Signature of Sticky Rouse Relaxation in Protein Gels. Shear rheology is performed in order to study the relationship between the dynamics on the molecular level measured by self-diffusion and a material's macroscopic relaxation. Dynamic moduli master curves are obtained in the frequency range from 10^{-4} to 10^2 rad/s by combining creep and frequency sweep measurements (Appendix A). As shown in Figure 3-6A, P_4 hydrogels exhibit a plateau storage modulus G'_∞ in the high-frequency regime (10–100 rad/s), and a crossover between G' and G'' at intermediate frequencies (0.1–1 rad/s) where the relaxation time of the coiled-coil domain can be assigned; both features are typically observed for physical hydrogels. In addition, a noticeable turn in G' is present in the frequency regime 0.001–0.01 rad/s before entering the terminal relaxation regime. Corresponding to this turn in G', there exists a second plateau in the relaxation modulus master curve (Figure 3-6B) and a local minimum in the van Gurp-Palmen plot (Figure A-7 in Appendix A). The existence of an additional relaxation in this low frequency range resembles the rheological responses from a variety of systems where the sticky Rouse theory can be applied, such as ionomers,[60, 61] hydrogen bond polymers[62] and small molecules[63]; but to the best of our knowledge, this has not been reported or thoroughly investigated in previous studies on gels. More importantly, this sticky Rouse relaxation can be observed in protein gels formed by the same coiled-coil domain but with different number of stickers or with different molecular architecture (multiblock vs. triblock) (Figure A-8 in Appendix A). The finding here agrees with a theoretical study from Indei *et al.* that the sticky Rouse relaxation is universal in transient networks formed by associating polymers.[64]

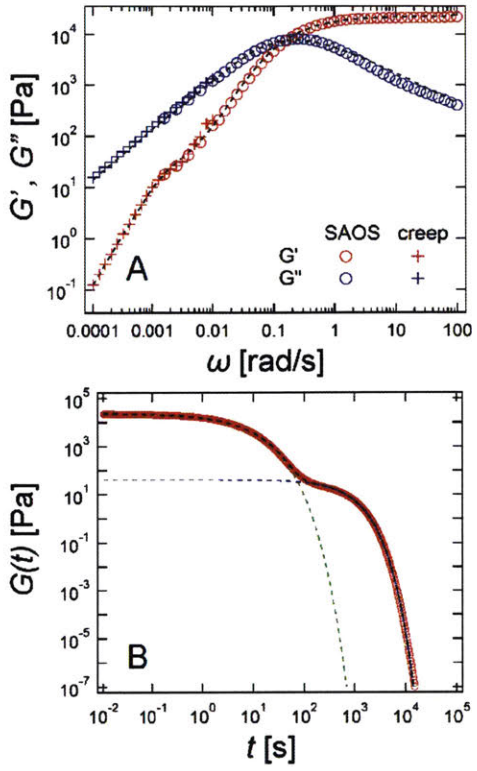

Figure 3-6. Representative dynamic moduli master curves (A) and relaxation modulus master curve (B) of protein gels at 25% (w/v) measured at 25 °C. Black dashed lines in figures represent the fit to a sum of two KWW functions. The green and the blue dashed lines in (B) illustrate the contribution of relaxation modulus from the fast mode and the slow mode relaxations, respectively.

In the high-frequency regime, despite precisely defined molar mass and spacing between stickers, the coiled-coil protein gels still show a broad relaxation distribution corresponding to network junction relaxation. In these protein gels, the relaxation process over the range 0.1 to 100 rad/s is broader than predicted by the Maxwell model (Figure A-9 in Appendix A), similar to phenomena observed in other physical gels.[31, 65, 66] A better fit is obtained using the Kohlrausch-Williams-Watts (KWW) model (Figure 3-6, see model description in Appendix A). A stretched exponent β of 0.620 ± 0.003 is obtained, which suggests significant inhomogeneity in the

relaxation process. Traditionally, the origin of this broader-than-Maxwell relaxation has been attributed to the molecular weight distribution of polymers/proteins, the non-uniform distribution of stickers, and possible effects from chain entanglement. In the coiled-coil protein hydrogel systems studied here, all of these plausible explanations can be ruled out since the protein is strictly monodisperse, the locations of the coiled-coil domains are precisely controlled, and the concentration is below the entanglement threshold.[30] Therefore, the dispersity of the relaxation modes is hypothesized to originate from other forms of dynamic heterogeneity.

The low-frequency rheological response can be fit by the sticky Rouse model or by the KWW model, although the empirical KWW model can provide a quantitative fit in the absence of specific information on the configuration of the proteins in solution. The sticky Rouse model is used to describe the dynamics of polymers with associating side groups below the entanglement threshold.[34-36] It was first proposed by Rubinstein, Semenov, Leibler and Colby, and has recently found great success in modeling the dynamics of ionomers.[60, 61] This model reasons that the relaxation motions of chains larger than the size of a sticky Rouse segment can be constrained by the association of the stickers, whereas the Rouse modes are unaffected for segments with sizes smaller than the chains between stickers. Hence the relaxation modulus has contributions from the normal Rouse modes (high order modes, $p > N_s$) and the sticky Rouse modes (low order modes, $p \leq N_s$):[60]

$$G(t) = \frac{\rho\varphi RT}{M}\left[\sum_{p=N_s+1}^{N} \exp\left(-\frac{tp^2}{\tau_0 N^2}\right) + \sum_{p=1}^{N_s} \exp\left(-\frac{tp^2}{\tau_s N_s^2}\right)\right] \tag{3-13}$$

where τ_0 is the relaxation time of the Rouse segment, τ_s is the relaxation time of the sticky segment, N is the number of Rouse segments in the chain, and N_s is the number of sticky Rouse segments in the chain. However, due to the difficulty in experimentally determining τ_0 and τ_s of coiled-coil

proteins, rheology data in this frequency regime is fit to the phenomenological KWW function, and a satisfactory fit is obtained (Figure 3-6). The stretched exponent in this regime is 0.868 ± 0.003, indicating that the distribution of relaxation modes in this regime is smaller than the one in the high frequency domain, but it does show some extent of dispersity in the relaxation modes. However, the origin of the less inhomogeneous relaxation in the low-frequency range is not well understood.

Taken together, the relaxation of associative protein gels over the frequencies range from 10^{-4} to 10^{2} rad/s can be described by a sum of two KWW functions.

$$G(t) = G_C \exp\left[-\left(\frac{t}{\tau_{KWW,\mathrm{C}}}\right)^{\beta_C}\right] + G_{SR} \exp\left[-\left(\frac{t}{\tau_{KWW,\mathrm{SR}}}\right)^{\beta_{SR}}\right] \tag{3-14}$$

where the subscripts C and SR denote the contribution from the coiled-coil exchange dynamics and from the sticky Rouse relaxation, respectively. Although this approach is entirely based on empirical models, it only uses six parameters and is able to capture most of the important features in the rheology data over six decades. This approach can be applied for gels at all investigated concentrations (Figure 3-7).

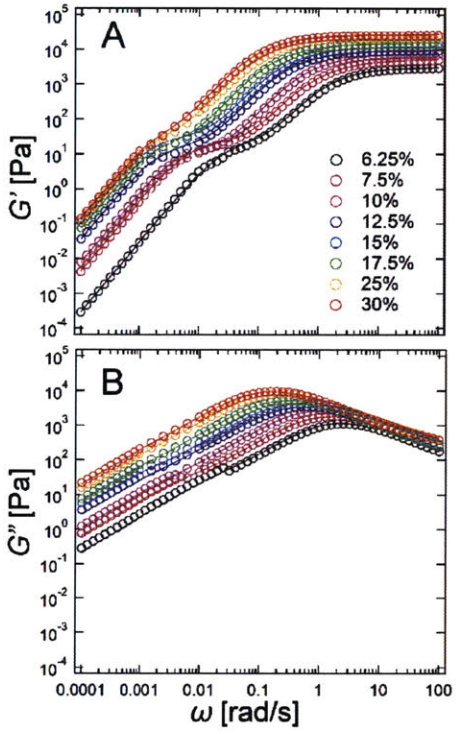

Figure 3-7. Dynamic shear moduli master curves of unentangled multiblock coiled-coil protein hydrogels at various concentrations (G' in panel A, and G'' in panel B). Experimental data are plotted in open circles and the solid lines are fits to eqn (3-14).

Collapsed Shear Rheology Master Curve. The dissociation rate of the coiled-coil domains in rheology directly correlates with the dissociation rate of protein molecules from diffusion measurements, which provides the fundamental basis for a time-concentration-temperature superposition in the rheology data over a certain concentration regime. Many previous studies have suggested that the relaxation of transient networks is primarily governed by the dissociation rate of stickers.[7, 62, 67, 68] In particular, a seminal study from Craig and coworkers[7] demonstrates that the rheological behavior is self-similar for various physical networks based upon different metal-ligand coordination bonds, and a flow master curve $\eta k_d \sim \omega/k_d$ can be obtained by

using molecular dissociation constant k_d as the scaling parameter.[7] However, for systems where the network junctions have a functionality greater than two, the dissociation dynamics used by Craig to rescale the rheological response cannot be clearly defined and be easily measured. In addition, it remains unclear whether Craig's approach can be applied to various concentration regimes under the Sticky Rouse framework. A recent study on low-concentration physical gels argues that the Arrhenius factor, not the dissociation rate, is the correct frequency scaling factor to obtain collapsed rheology curves.[69] Here, the average time constant from the KWW function at higher frequencies

$$\tau_1 = \frac{\tau_{KWW,C}}{\beta_C}\Gamma\left(\frac{1}{\beta_C}\right) \tag{3-15}$$

is assigned to be the hydrogel relaxation time (Γ is the gamma function), and its concentration dependence is plotted in Figure 3-8. A scaling relation $\tau_1 \sim \varphi^{1.64 \pm 0.45}$ is observed for gels at φ = 0.088 (corresponding to 12.5% w/v) and above, and the scaling exponent is close to the one in $\tau_d \sim \varphi^{1.57 \pm 1.26}$ ($\tau_d = 1/k_{off}$; and the relatively large error bar is due to a limited concentration range accessible in diffusion measurements). This suggests that τ_1 and τ_d might both originate from the dissociation of coiled-coil domains. However, τ_1 and τ_d are essentially different: τ_d describes the dissociation time of protein molecules from networks that demands simultaneous disengagement of all coiled-coil domains on a single chain, whereas τ_1 is the time of network relaxation, which only requires exchange between some of the coiled-coils that relaxes elastically effective midblock segments. Thus, it is not surprising that τ_d measured by diffusion is on the order of 1000 s, which is two to three orders of magnitude larger than the segmental relaxation time τ_1 measured by rheology (Figure A-10).

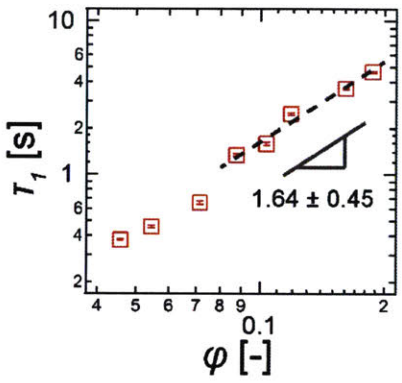

Figure 3-8. Concentration dependence of the time constant τ_1 from the KWW function at high frequencies. Error bars represent 95% confidence interval from fits to the KWW function. Only the concentration range for φ = 0.088 (corresponding to 12.5% w/v) and above is fitted because intermolecular coiled-coil association dominates in this range.

Nonetheless, because of the common molecular origin of both processes, the dissociation rate constant k_{off} from diffusion studies can be utilized to produce dynamic moduli master curves by defining a reduced angular frequency as $\tilde{\omega} = \omega/k_{off}$ (i.e., the shift factor is $1/k_{off}$) and reduced moduli as $\tilde{G}' = G'/G'_{max}$ and $\tilde{G}'' = G''/G'_{max}$, where G'_{max} is the high-frequency plateau modulus at that particular concentration. Rate constants k_{off} not measured at the reference temperature (25 °C) are calculated from the concentration scaling $k_{off} \sim \varphi^{-1.57}$ and the Arrhenius law $\ln k \sim E/RT$. As shown in Figure 3-9, the rheology data from gels at 12.5% (w/v) and above collapse at reduced frequencies from 10^6 to 10. Furthermore, the onset of the terminal regime appears where the reduced frequencies is on order one. This suggests that sticky protein molecules are able to "freely" diffuse for times longer than $1/k_{off}$, consistent with the definition of the terminal regime. While similar results have been reported,[44] previously findings and conclusions are confounded by the effect of structural polydispersity, which is absent in the protein gels studied here. Since the

method considers the effect of both concentration and temperature on the relaxation dynamics, it is termed *time-concentration-temperature* superposition. By examining the concentration dependence of the zero-shear-rate viscosity η_0 (Figure A-11), the concentration range in the rheological study may be divided into two regimes: the low concentration regime below $\varphi = 0.071$ (i.e., 10% w/v), and the high concentration regime above $\varphi = 0.088$ (i.e., 12.5% w/v), where the number fraction of elastically effective chains is 0.68 and above under the affine network assumption (Figure A-12). The scaling $\eta_0 \sim \varphi^{2.46}$ also shows qualitative agreement with the prediction from the sticky Rouse theory.[35] Note that the highest concentration 30% (w/v) is still below the threshold at which strands between two adjacent stickers overlap.[30] Therefore, the superposition of rheology data demonstrates that the network relaxation is indeed controlled by the dissociation rate of stickers. In addition, the superposition method applies when the concentration lies in the regime $\varphi_{ren} < \varphi < \varphi_s$, i.e., the concentration is high enough such that the intermolecular association dominates and bond lifetime renormalization should be considered ($\varphi_{ren} < \varphi$), but it is still below the overlap concentration of sticky Rouse segments (φ_s). It is important to point out that gels investigated in the seminal work from Craig also fall into the regime $\varphi_{ren} < \varphi < \varphi_s$ (see analysis in Appendix A). Finally, it is observed that the rheology data starts to diverge below a reduced frequency of 10 due to the sticky-Rouse-like relaxation, in agreement with previous studies on ionomers.[60]

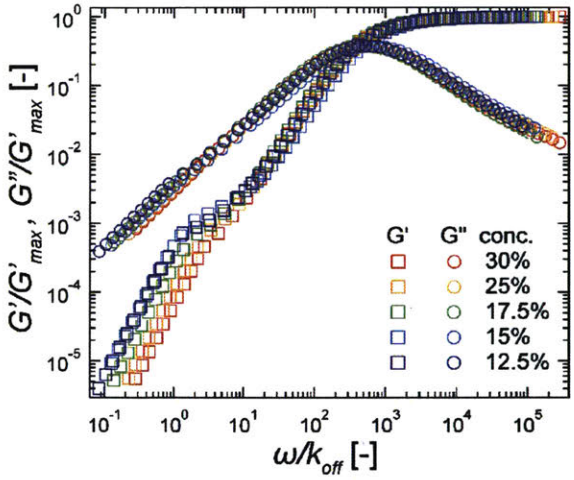

Figure 3-9. Rheology data plotted in the reduced parameter space. The parts in the high-frequency regime collapse onto a single curve. The reference temperature is at 25 °C.

The sticky-Rouse signature in the rheology data is hypothesized to originate from the collective motion of associative protein molecules in an aggregated state because of the high valency of coiled-coil junctions. It is important to emphasize that the gels are clear, showing no signs of macrophase separation, and that this motion of associated species cannot be correlated to a structural length scale within the gel. While the sticky Rouse model cannot be readily applied to quantitatively describe the rheological behavior of protein hydrogels, it provides an estimate of the size of a "dynamic relaxation unit". By setting $t = 0$ in eqn (3-13), the sticky Rouse model gives a molecular weight-modulus relationship,

$$G_{SR} = \frac{\rho\varphi RT}{M} N = \frac{\rho\varphi RT}{M_{eff}} \tag{3-16}$$

where M_{eff} is the effective molecular weight of a "relaxation unit" on the long time scale, ρ is the density of proteins (estimated to be 1.30 from previous work[30]), and G_{SR} is the sticky Rouse

modulus in eqn (3-13) whose value is obtained by fitting to the KWW model. Thus the number of protein molecules in a relaxation unit θ is calculated to be

$$\theta = \frac{M_{eff}}{M_0} = \frac{\rho \varphi RT}{G_{SR} M_0} \tag{3-17}$$

where M_0 is the molecular weight of a single protein P_4 (62.8 kDa). Figure 3-10 depicts the concentration dependence of G_{SR} and θ. Because the sticky Rouse modulus G_{SR} has a value of 20-45 Pa, θ is calculated to be in the range of 100-200. The large number suggests that the relaxation unit could be aggregated proteins originating from thermal fluctuation or dynamic heterogeneity within the transient network. This is a key difference between the protein gels studied here and other associating physical networks where the sticky Rouse rheological feature comes from the hindered motion of polymer chains;[60-62] but it is reminiscent of observation of the supramolecular structure in hydrogen-bonded monohydroxy alcohols where the sticky-Rouse-like relaxation is due to dynamic molecular aggregation.[63]

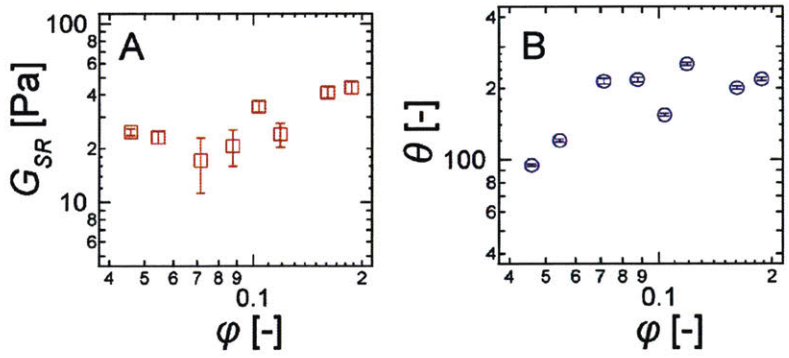

Figure 3-10. Concentration dependence of (A) the sticky Rouse relaxation modulus G_{SR} and (B) the number of proteins in a "dynamic relaxation unit" θ. Error bars represent 95% confidence intervals.

3.3. Conclusions

Unexpected anomalous self-diffusion is observed in associating polymer gels for the first time using a model system of associating coiled-coil protein hydrogels. On time scales approximately equal to the molecular dissociation time, super-diffusion is shown, which originates from the interplay between association dynamics and diffusion of proteins in an unbound state and an associated state. On large time scales, Fickian diffusion is recovered but is effectively slowed by the fraction of dissociated chains in the strong association limit. The observed anomalous behavior can be quantitatively explained by a simple two-state model for dynamic exchange of molecules between a free molecular state and an associated state, providing estimates on the diffusivities and the rate constants. Importantly, even in the associated state, molecules still have a small but non-zero diffusivity. Hindered diffusion of associating proteins in molecular and aggregated states also manifest in the shear rheology master curves, which displays sticky-Rouse-like relaxation at low frequencies. It is shown that high-frequency relaxation of the model transient network is primarily controlled by the dissociation rate of stickers, but the principle of time-concentration superposition only holds in a concentration regime where the intermolecular association becomes dominant. The concentration scaling relations of diffusivities and the zero-shear-rate viscosity and the concentration-dependent dissociation rate are qualitatively consistent with the sticky Rouse theory.

3.4. Experimental Methods

Protein Synthesis and Purification. The genes encoding for associating protein P_4 and P_4-Cys have been previously reported, and the full expressed protein sequences are available in the literature.[70, 71] Both proteins have four coiled-coils on the protein backbone joined by flexible

polyelectrolyte linkers C_{10}, and the protein P_4-Cys has a single cysteine residue near the C terminus that enables efficient labeling with maleimide-functionalized dye molecules (Scheme 2). The detailed procedure for protein synthesis and purification has been reported in previous work.[30, 72] Briefly, proteins were expressed in *Escherichia coli* and purified by ammonium sulfate precipitation and anion exchange chromatography using HiTrapQ Sepharose HP 5mL columns. Combined pure fractions (determined by SDS-PAGE) were dialyzed against MilliQ water extensively and lyophilized.

Synthesis and Purification of *ortho*-Nitrostilbene (ONS) Labeled Proteins P_4. The synthesis of the maleimide-functionalized photochromic 4'-(*N*,*N*'-dimethylamino)-2-nitrostilbene dye (ONS-M) followed a previously published procedure.[73] In a typical conjugation reaction (Scheme 3-2), protein P_4-Cys was first dissolved in a 3:1 (v/v) mixture of DMSO : (10 mM NaH_2PO_4) to a concentration of 1 mg/mL, and the solution was stirred at room temperature for 2 h to ensure complete dissolution of proteins. Next, a 20-fold excess of tris(2-carboxyethyl)phosphine (TCEP) and ONS-M relative to the cysteine residue were added, and the pH of the reaction mixture was adjusted to 7.5. After overnight reaction in the dark, the mixture was dialyzed against MilliQ water and lyophilized. To remove the unreacted free dye, the lyophilized powder was redissolved in a buffer with 6 M urea and 20 mM Tris at pH 8.0 (freshly prepared). The product was first purified by anion exchange using HiTrapQ Sepharose HP 5mL columns (GE Healthcare), and further purified by size exclusion with Sephadex LH-20 resins (GE healthcare). The conjugation efficiency was greater than 99% confirmed by UV/Vis spectroscopy.

Scheme 3-2. Efficient synthesis of ortho-nitrostilbene (ONS) labeled proteins P_4 via thiol-maleimide conjugation.

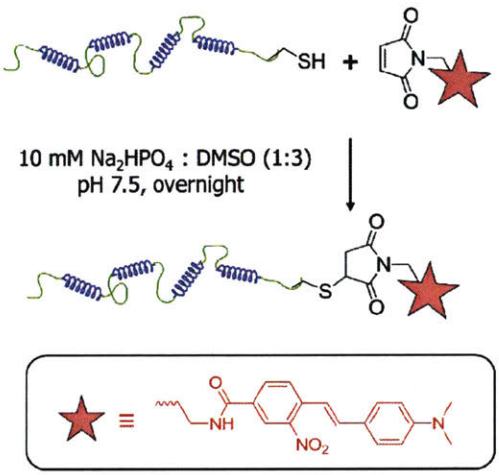

Forced Rayleigh Scattering Measurements. The protein gels for diffusion measurement were prepared by hydrating ONS-labeled P_4 and matrix P_4 in 100 mM sodium phosphate buffer at pH 7.6 to the desired concentrations at 4 °C for 2 days, and the concentration of ONS-P_4 was approximately at 150 μM. The gels were mixed periodically to ensure homogenous distribution of dye-labeled proteins, and then pressed in between two quartz disks (0.9 inches in diameter) with a 0.5 mm Teflon spacer in a brass sample holder. The specimens were annealed at 37 °C for 2 h in the dark to eliminate shear history from loading. Samples were equilibrated at the desired experimental temperature for at least 1 h before measurement. Diffusion was measured by forced Rayleigh scattering (FRS), a technique widely used in probing slow diffusion of molecules in colloids, micelles, and self-assembled block copolymers.[74, 75] Compared to other popular methods of studying diffusion, such as fluorescence recovery after photobleaching (FRAP), FRS has the advantage of accessing length scales close to the diffraction limit while measuring over timescales

comparable to FRAP.[74] FRS measurements were performed as previously described.[73,76] Briefly, a 100 mW continuous wave laser operating in single longitudinal mode at λ = 488 nm was split into two beams, which were individually refocused and crossed at an angle of θ onto the sample (Scheme 3-1C). This generated a holographic grating of characteristic spacing d that is determined by eqn (4). By exposing the sample for 250 ms, the photochromic ONS dye was irreversibly isomerized in the areas of constructive interference, resulting in an amplitude grating of dye concentration. The evolution of the resulting sinusoidal concentration profile by diffusion was monitored by diffraction of a single reading beam at the same wavelength and angle as one of the writing beams, but attenuated by 10^{-5}. The intensity of the reading beam was low enough such that the change of the profile was due only to diffusion. After a fast initial decay in the intensity with a time constant two orders of magnitude smaller than the time constant for the long decay (Figure A-1 and Appendix A), the signal was fit to a stretched exponential function

$$I = A\exp^2\left[-\left(\frac{t}{\tau}\right)^{\beta}\right] + B \tag{3-18}$$

where I is the intensity, τ is the time constant, β is the stretched exponent ranging from 0 to 1, and B is the incoherent background. Only the slow decay with a larger time constant was considered (Appendix A). The average decay time constant was calculated as the first moment of the stretched exponential

$$\langle\tau\rangle = \frac{\tau_{KWW}}{\beta}\Gamma\left(\frac{1}{\beta}\right) \tag{3-19}$$

where Γ is the gamma function.

Rheology Experiments and Data Analysis. Lyophilized proteins were hydrated in 100 mM sodium phosphate buffer (pH 7.6, filtered through 0.2 μm PES filters) to the specified concentrations. Hydrogel samples were kept at 4 °C for 2 days to allow complete hydration. Linear rheological measurements of protein hydrogels were performed on Anton Paar MCR 301 and MCR 702 rheometers. For consistency, motor adjustment and inertial calibration were performed before each experiment. A cone and plate geometry (25 mm, 1° cone) was used for all samples, and a larger cone (50 mm, 0.5°) was used to perform measurements at low torques. Hydrogel samples were coated at the edge with mineral oil to minimize dehydration. The effect of low-viscosity mineral oil on the rheological measurements was negligible as the torque generated from oil was over three orders of magnitude less than the torque generated from samples at all frequencies. Small angle oscillatory shear (SAOS) experiments were performed at 1 % strain (in the linear viscoelastic regime) from 100 rad/s to 0.001 rad/s. In creep experiments, samples were subjected to constant loads at 25, 50 and 100 Pa for 30 min and the recovery phase was monitored for 30 minutes after stress was removed.

In order to capture the rheological response of physical hydrogels over the entire frequency spectrum, dynamic moduli master curves were constructed using the method previously reported[72] and the details are provided in Appendix A. In this study, three different models were applied to examine their efficacy in describing the rheological behaviors of gels, including the Maxwell model, the stretched exponential model, and the Sticky Rouse model. Brief descriptions of the Maxwell model and the KWW model can be found in Appendix A, and the sticky Rouse model has been discussed in the main text. Detailed procedures for fitting each model to the experimental data are in Appendix A.

3.5. References

1. Aida, T.; Meijer, E. W.; Stupp, S. I. Functional Supramolecular Polymers. *Science* 2012, 335, 813-817.

2. Liu, K.; Kang, Y.; Wang, Z.; Zhang, X. 25th Anniversary Article: Reversible and Adaptive Functional Supramolecular Materials: "Noncovalent Interaction" Matters. *Advanced Materials* 2013, 25, 5530-5548.

3. Guo, M.; Pitet, L. M.; Wyss, H. M.; Vos, M.; Dankers, P. Y. W.; Meijer, E. W. Tough Stimuli-Responsive Supramolecular Hydrogels with Hydrogen-Bonding Network Junctions. *Journal of the American Chemical Society* 2014, 136, 6969-6977.

4. Albertazzi, L.; van der Zwaag, D.; Leenders, C. M. A.; Fitzner, R.; van der Hofstad, R. W.; Meijer, E. W. Probing Exchange Pathways in One-Dimensional Aggregates with Super-Resolution Microscopy. *Science* 2014, 344, 491-495.

5. Cordier, P.; Tournilhac, F.; Soulie-Ziakovic, C.; Leibler, L. Self-Healing and Thermoreversible Rubber from Supramolecular Assembly. *Nature* 2008, 451, 977-980.

6. Holten-Andersen, N.; Harrington, M. J.; Birkedal, H.; Lee, B. P.; Messersmith, P. B.; Lee, K. Y. C.; Waite, J. H. Ph-Induced Metal-Ligand Cross-Links Inspired by Mussel Yield Self-Healing Polymer Networks with near-Covalent Elastic Moduli. *Proceedings of the National Academy of Sciences* 2011, 108, 2651-2655.

7. Yount, W. C.; Loveless, D. M.; Craig, S. L. Small-Molecule Dynamics and Mechanisms Underlying the Macroscopic Mechanical Properties of Coordinatively Cross-Linked Polymer Networks. *Journal of the American Chemical Society* 2005, 127, 14488-14496.

8. Rowley, J. A.; Madlambayan, G.; Mooney, D. J. Alginate Hydrogels as Synthetic Extracellular Matrix Materials. *Biomaterials* 1999, 20, 45-53.

9. Hunt, J. N.; Feldman, K. E.; Lynd, N. A.; Deek, J.; Campos, L. M.; Spruell, J. M.; Hernandez, B. M.; Kramer, E. J.; Hawker, C. J. Tunable, High Modulus Hydrogels Driven by Ionic Coacervation. *Advanced Materials* 2011, 23, 2327-2331.

10. Lemmers, M.; Sprakel, J.; Voets, I. K.; van der Gucht, J.; Cohen Stuart, M. A. Multiresponsive Reversible Gels Based on Charge-Driven Assembly. *Angewandte Chemie International Edition* 2010, 49, 708-711.

11. Alexandridis, P.; Holzwarth, J. F.; Hatton, T. A. Micellization of Poly(Ethylene Oxide)-Poly(Propylene Oxide)-Poly(Ethylene Oxide) Triblock Copolymers in Aqueous Solutions: Thermodynamics of Copolymer Association. *Macromolecules* 1994, 27, 2414-2425.

12. Jeong, B.; Bae, Y. H.; Lee, D. S.; Kim, S. W. Biodegradable Block Copolymers as Injectable Drug-Delivery Systems. *Nature* 1997, 388, 860-862.

13. Harada, A.; Kobayashi, R.; Takashima, Y.; Hashidzume, A.; Yamaguchi, H. Macroscopic Self-Assembly through Molecular Recognition. *Nat Chem* 2011, 3, 34-37.

14. Appel, E. A.; Biedermann, F.; Rauwald, U.; Jones, S. T.; Zayed, J. M.; Scherman, O. A. Supramolecular Cross-Linked Networks Via Host−Guest Complexation with Cucurbit[8]Uril. *Journal of the American Chemical Society* 2010, 132, 14251-14260.

15. Schneider, J. P.; Pochan, D. J.; Ozbas, B.; Rajagopal, K.; Pakstis, L.; Kretsinger, J. Responsive Hydrogels from the Intramolecular Folding and Self-Assembly of a Designed Peptide. *Journal of the American Chemical Society* 2002, 124, 15030-15037.

16. Ortony, J. H.; Newcomb, C. J.; Matson, J. B.; Palmer, L. C.; Doan, P. E.; Hoffman, B. M.; Stupp, S. I. Internal Dynamics of a Supramolecular Nanofibre. *Nat Mater* 2014, 13, 812-816.

17. Nowak, A. P.; Breedveld, V.; Pakstis, L.; Ozbas, B.; Pine, D. J.; Pochan, D.; Deming, T. J. Rapidly Recovering Hydrogel Scaffolds from Self-Assembling Diblock Copolypeptide Amphiphiles. *Nature* 2002, 417, 424-428.

18. Petka, W. A.; Harden, J. L.; McGrath, K. P.; Wirtz, D.; Tirrell, D. A. Reversible Hydrogels from Self-Assembling Artificial Proteins. *Science* 1998, 281, 389-392.

19. Israelachvili, J. N. *Intermolecular and Surface Forces*. 3rd ed.; Academic Press: Burlington, Mass., 2011; p xxx, 674 p.

20. Ribbeck, K.; Görlich, D. *Kinetic Analysis of Translocation through Nuclear Pore Complexes*. 2001; Vol. 20, p 1320-1330.

21. Wang, C.; Wu, H.; Chen, Z.; McDowell, M. T.; Cui, Y.; Bao, Z. Self-Healing Chemistry Enables the Stable Operation of Silicon Microparticle Anodes for High-Energy Lithium-Ion Batteries. *Nat Chem* 2013, 5, 1042-1048.

22. Tee, B. C. K.; Wang, C.; Allen, R.; Bao, Z. An Electrically and Mechanically Self-Healing Composite with Pressure- and Flexion-Sensitive Properties for Electronic Skin Applications. *Nat Nano* 2012, 7, 825-832.

23. Chen, Y.; Kushner, A. M.; Williams, G. A.; Guan, Z. Multiphase Design of Autonomic Self-Healing Thermoplastic Elastomers. *Nat Chem* 2012, 4, 467-472.

24. Burnworth, M.; Tang, L.; Kumpfer, J. R.; Duncan, A. J.; Beyer, F. L.; Fiore, G. L.; Rowan, S. J.; Weder, C. Optically Healable Supramolecular Polymers. *Nature* 2011, 472, 334-337.

25. Sun, T. L.; Kurokawa, T.; Kuroda, S.; Ihsan, A. B.; Akasaki, T.; Sato, K.; Haque, M. A.; Nakajima, T.; Gong, J. P. Physical Hydrogels Composed of Polyampholytes Demonstrate High Toughness and Viscoelasticity. *Nat Mater* 2013, 12, 932-937.

26. Sun, J.-Y.; Zhao, X.; Illeperuma, W. R. K.; Chaudhuri, O.; Oh, K. H.; Mooney, D. J.; Vlassak, J. J.; Suo, Z. Highly Stretchable and Tough Hydrogels. *Nature* 2012, 489, 133-136.

27. Wong Po Foo, C. T. S.; Lee, J. S.; Mulyasasmita, W.; Parisi-Amon, A.; Heilshorn, S. C. Two-Component Protein-Engineered Physical Hydrogels for Cell Encapsulation. *Proceedings of the National Academy of Sciences* 2009, 106, 22067-22072.

28. Olsen, B. D.; Kornfield, J. A.; Tirrell, D. A. Yielding Behavior in Injectable Hydrogels from Telechelic Proteins. *Macromolecules* 2010, 43, 9094-9099.

29. Shen, W.; Kornfield, J. A.; Tirrell, D. A. Dynamic Properties of Artificial Protein Hydrogels Assembled through Aggregation of Leucine Zipper Peptide Domains. *Macromolecules* 2007, 40, 689-692.

30. Tang, S.; Glassman, M. J.; Li, S.; Socrate, S.; Olsen, B. D. Oxidatively Responsive Chain Extension to Entangle Engineered Protein Hydrogels. *Macromolecules* 2014, 47, 791-799.

31. McKinnon, D. D.; Domaille, D. W.; Cha, J. N.; Anseth, K. S. Biophysically Defined and Cytocompatible Covalently Adaptable Networks as Viscoelastic 3d Cell Culture Systems. *Advanced Materials* 2014, 26, 865-872.

32. Tanaka, F.; Edwards, S. F. Viscoelastic Properties of Physically Crosslinked Networks. 1. Transient Network Theory. *Macromolecules* 1992, 25, 1516-1523.

33. Green, M. S.; Tobolsky, A. V. A New Approach to the Theory of Relaxing Polymeric Media. *The Journal of Chemical Physics* 1946, 14, 80-92.

34. Rubinstein, M.; Semenov, A. N. Thermoreversible Gelation in Solutions of Associating Polymers. 2. Linear Dynamics. *Macromolecules* 1998, 31, 1386-1397.

35. Rubinstein, M.; Semenov, A. N. Dynamics of Entangled Solutions of Associating Polymers. *Macromolecules* 2001, 34, 1058-1068.

36. Leibler, L.; Rubinstein, M.; Colby, R. H. Dynamics of Reversible Networks. *Macromolecules* 1991, 24, 4701-4707.

37. Cates, M. E. Reptation of Living Polymers: Dynamics of Entangled Polymers in the Presence of Reversible Chain-Scission Reactions. *Macromolecules* 1987, 20, 2289-2296.

38. Tripathi, A.; Tam, K. C.; McKinley, G. H. Rheology and Dynamics of Associative Polymers in Shear and Extension: Theory and Experiments. *Macromolecules* 2006, 39, 1981-1999.

39. Sing, M. K.; Wang, Z.-G.; McKinley, G. H.; Olsen, B. D. Chain Configuration and Rate-Dependent Mechanical Properties in Transient Networks. *Soft Matter* 2015.

40. Gilbert, J. B.; Rubner, M. F.; Cohen, R. E. Depth-Profiling X-Ray Photoelectron Spectroscopy (Xps) Analysis of Interlayer Diffusion in Polyelectrolyte Multilayers. *Proceedings of the National Academy of Sciences* 2013, 110, 6651-6656.

41. Ader, C.; Frey, S.; Maas, W.; Schmidt, H. B.; Görlich, D.; Baldus, M. Amyloid-Like Interactions within Nucleoporin Fg Hydrogels. *Proceedings of the National Academy of Sciences* 2010, 107, 6281-6285.

42. van Meer, G.; Voelker, D. R.; Feigenson, G. W. Membrane Lipids: Where They Are and How They Behave. *Nat Rev Mol Cell Biol* 2008, 9, 112-124.

43. Stukalin, E. B.; Cai, L.-H.; Kumar, N. A.; Leibler, L.; Rubinstein, M. Self-Healing of Unentangled Polymer Networks with Reversible Bonds. *Macromolecules* 2013, 46, 7525-7541.

44. Hackelbusch, S.; Rossow, T.; van Assenbergh, P.; Seiffert, S. Chain Dynamics in Supramolecular Polymer Networks. *Macromolecules* 2013, 46, 6273-6286.

45. Rossow, T.; Habicht, A.; Seiffert, S. Relaxation and Dynamics in Transient Polymer Model Networks. *Macromolecules* 2014, 47, 6473-6482.

46. Mi, L.; Fischer, S.; Chung, B.; Sundelacruz, S.; Harden, J. L. Self-Assembling Protein Hydrogels with Modular Integrin Binding Domains. *Biomacromolecules* 2005, 7, 38-47.

47. Yao, M.-H.; Yang, J.; Du, M.-S.; Song, J.-T.; Yu, Y.; Chen, W.; Zhao, Y.-D.; Liu, B. Polypeptide-Engineered Physical Hydrogels Designed from the Coiled-Coil Region of Cartilage Oligomeric Matrix Protein for Three-Dimensional Cell Culture. *Journal of Materials Chemistry B* 2014, 2, 3123-3132.

48. Collier, J. H.; Rudra, J. S.; Gasiorowski, J. Z.; Jung, J. P. Multi-Component Extracellular Matrices Based on Peptide Self-Assembly. *Chemical Society Reviews* 2010, 39, 3413-3424.

49. Wheeldon, I. R.; Gallaway, J. W.; Barton, S. C.; Banta, S. Bioelectrocatalytic Hydrogels from Electron-Conducting Metallopolypeptides Coassembled with Bifunctional Enzymatic Building Blocks. *Proceedings of the National Academy of Sciences* 2008, 105, 15275-15280.

50. Kim, Y. H.; Campbell, E.; Yu, J.; Minteer, S. D.; Banta, S. Complete Oxidation of Methanol in Biobattery Devices Using a Hydrogel Created from Three Modified Dehydrogenases. *Angewandte Chemie International Edition* 2013, 52, 1437-1440.

51. Zhang, L.; Furst, E. M.; Kiick, K. L. Manipulation of Hydrogel Assembly and Growth Factor Delivery Via the Use of Peptide–Polysaccharide Interactions. *Journal of Controlled Release* 2006, 114, 130-142.

52. Ott, A.; Bouchaud, J. P.; Langevin, D.; Urbach, W. Anomalous Diffusion in "Living Polymers": A Genuine Levy Flight? *Physical Review Letters* 1990, 65, 2201-2204.

53. Upadhyaya, A.; Rieu, J.-P.; Glazier, J. A.; Sawada, Y. Anomalous Diffusion and Non-Gaussian Velocity Distribution of Hydra Cells in Cellular Aggregates. *Physica A: Statistical Mechanics and its Applications* 2001, 293, 549-558.

54. Sprague, B. L.; Pego, R. L.; Stavreva, D. A.; McNally, J. G. Analysis of Binding Reactions by Fluorescence Recovery after Photobleaching. *Biophysical Journal* 2004, 86, 3473-3495.

55. Gunasekar, S. K.; Asnani, M.; Limbad, C.; Haghpanah, J. S.; Hom, W.; Barra, H.; Nanda, S.; Lu, M.; Montclare, J. K. N-Terminal Aliphatic Residues Dictate the Structure, Stability, Assembly, and Small Molecule Binding of the Coiled-Coil Region of Cartilage Oligomeric Matrix Protein. *Biochemistry* 2009, 48, 8559-8567.

56. Zettl, U.; Hoffmann, S. T.; Koberling, F.; Krausch, G.; Enderlein, J.; Harnau, L.; Ballauff, M. Self-Diffusion and Cooperative Diffusion in Semidilute Polymer Solutions as Measured by Fluorescence Correlation Spectroscopy. *Macromolecules* 2009, 42, 9537-9547.

57. King, J. T.; Yu, C.; Wilson, W. L.; Granick, S. Super-Resolution Study of Polymer Mobility Fluctuations near C*. *ACS Nano* 2014, 8, 8802-8809.

58. Rubinstein, M.; Colby, R. H. *Polymer Physics*. Oxford University Press: Oxford ; New York, 2003; p xi, 440 p.

59. Masaro, L.; Zhu, X. X. Physical Models of Diffusion for Polymer Solutions, Gels and Solids. *Progress in Polymer Science* 1999, 24, 731-775.

60. Chen, Q.; Tudryn, G. J.; Colby, R. H. Ionomer Dynamics and the Sticky Rouse Modela). *Journal of Rheology* 2013, 57, 1441-1462.

61. Chen, Q.; Liang, S.; Shiau, H.-s.; Colby, R. H. Linear Viscoelastic and Dielectric Properties of Phosphonium Siloxane Ionomers. *ACS Macro Letters* 2013, 2, 970-974.

62. Lewis, C. L.; Stewart, K.; Anthamatten, M. The Influence of Hydrogen Bonding Side-Groups on Viscoelastic Behavior of Linear and Network Polymers. *Macromolecules* 2014, 47, 729-740.

63. Gainaru, C.; Figuli, R.; Hecksher, T.; Jakobsen, B.; Dyre, J. C.; Wilhelm, M.; Böhmer, R. Shear-Modulus Investigations of Monohydroxy Alcohols: Evidence for a Short-Chain-Polymer Rheological Response. *Physical Review Letters* 2014, 112, 098301.

64. Indei, T.; Takimoto, J.-i. Linear Viscoelastic Properties of Transient Networks Formed by Associating Polymers with Multiple Stickers. *The Journal of Chemical Physics* 2010, 133, -.

65. Seitz, M. E.; Burghardt, W. R.; Faber, K. T.; Shull, K. R. Self-Assembly and Stress Relaxation in Acrylic Triblock Copolymer Gels. *Macromolecules* 2007, 40, 1218-1226.

66. He, Y.; Lodge, T. P. Thermoreversible Ion Gels with Tunable Melting Temperatures from Triblock and Pentablock Copolymers. *Macromolecules* 2007, 41, 167-174.

67. Fullenkamp, D. E.; He, L.; Barrett, D. G.; Burghardt, W. R.; Messersmith, P. B. Mussel-Inspired Histidine-Based Transient Network Metal Coordination Hydrogels. *Macromolecules* 2013, 46, 1167-1174.

68. Xu, D.; Craig, S. L. Scaling Laws in Supramolecular Polymer Networks. *Macromolecules* 2011, 44, 5465-5472.

69. Appel, E. A.; Forster, R. A.; Koutsioubas, A.; Toprakcioglu, C.; Scherman, O. A. Activation Energies Control the Macroscopic Properties of Physically Cross-Linked Materials. *Angewandte Chemie International Edition* 2014, 53, 10038-10043.

70. Glassman, M. J.; Chan, J.; Olsen, B. D. Reinforcement of Shear Thinning Protein Hydrogels by Responsive Block Copolymer Self-Assembly. *Advanced Functional Materials* 2013, 23, 1182-1193.

71. Glassman, M. J.; Olsen, B. D. Structure and Mechanical Response of Protein Hydrogels Reinforced by Block Copolymer Self-Assembly. *Soft Matter* 2013, 9, 6814-6823.

72. Tang, S.; Olsen, B. Controlling Topological Entanglement in Engineered Protein Hydrogels with a Variety of Thiol Coupling Chemistries. *Frontiers in Chemistry* 2014, 2.

73. Wang, M.; Timachova, K.; Olsen, B. D. Experimental Measurement of Coil–Rod–Coil Block Copolymer Tracer Diffusion through Entangled Coil Homopolymers. *Macromolecules* 2013, 46, 1651-1658.

74. Schärtl, W. Forced Rayleigh Scattering – Principles and Application (Self Diffusion of Spherical Nanoparticles and Copolymer Micelles). In *Soft Matter Characterization*, Borsali, R.; Pecora, R., Eds. Springer Netherlands: Dordrecht, 2008; pp 677-703.

75. Hamersky, M. W.; Hillmyer, M. A.; Tirrell, M.; Bates, F. S.; Lodge, T. P.; von Meerwall, E. D. Block Copolymer Self-Diffusion in the Gyroid and Cylinder Morphologies. *Macromolecules* 1998, 31, 5363-5370.

76. Liu, K.; Kang, Y.; Wang, Z.; Zhang, X. 25th Anniversary Article: Reversible and Adaptive Functional Supramolecular Materials: "Noncovalent Interaction" Matters. *Advanced Materials (Deerfield Beach, Fla.)* 2013, 25, 5530-5548.

Chapter 4 Self-Diffusion of Associating Star-Shaped Polymers

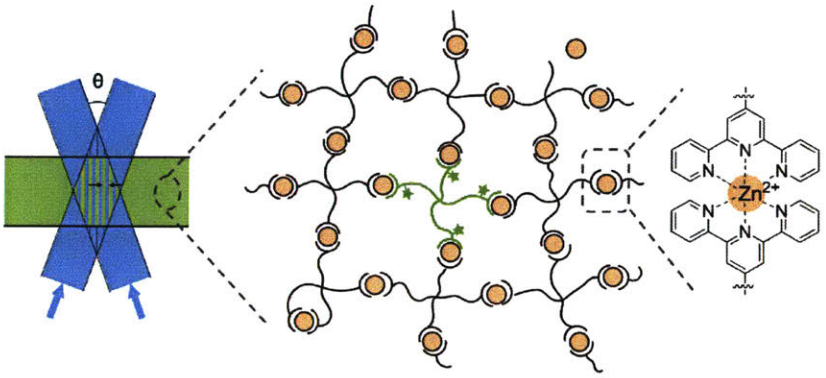

Reproduced with permission from S. Tang and A. Habicht et al., *Macromolecules*, 2016 (accepted). Materials used in this chapter were synthesized by A. Habicht.

The dynamics of associating bonds in transient polymer networks exerts a paramount influence on their relaxation and time-dependent mechanical properties. In particular, diffusive motion of polymers mediated by the dissociation and association equilibrium of reversible junctions can affect the materials' structural stability, dynamic mechanical properties, and a broad spectrum of functionality that arises from the constant motion of polymer chains. In this work, forced Rayleigh scattering is used to measure the diffusion of terpyridine end-functionalized four-arm poly(ethylene glycol) polymers transiently interlinked by zinc ions in organic solvent across a wide range of length and time scales. Phenomenological super-diffusion, where the scaling of the mean-square displacement vs. time has a power-law exponent larger than one, is demonstrated as an intrinsic feature of these networks due to the interplay of chain dissociation and diffusion. Outside the super-diffusive regime, normal Fickian diffusion is recovered on both large and small

length scales. The data are quantitatively described with a previously developed two-state model of one fast and one slow diffusing species that are allowed to interconvert. The extracted diffusivities show concentration-dependent scaling in good agreement with the sticky Rouse model. Diffusion of the same polymers but with only three associating arms through the same transient networks is also investigated, which exhibits faster chain diffusivities compared to the case of the polymers with four associating arms. These experimental results quantitatively show the effect of sticker density and valency on chain diffusion in transient polymer networks.

4.1. Introduction

Associating polymers represent a family of macromolecules that contain dynamic bonds primarily based on non-covalent physical interactions such as metal–ligand coordination[1-4], hydrogen-bonding[4-6], and host–guest interactions[4, 7, 8] or by reversible chemical reactions such as transesterification[9, 10], oxime[11], hydrazone[12], and disulfide[13] formation. Above the percolation threshold, associating polymers form a three-dimensionally crosslinked network where the junctions are held together by attractive interactions between the dynamic bonds. Due to the dynamic characteristics of these junctions, associating polymer networks are often referred to as transient networks to emphasize the kinetic effect on the materials properties and to distinguish them from permanent networks formed by irreversible chemical crosslinking reactions.[14-22] The importance of the junction chemistry has been well recognized, and much effort has been devoted to controlling the dynamic properties of associating networks such as their ability to self-heal[1, 5, 9, 23, 24] and respond to various forms of environmental stimuli such as light[2], pH[1, 11, 12], magnetic fields[24], temperature[6], and small molecule redox modulators[13, 25]. An advanced understanding of

and control over the structure–property relationships of associating networks[26] has furthered their application in catalysis[27], biomaterials[28, 29], sustainable materials[5], and soft actuators[30].

In many applications, self-diffusion of associating polymers can be very important, because it affects the structural stability of the networks[31, 32], their macroscopic mechanical response[25, 33], and their kinetics of autonomous self-healing[23, 34]. From a fundamental perspective, self-diffusion of associating polymers differs significantly from their non-associating counterparts in that diffusion of an entire polymer chain is only permitted upon partial-sequential or complete-concurrent release of the associative bonds from the networks. The complex interplay of the type and position of associative motifs on the polymer backbones, hereinafter referred to as "stickers", and polymer architecture can have a profound influence on the diffusive motion of the polymer chains. On the segment level, Rouse relaxation of a chain segment containing two or more associating domains can be delayed if the sticker lifetime is longer than the Rouse time of that chain segment without stickers.[35] On the molecular or supramolecular scale, dynamic bonds can effectively increase the molecule size through "supramolecular polymerization"[36], a process akin to traditional step-growth polymerization[37]. When the size of the original molecules or the assembled supramolecules is above the entanglement threshold, additional relaxation mechanisms such as reptation, constraint release, and arm retraction must also be considered.[25, 33, 38]

Two different theories are widely used to understand the dynamics of associative polymers. In one theory, Leibler, Rubinstein, Semenov, and Colby employed scaling arguments and modified the Rouse and reptation models by considering the effect of sticker-bond energetics and kinetics on the motion of chains.[16-18, 39, 40] The sticky Rouse and reptation theories find a strong concentration dependence of many network dynamic properties such as the junction relaxation time and zero-shear-rate viscosity. In addition, the theories suggest an important concept of

renormalization of the sticker-bond lifetime by considering that junctions break and reform many times before changes in the network topology occur due to stickers exchanging partners. In a second theory, an alternative framework was developed by Cates and Candau,[19, 41] focusing on systems in which the average size of transiently polymerized linear chains reaches beyond the entanglement threshold. A new relaxation mechanism emerges when the average junction lifetime is smaller than the reptation time of the living polymers.

Compared to the rich efforts in developing and refining these theories, experimental studies on diffusion of associating polymers are relatively limited, especially in concentrated solutions or gels.[42-45] Furthermore, quantitative comparisons between experimental findings and the sticky Rouse/reptation theories or the Cates–Candau theory are still lacking. To provide a better understanding of self-diffusion, recently both our groups have independently investigated diffusion of associating polymers in gels using fluorescence recovery after photobleaching (FRAP) and forced Rayleigh scattering (FRS) on dissimilar associating networks.[46-48] Both techniques generate a concentration gradient of dye-labeled macromolecules and measure the ensemble relaxation rate of the gradient to extract the diffusivities of associating polymers. All experimental investigations revealed Fickian diffusion on length scales much larger than the radius of gyration of the polymer chains (usually 100–1000 times) and demonstrate that the dissociation–reassociation kinetics slow down the polymer mobility in this regime. By contrast, when forced Rayleigh scattering was employed to study the self-diffusion of associative coiled-coil proteins on length scales closer to the diffraction limit yet larger than the polymer size, phenomenological super-diffusion, characterized by a power-law scaling of the mean-square displacement vs. time with an exponent than one, was observed.[48] The physical origin of the super-diffusive regime was explained by a phenomenological two-state model accounting for the interconversion dynamics of

molecules between two different states with drastically different diffusivities. Since the model does not contain any details regarding the association chemistry or polymer architecture, it may be generally applicable for associating networks provided that molecular diffusion is greatly hindered by the dissociation rate of macromolecules from the surrounding networks, and the molecular dissociation rate is experimentally accessible. However, to date the model has only been tested in the coiled-coil protein gel system.

Herein, the self-diffusion dynamics of unentangled associating polymers based on four-arm poly(ethylene glycol) (PEG) end-functionalized with terpyridine moieties complexed by Zn^{2+} in *N,N*-dimethylformamide (DMF) (Figure 4-1A) is measured by forced Rayleigh scattering at varying grating spacings ranging from 0.5 to 50 μm. This model system is chosen for its narrowly disperse molecular weight of the star-polymer building blocks, its well-defined terpyridine-based sticker chemistry,[49, 50] and its robustly tunable strength of the metal coordinative bonds[3]. It also has the advantage that different relaxation time scales of the supramolecular network, including junction dissociation and chain diffusion, are readily accessible by oscillatory shear rheology and forced Rayleigh scattering at a single temperature. Experimental results of the diffusion dynamics are analyzed by the two-state model, showing phenomenologically similar behavior to the coiled-coil proteins previously studied. In addition, tracer diffusion of four-arm PEG polymers with just three associating arms is investigated through the same model transient network (Figure 4-1B), providing insight into the diffusion mechanisms based on comparisons of self- and tracer diffusion.

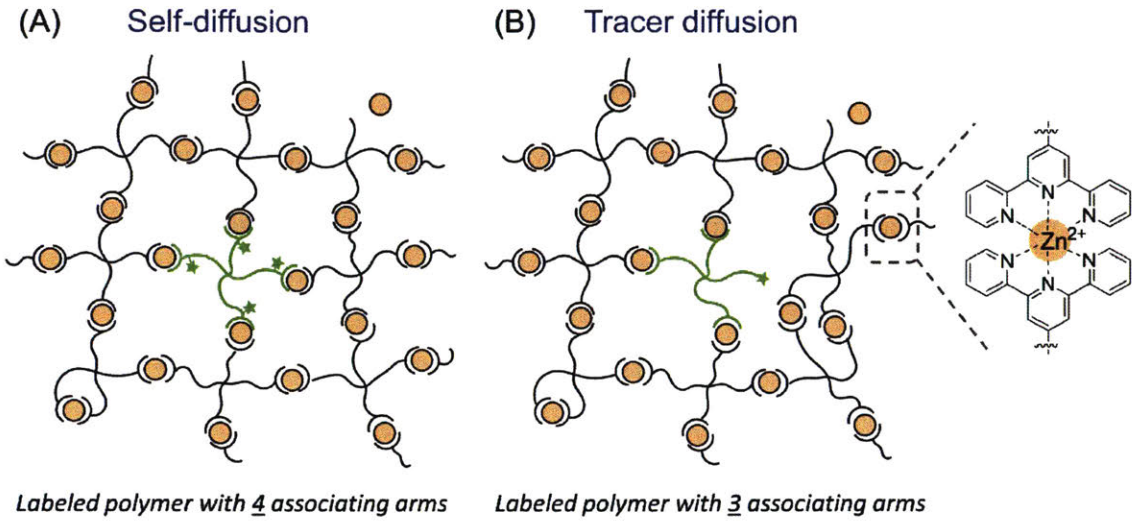

Figure 4-1. The diffusion of fluorescently tagged four-arm PEG polymers with (A) four and (B) just three associating arms is probed in model transient networks formed by complexation between Zn^{2+} and terpyridine end-modified four-arm PEG polymers in (A) self-diffusion and (B) tracer diffusion configurations. Intra-molecular primary loops and dangling chains are shown as two possible defects in the model transient networks. Green stars on the labeled polymers represent the locations of nitrobenzofurazan labels.

4.2. Experimental Section

Tetra-arm PEG-terpyridine. Tetra-arm star-shaped poly(ethylene glycol) (PEG, M_w = 10 kg mol^{-1}, M_w/M_n = 1.03) functionalized with four terpyridine end groups was prepared as detailed previously.[3] In short, four-arm star-shaped hydroxy-terminated PEG was obtained commercially (Creative PEGWorks) and then first reacted with mesyl chloride and then with sodium azide to obtain an azide-terminated four-arm star-shaped PEG. This reactive polymer was then converted in an azide–alkyne Huisgen cycloaddition with terpyridine.

Nitrobenzofurazan-labeled tracer with 3 associating arms. Terpyridine-capped tetra-arm PEG with ~2 mol% of nitrobenzofurazan (NBD) labeling was prepared as detailed previously.[47] In short, four-arm star-shaped hydroxy-terminated PEG was obtained commercially (Creative PEGWorks) and then modified to obtain tetra-arm PEG in an end-activated form, of which ~2 mol% were then labeled with NBD. The rest of the end-activated OH-groups were reacted with an amine-functionalized terpyridine. As a result, a polymer mixture was obtained that consisted of 98% of tetra-arm PEG-terpyridine as described above and of 2% of tetra-arm PEG with three arms modified with terpyridine-caps, whereas the fourth arm was capped with a nitrobenzofurazan unit.

Nitrobenzofurazan-labeled tetra-arm PEG with 4 associating arms. The synthesis procedure is described below, and the synthetic routes are shown in Scheme 4-1.

Tetra-arm PEG-epoxide (1). Tetra-arm PEG-OH (2.00 g, 0.20 mmol, M_w = 10 kg mol^{-1}, M_w/M_n = 1.03) was melted at 70 °C and dried *in vacuo* for 1 h, cooled down to room temperature and then dissolved in dry tetrahydrofuran (50 mL). Sodium hydride (0.26 g, 6.4 mmol, 60% in mineral oil) was added to the yellowish solution, which was then stirred at room temperature for 3 d. Then, epichlorohydrin (1.25 mL, 16.0 mmol) was added, and the solution was stirred at room temperature overnight. The solution was cooled down to 0 °C and quenched with water (2 mL). Brine was added (100 mL), and the mixture was extracted with dichloromethane (2 × 500 mL). The organic layer was dried over $MgSO_4$ and concentrated *in vacuo*. The raw product was precipitated by pouring the concentrate into cold diethyl ether to obtain the product as a white solid (1.99 g, 99%). ^{1}H-NMR (DMSO-d$_6$, 700 MHz): δ = 3.70 (dd, J = 8.5, 2.5 Hz, 4H), 3.61–3.38 (m, 902H, PEG-backbone), 3.25 (dd, J = 11.5, 6.5 Hz, 4H), 3.09 (m, 4H), 2.71 (m, 4H) ppm.

Scheme 4-1. Synthesis of nitrobenzofurazan-labeled tetra-arm PEG with 4 associating arms.

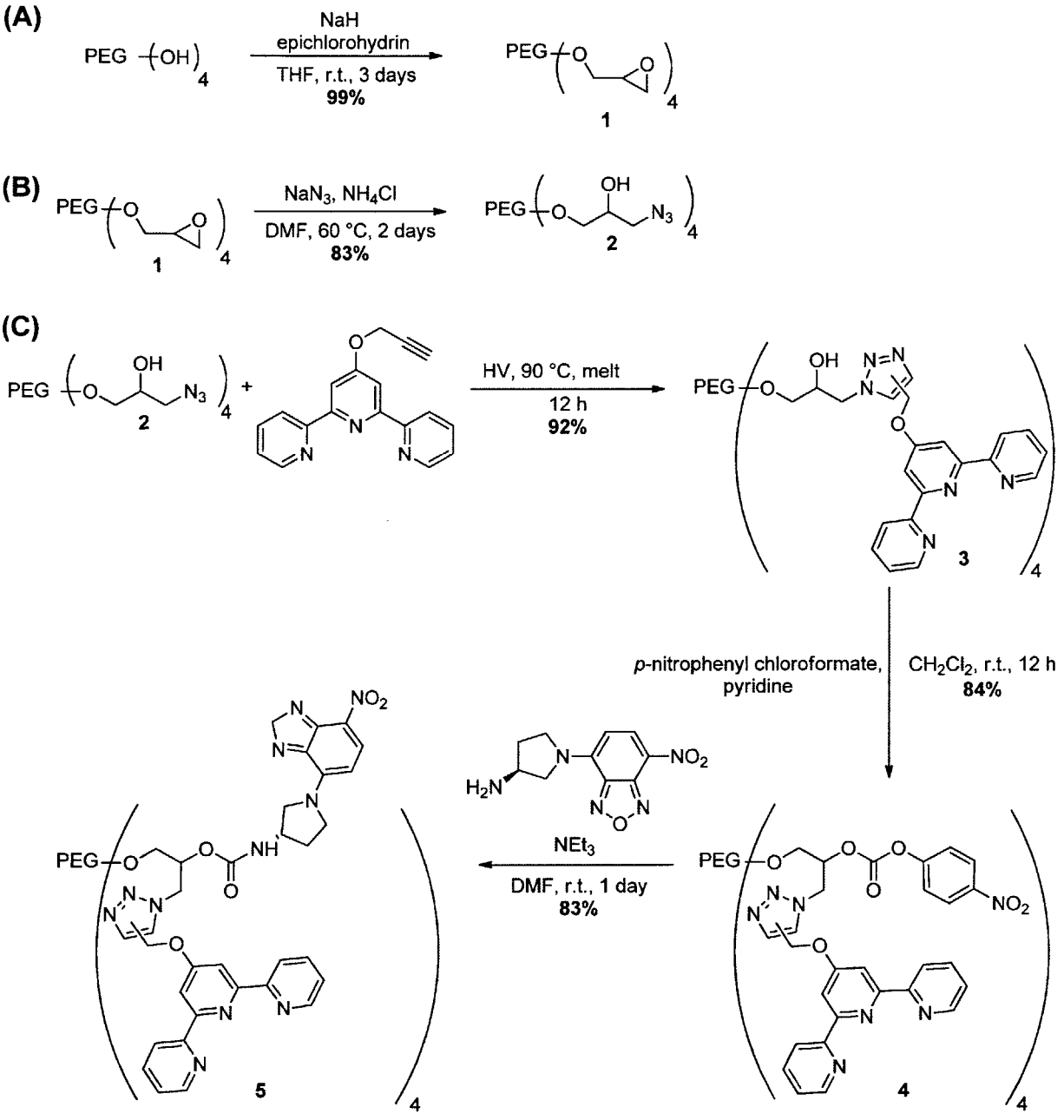

Tetra-arm PEG-hydroxy-azide (2). Sodium azide (0.52 g, 7.98 mmol) was added to a solution of tetra-arm PEG-epoxide **1** (1.99 g, 0.20 mmol) in dimethylformamide (20 mL), followed by addition of ammonium chloride (0.85 g, 15.95 mmol) and stirring at 60 °C for 48 h. The suspension was filtered to remove remaining sodium azide and ammonium chloride, and the

filtrate was concentrated *in vacuo*. The residue was dissolved in dichloromethane (100 mL), then brine (50 mL) was added, and the mixture was extracted with dichloromethane (2 × 200 mL). The organic layer was dried over $MgSO_4$, concentrated *in vacuo*, and the product was precipitated by pouring the concentrate into cold diethyl ether. The precipitate was collected by filtration and washed with cold diethyl ether to obtain the product as a white solid (1.66 g, 83%). ^{1}H-NMR (DMSO-d$_6$, 700 MHz): δ = 5.24 (d, J = 5.6 Hz, 4H), 3.77 (m, 4H), 3.61 (t, J = 4.9 Hz, 6H), 3.55–3.47 (m, 902H, PEG-backbone), 3.41–3.37 (m, 12H), 3.35–3.32 (m, 4H), 3.27 (dd, J = 12.6, 3.5 Hz, 4H), 3.19 (dd, J = 12.6, 6.3 Hz, 4H) ppm.

Tetra-arm PEG-hydroxy-terpyridine (3). Propargyl-terpyridine (0.28 g, 0.96 mmol), which was prepared as detailed previously,[3] was added to a melt of tetra-arm PEG-hydroxy-azide **2** (1.61 g, 0.16 mmol). The melt was stirred at 90 °C under high vacuum for 12 h, whereupon it turned brown, then cooled down to room temperature, and dissolved in dichloromethane (20 mL). The solution was precipitated into cold diethyl ether. The precipitated solid was collected by filtration and washed with cold diethyl ether to obtain the product as a white solid (1.66 g, 92 %). ^{1}H-NMR (DMSO-d$_6$, 500 MHz): δ = 8.74–8.71 (m, 8H), 8.64–8.61 (m, 8H), 8.21 (s, 3H), 8.09 (s, 8H), 8.04–7.99 (m, 8H), 7.88 (s, 1H), 7.55–7.49 (m, 8H), 5.61 (s, 3H), 5.45 (s, 5H), 5.36 (d, J = 4.5 Hz, 2H), 5.31 (d, J = 3.5 Hz, 3H), 4.59 (dd, J = 10.5, 3.5 Hz, 3H), 4.49 (dd, J = 9.5, 2.5 Hz , 3H), 4.40 (dd, J = 11.0, 6.0 Hz, 3H), 4.32 (dd, J = 10.0, 5.5 Hz, 4H), 4.07–4.03 (m, 3H), 4.01–3.97 (m, 4H), 3.57–3.42 (m, 902H, PEG-backbone) ppm.; IR (ATR, cm^{-1}): 3501 (w), 2881 (m), 2741 (w), 2696 (w), 2360 (w), 2341 (w), 1977 (w), 1645 (w), 1600 (w), 1581 (w), 1563 (w), 1466 (m), 1406 (w), 1359 (m), 1342 (m), 1279 (m), 1240 (m), 1198 (w), 1145 (m), 1099 (s), 1059 (s), 961 (s), 841 (s), 797 (m), 747 (m), 738 (m), 693 (m), 658 (m).

Tetra-arm PEG-terpyridinyl-*p*-nitrophenylcarbonate (4). Tetra-arm PEG-hydroxy-terpyridine **3** (1.61 g, 0.14 mmol) was dissolved in dry dichloromethane (50 mL). Dry pyridine (0.19 mL, 2.3 mmol) was added to the solution, followed by addition of *p*-nitrophenylchloroformate (0.23 g, 1.2 mmol). The resulting suspension was stirred at room temperature overnight, the precipitate was filtered off, and brine (250 mL) was added to the filtrate. The mixture was extracted with dichloromethane (2 × 300 mL), the organic layer was dried over $MgSO_4$ and then concentrated *in vacuo*. The product was precipitated by pouring the concentrate into cold diethyl ether to obtain the product as a slightly violet solid (1.43 g, 84%). ^{1}H-NMR (DMSO-d_6, 700 MHz): δ = 8.72–8.69 (m, 8H), 8.62–8.60 (m, 8H), 8.35 (s, 2H), 8.29–8.27 (m, 5H), 8.22–8.20 (m, 3H), 8.10 (s, 3H), 8.08 (s, 5H), 8.00 (td, J = 9.1, 2.1 Hz, 8H), 7.96 (s, 1H), 7.52–7.48 (m, 8H), 7.44–7.41 (m, 5H), 7.40–7.38 (m, 3H), 5.67–5.62 (m, 2H), 5.49 (s, 5H), 5.40–5.37 (m, 1H), 5.31–5.28 (m, 2H), 4.92 (dd, J = 15.4, 3.5 Hz, 1H), 4.88–4.83 (m, 4H), 4.78 (dd, J = 14.7, 7.7 Hz, 2H), 3.81 (dd, J = 11.2, 4.2 Hz, 1H), 3.77–3.72 (m, 5H), 3.67–3.65 (dd, J = 10.5, 6.3 Hz, 3H), 3.62–3.59 (m, 8H), 3.53–3.48 (m, 902H, PEG-backbone), 3.44 (s, 8H), 3.41–3.38 (m, 6H) ppm.

Tetra-arm PEG-terpyridinyl-NBD (5). Triethylamine (47 µl, 0.34 mmol) was added to a solution of tetra-arm PEG-terpyridinyl-*p*-nitrophenylcarbonate **4** (0.5 g, 0.042 mmol) in dimethylformamide (5 mL, HPLC grade), followed by addition of (S)-(+)-4-(3-aminopyrrolidino)-7-nitrobenzofurazan (NBD) (0.051 g, 0.20 mmol). The orange mixture was stirred for 1 d at room temperature, purified by dialysis in water, and lyophilized to obtain an orange solid (0.41 g, 83%). The degree of substitution of the chain-end pendant *p*-nitrophenylcarbonate groups by NBD tags was determined to be 97% by UV absorption spectroscopy; in addition, in ^{1}H NMR, the peaks addressable to *p*-nitrophenylcarbonate have disappeared after this conversion. ^{1}H-NMR (DMSO-

d_6, 700 MHz): δ = 8.74–8.65 (m, 8H), 8.64–8.58 (m, 6H), 8.57–8.29 (m, 2H), 8.25–8.15 (m, 2H) 8.1 (d, J = 13.4 Hz, 6H), 8.06–7.94 (m, 10H), 7.55–7.44 (m, 8H), 5.66–5.59 (m, 1H), 5.48–5.44 (m, 3H), 3.54–3.47 (m, 902H, PEG-backbone) ppm.

Forced Rayleigh Scattering Measurements. Preparation of gel samples for diffusion measurements followed a published procedure[3] with minor modifications. First, an appropriate mass of terpyridine end-functionalized four-arm PEG polymers was dissolved in 500 μL of DMF. Separately, $Zn(NO_3)_2 \cdot 6H_2O$ in a 2:1 stoichiometric concentration to the PEG polymer was dissolved in 500 μL of DMF and vortexed to reach complete dissolution of solids. Equal volumes of the two solutions were then combined in an Eppendorf tube and mixed rigorously with a micro spatula to ensure homogenous mixing. The sample was centrifuged at 21,000 ×g for 10 min to remove bubbles. To prepare samples for self-diffusion measurements, 2 mol% of **5** was added and dissolved together with the matrix polymers in the first step. For the samples used in tracer-diffusion measurements, the synthesis method introduced 2 mol% of the NBD labeled tracers in the matrix. Therefore, the concentration of dye labeled polymers was nearly two orders of magnitude lower than the estimated overlap concentration of the star-shaped polymer building block in DMF ($c^* \approx 94$ g L^{-1})[47]. This condition ensures that interactions between tracers could be neglected. Gels were sealed between two quartz disks (17 mm in diameter) separated by a 0.5 mm thick Teflon spacer. Specimens were equilibrated at 25 °C for at least 30 min using a recirculating water bath before further experiments were conducted.

Diffusion of four-arm PEG polymers with a varying number of associating endgroups through the model networks were measured by forced Rayleigh scattering, following the procedure described in a previous publication[48]. Briefly, an amplitude grating of dye concentration was generated by exposing the sample to two coherent laser beams (λ = 488 nm) crossing at an angle

θ. The duration for writing the grating is 500–1,000 ms. This time period is at least an order of magnitude shorter than the diffusion time scales (larger than 10 s) such that the effect of diffusion during writing is negligible. The time-dependent intensity of the diffracted beam was fit to a stretched exponential function, and the average decay time constant $<\tau>$ was calculated as the first moment of the stretched exponential function. Representative decay profiles and fits are shown in Figure B-1.

4.3. Results and Discussion

Observation of anomalous diffusion in four-arm associating PEG star polymers. In this work, Forced Rayleigh scattering is deployed to probe the diffusive motion of four-arm poly(ethylene glycol) (PEG) end-functionalized with terpyridine moieties that form model transient networks by complexation of these motifs to Zn^{2+} in DMF, as shown in Figure 4-1. Inside the networks, a small fraction of the polymers is labeled with the photochromic dye nitrobenzofurazan (NBD), as also shown in Figure 4-1. This configuration is referred to as self-diffusion hereafter (Figure 4-1A). The experimental technique exposes the gel sample to two coherent laser beams at λ = 488 nm intersecting at an angle of θ, creating one-dimensional holographic amplitude gratings of the dye-labeled polymers. The characteristic grating spacing, d, is determined by

$$d = \frac{\lambda}{2\sin(\theta/2)} \tag{4-1}$$

The crossing angle θ is then changed to generate grating spacings in a range of 0.5 to 50 μm, enabling diffusion measurements to be performed at varying length scales over two orders of

magnitude. The initial concentration profile evolves with time due to diffusion, and the decay of the grating can be described by a stretched exponential function (Figure B-1 in the Appendix B),

$$I = \left[A \exp\left(-\frac{t}{\tau} \right)^{\beta} \right]^2 + B \tag{4-2}$$

where A is the grating amplitude, B is the incoherent background, τ is the decay time, and β is the stretched exponent that quantifies a narrow distribution of the relaxation spectrum due to polydispersity. The mean decay relaxation time is then calculated as

$$\langle \tau \rangle = \frac{\tau}{\beta} \Gamma\left(\frac{1}{\beta} \right) \tag{4-3}$$

Experimental results of the mean grating relaxation time, $<\tau>$, with respect to the squared holographic grating spacing, d^2, can be captured by a power-law relation, $<\tau> \sim d^{2\mu}$, where the exponent μ changes with d^2 (Figure 4-2A). For example, gels at 10% (w/v) concentration show an exponent $\mu \approx 1$ at d^2 beyond ca. 400 μm^2. Compared to the power-law exponent α in the common relation of the mean-square displacement vs. time, $<X^2> \sim t^{\alpha}$, μ is the inverse of α. Therefore, a scaling of $<\tau> \sim d^2$ is an evidence of Fickian diffusion ($\alpha = 1$) on these large length scales. In contrast, the scaling exponent μ is less than 1, or equivalently, $\alpha > 1$, at intermediate d^2 ranging from 2 to 100 μm^2. Phenomenologically, this observation can be termed as anomalous diffusion, more specifically, as super-diffusion. At smaller d^2 below 0.5 μm^2, μ increases with decreasing d^2, indicating that on these small length scales the diffusion approaches Fickian scaling again. Qualitatively similar trends are observed for gels at all concentrations investigated up to 30% (w/v). However, with increasing polymer concentration, $<\tau>$ increases, the large-length-scale Fickian diffusion regime starts at a smaller d^2, and the width of the super-diffusive regime narrows.

The previously proposed two-state model fits the anomalous self-diffusion data over the entire range of d^2 (Figure 4-2A), suggesting that this model may be generally applicable to associating polymers. The full model details have been thoroughly described in a previous publication.[48] Briefly, the model hypothesizes that associating polymers are present in the networks at two different states: one diffuses relatively fast and is referred to as the molecular state (although the specific association state of the molecules is not specified by the model), whereas the other has a slower diffusivity and is termed as the associative state. Species interconvert between the molecular and associative states with pseudo first-order kinetics. Based on these assumptions, a set of two-component reaction–diffusion equations governs the diffusion process:

$$\begin{aligned}\frac{\partial C_M}{\partial t} &= D_M \frac{\partial^2 C_M}{\partial x^2} - k_{on} C_M + k_{off} C_A \\ \frac{\partial C_A}{\partial t} &= D_A \frac{\partial^2 C_A}{\partial x^2} + k_{on} C_M - k_{off} C_A\end{aligned} \tag{4-4}$$

where C_M and C_A are the concentrations of the molecular and the associative species (unit: M), D_M and D_A are the diffusivities of the molecular and the associative species (units: $\mu m^2\ s^{-1}$), and k_{on} and k_{off} are the rate constants that characterize the interconversion dynamics (units: s^{-1}). The subscripts M and A are used to denote the molecular and the associative species, respectively. Since the physical details of the two diffusing states are not specified in the model, the interconversion rates k_{on} and k_{off} should not be taken as physical rate constants that are functions of temperature only, but instead, both parameters may have implicit concentration dependence.[48] In addition, an equilibrium constant is defined as $K_{eq} = k_{on}/k_{off}$, and the ratio of the two diffusivities is $\gamma = D_A/D_M$. The relation $\langle\tau\rangle$ vs. d^2 is obtained by analytically solving eq 4 in the Fourier space.[48] The model provides an excellent fit across a wide range of concentration for the star-shaped associative polymers (Figure 4-2A).

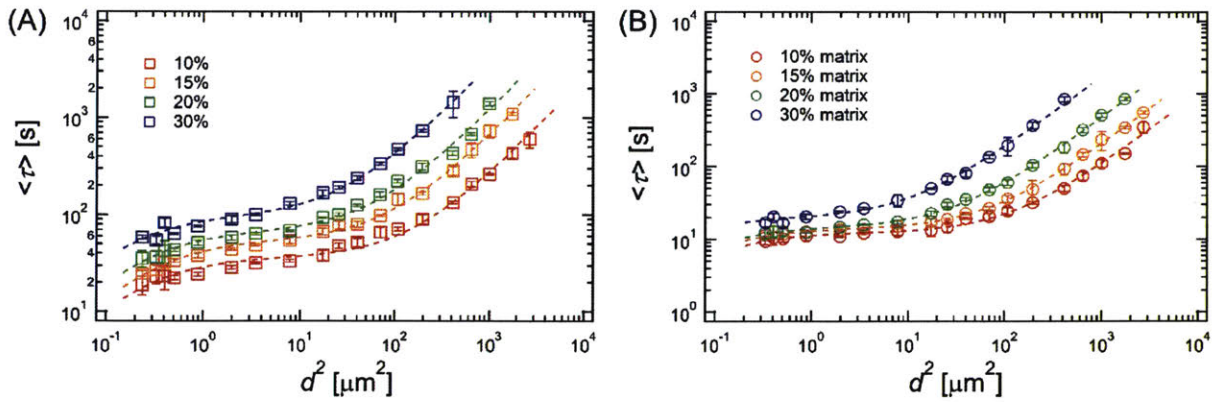

Figure 4-2. Relation of mean decay relaxation times $\langle\tau\rangle$ vs. the squared holographic grating spacing d^2 for self-diffusion (A) and tracer diffusion (B) (acc. to Figure 4-1A and B) of associating star-shaped polymers in model transient networks based on four-arm PEG end-capped with terpyridines and complexed to Zn^{2+} ions at a ratio of 2:1 in DMF. All measurements were performed at 25 °C. Error bars represent one standard deviation based upon measurement in triplicate. Dashed lines are fits to the two-state model.

Anomalous self-diffusion of star-shaped polymers in these model transient networks resembles findings from hydrogels formed by linear proteins with associating coiled-coil domains[48]. However, the supramolecular metallogels in this work have a drastically different molecular architecture (star-shaped vs. linear), sticker chemistry (metal–ligand complexation vs. associating protein domains), sticker valency (divalent vs. pentavalent), sticker position (chain-end vs. side-group), and solvent environment (polar organic solvent DMF vs. aqueous buffer) than the coiled-coil protein gels. This circumstance suggests that the relevant physics of anomalous diffusion does not depend on fine chemical or structural details of the associating polymers in the networks.

In addition to the diffusion of four-arm PEG polymers where each arm has an associative group, for comparison, the diffusion of four-arm PEG where only three arms have associating groups (Figure 4-1B; tracer diffusion as opposed to self-diffusion) in the same model transient networks is also investigated (Figure 4-1B). Consideration of this sort of tracer diffusion is interesting because the number of associating arms on the labeled polymers differs, but the matrixes are essentially identical. These tracer diffusion experiments also allow quantitative comparison of two experimental techniques to probe diffusion, forced Rayleigh scattering used in this study and fluorescence recovery after photobleaching used in previous work[47]. The concentration of tracers in the tracer diffusion experiments is fixed at 2 mol% of the total polymer, and it is two orders of magnitude lower than the overlap concentration.[3] Therefore, the transient network is minimally perturbed on length scales larger than the radius gyration (R_g) of the tracer, and there are negligible tracer-tracer interactions.

Analogous to the observations from self-diffusion measurements, the overall relation $<\tau>$ vs. d^2 in the case of tracer diffusion is comprised of a Fickian diffusive regime at large length scales and an anomalous diffusion regime in the intermediate range of d^2 (Figure 4-2B). Compared to the self-diffusion measurements at the same matrix concentration, $<\tau>$ is consistently smaller in the tracer diffusion measurements due to fewer associating interactions with the surrounding network. For the tracer diffusion measurements, the two-state model also provides an excellent fit to the observed diffusion data (Figure 4-2B). However, the anomalous diffusive regime is only observed when the characteristic time and length scales are accessible with the experimental technique employed. For instance, when similar tracer diffusion measurements were performed by photobleaching techniques starting with an initial Gaussian profile with an $e^{-1/2}$ radius of ca. 5 μm, only Fickian diffusion was observed.[47]

For both the self- and the tracer diffusion measurements, three derivative model parameters are extracted from nonlinear fitting of the data to the two-state model: the effective diffusivity in the large-length-scale Fickian regime, $D_{M,eff}$ [equivalent to $D_M/(1 + K_{eq})$ under the condition of $\gamma K_{eq} << 1$ when anomalous diffusion is observed], the molecular dissociation rate constant, k_{off}, and the anomaly index, γK_{eq} (equivalent to the combined ratio of the two diffusivities and rate constants, $D_A/D_M \cdot k_{on}/k_{off}$). The values of these fitting parameters are compared in Figure 4-3.

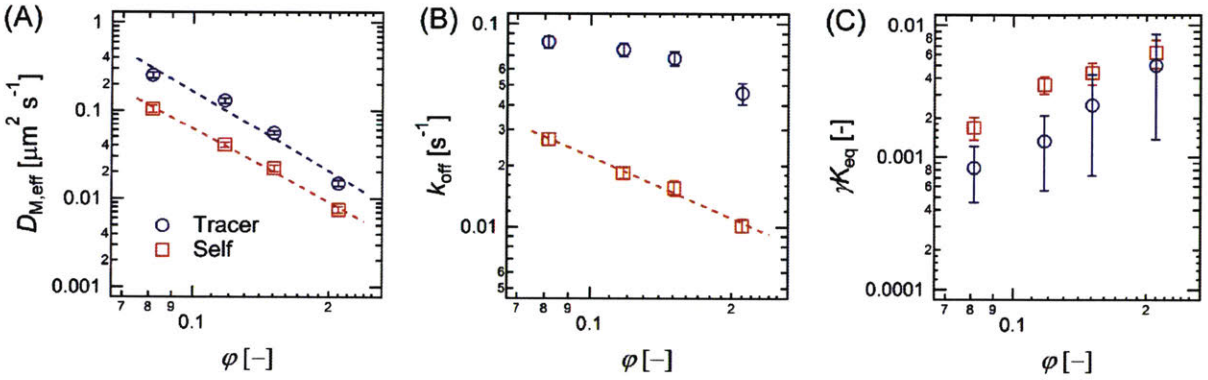

Figure 4-3. Concentration dependencies of (A) the effective diffusivity in the large-length-scale Fickian regime $D_{M,eff}$, (B) the molecular dissociation rate k_{off}, and (C) γK_{eq} in self-diffusion (red squares) and tracer diffusion (blue circles). All parameters were obtained by fitting the analytical solution of the two-state model to the experimentally derived relation $<\tau>$ vs. d^2 at varying gel concentrations. The dashed lines show power-law trends as described in the text.

Interpretation of the Two-State Model Parameters. The diffusion coefficients on the large length scales $D_{M,eff}$ strongly depend on the polymer concentration, and this concentration scaling agrees with the predictions from the sticky Rouse theory. The effective diffusion coefficients $D_{M,eff}$ can also be simply obtained from the data in the Fickian regime by linear regression using

$$D_{\mathrm{M,eff}} = \frac{d^2}{4\pi^2 \langle \tau \rangle}. \tag{4-5}$$

For self-diffusion, $D_{\mathrm{M,eff,self}}$ ranges from 1.05×10^{-1} to 7.52×10^{-3} $\mu m^2\ s^{-1}$ (Figure 4-3A). The concentration dependence of $D_{\mathrm{M,eff,self}}$ can be captured by a power-law scaling of $D_{\mathrm{M,eff,self}} \sim \varphi^{-2.8\pm0.5}$, where φ is the volume fraction of polymers in the gels (see calculation in Appendix B) and the error bar represents a 95% confidence interval (Figure 4-3A). This scaling is in excellent quantitative agreement with the sticky Rouse model[16-18], which predicts $D \sim \varphi^{-3}$ in the concentration regime $\varphi_s < \varphi < \varphi_e$. The concentrations of the model transient networks in this manuscript (φ = 0.081, 0.12, 0.15, and 0.21) are mostly above the overlap concentration of the segment between two stickers ($\varphi_s \approx 0.089$), but below the entanglement concentration ($\varphi_e \approx 0.44$) (see calculation details in Appendix B). Therefore, theoretical approaches for the entanglement regime are not applicable.[19, 37] While the sticky Rouse theory has mostly been used to describe linear polymers with associating side groups at regular spacing[35, 51, 52], the phenomenology appears to be successful in describing associating systems of other polymer architectures and junction positions considered here. Like the linear chains originally considered in the sticky Rouse theory, the faster dynamic modes of the four-arm PEG chains are affected by the presence of associating groups, resulting in strong similarities regardless of differences in chain topology and sticker position. However, as in most other studies of gels,[17, 25, 47, 48] the concentration range covered in this work is less than a decade and may therefore not be wide enough to clearly establish a true scaling regime. As a result, there are inevitable uncertainties in calculating scaling exponents. Nonetheless, estimation of the average scaling exponent is still valuable for comparing experimental results to theoretical models.

Compared to the previously studied multiblock pentavalent coiled-coil proteins[48] that show $D_{M,eff,self} \sim \varphi^{-6\pm1}$, the concentration effect is less pronounced in the supramolecular metallogels. The reasons are two-fold. First, the terpyridine–Zn^{2+} complexes have a smaller coordination number compared to the coiled-coil proteins (2 vs. 5). Second, the sticky Rouse theory predicts that the polymer diffusivity in transient gels in the concentration range of $\varphi_s < \varphi < \varphi_e$ should have a weaker concentration dependence than that in gels in the regime of $\varphi_{ren} < \varphi < \varphi_s$ (where φ_{ren} is the characteristic concentration at which sticker association transitions from intra-molecular dominating to inter-molecular dominating, and φ_s is the overlap concentration of segments between two stickers); the scaling exponents in $D_{M,eff,self}$ vs. φ in these two regimes are –3 and –5.19, respectively[16, 17, 46]. Therefore, the metallogels studied in this work located in $\varphi_s < \varphi < \varphi_e$ exhibit diffusivities less strongly affected by the polymer concentration than that of the protein gels in $\varphi_{ren} < \varphi < \varphi_s$.

The effective tracer diffusivities in the large d^2 Fickian regime, $D_{M,eff,tracer}$, are slightly larger than the self-diffusivities at the same matrix concentration (Figure 4-3A). This can be attributed to the lesser number of associative interactions between the 3-associating-arm tracers and the surrounding matrix in the tracer diffusion measurements. The concentration dependence of tracer diffusivities can be moderately captured by a scaling of $D_{M,eff,tracer} \sim \varphi^{-3\pm2}$. The mean estimate of the power-law exponent –3 is close to that in self-diffusion, –2.8, and it is also in good agreement with the prediction of the sticky Rouse model. However, this close agreement of the scaling exponents does not imply that the sticky Rouse model can perfectly describe the all dynamic features of the four-arm associating polymers. For example, the model predicts that the chain diffusivity scales inversely proportional to the square of the number of stickers,[17] which leads to a prediction of the diffusivity ratio $D_{M,eff,tracer}/D_{M,eff,self} = (4/3)^2 \approx 1.8$. This predicted value,

however, is slightly smaller than the experimentally derived results ranging from 2.0 to 3.2 (Figure 4-3A). The discrepancy is understandable, because the sticky Rouse theory is strictly valid only for linear chains with a large number of stickers separated by segments of a high degree of polymerization; these characteristics are absent in the four-arm associating polymers.

Both tracer and self-diffusion are much slower than that of an unassociating four-arm PEG through the associating polymer matrix (see more details in Appendix B and Figure B-2). The values of D_M are obtained from linear regressions of slope 1 in the relation $\log \langle \tau \rangle \sim \log d^2$, which are 10.2 ± 0.2 and 4.55 ± 0.09 $\mu m^2 s^{-1}$ for diffusion in the matrix at concentrations of 20 and 30% (w/v), respectively. The estimates of D_M are over two orders of magnitude larger than the corresponding effective diffusion coefficients in both cases of self- and tracer diffusion. This comparison is consistent with the fact that associating groups drastically reduce the mobility of polymers.

While both forced Rayleigh scattering (FRS) and fluorescence recovery after photobleaching (FRAP) uncover Fickian diffusion on the large length scales, the diffusion coefficients determined by FRAP[47] are larger than the ones obtained by FRS and show a weaker concentration dependence of just $D_{M,eff,tracer} \sim c^{-1}$. This discrepancy could be attributed to the differences in the length and time scales probed by two different experimental techniques. In FRAP, the initial feature size is located in the regime where the Fickian behavior is nearly but not completely developed (see Figure4- 2B). Therefore, the diffusivities measured from FRAP are bigger than the ones measured by FRS and have a weaker concentration dependence. In addition, according to the two-state model, relaxation of the imposed concentration gradient exhibits two decay processes, and their characteristic time constants differ significantly.[48] While FRS mainly

detects the large time constant, the acquisition times in FRAP measurements are relatively short and might be more sensitive to the fast decay process.

The molecular dissociation rate k_{off} is influenced by the sticker valency and the sticker density of the associating polymers (tracer vs. self-diffusion in Figure 4-1). k_{off} is of fundamental importance because it characterizes the rate at which molecules dynamically convert from the associative to the molecular state. Because the associative and molecular states are not specifically defined in the two state model, k_{off} is neither a molecular dissociation rate nor a bond dissociation rate. Instead, it is the phenomenological rate of conversion between the two apparent diffusing species postulated by the model. The inverse of k_{off}, or the dissociation time τ_d, locates the center of the super-diffusion regime. For self-diffusion in the supramolecular networks in this study, the values of $k_{off,self}$ are in the range from 2.71×10^{-2} to 1.02×10^{-2} s^{-1} and decrease with increasing polymer concentration (Figure 4-3B). Similar to the results shown here, a concentration dependent $k_{off,self}$ was previously observed in coiled-coil protein gels.[48] The magnitude of the scaling exponent in the relation $k_{off,self} \sim \varphi^{-1.0\pm0.3}$ for the present set of supramolecular metallogels is smaller than that observed in the coiled-coil protein gels[48] (–1.57). This finding shows that $k_{off,self}$ is less affected by concentration in the metallogels, possibly due to a lower sticker valency in the terpyridine–Zn^{2+} complexes compared to the pentameric coiled-coil bundles. In addition, $k_{off,tracer}$ remains larger than $k_{off,self}$ at all matrix concentrations (Figure 4-3B), suggesting that the conversion rate from the associative to the molecular state for the 3-associating-arm tracers is faster. Due to a lower sticker density per polymer chain in the case of tracer diffusion, $k_{off,tracer}$ should be less dependent on the matrix concentration in comparison to $k_{off,self}$. It is also observed that $k_{off,tracer}$ does not follow an empirical power-law scaling; the exponent in fitting $k_{off,tracer}$ vs. φ to a power-law function has a large uncertainty, -0.6 ± 0.7. However, the reason behind this

phenomenon is not well understood. It is possibly due to some inherent errors in extracting $k_{off,self}$ when the small-length-scale Fickian regime is not experimentally accessible.

The inverse of $k_{off,self}$, or $\tau_{d,self}$, is at least one order of magnitude larger than τ_{ex}, the characteristic time constant of sticker exchange between junctions (Figure 4-4A). Here, τ_{ex} is defined as $2\pi/\omega_c$, where ω_c is the *G'–G"* (storage modulus–loss modulus) crossover frequency from frequency sweep measurements (Figure 4-4B). It is hypothesized that the process in which molecules covert from the associative to the molecular states involves participation of more stickers per chain in comparison to the case of sticker exchange between junctions. The junction lifetime shows a concentration scaling of $\tau_{ex} \sim \varphi^{0.2\pm0.1}$, and the scaling exponent is close to the predicted value of 0.17 from the sticky Rouse theory.[16] In addition, the numerical difference between $\tau_{d,self}$ and τ_{ex} increases with concentration. For gels at 30% (w/v), $\tau_{d,self}$ and τ_{ex} differ by more than one order of magnitude. A separation of the two time scales demands more than one Maxwell mode to completely describe the rheological relaxation over the entire frequency window (Figure B-4). This phenomenology is similar to the sticky Rouse model where the presence of stickers delays the Rouse relaxation and the terminal relaxation, thereby effectively introducing new relaxation modes.[35]

The fact that the concentration dependencies of the τ_{ex} and $\tau_{d,self}$ follow two different power-law scalings indicates that $\tau_{d,self}$ may not be the appropriate frequency scaling factor to collapse the shear rheology data of the metallogels in the concentration regime $\varphi_s < \varphi < \varphi_e$. As demonstrated in many studies, network relaxation in the high-frequency regime is governed by the rate of junction exchange, which is mediated by the dissociation of stickers.[48, 51, 53, 54] In the previous investigation on unentangled coiled-coil protein gels in the concentration regime of $\varphi_{ren} < \varphi < \varphi_s$, τ_{ex} and $\tau_{d,self}$ followed the same concentration dependence. This enabled the use of $\tau_{d,self}$, or $k_{off,self}$,

to rescale the frequency response to yield collapsed shear rheology master curves, which was termed as time–concentration superposition.[48] However, such coincidence may not hold outside the concentration regime of $\varphi_{ren} < \varphi < \varphi_s$. The exponent in the scaling of τ_d with φ is often larger than the exponent in the scaling of τ_{ex} with φ, due to the difference in the number of stickers participating in the two processes and/or the cooperative effect between stickers. The largest possible exponent in the scaling τ_{ex} vs. φ is obtained when the concentration effect on junction lifetime is the most pronounced. This is observed in the regime of $\varphi_{ren} < \varphi < \varphi_s$, where junctions are transitioning from intra- to inter-molecular based association.[16] However, in this study, the concentrations of metallogels are mostly above φ_s, and the junction lifetime exhibits a weaker concentration scaling than τ_d. Therefore, τ_d overestimates the concentration effect on τ_{ex} and does not yield perfect renormalization of the time-dependent materials properties (Figure 4-4B and B-3).

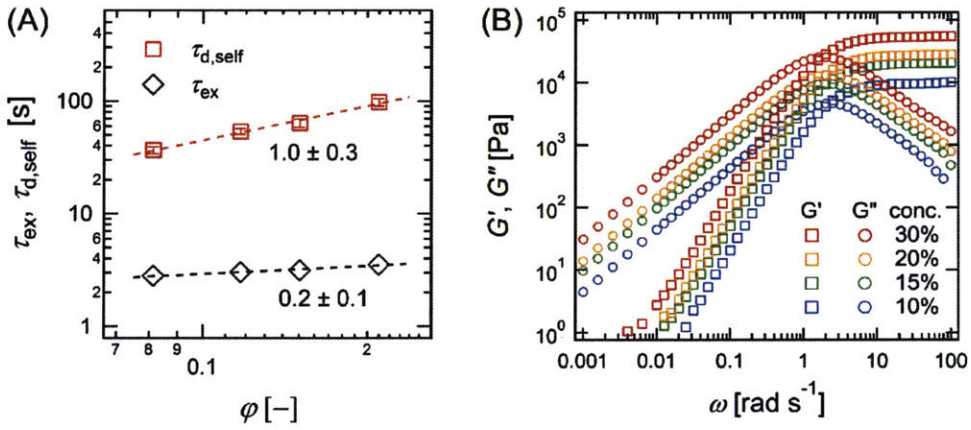

Figure 4-4. (A) Comparison of the junction exchange time constant τ_{ex} (black diamonds) and the molecular dissociation time $\tau_{d,self}$ (red squares) at different gel concentrations. The scaling exponents shown in the figure are reported as 95% confidence intervals. (B) Frequency sweeps of the model transient network at 25 °C.

The product γK_{eq} also depends on the matrix concentration and the number of sticky groups on the labeled star-shaped polymers (Figure 4-3C). It has been shown previously that the product γK_{eq} quantifies the extent of anomalous diffusion because it defines the separation distance between the two Fickian regimes.[48] A larger value of γK_{eq} correlates with a narrower phenomenological super-diffusive regime and a steeper slope of the power-law curve in the super-diffusive regime, as also observed in our present experiments (Figures 4-2A, B). Consistent with the previous observation in the coiled-coil protein gel system,[48] γK_{eq} increases with concentration. Since γK_{eq} can be recast as $D_A/D_{M,eff}$, it suggests that the difference of apparent mobilities of molecules in the associative and the molecular states becomes smaller with increasing concentration. In addition, the estimated values of γK_{eq} from the self-diffusion measurements are all larger than those from the tracer diffusion measurements. This difference suggests that changes in the mobility of molecules upon association are less pronounced in the case of tracer diffusion. The associated errors of γK_{eq} in tracer diffusion are significantly larger, mainly because the onset of the small d^2 Fickian cannot be clearly resolved in this case.

4.4. Conclusions

Self-diffusion of star-shaped PEG polymers in model transient networks formed by complexation of chain-capping terpyridine motifs to Zn^{2+} ions was probed by forced Rayleigh scattering over a large window of squared length scales. Observed grating relaxation times as a function of the squared grating size show a Fickian diffusive regime at large length scales, a phenomenological super-diffusive regime at intermediate length scales, and a second Fickian regime on small length scales that are still larger than the radius gyration of the associating polymers. Qualitatively similar behavior is observed in a tracer-diffusion variant of these studies,

realized by the same star-shaped polymers with a reduced number of associating endgroups. Experimental results both these different sets of diffusion measurements are quantitatively captured by our previously-developed two-state model, which postulates that molecules in the gel are in either a high-mobility state or a low-mobility state that dynamically interconvert. On large length scales, chain diffusion is hindered by the association–dissociation kinetics between the macromolecules and the surrounding associating network. The concentration scalings of the diffusivities in the self- and tracer diffusion measurements both follow the prediction from the sticky Rouse theory. Complemented by previous observations of anomalous diffusion in other systems, these findings suggest that anomalous diffusion should be a prevalent phenomenon in a wide variety of associating networks, despite differences in the polymer architecture and the chemical structure of associating bonds. It is anticipated that the four-arm associating polymers studied in this work can serve as a simple yet general model for further theory and modeling efforts to interrogate the physical origins of the two mobility states in transient networks.

4.5. References

1. Holten-Andersen, N.; Harrington, M. J.; Birkedal, H.; Lee, B. P.; Messersmith, P. B.; Lee, K. Y. C.; Waite, J. H. Ph-Induced Metal-Ligand Cross-Links Inspired by Mussel Yield Self-Healing Polymer Networks with near-Covalent Elastic Moduli. *Proceedings of the National Academy of Sciences* 2011, 108, 2651-2655.

2. Burnworth, M.; Tang, L.; Kumpfer, J. R.; Duncan, A. J.; Beyer, F. L.; Fiore, G. L.; Rowan, S. J.; Weder, C. Optically Healable Supramolecular Polymers. *Nature* 2011, 472, 334-337.

3. Rossow, T.; Seiffert, S. Supramolecular Polymer Gels with Potential Model-Network Structure. *Polymer Chemistry* 2014, 5, 3018-3029.

4. Zhou, Z.; Yan, X.; Cook, T. R.; Saha, M. L.; Stang, P. J. Engineering Functionalization in a Supramolecular Polymer: Hierarchical Self-Organization of Triply Orthogonal Non-Covalent

Interactions on a Supramolecular Coordination Complex Platform. *Journal of the American Chemical Society* 2016, 138, 806-809.

5. Cordier, P.; Tournilhac, F.; Soulie-Ziakovic, C.; Leibler, L. Self-Healing and Thermoreversible Rubber from Supramolecular Assembly. *Nature* 2008, 451, 977-980.

6. Guo, M.; Pitet, L. M.; Wyss, H. M.; Vos, M.; Dankers, P. Y. W.; Meijer, E. W. Tough Stimuli-Responsive Supramolecular Hydrogels with Hydrogen-Bonding Network Junctions. *Journal of the American Chemical Society* 2014, 136, 6969-6977.

7. Appel, E. A.; Forster, R. A.; Koutsioubas, A.; Toprakcioglu, C.; Scherman, O. A. Activation Energies Control the Macroscopic Properties of Physically Cross-Linked Materials. *Angewandte Chemie International Edition* 2014, 53, 10038-10043.

8. Harada, A.; Kobayashi, R.; Takashima, Y.; Hashidzume, A.; Yamaguchi, H. Macroscopic Self-Assembly through Molecular Recognition. *Nat Chem* 2011, 3, 34-37.

9. Cromwell, O. R.; Chung, J.; Guan, Z. Malleable and Self-Healing Covalent Polymer Networks through Tunable Dynamic Boronic Ester Bonds. *Journal of the American Chemical Society* 2015, 137, 6492-6495.

10. Brooks, W. L. A.; Sumerlin, B. S. Synthesis and Applications of Boronic Acid-Containing Polymers: From Materials to Medicine. *Chemical Reviews* 2016, 116, 1375-1397.

11. Lin, F.; Yu, J.; Tang, W.; Zheng, J.; Defante, A.; Guo, K.; Wesdemiotis, C.; Becker, M. L. Peptide-Functionalized Oxime Hydrogels with Tunable Mechanical Properties and Gelation Behavior. *Biomacromolecules* 2013, 14, 3749-3758.

12. McKinnon, D. D.; Domaille, D. W.; Cha, J. N.; Anseth, K. S. Bis-Aliphatic Hydrazone-Linked Hydrogels Form Most Rapidly at Physiological Ph: Identifying the Origin of Hydrogel Properties with Small Molecule Kinetic Studies. *Chemistry of Materials* 2014, 26, 2382-2387.

13. Barcan, G. A.; Zhang, X.; Waymouth, R. M. Structurally Dynamic Hydrogels Derived from 1,2-Dithiolanes. *Journal of the American Chemical Society* 2015, 137, 5650-5653.

14. Green, M. S.; Tobolsky, A. V. A New Approach to the Theory of Relaxing Polymeric Media. *The Journal of Chemical Physics* 1946, 14, 80-92.

15. Tanaka, F.; Edwards, S. F. Viscoelastic Properties of Physically Crosslinked Networks. 1. Transient Network Theory. *Macromolecules* 1992, 25, 1516-1523.

16. Rubinstein, M.; Semenov, A. N. Thermoreversible Gelation in Solutions of Associating Polymers. 2. Linear Dynamics. *Macromolecules* 1998, 31, 1386-1397.

17. Rubinstein, M.; Semenov, A. N. Dynamics of Entangled Solutions of Associating Polymers. *Macromolecules* 2001, 34, 1058-1068.

18. Leibler, L.; Rubinstein, M.; Colby, R. H. Dynamics of Reversible Networks. *Macromolecules* 1991, 24, 4701-4707.

19. Cates, M. E. Reptation of Living Polymers: Dynamics of Entangled Polymers in the Presence of Reversible Chain-Scission Reactions. *Macromolecules* 1987, 20, 2289-2296.

20. Tripathi, A.; Tam, K. C.; McKinley, G. H. Rheology and Dynamics of Associative Polymers in Shear and Extension: Theory and Experiments. *Macromolecules* 2006, 39, 1981-1999.

21. Sing, M. K.; Wang, Z.-G.; McKinley, G. H.; Olsen, B. D. Celebrating Soft Matter's 10th Anniversary: Chain Configuration and Rate-Dependent Mechanical Properties in Transient Networks. *Soft Matter* 2015, 11, 2085-2096.

22. Suzuki, S.; Uneyama, T.; Watanabe, H. Concentration Dependence of Nonlinear Rheological Properties of Hydrophobically Modified Ethoxylated Urethane Aqueous Solutions. *Macromolecules* 2013, 46, 3497-3504.

23. Blaiszik, B. J.; Kramer, S. L. B.; Olugebefola, S. C.; Moore, J. S.; Sottos, N. R.; White, S. R. Self-Healing Polymers and Composites. *Annual Review of Materials Research* 2010, 40, 179-211.

24. Zhang, Y.; Yang, B.; Zhang, X.; Xu, L.; Tao, L.; Li, S.; Wei, Y. A Magnetic Self-Healing Hydrogel. *Chemical Communications* 2012, 48, 9305-9307.

25. Tang, S.; Glassman, M. J.; Li, S.; Socrate, S.; Olsen, B. D. Oxidatively Responsive Chain Extension to Entangle Engineered Protein Hydrogels. *Macromolecules* 2014, 47, 791-799.

26. Seiffert, S.; Sprakel, J. Physical Chemistry of Supramolecular Polymer Networks. *Chemical Society Reviews* 2012, 41, 909-930.

27. Weingarten, A. S.; Kazantsev, R. V.; Palmer, L. C.; Fairfield, D. J.; Koltonow, A. R.; Stupp, S. I. Supramolecular Packing Controls H2 Photocatalysis in Chromophore Amphiphile Hydrogels. *Journal of the American Chemical Society* 2015, 137, 15241-15246.

28. Webber, M. J.; Appel, E. A.; Meijer, E. W.; Langer, R. Supramolecular Biomaterials. *Nat Mater* 2016, 15, 13-26.

29. Rosales, A. M.; Anseth, K. S. The Design of Reversible Hydrogels to Capture Extracellular Matrix Dynamics. *Nature Reviews Materials* 2016, 1, 15012.

30. Ma, M.; Guo, L.; Anderson, D. G.; Langer, R. Bio-Inspired Polymer Composite Actuator and Generator Driven by Water Gradients. *Science* 2013, 339, 186-189.

31. Weinbreck, F.; Rollema, H. S.; Tromp, R. H.; de Kruif, C. G. Diffusivity of Whey Protein and Gum Arabic in Their Coacervates. *Langmuir* 2004, 20, 6389-6395.

32. Gilbert, J. B.; Rubner, M. F.; Cohen, R. E. Depth-Profiling X-Ray Photoelectron Spectroscopy (Xps) Analysis of Interlayer Diffusion in Polyelectrolyte Multilayers. *Proceedings of the National Academy of Sciences* 2013, 110, 6651-6656.

33. Tang, S.; Olsen, B. Controlling Topological Entanglement in Engineered Protein Hydrogels with a Variety of Thiol Coupling Chemistries. *Frontiers in Chemistry* 2014, 2.

34. Stukalin, E. B.; Cai, L.-H.; Kumar, N. A.; Leibler, L.; Rubinstein, M. Self-Healing of Unentangled Polymer Networks with Reversible Bonds. *Macromolecules* 2013, 46, 7525-7541.

35. Chen, Q.; Tudryn, G. J.; Colby, R. H. Ionomer Dynamics and the Sticky Rouse Modela). *Journal of Rheology* 2013, 57, 1441-1462.

36. De Greef, T. F. A.; Smulders, M. M. J.; Wolffs, M.; Schenning, A. P. H. J.; Sijbesma, R. P.; Meijer, E. W. Supramolecular Polymerization. *Chemical Reviews* 2009, 109, 5687-5754.

37. Odian, G. G. *Principles of Polymerization.* 4th ed.; Wiley-Interscience: Hoboken, N.J., 2004; p xxiv, 812 p.

38. McLeish, T. C. B. Tube Theory of Entangled Polymer Dynamics. *Advances in Physics* 2002, 51, 1379-1527.

39. Semenov, A. N.; Rubinstein, M. Thermoreversible Gelation in Solutions of Associative Polymers. 1. Statics. *Macromolecules* 1998, 31, 1373-1385.

40. Semenov, A. N.; Rubinstein, M. Dynamics of Entangled Associating Polymers with Large Aggregates. *Macromolecules* 2002, 35, 4821-4837.

41. Cates, M. E.; Candau, S. J. Statics and Dynamics of Worm-Like Surfactant Micelles. *Journal of Physics: Condensed Matter* 1990, 2, 6869.

42. Rao, B.; Uemura, Y.; Dyke, L.; Macdonald, P. M. Self-Diffusion Coefficients of Hydrophobic Ethoxylated Urethane Associating Polymers Using Pulsed-Gradient Spin-Echo Nuclear Magnetic Resonance. *Macromolecules* 1995, 28, 531-538.

43. Joabsson, F.; Nydén, M.; Thuresson, K. Temperature-Induced Fractionation of a Quasi-Binary Self-Associating Polymer Solution. Λ Phase Behavior and Polymer Self-Diffusion Investigation. *Macromolecules* 2000, 33, 6772-6779.

44. Walderhaug, H.; Hansen, F. K.; Abrahmsen, S.; Persson, K.; Stilbs, P. Associative Thickeners: Nmr Self-Diffusion and Rheology Studies of Aqueous Solutions of Hydrophobically Modified Poly(Oxyethylene) Polymers. *The Journal of Physical Chemistry* 1993, 97, 8336-8342.

45. Haino, T.; Watanabe, A.; Hirao, T.; Ikeda, T. Supramolecular Polymerization Triggered by Molecular Recognition between Bisporphyrin and Trinitrofluorenone. *Angewandte Chemie International Edition* 2012, 51, 1473-1476.

46. Hackelbusch, S.; Rossow, T.; van Assenbergh, P.; Seiffert, S. Chain Dynamics in Supramolecular Polymer Networks. *Macromolecules* 2013, 46, 6273-6286.

47. Rossow, T.; Habicht, A.; Seiffert, S. Relaxation and Dynamics in Transient Polymer Model Networks. *Macromolecules* 2014, 47, 6473-6482.

48. Tang, S.; Wang, M.; Olsen, B. D. Anomalous Self-Diffusion and Sticky Rouse Dynamics in Associative Protein Hydrogels. *Journal of the American Chemical Society* 2015, 137, 3946-3957.

49. Constable, E. C. The Coordination Chemistry of 2,2′:6′,2″-Terpyridine and Higher Oligopyridines. In *Advances in Inorganic Chemistry*, Emeléus, H. J., Ed. Academic Press: 1986; Vol. Volume 30, pp 69-121.

50. Schubert, U. S.; Eschbaumer, C. Macromolecules Containing Bipyridine and Terpyridine Metal Complexes: Towards Metallosupramolecular Polymers. *Angewandte Chemie International Edition* 2002, 41, 2892-2926.

51. Lewis, C. L.; Stewart, K.; Anthamatten, M. The Influence of Hydrogen Bonding Side-Groups on Viscoelastic Behavior of Linear and Network Polymers. *Macromolecules* 2014, 47, 729-740.

52. Spruijt, E.; Cohen Stuart, M. A.; van der Gucht, J. Linear Viscoelasticity of Polyelectrolyte Complex Coacervates. *Macromolecules* 2013, 46, 1633-1641.

53. Yount, W. C.; Loveless, D. M.; Craig, S. L. Small-Molecule Dynamics and Mechanisms Underlying the Macroscopic Mechanical Properties of Coordinatively Cross-Linked Polymer Networks. *Journal of the American Chemical Society* 2005, 127, 14488-14496.

54. Fullenkamp, D. E.; He, L.; Barrett, D. G.; Burghardt, W. R.; Messersmith, P. B. Mussel-Inspired Histidine-Based Transient Network Metal Coordination Hydrogels. *Macromolecules* 2013, 46, 1167-1174.

Chapter 5 Relaxation Processes in Supramolecular Metallogels Based on Histidine-Nickel Coordination Bonds

Adapted from a manuscript to be submitted to *Macromolecules*.

Understanding the quantitative relationship between the dynamic mechanical properties of associating polymer networks and the dynamics of sticker bonds represents an important problem in polymer science because materials mechanics are affected by not only the sticker bond chemistry but also the sticker position, the polymer structure and the physical environment of associating polymers such as concentration and solvent quality. In this study, associating networks formed by structurally well-defined linear poly(*N*,*N*-dimethylacrylamide) polymers with histidine side groups in complexation with Ni^{2+} ions are chosen as a model system. "Sticker diffusion and dissociation spectrometry" is developed as a new method to quantify the dissociation dynamics of stickers within the network environment where the stickers are covalently attached to polymers above their overlap concentration. The estimated time constants for junction dissociation in gels are shown to be substantially different than the ones measured by metal exchange experiments on small-molecule junctions in the dilute solution limit. Additionally, the in-gel dissociation time constants exhibit the same temperature dependence as the network relaxation times inferred from rheological characterization, which serves as the basis for time-temperature superposition, provided that the network relaxation is governed by the dissociation kinetics of stickers. Furthermore, self-diffusion of these associating polymers is probed by forced Rayleigh scattering, and pure Fickian diffusive behavior is revealed. The characteristic time constants for all the explored dynamic processes are finally viewed in the superimposed frequency sweep spectrum,

demonstrating the inherent hierarchical relaxation in associating polymer networks even with only a single type of junction functionality.

5.1. Introduction

Associating polymers are an important class of materials that can be tailored for a variety of applications such as self-healing materials[1-4], biomaterials[5-7], rheological modifiers[8-10], sensors[11], actuators[12], and biological filters[13]. Above the percolation threshold, a single-phase associating network is formed.[14] The reversible nature of the associating bonds (sometimes referred to as stickers) allows dynamic rearrangement of the network structure. This feature distinguishes associating networks from their permanent chemically crosslinked counterparts and also gives rise to their time-dependent mechanical properties.[15-20] Understanding the relaxation mechanisms of associating networks on time scales relevant to materials applications is central to control materials properties and therefore represents a classical problem in polymer physics.[18, 20-24]

On time scales comparable to the lifetime of an associative bond, relaxation of transient networks is mainly governed by the kinetics of bond exchange, provided that other relaxation time scales such as the chain Rouse time are well separated from the bond lifetime.[4, 15, 18-20, 22, 23, 25-28] Pioneering work by Craig and coworkers measured the exchange rates of various pincer–pyridine complexes in dilute solution using NMR spectroscopy, which yielded a master flow curve by normalizing the shear rate and viscosity using the junction dissociation rate.[23, 25] Shen *et al.* measured the exchange rate of coiled-coils in fluorescence quenching experiments and found a qualitative correlation between the sticker exchange time and the longest relaxation time of coiled-coil hydrogels derived from macroscopic creep tests.[26] Similar observation was also found in star-

shaped poly(ethylene glycol) hydrogels based on reversible hydrazone junctions[27] or bis-histidine-nickel coordination bonds[28]. Furthermore, Guan and coworkers demonstrated that the self-healing kinetics of bulk solid materials could be varied greatly by controlling the exchange rates of dynamic junctions.[4] While all of these experimental investigations support the idea that the junction exchange kinetics governs the relaxation of physical networks on time scales in the vicinity of the junction lifetime, it remains unclear how junction relaxation quantitatively relates to the rate of network relaxation. Because the junction dynamics in networks are often approximated with the dynamics measured in dilute solutions[4, 23, 26, 27], the actual chemical and physical environments of the associating motifs are not captured, making quantitative matching difficult. Within the associating networks, the associating domains are covalently linked to polymers that are above their overlap concentration. Neglecting the effects of chain connectivity, cooperativity among junctions, and polymer concentrations can lead to conflicting conclusions.[19, 25, 29, 30] Moreover, the aforementioned strategies of estimating bond lifetime cannot explain its dependence on polymer concentration, a phenomenon commonly found in physical gels both theoretically[22, 30] and experimentally[18, 19, 24, 31-33].

In the long-time limit, network viscoelasticity and chain self-diffusion (i.e., the diffusive motion of polymer chains that form the associating networks) originate from the same molecular mechanisms.[24, 31, 34] The common origins of both dynamic processes allows knowledge gained through studies of diffusion to be applied to better understand mechanical relaxation of materials. For example, it has been demonstrated that hindered self-diffusion of unentangled associative polymers is directly related to the sticky Rouse relaxation shown in the rheological characterization of materials and a delayed entrance to the terminal regime.[24, 35] Due to the existence of the sticky Rouse relaxation, at least two Maxwell modes are typically required to completely describe the

rheological response of associating networks over a wide frequency window.[24, 35, 36] One Maxwell mode corresponds to the dynamics of the associative junctions only, and the other is related to hindered chain diffusion. The latter can be further tuned by increasing the polymer molecular weight to control the network mechanics in the long-time limit.[33, 37] However, there is still a lack of systematic studies to compare or even correlate the junction dynamics with the time scales associated with self-diffusion or the long-time materials relaxation.

In this work, we choose physical networks based on histidine-nickel coordination bonds as a model system and examine various relaxation processes within the networks over a broad spectrum of time scales. The use of various metal-ligand coordination bonds in biological systems has inspired the development of these robust, versatile motifs to engineering the mechanical properties of synthetic materials for a wide range of applications.[2, 3, 28, 38-41] Here, the bis-histidine-nickel complexation bond[28, 42] is chosen for its experimentally accessible dissociation-reassociation dynamics (from rheological characterization)[28], well characterized bond association constants,[28, 43] and sufficient optical transparency in the wavelength range[28] that permits diffusion measurements by forced Rayleigh scattering. The time constants for junction dissociation in dilute solution and for self-diffusion are experimentally determined by metal exchange experiments and forced Rayleigh scattering, respectively. In addition, this study develops a new method termed "sticker dissociation and diffusion spectrometry" to directly measure junction dissociation in a network environment, with its physical basis supported by a modified two-state model that considers the dissociation-diffusion coupling of small-molecule stickers inside the associative networks. The characteristic time scales for these different relaxation processes are projected in the frequency window covered by small-amplitude oscillatory shear rheology, providing a comprehensive demonstration on how the dissociation dynamics translate from a single junction

to various modes of molecular motions up to the network relaxation. The experimental findings are discussed in the context of the sticky Rouse model to further the understanding of relaxation dynamics in transient networks.

5.2. Eexperimental Section

Materials. Boc-His(Trt)-OH and L-histidine methyl ester dihydrochloride were purchased from Chem-Impex International Inc. (Wood Dale, IL). *N*-(3-aminopropyl)methacrylamide hydrochloride was purchased from Polysciences Inc. (Warrington, PA). Carbonyl diimidazole was purchased from Alfa Aesar. 2-(dodecylthiocarbonothioylthio)-2-methylpropionic acid (DMP)[44], and maleimide-functionalized 4′-(*N*,*N*′-dimethylamino)-2-nitrostilbene (ONS-M)[45] were synthesized following published procedures. *N*,*N*-dimethylacrylamide (DMA) was purified through a basic alumina column to remove inhibitor before polymerization. Azobisisobutylonitrile (AIBN) was recrystallized twice from ethanol. All other chemical reagents were purchased from Sigma-Aldrich or VWR and used as received.

Characterizations. NMR spectra were recorded on a Mercury 300 MHz spectrometer or an INOVA 500 MHz spectrometer. The residual undeuterated solvent peaks were used as references (7.27 pm for $CDCl_3$, 4.79 ppm for D_2O, and 3.30 ppm for CD_3OD). Gel permeation chromatography (GPC) measurements were performed on an Agilent 1260 LC system with two ResiPore columns (300 × 7.5 mm, Agilent Technologies, CA) in series at a flow rate of 1 mL/min at 70 °C, where DMF with 0.02 M LiBr was used as the mobile phase. The molecular weights were determined using a Wyatt miniDAWN TREOS multi-angle light scattering detector and a Wyatt Optilab T-rEX differential refractive index detector. Liquid chromatrography-mass spectrometry (LC-MS) analysis was performed using an Agilent 1260 Infinity LC system coupled

with a 6130 quadrupole mass spectrometer. A mixture of 0.1% formic acid in water and MeCN was used as the mobile phase.

Synthesis of *N*-Boc-N^{im}-Trityl-*N*-3-methacrylamidopropyl-L-histidinamide (1). Boc-His(Trt)-OH (5.00 g, 10.0 mmol), *N*-(3-aminopropyl)methacrylamide hydrochloride (1.79 g, 10.0 mmol) and 4-(dimethylamino)pyridine (DMAP, 2.44 g, 20.0 mmol) were dissolved in 100 mL of DCM/DMF mixture (1:1 v/v). *N*-(3-Dimethylaminopropyl)-*N'*-ethylcarbodiimide hydrochloride (EDC·HCl, 2.30 g, 12.0 mmol) was added to the solution, and the reaction was stirred at room temperature overnight. The reaction mixture was diluted with 50 mL DCM and washed with 0.1 N HCl (a.q.), water, saturated $NaHCO_3$ (a.q.), water, and brine. The organic phase was dried over Na_2SO_4, and the solvent was removed under vacuum. The crude product was further purified by silica gel flash chromatography using 0–10% MeOH in DCM to give **1** a white solid (4.80 g, 77.2% yield). ^{1}H NMR (300 MHz, $CDCl_3$) δ 7.42 (s, 1H), 7.36–7.29 (m, 9H), 7.17–7.02 (m, 8H), 6.85 (s, 1H), 6.43 (s, 1H), 5.78 (s, 1H), 5.30 (m, 1H), 4.44 (s, 1H), 3.32–3.18 (m, 3H), 3.17–3.02 (m, 2H), 2.99–2.92 (m, 1H), 1.96 (s, 3H), 1.64–1.55 (m, 2H), 1.42 (s, 9H). LRMS (ESI) m/z calculated for $C_{37}H_{44}N_5O_4$ $[M + H]^+$ 622.3, found 622.4.

Scheme 5-1. Synthesis of *N*-Boc-N^{im}-Trityl-*N*-3-methacrylamidopropyl-L-histidinamide.

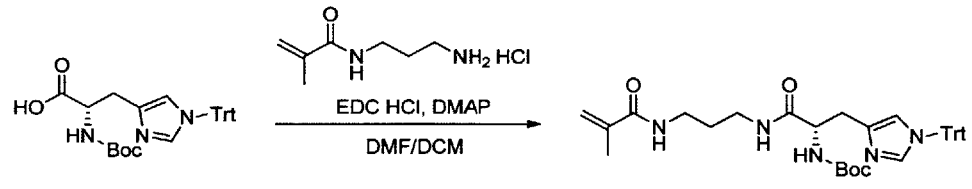

1

Synthesis of PDMA polymers with pendant histidine side groups (P2). Copolymers from DMA and **1** were synthesized by reversible addition-fragmentation chain transfer (RAFT) polymerization (Scheme 5-2). The total monomer concentration in polymerization was 2.0 M, and

the ratio of DMA/**1**/DMP/AIBN was 342:18:1:0.2. Polymerization was performed in MeCN at 60 °C for 4 h. Then the reaction flask was immersed into liquid nitrogen and exposed to air. Polymers were purified by precipitation into diethylether three times and dried under vacuum. This monomer pair was chosen because previous work by others has shown that the product of the reactivity ratios for acrylamide and methacrylamide is close to unity.[46, 47] Therefore, it was expected that the two monomers were copolymerized in a nearly statistical manner, and monomer **1** was evenly distributed along the polymer backbone. The mole fraction of **1** in the polymer **P1** was 5.3%, determined by ^{1}H NMR (Figure C-1), close to the feed ratio of 5.0%. The molecular weight of polymer **P1** was 42.5 kg mol^{-1}, characterized by DMF GPC (Figure C-2).

Scheme 5-2. Synthesis of linear PDMA polymers with pendant histidine side groups. For the final polymers, M_n = 36.2 kg mol^{-1}, $Đ$ = 1.06.

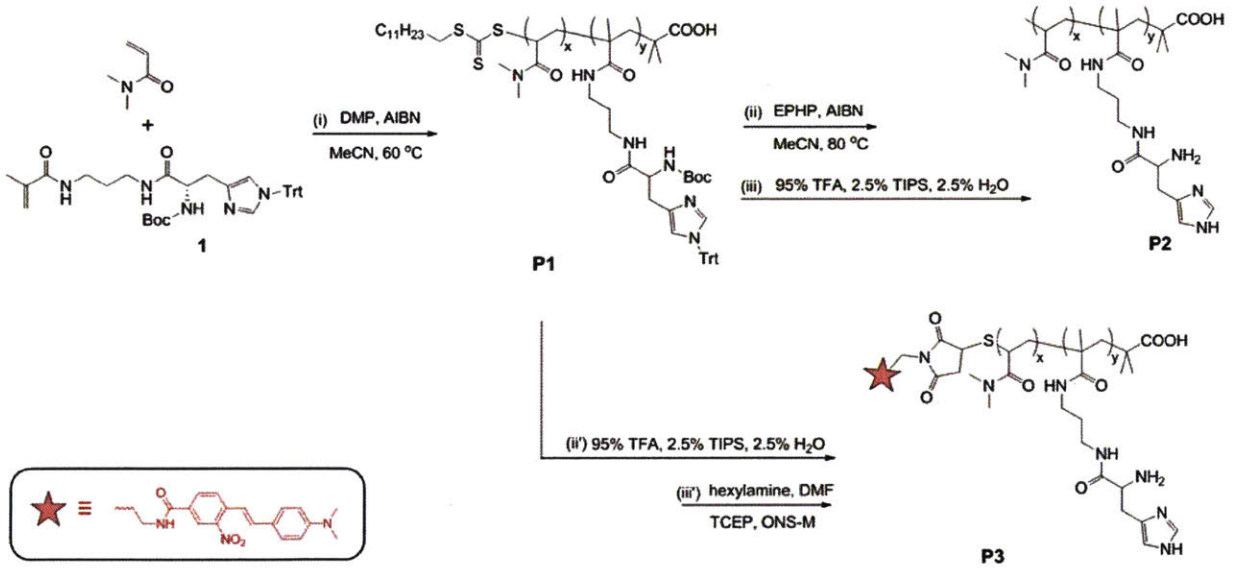

The trithiocarbonate end group was then removed by radical-induced reduction. Polymers (500 mg, 11.8 μmol), 1-ethylpiperidine hypophosphite (105 mg, 588 μmol), AIBN (0.97 mg, 5.90

μmol), and MeCN (5 mL) were added to a Schlenk tube. The mixture was degassed by three cycles of freeze-pump-thaw. After the reaction was heated at 85 °C overnight, the solvent was removed under vacuum. The residue was dissolved in DCM (20 mL) and washed with brine (20 mL × 3). The organic phase was dried over Na_2SO_4 and concentrated under vacuum. The polymers were recovered by precipitation into diethylether. Yield: 392 mg. The resulting polymers showed nearly identical molecular weight and composition as shown in GPC (Figure C-2). Complete removal of the trithiocarbonate was evidenced by the disappearance of the absorbance peak at 312 nm in UV-vis spectrum (Figure C-3). This argument was also supported by suppression of peaks at 1.24 and 0.86 ppm in ^{1}H NMR spectrum (Figure C-4).

To remove the Boc and Trt protecting groups, the resulting polymers (300 mg) were dissolved in DCM (5 mL). Water (125 μL), triisopropylsilane (TIPS, 125 μL) and trifluoroacetic acid (TFA, 5 mL) were sequentially added to the solution. The mixture was stirred at room temperature for 2 h. The volatiles were removed under vacuum, and the residue was dissolved in a small amount of MeOH. The polymers were recovered by precipitation into diethylether twice. The polymers were dissolved in water, dialyzed, filtered through a 0.45 μm filter, and lyophilized. Yield: 168 mg. Complete removal of the Boc and Trt groups was evidenced by ^{1}H NMR (Figure C-5). The final polymer molecular weight was calculated to be 36.2 kg mol^{-1} with a dispersity $Đ$ of 1.06 (Appendix C).

Synthesis of *ortho*-nitrostilbene (ONS) labeled PDMA polymers with pendant histidine groups (P3). As shown in Scheme 2, copolymers **P1** from DMA and **1** were first polymerized under the same condition as previously described. In the second step for removing the Boc and Trt protecting groups, copolymer (150 mg) was then dissolved in DCM (3.3 mL), to which water (83 μL), TIPS (83 μL), and TFA (3.2 mL) were added. After the reaction was stirred at room temperature for 2 h, volatiles were removed under vacuum. The residue was redissolved

in a small amount of DCM, and polymers were purified by precipitation into diethylether three times. For dye conjugation, polymers from the previous step (74 mg, 2 μmol) were first dissolved in DMF, and then hexylamine (5.3 μL, 40 μmol) was added. The reaction was stirred overnight under a nitrogen atmosphere to ensure complete aminolysis and to minimize undesirable cysteine oxidation. Then tris(2-carboxyethyl)phosphine hydrochloride (TCEP·HCl, 5.7 mg, 2 μmol) and maleimide-functionalized 4′-(*N*,*N*′-dimethylamino)-2-nitrostilbene (8.7 mg in 200 μL DMSO, 40 μmol) were added to the reaction mixture. After the reaction was stirred for 6 h in the dark, the solution was diluted with 30% MeOH in water. The mixture was transferred to a centrifugal filter (10 kDa MWCO), spun at 4,000 ×g for 12 min at room temperature, and more solution of 30% MeOH in water was added. This process was repeated several times until the spin-through fraction was nearly colorless. The resulting polymer solution was further purified over a Sephadex LH-20 resin to ensure complete removal of free dyes. Polymers **P3** were recovered after dialysis and lyophilization.

Synthesis of fluorescein-labeled histidine. The synthesis of *N*-[2-[[[(fluorescein-5-yl)amino]-thioxomethyl]amino]ethyl]-L-histidinamide was performed using a procedure for preparing a fluorescein-labeled cysteine analogue[48] (Scheme 5-3).

Scheme 5-3. Synthesis of N-[2-[[[(fluorescein-5-yl)amino]-thioxomethyl]amino]ethyl]-L-histidinamide.

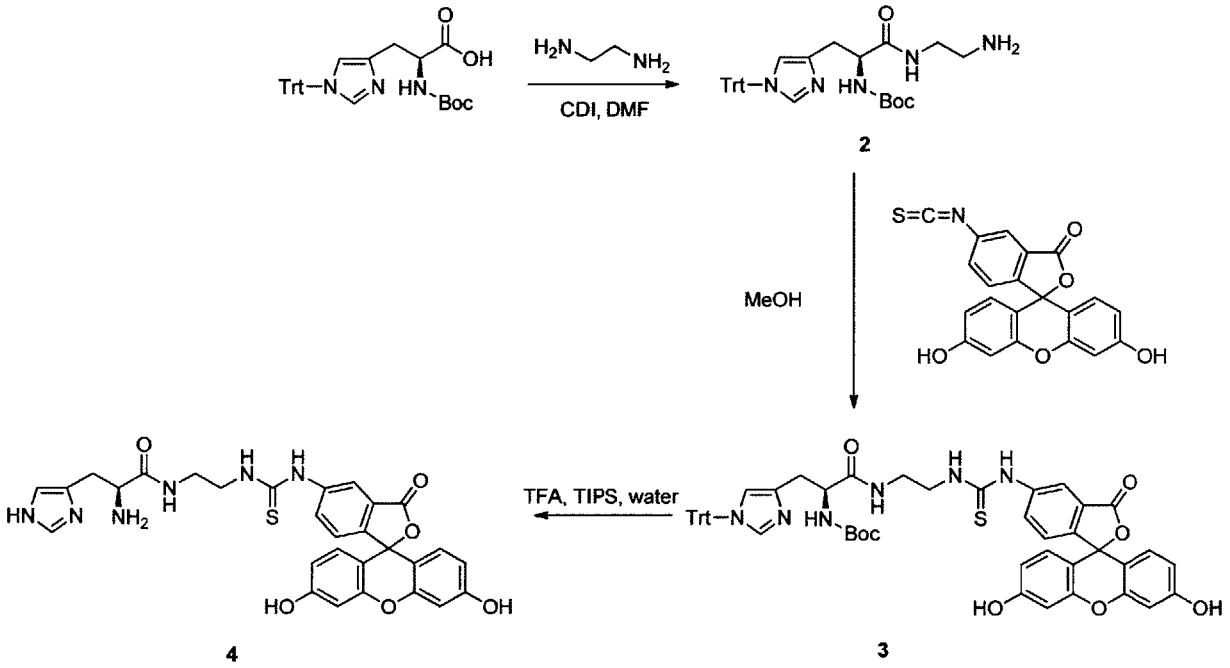

Synthesis of *N*-Boc-N^{im}-Trityl-*N*-2-aminoethyl-L-histidinamide (2). To a solution containing Boc-His(Trt)-OH (250 mg, 0.502 mmol) in 2.5 mL DMF was added carbonyl diimidazole (CDI, 1.22 g, 0.753 mmol). After the mixture was stirred at room temperature for 30 min, ethylenediamine (336 μL, 5.02 mmol) was added in one portion. After 2 h, volatiles were removed under vacuum, and the residue was redissolved in 15 mL DCM. The solution was washed with MilliQ water (15 mL × 5) and brine (15 mL × 1). The organic phase was dried over Na_2SO_4. The solvent was removed under vacuum to yield an off-white solid (189 mg, 69.8% yield). ^{1}H NMR (300 MHz, CD_3OD) δ 7.41–7.33 (m, 10H), 7.17–7.10 (m, 6H), 6.75 (s, 1H), 4.25–4.17 (m, 1H), 3.28–3.12 (m, 2H), 3.02–2.90 (m, 1H), 2.87–2.76 (m, 1H), 2.75–2.64 (m, 2H), 1.39 (s, 9H). LRMS (ESI) m/z calculated for $C_{32}H_{38}N_5O_3$ $[M + H]^+$ 540.3, found 540.3.

Synthesis of *N*-Boc-N^{im}-Trityl-*N*-[2-[[[(fluorescein-5-yl)amino]-thioxomethyl]amino]ethyl]-L-histidinamide (3). Fluorescein isothiocyanate (119 mg, 306 μmol) was dissolved in anhydrous MeOH (20 mL), and was added dropwise to a solution containing **2** (150 mg, 278 μmol) in anhydrous MeOH (6 mL). The reaction was stirred at room temperature for 20 h in the dark under N_2. The formation of **3** was confirmed by LC-MS. The mixture was then concentrated under vacuum. The product was purified by precipitation into water three times and dried *in vacuo* to give an orange solid. The crude product was directly used in the next step without further separation and purification.

Synthesis of *N*-[2-[[[(fluorescein-5-yl)amino]-thioxomethyl]amino]ethyl]-L-histidinamide (4). MilliQ water (200 μL), TIPS (200 μL), and TFA (7.6 mL) were added to the crude product **3** (200 mg). The reaction proceeded at room temperature for 2 h. The solvent was removed under vacuum, and the residue was redissolved in a small amount of MeOH. The product was recovered by precipitation into cold diethylether three times to give **4** as an orange solid (78.1 mg, 47.8% yield). ^{1}H NMR (300 MHz, CD_3OD) δ 8.09 (d, 1H, J = 1.5 Hz), 7.98 (s, 1H), 7.69 (d, 1H, J = 8.4 Hz), 7.16 (d, 1H, J = 8.4 Hz), 7.14 (s, 1H), 6.67 (d, 2H, J = 2.4 Hz), 6.60 (dd, 2H, J = 3.3, 8.7 Hz), 6.52 (dd, 2H, J = 2.4, 8.7 Hz), 4.10 (m, 1H), 3.78 (m, 2H), 3.64–3.43 (m, 2H), 3.24–3.12 (m, 2H). LRMS (ESI) m/z calculated for $C_{29}H_{27}N_6O_6S$ $[M + H]^+$ 587.2, found 587.2.

Gel preparation. Preparation of hydrogels from the histidine modified PDMA polymers followed the procedure[28] developed by Fullenkamp *et al.* with some modifications. Polymers **P2** were first dissolved in a buffer containing 100 mM Bis-Tris (pH 7.0). Then a stock solution containing 100 mM $NiCl_2$ and 100 mM Bis-Tris was added to the polymer solution such that the ratio of histidine groups to nickel ions was 2:1. The mixture was vortexed for 30 s. Separately, a 10 M NaOH solution was diluted 10 times with 100 mM Bis-Tris buffer (pH 7.0). This stock

solution of NaOH was added to the polymer-$NiCl_2$ mixture to adjust the pH to 7.0. The amount of NaOH stock solution needed was determined from titration experiments on dilute solutions with polymers and $NiCl_2$. This pH jump induced physical gelation, and the gels turned a light purple color. Finally, the gels were mixed with a micro spatula and centrifuged at 21,100 ×g. The mechanical mixing procedure was practiced several times to achieve macroscopically homogenous gels (Figure 5-1).

Rheology. Frequency sweep experiments were performed on an Anton Paar 301 Physica rheometer using a stainless steel cone-plate upper geometry (25 mm in diameter, 1° angle). Inertial calibration and motor adjustment were performed before each measurement. Hydrogel samples were centrifuged at 21,100 ×g for 10 min at room temperature to remove bubbles before loading onto the rheometer. Mineral oil was added to the sample edge to minimize dehydration. Experiments were performed at four temperatures, 5, 15, 25 and 35 °C, where the temperature was controlled by a Peltier plate. Frequency sweep experiments were performed at 1% strain from 100 to 0.001 rad s^{-1}, which was within the linear viscoelastic (LVE) region as determined by strain sweep experiments.

Metal exchange experiments. The dissociation rate of stickers in isolated junctions in dilute solution was estimated using metal exchange experiments[49] described by Hoyler *et al.* First, 2 mL of stock solution A containing 20 mM $CuCl_2$ and 100 mM Bis-Tris (pH 7.0) was added into a cuvette and equilibrated at the desired temperature for 10 min. Then 10 μL of stock solution B containing 200 mM $NiCl_2$, 400 mM L-histidine methyl ester dihydrochloride and 100 mM Bis-Tris (pH 7.0) were quickly injected into the stirring solution A. Solution B was also pre-equilibrated at the desired temperature. The change in absorption at 598 nm was monitored over time with a Cary 50 Bio UV/Vis spectrophotometer until the mixture absorbance reached a plateau,

during which data was averaged and recorded every 0.1 s. Experiments at each temperature were performed in triplicate. The use of Bis-Tris as a buffering agent was necessary for preparing solutions of $CuCl_2$ and $NiCl_2$ at the desired concentration at pH 7.0 and for maintaining the mixture pH throughout the kinetics measurements. This buffering condition was the same as the one under which hydrogels were formed.

Forced Rayleigh scattering measurements. Diffusion of fluorescein-labeled histidine molecules **4** (i.e., tracer diffusion) or ONS-labeled polymers **P3** (i.e., self-diffusion) in gels formed by polymers **P2** mixed with $NiCl_2$ at a histidine-to-nickel ratio of 2:1 in 100 mM Bis-Tris (pH 7.0) was measured by forced Rayleigh scattering (FRS). For preparing samples for tracer diffusion measurements, 0.1 mol% of **4** relative to the total histidine groups was added before the base addition step. Samples for self-diffusion measurements were prepared in a similar way, but contained 200 μM **P3**. All samples were sealed between two quartz disks (17 mm in diameter) separated by a 0.5 mm thick Teflon spacer, and were equilibrated at the desired temperature for 2 h before further experiments were performed. FRS measurements were conducted as previously described[24] using a 100 mW laser at 488 nm. The grating writing time was 500 ms.

5.3. Results and Discussion

Linear mechanics. The linear mechanical response of model associating networks formed by linear PDMA polymers with pendant histidine side groups complexed to Ni^{2+} ions (Figure 5-1) is typical for that of a physical gel. The dynamic mechanical properties of gels at two different concentrations, 10 and 20% (w/v), respectively, were measured within the linear viscoelastic regime (Figure 5-2). The characteristic rheological features include a plateau modulus at high frequencies, a crossover of the storage modulus G' and the loss modulus G'', and terminal

relaxation where $G' \sim \omega^2$ and $G'' \sim \omega$. A subtle deviation from the expected scalings in the terminal regime is observed, which can be attributed to the sticky-Rouse relaxation of the associating polymers as discussed in previous works[24, 35]. At low frequencies, G' is smaller than G'', which suggests that both concentrations are below the critical entanglement threshold. This observation is in good agreement with theoretical prediction (see calculation details in Appendix C). At high frequencies, the network plateau modulus increases dramatically by over 40-fold, from 0.64 kPa at 10% (w/v) to 26.4 kPa at 20% (w/v), both at 35 °C. Additionally, the G'-G'' crossover frequency ω_c decreases with increasing gel concentration. For example, at 35 °C, ω_c is observed at 0.59 rad s^{-1} for gels at 10% (w/v) and decreases to 0.18 rad s^{-1} at 20% (w/v). The effects of concentration on the network modulus and the relaxation rate can be explained by the changes of chain topology as a function of polymer concentration. The type of junction association transitions from intra- to intermolecular association with increasing polymer concentration, which affords more elastically effective chains and thereby a higher network modulus, as well as an increasing network relaxation time (or a decreasing ω_c).

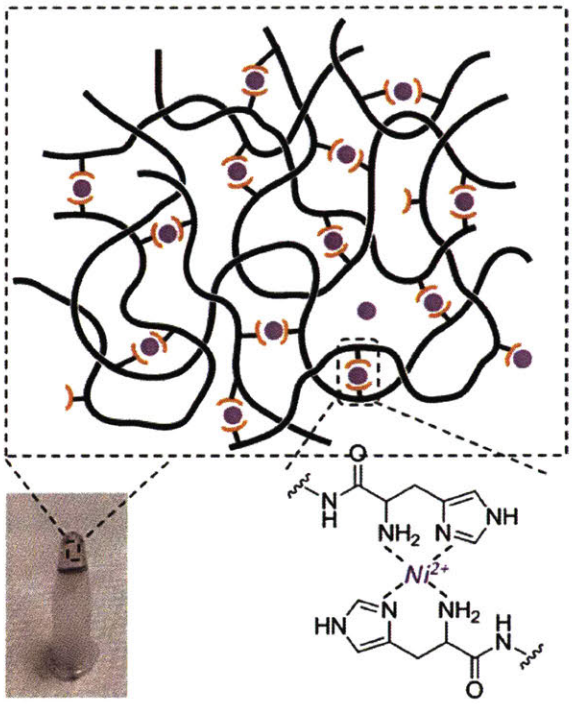

Figure 5-1. Hydrogels based on bis-histidine-nickel coordination bonds. Dangling stickers and intramolecular loops are shown as two types of network imperfections. A proposed structure for the bis-histidine-nickel complexes at the bottom right.

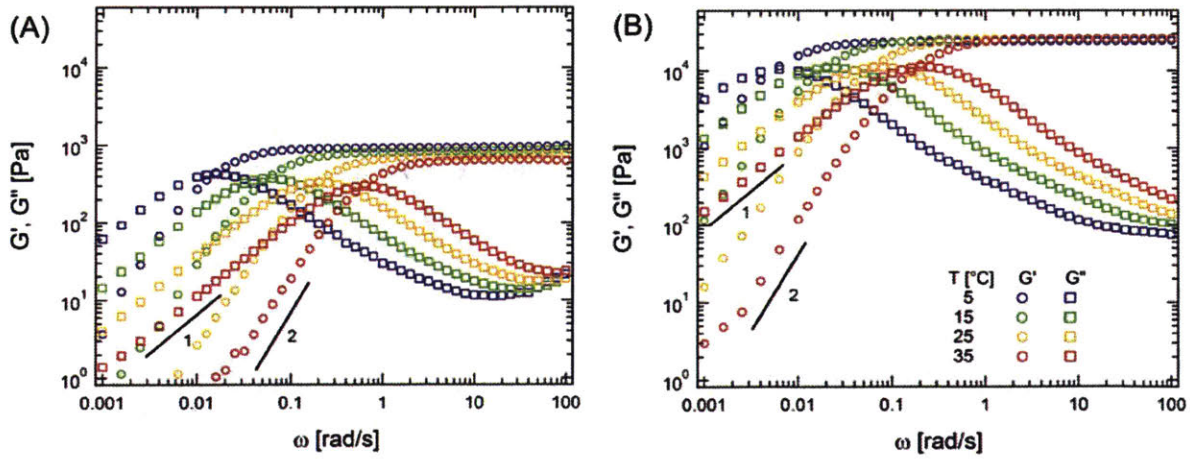

Figure 5-2. Frequency sweeps of gels at 10 and 20% (w/v) at varying temperatures. The expected slopes in the terminal regime for *G'* and *G"* are 2 and 1, respectively (shown as black lines).

A thorough understanding of the quantitative relationship between bond dynamics and rheological response is important because the dynamic mechanical properties of associating networks are affected not only by the type of stickers but also by the sticker-linked polymer scaffold and the sticker position (end groups vs. pendant side groups). Previous work[28] by Fullenkamp *et al.* modified the chain ends of four-arm poly(ethylene glycol) polymers with histidine moieties and prepared hydrogels under the same condition as in the current study. While the sticker density in their system is approximately 1/3 of that in this work (Appendix C), their system has a lower gelation concentration and a higher network modulus at the same gel concentration. For example, the gelation concentration of the histidine modified linear PDMA polymers is ca. 8% (w/v), as determined by an inversion test. This concentration is equivalent to a volume fraction φ of 0.058 and is 3 times larger than the estimated polymer overlap volume fraction ($\varphi^* \approx 0.019$, Appendix C). In contrast, gels prepared by Fullenkamp *et al.* at 2.5 and 5.0% (w/v) show well-defined high-frequency plateau moduli from rheology characterization, yet both concentrations are below the overlap threshold ($\varphi^* \approx 0.062$). At the same gel concentration of 10% (w/v) at 25 °C, their gels show an elastic modulus of nearly 11 kPa, much larger than the modulus obtained from the gels in this work (0.78 kPa). In addition to the aforementioned influences on gelation and network modulus, the polymer scaffold and the sticker position also cause differences in network relaxation. When the two types of gels are prepared at the same polymer concentration of 10% (w/v) at 25 °C, they show comparable ω_c around 0.2 rad s^{-1} while the sticker density of the four-arm PEG polymers is just 1/3 of the linear PDMA polymers. Therefore, it is expected that the gels in this study should exhibit a faster network relaxation rate at the same sticker concentration. The observations of faster network relaxation dynamics, a smaller modulus, and a higher gelation threshold can all be explained by a greater likelihood of

forming intramolecular junctions for the linear polymers with associating side groups. Together, these comparisons emphasize the needs for understanding the structure-mechanics-dynamics relationships in associating networks and suggest many engineering opportunities to tune the network mechanics by changing the polymer structure, even using the same sticker bond chemistry.

As an important measure for the network relaxation dynamics, the characteristic time of sticker exchange between network junctions depends strongly on temperature, and the corresponding activation energy provides a reference for further understanding the network relaxation dynamics. The mechanical properties of gels were characterized at four different temperatures, 5, 15, 25 and 35 °C (Figure 5-2). When the temperature is increased by 10 °C within this window, the frequency sweep spectrum shifts to higher frequencies by approximately half a decade. Here, the network relaxation time is determined from the G'-G'' crossover frequency, $\tau_r = \omega_c/2\pi$. Since the macroscopic network relaxation is directly related to the association-dissociation dynamics of the associating junctions, τ_r can be interpreted as the time for sticker exchange between junctions, τ_{ex}. This molecular interpretation is based on a widely accepted perspective that sticker exchange leads to changes in the number of elastically effective chains and hence induces network relaxation.[15, 22, 50] As shown in Figure 3, τ_{ex} decreases with temperature. Its temperature dependency can be described by an empirical Arrhenius law, from which an empirical activation energy $E_{a,ex}$ is obtained from the slope of an Arrhenius plot. The estimated values of $E_{a,ex}$ are 87 ± 3 and 83 ± 3 kJ mol^{-1} for gels at 10 and 20% (w/v), respectively (note that the error bars have accounted for deviations in ω_c from repeated measurements), which are statistically indistinguishable. Hereafter, $E_{a,ex}$ will be used as an energy reference to further investigate the mechanism of sticker exchange.

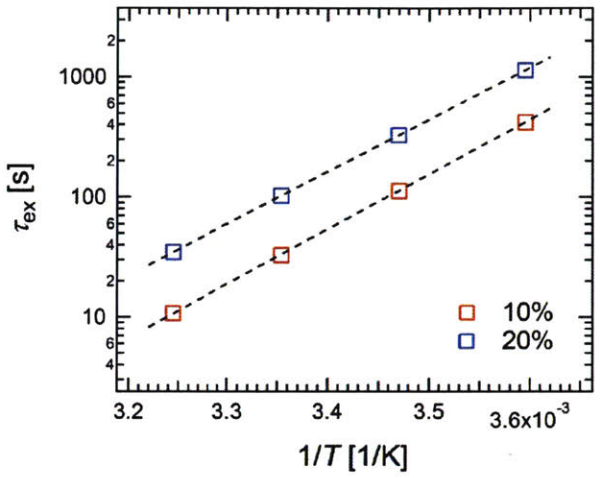

Figure 5-3. Sticker exchange time τ_{ex} at varying temperatures for gels at 10 and 20% (w/v). The black dashed lines are fits to an Arrhenius law.

Sticker dissociation in the dilute limit. Investigation of the kinetics of the dissociation step alone is important for understanding whether or not the dynamic stability of associating junctions or network relaxation in this work is governed by the dissociation step, as in many previous studies[18-20, 22, 23, 25, 28]. To this end, metal exchange experiments[49] were performed to quantify the dissociation kinetics of stickers in isolated junctions. Here, L-histidine methyl ester was chosen as an analogue to the polymer conjugated histidine side groups for two reasons. First, the absence of a free carboxylic acid ensures that chelation between histidine and metal ions is only through the free amine and nitrogen atom in the 3 position of imidazole (Figure 5-1), which excludes potential confounding glycine-like chelation mechanism[51, 52]. Second, DFT calculation confirms that change from an amide to an ester bond minimally affects the electron density map of the histidine moiety (Figure C-6). In the metal exchange experiments, dissociation of the bis-histidine-nickel complexes (His_2Ni) was driven by adding a 20-fold excess of Cu^{2+} competing ions

to form stronger complexes with histidine[43], as compared to Ni^{2+} (Figure 5-4A). The dissociation process was then monitored by changes in the metal ligand charge transfer band in the UV-vis absorption spectrum (Figure C-7).

To extract the dissociation time constant for the His_2Ni complexes, several simplifying assumptions are made. First, the influence of water molecules and Cl^- ions on the species equilibrium and kinetics are neglected. Second, pseudo steady-state approximations are applied to the free histidine ligands and HisNi complexes, which suggests that the concentrations of free histidine and HisNi complexes remain nearly constant during the experiment. Third, because Ni^{II} complexes absorb negligibly compared to Cu^{II} complexes (Table C-1) and the concentrations of Ni^{II} complexes are at least an order of magnitude smaller (Appendix C), only the contributions from Cu^{II} complexes to the total absorbance are considered. Fourth, an empirical stretched exponential function is used for fitting the experimental data instead of a theoretically derived pure exponential function to account for the errors due to simplification of the dissociation mechanism (Appendix C). Representative time-dependent absorbance profiles at varying temperatures are shown in Figure 5-4B. The average dissociation time constant, τ_d, is calculated from the first moment average (Appendix C).

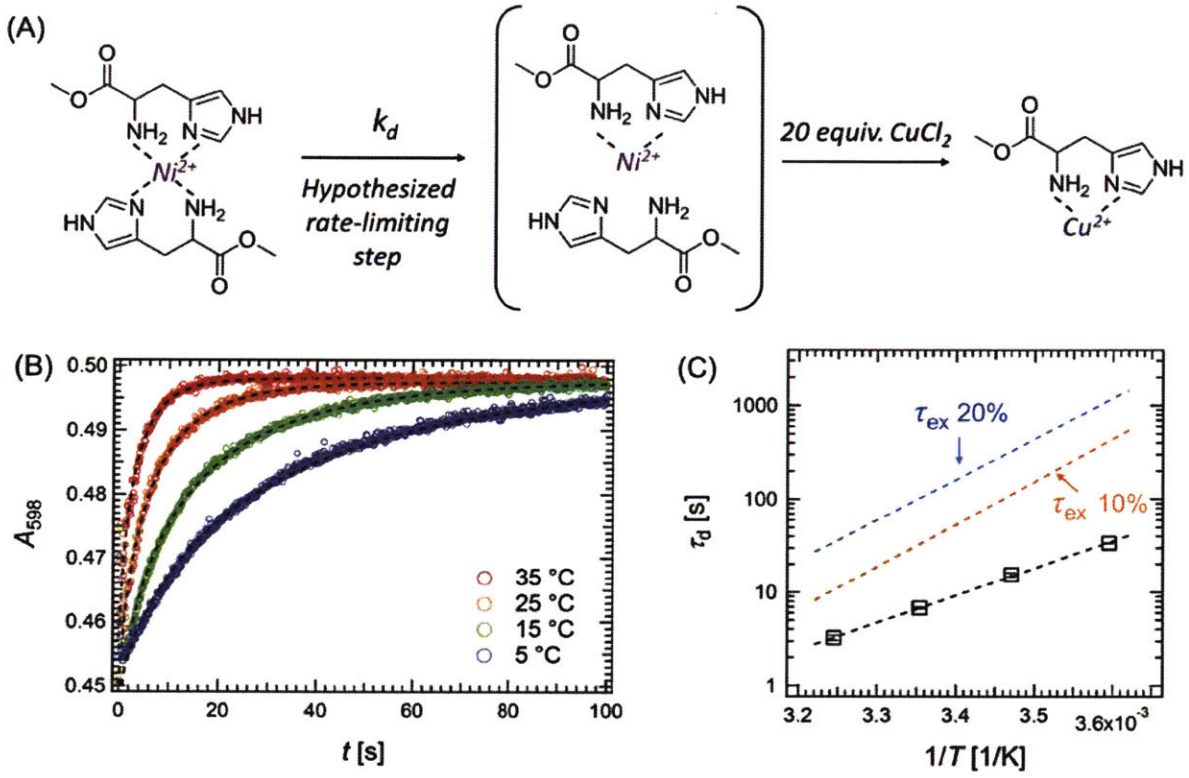

Figure 5-4. Probing the characteristic dissociation time τ_d of bis-histidine-nickel (His2Ni) complexes. (A) A proposed reaction scheme for the metal exchange experiments. (B) Representative time-dependent absorbance profiles at 598 nm at varying temperatures. Data points are shown in open circles, and the black dashed lines are fits to the stretched exponential functions. (C) An Arrhenius plot showing τ_d at varying temperatures. Data points are shown in black squares with error bars being the 95% confidence interval. The dashed line in black is the fit to the Arrhenius equation. The dashed lines in light orange and blue represent the junction exchange time constants from rheology measurements at 10 and 20% (w/v), respectively.

Dissociation of stickers in isolated junctions occurs at a significantly different rate than the process of sticker exchange between junctions in networks. The dissociation time constants of isolated His_2Ni complexes in the dilute limit, τ_d, at varying temperatures are plotted in Figure 5-

4B. Within the entire temperature window, the values of τ_d are always smaller than the sticker exchange time constants τ_{ex}. The temperature dependence of τ_d shows an Arrhenius-type behavior. The corresponding activation energy $E_{a,d}$ is estimated to be 56 ± 4 kJ mol^{-1}, which is less than the activation energy for sticker exchange $E_{a,ex}$ by approximately 30 kJ mol^{-1}. The differences in the magnitude of the time constants and the activation energies most likely originate from the differences in the physical environment of the histidine ligands and/or the distinct natures of the two processes. The comparison above also suggests that τ_d does not superimpose the rheology data following an empirical time-temperature superposition. However, it should be noted that these results do not contradict to the findings in Craig's work[23], where the dilute dissociation rates of different types of pincer–pyridine complexes are used to renormalize the rheological data of the corresponding networks into a single master curve, at the same temperature. While Craig's seminal investigation offers important insights into the relaxation mechanism of the junctions and the associating networks, it does not imply time-temperature superposition for networks with the same type of associating junctions using the dilute dissociation rate. Furthermore, the conclusion found in the current study is not restricted to only metal-ligand coordination bonds. Previous works by many others[4, 26, 27] have observed similar weak quantitative correlation between τ_d and τ_{ex}. For example, the study[4] by Guan and coworkers reports a five-order-of-magnitude difference in the exchange rates of two types of small-molecule reversible boronic ester junctions, but the *G'*-*G"* crossover frequencies from shear rheology characterizations of the two types of networks only show a three-order-of-magnitude difference.

Sticker dissociation and diffusion spectrometry. "Sicker dissociation and diffusion spectrometry" (SDDS) is developed here to quantify the kinetics of sticker dissociation within the network environment and to further investigate the similarity and difference in the dynamic

processes of junction dissociation and exchange. The use of SDDS to measure junction dissociation is fundamentally different than the previous approach that relies on metal exchange because the influence from the polymer networks at a particular concentration on junction dissociation is naturally reflected in SDDS. First, a small number of dye-labeled small molecules are added to the network, where both the network and the small molecules bear the same stickers (Figure 5-5A). Then forced Rayleigh scattering is employed to generate a one-dimensional concentration gradient with respect to the dye-labeled small molecules and monitor the gradient evolution as a function of time due to diffusion. During this process, the dye-labeled small-molecule stickers are expected to undergo association and dissociation with the surrounding networks, which can be described by the following reversible binding reaction:

$$S + F \underset{k_{off}}{\overset{k_{on}}{\rightleftharpoons}} A, \tag{1}$$

where symbols *S*, *F*, and *A* denote the dye-labeled small-molecule stickers, the open stickers on the polymers and the associated junctions formed between the previous two, respectively; k_{on} and k_{off} are the rate constants for association and dissociation, respectively. The diffusion and interconversion among all species are described by the following reaction-diffusion equations:

$$\begin{aligned}
\frac{\partial C_S}{\partial t} &= D_S \frac{\partial^2 C_S}{\partial x^2} - k_{on} C_S C_F + k_{off} C_A \\
\frac{\partial C_F}{\partial t} &= D_F \frac{\partial^2 C_F}{\partial x^2} - k_{on} C_S C_F + k_{off} C_A \\
\frac{\partial C_A}{\partial t} &= D_A \frac{\partial^2 C_A}{\partial x^2} + k_{on} C_S C_F - k_{off} C_A
\end{aligned}, \tag{2}$$

where C_i are the concentrations, and D_i are the diffusion coefficients (i = S, F and A). Because the total concentration of open stickers should only depend upon equilibrium parameters, when the concentration of the small-molecular stickers is negligible compared to the total number of stickers

inside the network, it is expected that C_F should remain constant during the diffusion measurements while fluctuating near its equilibrium concentration, $C_{F,eq}$. Therefore, eq. 2 can be simplified as:

$$\begin{aligned} \frac{\partial C_S}{\partial t} &= D_S \frac{\partial^2 C_S}{\partial x^2} - k_{on}^* C_S + k_{off} C_A \\ \frac{\partial C_A}{\partial t} &= D_A \frac{\partial^2 C_A}{\partial x^2} + k_{on}^* C_S - k_{off} C_A \end{aligned}, \tag{3}$$

where $k_{on}^* = k_{on} C_{F,eq}$, and the total concentration of the dye-labeled stickers is the sum of C_S and C_A. This simplified model is identical to the model[24, 36] previously used to explain both self- and tracer diffusion of associating polymers in the networks. Both the original and the modified models assume that the dimensionless equilibrium constant defined as the ratio of the association rate to the dissociation rate is larger than unity, i.e., $K_{eq} = k_{on}^*/k_{off} > 1$. However, for the small-molecule stickers studied in the work, it is further expected that the diffusivity ratio $\gamma = D_A/D_S$ is vanishingly small because the sticker diffusivity decreases by many orders of magnitude upon association with polymers.

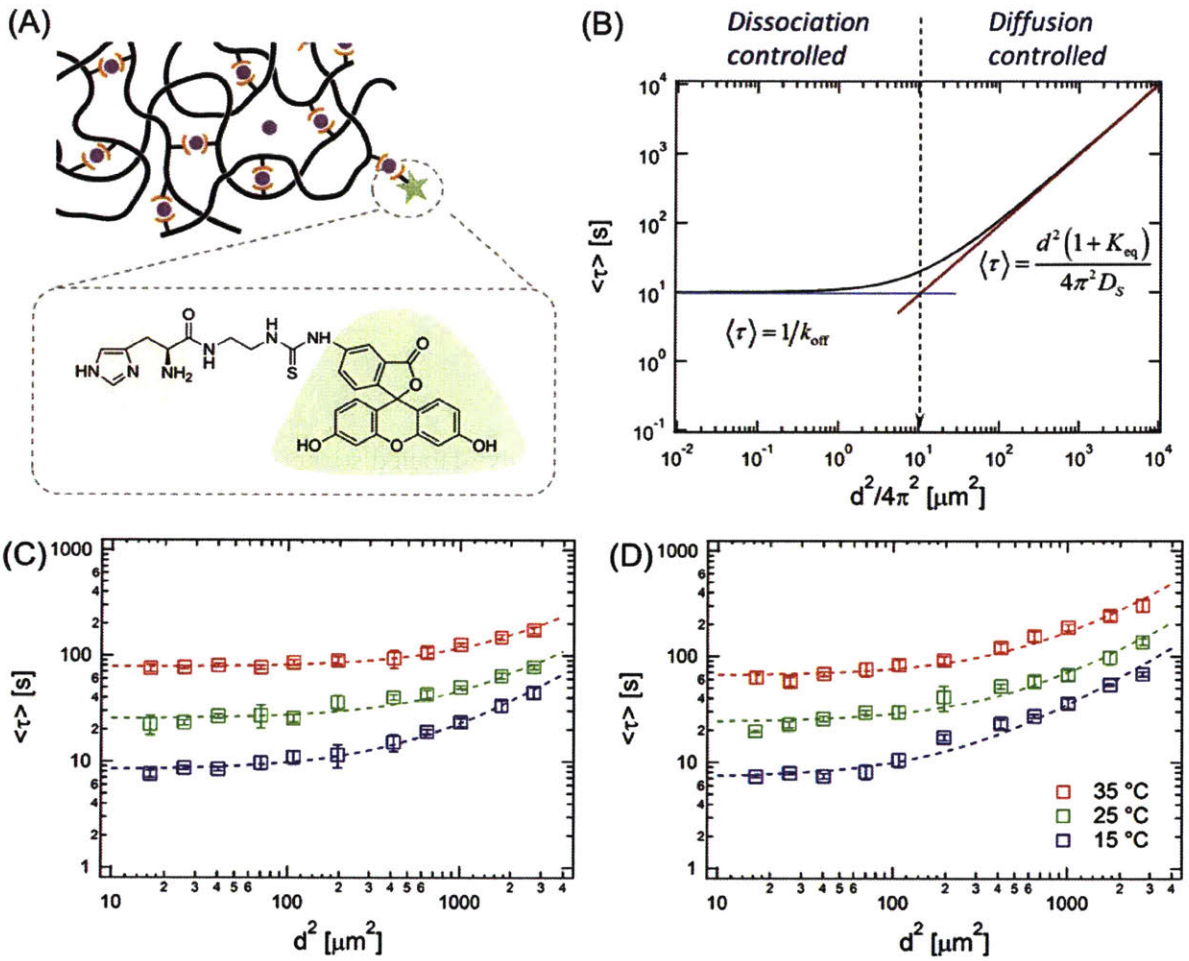

Figure 5-5. Sticker dissociation and diffusion spectrometry. (A) Schematic presentation showing a fluorescein-labeled histidine molecule within gels formed by histidine-nickel coordination bonds. (B) Relation of grating relaxation time $\langle\tau\rangle$ vs. squared grating spacing d^2. The equations shown in the figure demonstrate the asymptotic behavior at the small and large d^2, corresponding to the dissociation-controlled (blue line) and diffusion-controlled cases, respectively. Model parameters: $k_{on}^* = 10\ s^{-1}$, $k_{off} = 0.1\ s^{-1}$, $D_S = 100\ \mu m^2\ s^{-1}$. (C, D) Experimental results of the $\langle\tau\rangle$ vs. d^2 at varying temperatures at gel concentrations of 10 and 20% (w/v), respectively. Dashed lines are fits to the modified two-state model.

The solution to the modified two-state model provides a solid mathematical and physical basis for SDDS. The relationship of the ensemble average gradient relaxation time $<\tau>$ and the squared grating spacing d^2 can be solved analytically using Fourier transform, as previously described[24], and the solution is graphically presented in Figure 5-5B. On large length scales, gradient relaxation is controlled by diffusion, and the relation $<\tau>$ vs. d^2 shows Fickian scaling,

$$\langle \tau \rangle = \frac{d^2}{4\pi^2 D_{S,eff}}, \tag{4}$$

where the effective diffusivity $D_{S,eff}$ is defined as

$$D_{S,eff} = \frac{D_S}{1 + K_{eq}} = fD_S. \tag{5}$$

The functional form of eq 4 suggests the probe can effectively diffuse inside the networks on these large length scales. However, due to the associative interactions between the dye-labeled stickers and the network, the sticker diffusivity is reduced by a factor of the equilibrium constant K_{eq}, or by the fraction of free stickers $f = 1/(1 + K_{eq})$, as suggested in eq 5. In contrast, when diffusion measurements are performed on small length scales, the relation $<\tau>$ vs. d^2 becomes,

$$\langle \tau \rangle = \frac{1}{k_{off}}. \tag{6}$$

In this regime, the gradient relaxation time is no longer dependent on d^2. Instead, it is entirely determined by the average time of the dye-labeled stickers being bound to the networks, $1/k_{off}$. This suggests that the dissociation is a prerequisite step for diffusion. When this dissociation-controlled regime (Figure 5-5B) is observed, one can extract an ensemble sticker dissociation time inside the networks.

Experimental results from SDDS are consistent with the predictions from the modified two-state model. The design of the small-molecule sticker **4** is shown in Figure 5-5A (see synthesis details in the Experimental Section), where a histidine moiety is covalently linked to fluorescein through a two-carbon spacer. Fluorescein is chosen as a photochromic dye because of its sufficient solubility in aqueous solution, which prevents aggregation, and because of its successful use in forced Rayleigh scattering experiments[53, 54]. Notably, only 0.1 mol% **4** of the total number of histidine groups is needed to generate enough signal, and such small amount of added stickers should not significantly change the properties of the networks. As expected, on length scales with d^2 smaller than ca. 100 μm^2, the grating relaxation time $<\tau>$ seems to be independent of the length scale probed at all tested temperatures and concentrations (Figures 5-5C and 5-5D), from which a dissociation time of the dye-labeled stickers from the network can be extracted. Because the associative group in the small-molecule stickers is identical to the ones forming the network junctions, the result from SDDS measurements also reflects the dissociation of all stickers within the network. With increasing d^2, the slope in the log-log plot increases. However, pure Fickian scaling is not observed (Figures 5-5C and 5-5D). Given the large diffusivities of the small-molecule stickers, pure Fickian scaling is expected at larger length scales beyond the experimentally accessible window of forced Rayleigh scattering. The modified two-state model can also be used to quantitatively describe experimental results from SDDS (Figures 5-5C and 5-5D). By fitting the model solution to the experimental data, the dissociation rate of stickers k_{off}, (or its inverse, the dissociation time constant τ_{off}) and the apparent sticker diffusivity $D_{s,eff}$, can be obtained (Figure 5-6). However, K_{eq} cannot be independently determined because the relation of $<\tau>$ vs. d^2 is not sensitive to the value of K_{eq} in the limit of $K_{eq} >> 1$ (Appendix C).

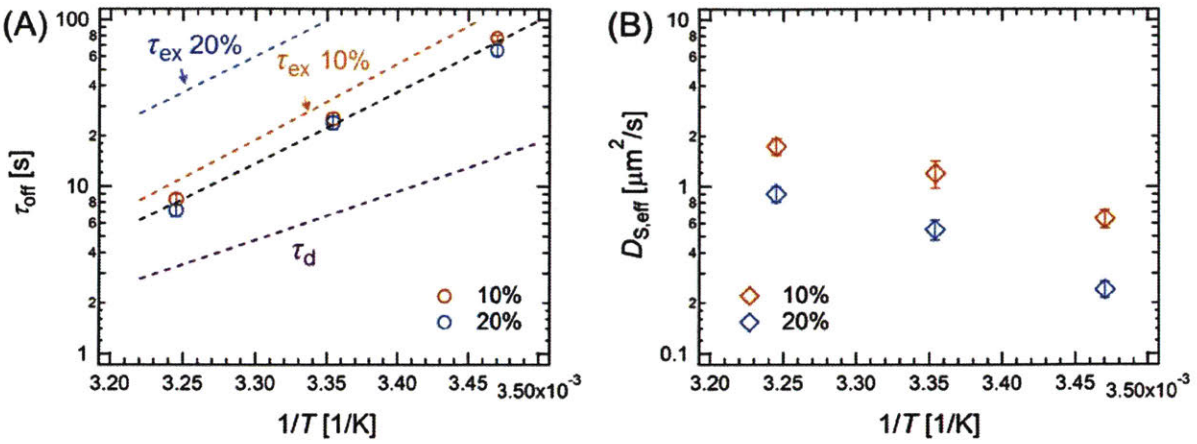

Figure 5-6. Estimated values of (A) sticker dissociation time constant in gels τ_{off} (i.e., $1/k_{off}$), and (B) the effective sticker diffusivity $D_{S,eff}$ at different temperatures and gel concentrations. Error bars represent 95% confidence intervals. In panel (A), dashed lines in light orange and blue are the sticker exchange time constants τ_{ex}, the purple dashed line represents the sticker dissociation time constant in the dilute limit τ_d, and the black dashed line is a fit of relation τ_{off} vs. $1/T$ to an empirical Arrhenius law.

The use of SDDS allows the sticker dissociation time constant in the networks, τ_{off}, to be reliably determined. Compared to the determination of τ_d (the dissociation rate in the dilute limit), the kinetic description of sticker dissociation in SDDS is much simpler and more well-defined. The estimated τ_{off} ranges approximately from 8 to 70 s (Figure 5-6A). At a given temperature, the estimated values of τ_{off} are nearly the same for gels at 10 and 20% (w/v), with overlapping 95% confidence intervals, suggesting that τ_{off} is indeed a physical time constant. The values of τ_{off} are larger than τ_d, which is not a function of concentration either. In many cases, dissociation of metal-ligand coordination bonds is initiated by solvent molecules displacing the ligands in the metal-ligand complexes.[23, 55] If this solvent-assisted dissociation mechanism applies, then the relation $\tau_{off} > \tau_d$ can possibly be attributed to a steric effect. Specifically, in the gel state, it becomes less

accessible for solvent and/or buffering agent (water and Bis-Tris molecules, respectively) to attack the His_2Ni complexes, therefore yielding a longer sticker dissociation time.

Another interesting finding is that the values of τ_{off} are always smaller than τ_{ex} (the time constant for sticker exchange), and the difference between the two time constants is more pronounced at higher gel concentration. Even though the sticker dissociation rate remains constant when the gel concentration varies, exchange of stickers is detected from rheological measurements only when a dissociated sticker finds and combines with a new partner instead of associating with its old one. The likelihood for successful sticker exchange decreases at higher gel concentration, although the total concentration of open stickers increases. This can be explained by the hindered chain relaxation that limits the molecular motion to search for and combine with new sticker partners, and/or by an hypothesis that most of the stickers are in the closed state and thus not available for forming new associative bonds. Part of the aforementioned arguments was first proposed in the sticky Rouse/reptation models by Rubinstein and coworkers and is often referred to as the renormalization of bond lifetime.[22] The experimental results shown in this study provide direct evidence to support this argument. However, since only two concentrations were examined, experiments on a wider concentration range are needed to further verify the conclusion.

Furthermore, the relation of $\tau_{off} < \tau_{ex}$ suggests that τ_{off} gives the lower bound for the sticker exchange time in gels. Since τ_{ex} decreases with concentration, the smallest τ_{ex} is achieved at the lowest gel concentration, i.e., the gel point. From this perspective, the physical meaning of τ_{off} can also be interpreted as an "intrinsic" sticker exchange time constant. Even though the inherent quantitative relations between τ_{off} and molecular parameters such as molecular weight and sticker density remain elusive, the determination of τ_{off} allows to pinpoint the fastest network relaxation time, providing an important insight for designing associating networks with desirable relaxation

dynamics. The interpretation of intrinsic network relaxation time in this study is similar to the one discussed in the Craig's work[23], but there it was determined by extrapolating an empirical scaling relation of the network relaxation time vs. the sticker density to the gel point. Subtle differences in the two definitions of intrinsic network relaxation time remain to be explored.

The temperature dependence of τ_{off} can be adequately captured by an Arrhenius-type behavior (Figure 5-6A), from which an activation energy $E_{a,off}$ is estimated to be 80 ± 10 kJ mol^{-1}. Within experimental errors, $E_{a,off}$ is very close to the one for sticker exchange $E_{a,ex}$ (ca. 85 kJ mol^{-1}). Since SDDS directly probes the dissociation of individual stickers under the same condition that gels are formed, the two comparable activation energies for sticker dissociation and exchange suggests that the dissociation is most likely the rate-limiting step for sticker exchange between junctions. This conclusion is expected to hold for associating networks where sticker exchange are dissociation-controlled, but may not be true for networks whose junctions can undergo direct exchange. The two statistically indistinguishable activation energies may also provide a physical explanation for the applicability of an empirical time-temperature superposition of rheological data for a wide variety of associating networks where the junction dynamic stability is most likely controlled by dissociation.[35, 56-59] In contrast, the activation energy for sticker dissociation in the dilute limit $E_{a,d}$ is smaller than both of $E_{a,off}$ and $E_{a,ex}$. Again, this is because the dilute solution measurements fail to include the effects from the networks on the stickers.

The effective diffusivity of the stickers $D_{S,eff}$ can be obtained even though the Fickian regime is not fully developed within the experimental window. As shown in Figure 5-6B, the values of $D_{S,eff}$ are on the orders of 0.1–1 μm^2 s^{-1}, about two orders of magnitude smaller than the diffusivities of fluorescein[60, 61] or other small molecules[61-63] (molecular weight less than 1,000 g mol^{-1}) in aqueous solutions. The results shown in Figures 5-6A and 5-6B together suggest that

increasing the gel concentration leads to a decrease in the effective diffusivity of stickers, but does not alter the dissociation kinetics. In addition, the transition d_c^2 from the dissociation-controlled regime to the diffusion-controlled regime is given by

$$d_c^2 = \frac{4\pi^2 D_{S,eff}}{k_{off}}. \quad (7)$$

which is obtained by equating eqs 4 and 6, the two theoretical asymptotes shown in Figure 5-5B. Based on the estimation of parameters $D_{S,eff}$ and k_{off}, the numerical values of d_c^2 are calculated (Figure C-9). It is found that d_c^2 decreases with both gel concentration and temperature. This explains the observed changes of slope in the large d^2 range in the SDDS data as a function of gel concentration and temperature (Figures 5-4C and 5-4D). Moreover, because the pure Fickian regime is seen when $d^2 >> d_c^2$ (Figure 5-4B), which is not met for all the experimental conditions, this finding also quantitatively explains why the expected Fickian scaling $<\tau> \sim d^2$ is not shown within the experiment window.

Two important physical insights can be further inferred from the estimates of $D_{S,eff}$. First, the dimensionless equilibrium constant K_{eq} in the modified two-state model can be calculated from the relationship $K_{eq} = D_S/D_{S,eff}$, where D_S is the diffusivity for non-associative small-molecules. The estimated values of K_{eq} at 25 °C are $(2.5 \pm 0.5) \times 10^2$ and $(4.2 \pm 0.7) \times 10^2$ for gels at 10 and 20% (w/v), respectively (see calculation details in Appendix C). These results are consistent with the previous assumption $K_{eq} >> 1$, i.e., strong association between the small-molecule stickers and the open stickers on polymers. Interestingly, K_{eq} shows a dependence on the gel concentration. However, this finding should not be surprising because the apparent association rate k_{on}^* is defined as $k_{on}^* = k_{on}C_{F,eq}$, and K_{eq} is then related to the junction binding constant $K_{eq,j}$ through $K_{eq} = K_{eq,j}C_{F,eq}$. Therefore, it is clear that K_{eq} in the modified two-state model is linear in the

concentration of open stickers on the polymers. Based on these results, the fractions of dangling stickers, f, are estimated to be $(3.3 \pm 0.7) \times 10^{-2}$ and $(3.0 \pm 0.5) \times 10^{-2}$ for gels at 10 and 20% (w/v), respectively, at 25 °C. These values of f are comparable to the total fraction of mono-histidine-nickel complexes and the free histidine groups in the gels.

Self-diffusion measurements. Finally, the longest relaxation process in the gels, self-diffusion of unentangled histidine modified PDMA polymers in hydrogels was measured by forced Rayleigh scattering (FRS), where a fraction of the polymers was labeled with *ortho*-nitrostilbene (Scheme 5-2). Within the experimentally accessible time window, self-diffusion only shows Fickian scaling, $\langle\tau\rangle \sim d^2$ (Figure 5-7). This observation is in contrast with previous measurements on associative coiled-coil proteins[24] and terpyridine end-functionalized four-arm poly(ethylene glycol) polymers complexed to Zn^{2+} ions[36], where similar phenomenological super-diffusion was seen in both cases. These different diffusive behaviors might be attributed to differences in the sticker density of different gels. Specifically, in both previous studies[24, 36], each polymer has four stickers, whereas there are ca. 18 stickers per polymer chain in the current work (Appendix C). However, further investigations are needed to conclusively identify the molecular basis for the phenomenological super-diffusion in associative networks. For gels at 10% (w/v) and at 35 °C, chain diffusivity D_{self} is calculated to be $(2.1 \pm 0.2) \times 10^{-5}$ μm^2 s^{-1} (errors bars representing 95% confidence interval), which is 2–3 orders of magnitude smaller than the self-diffusivities[24, 36] of associating polymers preciously obtained under the same condition. Based on D_{self}, the parameter γ defined in the modified two-state model is estimated to be on the order of 10^{-7} (Appendix C), which justifies the hypothesis $\gamma \approx 0$. Chain diffusion is too slow to be accurately measured for gels at other conditions.

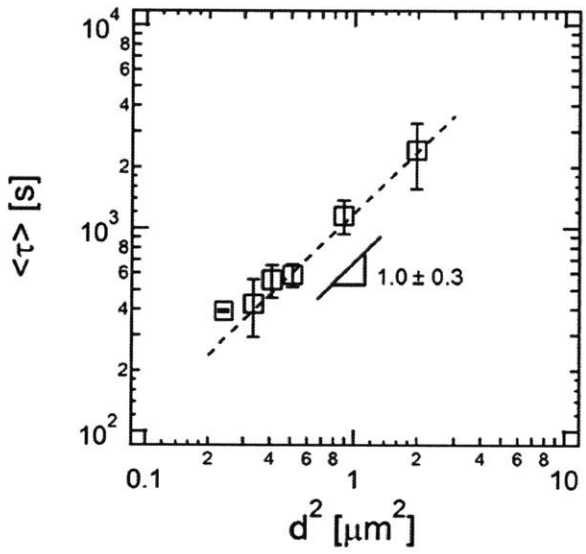

Figure 5-7. Self-diffusion of histidine modified PDMA polymers in gels at 10% (w/v) and at 35 °C. The linear fit is performed on the data points with d^2 larger than 0.3 μm^2. The error bar in the slope represents 95% confidence interval.

Comparison of time constants. For the relaxation processes studied in this work, the corresponding relaxation time constants follow the order $\tau_d < \tau_{off} < \tau_{ex} < \tau_{diff}$. For gels at 10% (w/v) and at 35 °C, the values of these time constants are directly plotted above the frequency sweep spectrum obtained from a time-temperature superposition, referenced at 35 °C (Figure 5-8). By definition, τ_{ex} is calculated from the *G'-G"* crossover frequency, and it denotes the time scale for sticker exchange. Compared to τ_{ex}, the time scale for sticker dissociation inside the networks τ_{off} is smaller. This is because multiple sticker dissociation events must occur before a successful sticker exchange is achieved. The number of attempts needed for sticker exchange may be estimated based on the ratio of τ_{ex} to τ_{off}, which suggests less than two attempts are needed on average for gels at 10% (w/v). However, even though dissociation is a prerequisite step for sticker

exchange, no rheological signature is found to directly correlate with the dissociation of stickers. Unlike other time constants, the time scale for self-diffusion is proportional to the square of length dimension. The relation $\tau_{ex} < \tau_{diff}$ suggests that for relaxation processes longer than τ_{ex}, such as chain diffusion, the related length scale is polymer segments containing one or more of these associative stickers. The region highlighted from ca. 400 to 3,000 s in Figure 8 corresponds to the regime in which Fickian scaling is observed in self-diffusion measurements (Figure 5-7). Within this time window, a sticky-Rouse type relaxation is found in rheology, shown as an increase of slope in the relation G' vs. ω. A similar observation was reported in multi-block coiled-coil protein gels.[24] In both cases, the onset frequency of the sticky-Rouse relaxation correlates well with the shortest Fickian diffusion time. However, it should be pointed out that the sticky-Rouse signature for the gels studied here is most likely related to the partial-sequential release of the stickers on the chain from the surrounding networks, because simultaneous dissociation for all stickers is highly unlikely.

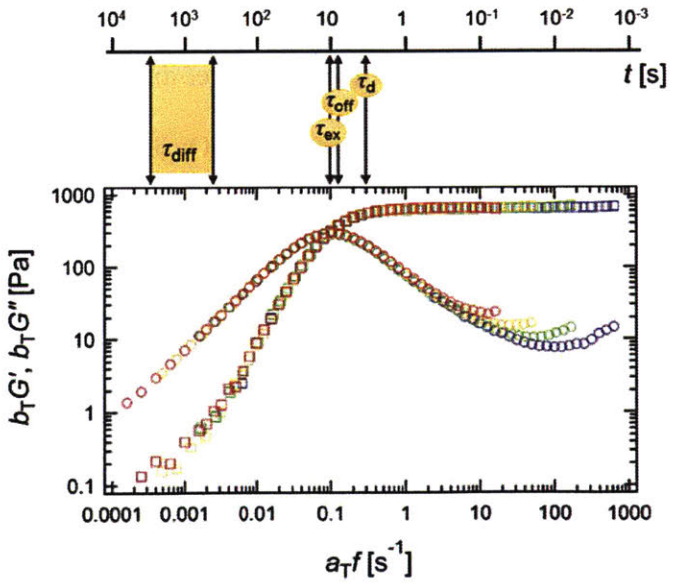

Figure 5-8. Direct comparison of relevant relaxation time scales. The rheology master curves are obtained from empirical time-temperature superposition referenced at 35 °C.

5.4. Conclusions

This study investigates a model transient network formed by linear poly(*N*,*N*-dimethylacrylamide) polymers with pendant histidine side groups transiently linked to nickel ions in aqueous solution. The dynamic mechanical properties of the networks measured by oscillatory shear rheology show quantitative differences compared to the ones based on the same associating junctions, suggesting the importance and necessity of thoroughly understanding the structure-mechanics-dynamics relationships in transient networks. A new technique referred to as "sticker dissociation and diffusion spectrometry" (SDDS) is developed to quantify the dissociation dynamics of stickers within the network environment. The physical picture of SDDS is adequately described by a modified two-state model that accounts for the dynamic equilibrium of stickers in the closed and open states upon associating with and dissociating from the surrounding networks. Unlike the dissociation time constant in the dilute limit, the dissociation time in gels shows a nearly identical activation energy to the one of sticker exchange between junctions, while providing the lower bound for the time constant of sticker exchange. These findings unambiguously demonstrate that on time scales in the vicinity of the bond lifetime, sticker dissociation governs the relaxation dynamics for the currently studied associating networks. On larger time scales, hindered self-diffusion of the linear associating polymers is found to correlate with the sticky Rouse rheological signature, but it only shows Fickian scaling in contrast to previously observed phenomenological super-diffusion in associating polymers that have a much lower sticker density. This combination of experimental approaches offers complementary and consistent insights into the molecular mechanisms of the dynamic relaxation of associating networks. It is expected that the approaches used in this work can be easily applied for studying other associating networks.

5.5. References

1. Enke, M.; Döhler, D.; Bode, S.; Binder, W. H.; Hager, M. D.; Schubert, U. S. Intrinsic Self-Healing Polymers Based on Supramolecular Interactions: State of the Art and Future Directions. Springer Berlin Heidelberg: Berlin, Heidelberg, pp 1-54.

2. Holten-Andersen, N.; Harrington, M. J.; Birkedal, H.; Lee, B. P.; Messersmith, P. B.; Lee, K. Y. C.; Waite, J. H. Ph-Induced Metal-Ligand Cross-Links Inspired by Mussel Yield Self-Healing Polymer Networks with near-Covalent Elastic Moduli. *Proceedings of the National Academy of Sciences* 2011, 108, 2651-2655.

3. Li, C.-H.; Wang, C.; Keplinger, C.; Zuo, J.-L.; Jin, L.; Sun, Y.; Zheng, P.; Cao, Y.; Lissel, F.; Linder, C., *et al.* A Highly Stretchable Autonomous Self-Healing Elastomer. *Nat Chem* 2016, 8, 618-624.

4. Cromwell, O. R.; Chung, J.; Guan, Z. Malleable and Self-Healing Covalent Polymer Networks through Tunable Dynamic Boronic Ester Bonds. *Journal of the American Chemical Society* 2015, 137, 6492-6495.

5. Webber, M. J.; Appel, E. A.; Meijer, E. W.; Langer, R. Supramolecular Biomaterials. *Nat Mater* 2016, 15, 13-26.

6. Rosales, A. M.; Anseth, K. S. The Design of Reversible Hydrogels to Capture Extracellular Matrix Dynamics. *Nature Reviews Materials* 2016, 1, 15012.

7. Chaudhuri, O.; Gu, L.; Klumpers, D.; Darnell, M.; Bencherif, S. A.; Weaver, J. C.; Huebsch, N.; Lee, H.-p.; Lippens, E.; Duda, G. N., *et al.* Hydrogels with Tunable Stress Relaxation Regulate Stem Cell Fate and Activity. *Nat Mater* 2016, 15, 326-334.

8. Wei, M.-H.; Li, B.; David, R. L. A.; Jones, S. C.; Sarohia, V.; Schmitigal, J. A.; Kornfield, J. A. Megasupramolecules for Safer, Cleaner Fuel by End Association of Long Telechelic Polymers. *Science* 2015, 350, 72-75.

9. Volpert, E.; Selb, J.; Candau, F. Associating Behaviour of Polyacrylamides Hydrophobically Modified with Dihexylacrylamide. *Polymer* 1998, 39, 1025-1033.

10. Winnik, M. A.; Yekta, A. Associative Polymers in Aqueous Solution. *Current Opinion in Colloid & Interface Science* 1997, 2, 424-436.

11. You, L.; Zha, D.; Anslyn, E. V. Recent Advances in Supramolecular Analytical Chemistry Using Optical Sensing. *Chemical Reviews* 2015, 115, 7840-7892.

12. Ma, M.; Guo, L.; Anderson, D. G.; Langer, R. Bio-Inspired Polymer Composite Actuator and Generator Driven by Water Gradients. *Science* 2013, 339, 186-189.

13. Kim, M.; Chen, W. G.; Kang, J. W.; Glassman, M. J.; Ribbeck, K.; Olsen, B. D. Artificially Engineered Protein Hydrogels Adapted from the Nucleoporin Nsp1 for Selective Biomolecular Transport. *Advanced Materials* 2015, 27, 4207-4212.

14. Semenov, A. N.; Rubinstein, M. Thermoreversible Gelation in Solutions of Associative Polymers. 1. Statics. *Macromolecules* 1998, 31, 1373-1385.

15. Leibler, L.; Rubinstein, M.; Colby, R. H. Dynamics of Reversible Networks. *Macromolecules* 1991, 24, 4701-4707.

16. Rubinstein, M.; Semenov, A. N. Thermoreversible Gelation in Solutions of Associating Polymers. 2. Linear Dynamics. *Macromolecules* 1998, 31, 1386-1397.

17. Tanaka, F.; Edwards, S. F. Viscoelastic Properties of Physically Crosslinked Networks. 1. Transient Network Theory. *Macromolecules* 1992, 25, 1516-1523.

18. Tripathi, A.; Tam, K. C.; McKinley, G. H. Rheology and Dynamics of Associative Polymers in Shear and Extension: Theory and Experiments. *Macromolecules* 2006, 39, 1981-1999.

19. Annable, T.; Buscall, R.; Ettelaie, R.; Whittlestone, D. The Rheology of Solutions of Associating Polymers: Comparison of Experimental Behavior with Transient Network Theory. *Journal of Rheology* 1993, 37, 695-726.

20. Sing, M. K.; Wang, Z.-G.; McKinley, G. H.; Olsen, B. D. Celebrating Soft Matter's 10th Anniversary: Chain Configuration and Rate-Dependent Mechanical Properties in Transient Networks. *Soft Matter* 2015, 11, 2085-2096.

21. Seiffert, S.; Sprakel, J. Physical Chemistry of Supramolecular Polymer Networks. *Chemical Society Reviews* 2012, 41, 909-930.

22. Rubinstein, M.; Semenov, A. N. Dynamics of Entangled Solutions of Associating Polymers. *Macromolecules* 2001, 34, 1058-1068.

23. Yount, W. C.; Loveless, D. M.; Craig, S. L. Small-Molecule Dynamics and Mechanisms Underlying the Macroscopic Mechanical Properties of Coordinatively Cross-Linked Polymer Networks. *Journal of the American Chemical Society* 2005, 127, 14488-14496.

24. Tang, S.; Wang, M.; Olsen, B. D. Anomalous Self-Diffusion and Sticky Rouse Dynamics in Associative Protein Hydrogels. *Journal of the American Chemical Society* 2015, 137, 3946-3957.

25. Yount, W. C.; Loveless, D. M.; Craig, S. L. Strong Means Slow: Dynamic Contributions to the Bulk Mechanical Properties of Supramolecular Networks. *Angewandte Chemie International Edition* 2005, 44, 2746-2748.

26. Shen, W.; Kornfield, J. A.; Tirrell, D. A. Dynamic Properties of Artificial Protein Hydrogels Assembled through Aggregation of Leucine Zipper Peptide Domains. *Macromolecules* 2007, 40, 689-692.

27. McKinnon, D. D.; Domaille, D. W.; Cha, J. N.; Anseth, K. S. Bis-Aliphatic Hydrazone-Linked Hydrogels Form Most Rapidly at Physiological Ph: Identifying the Origin of Hydrogel Properties with Small Molecule Kinetic Studies. *Chemistry of Materials* 2014, 26, 2382-2387.

28. Fullenkamp, D. E.; He, L.; Barrett, D. G.; Burghardt, W. R.; Messersmith, P. B. Mussel-Inspired Histidine-Based Transient Network Metal Coordination Hydrogels. *Macromolecules* 2013, 46, 1167-1174.

29. Appel, E. A.; Forster, R. A.; Koutsioubas, A.; Toprakcioglu, C.; Scherman, O. A. Activation Energies Control the Macroscopic Properties of Physically Cross-Linked Materials. *Angewandte Chemie International Edition* 2014, 53, 10038-10043.

30. Marrucci, G.; Bhargava, S.; Cooper, S. L. Models of Shear-Thickening Behavior in Physically Crosslinked Networks. *Macromolecules* 1993, 26, 6483-6488.

31. Hackelbusch, S.; Rossow, T.; van Assenbergh, P.; Seiffert, S. Chain Dynamics in Supramolecular Polymer Networks. *Macromolecules* 2013, 46, 6273-6286.

32. Skrzeszewska, P. J.; de Wolf, F. A.; Werten, M. W. T.; Moers, A. P. H. A.; Cohen Stuart, M. A.; van der Gucht, J. Physical Gels of Telechelic Triblock Copolymers with Precisely Defined Junction Multiplicity. *Soft Matter* 2009, 5, 2057-2062.

33. Tang, S.; Glassman, M. J.; Li, S.; Socrate, S.; Olsen, B. D. Oxidatively Responsive Chain Extension to Entangle Engineered Protein Hydrogels. *Macromolecules* 2014, 47, 791-799.

34. Goldansaz, H.; Voleppe, Q.; Pioge, S.; Fustin, C. A.; Gohy, J. F.; Brassinne, J.; Auhl, D.; van Ruymbeke, E. Controlling the Melt Rheology of Linear Entangled Metallo-Supramolecular Polymers. *Soft Matter* 2015, 11, 762-774.

35. Chen, Q.; Tudryn, G. J.; Colby, R. H. Ionomer Dynamics and the Sticky Rouse Modela). *Journal of Rheology* 2013, 57, 1441-1462.

36. Tang, S.; Habicht, A.; Li, S.; Seiffert, S.; Olsen, B. D. Self-Diffusion of Associating Star-Shaped Polymers. *Submitted* 2016.

37. Tang, S.; Olsen, B. Controlling Topological Entanglement in Engineered Protein Hydrogels with a Variety of Thiol Coupling Chemistries. *Frontiers in Chemistry* 2014, 2.

38. Rossow, T.; Hackelbusch, S.; van Assenbergh, P.; Seiffert, S. A Modular Construction Kit for Supramolecular Polymer Gels. *Polymer Chemistry* 2013, 4, 2515-2527.

39. Schubert, U. S.; Eschbaumer, C. Macromolecules Containing Bipyridine and Terpyridine Metal Complexes: Towards Metallosupramolecular Polymers. *Angewandte Chemie International Edition* 2002, 41, 2892-2926.

40. Cao, Y.; Yoo, T.; Li, H. Single Molecule Force Spectroscopy Reveals Engineered Metal Chelation Is a General Approach to Enhance Mechanical Stability of Proteins. *Proceedings of the National Academy of Sciences* 2008, 105, 11152-11157.

41. Degtyar, E.; Harrington, M. J.; Politi, Y.; Fratzl, P. The Mechanical Role of Metal Ions in Biogenic Protein-Based Materials. *Angewandte Chemie International Edition* 2014, 53, 12026-12044.

42. Schmitt, C. N. Z.; Politi, Y.; Reinecke, A.; Harrington, M. J. Role of Sacrificial Protein–Metal Bond Exchange in Mussel Byssal Thread Self-Healing. *Biomacromolecules* 2015, 16, 2852-2861.

43. Conley, H. L.; Martin, R. B. Transition Metal Ion Promoted Hydrolyses of Amino Acid Esters1. *The Journal of Physical Chemistry* 1965, 69, 2923-2935.

44. Lai, J. T.; Filla, D.; Shea, R. Functional Polymers from Novel Carboxyl-Terminated Trithiocarbonates as Highly Efficient Raft Agents. *Macromolecules* 2002, 35, 6754-6756.

45. Wang, M.; Timachova, K.; Olsen, B. D. Experimental Measurement of Coil–Rod–Coil Block Copolymer Tracer Diffusion through Entangled Coil Homopolymers. *Macromolecules* 2013, 46, 1651-1658.

46. Dainton, F. S.; Sisley, W. D. Polymerization of Methacrylamide in Aqueous Solution. Part 3.-Copolymerization with Acrylamide. *Transactions of the Faraday Society* 1963, 59, 1385-1389.

47. Durmaz, S.; Okay, O. Acrylamide/2-Acrylamido-2-Methylpropane Sulfonic Acid Sodium Salt-Based Hydrogels: Synthesis and Characterization. *Polymer* 2000, 41, 3693-3704.

48. Wood, R. J.; Pascoe, D. D.; Brown, Z. K.; Medlicott, E. M.; Kriek, M.; Neylon, C.; Roach, P. L. Optimized Conjugation of a Fluorescent Label to Proteins Via Intein-Mediated Activation and Ligation. *Bioconjugate Chemistry* 2004, 15, 366-372.

49. Holyer, R. H.; Hubbard, C. D.; Kettle, S. F. A.; Wilkins, R. G. The Kinetics of Replacement Reactions of Complexes of the Transition Metals with 2,2',2"-Terpyridine. *Inorganic Chemistry* 1966, 5, 622-625.

50. Tanaka, F.; Edwards, S. F. Viscoelastic Properties of Physically Crosslinked Networks. *Journal of Non-Newtonian Fluid Mechanics* 1992, 43, 273-288.

51. Leberman, R.; Rabin, B. R. Metal Complexes of Histidine. *Transactions of the Faraday Society* 1959, 55, 1660-1670.

52. Sundberg, R. J.; Martin, R. B. Interactions of Histidine and Other Imidazole Derivatives with Transition Metal Ions in Chemical and Biological Systems. *Chemical Reviews* 1974, 74, 471-517.

53. Chang, T.; Yu, H. Self-Diffusion of Gelatin by Forced Rayleigh Scattering. *Macromolecules* 1984, 17, 115-117.

54. Schaertl, W.; Tsutsumi, K.; Kimishima, K.; Hashimoto, T. Frs Study of Diffusional Processes in Block Copolymer/Homopolymer Blends Containing Glassy Spherical Micelles. *Macromolecules* 1996, 29, 5297-5305.

55. Li, C.-P.; Du, M. Role of Solvents in Coordination Supramolecular Systems. *Chemical Communications* 2011, 47, 5958-5972.

56. Cordier, P.; Tournilhac, F.; Soulie-Ziakovic, C.; Leibler, L. Self-Healing and Thermoreversible Rubber from Supramolecular Assembly. *Nature* 2008, 451, 977-980.

57. Rossow, T.; Habicht, A.; Seiffert, S. Relaxation and Dynamics in Transient Polymer Model Networks. *Macromolecules* 2014, 47, 6473-6482.

58. Noro, A.; Matsushita, Y.; Lodge, T. P. Thermoreversible Supramacromolecular Ion Gels Via Hydrogen Bonding. *Macromolecules* 2008, 41, 5839-5844.

59. Li, L.; Guo, X.; Wang, J.; Liu, P.; Prud'homme, R. K.; May, B. L.; Lincoln, S. F. Polymer Networks Assembled by Host–Guest Inclusion between Adamantyl and B-Cyclodextrin Substituents on Poly(Acrylic Acid) in Aqueous Solution. *Macromolecules* 2008, 41, 8677-8681.

60. Dursch, T. J.; Taylor, N. O.; Liu, D. E.; Wu, R. Y.; Prausnitz, J. M.; Radke, C. J. Water-Soluble Drug Partitioning and Adsorption in Hema/Maa Hydrogels. *Biomaterials* 2014, 35, 620-629.

61. Culbertson, C. T.; Jacobson, S. C.; Michael Ramsey, J. Diffusion Coefficient Measurements in Microfluidic Devices. *Talanta* 2002, 56, 365-373.

62. Müller, C. B.; Loman, A.; Pacheco, V.; Koberling, F.; Willbold, D.; Richtering, W.; Enderlein, J. Precise Measurement of Diffusion by Multi-Color Dual-Focus Fluorescence Correlation Spectroscopy. *EPL (Europhysics Letters)* 2008, 83, 46001.

63. Gendron, P.-O.; Avaltroni, F.; Wilkinson, K. J. Diffusion Coefficients of Several Rhodamine Derivatives as Determined by Pulsed Field Gradient–Nuclear Magnetic Resonance and Fluorescence Correlation Spectroscopy. *Journal of Fluorescence* 2008, 18, 1093-1101.

Chapter 6 A Preliminary Comparative Study of Using Fluorescence Bleaching after Recovery and Forced Rayleigh Scattering to Measure Self-Diffusion of Associating Polymers

6.1. Introduction

Diffusion of polymers has important technological implications because it greatly affects the processing conditions[1, 2], stability[3, 4] and mechanics[5-8] of polymeric materials. The design of advanced materials requires fundamental knowledge of polymers' diffusion under different conditions. The diffusive behavior of polymers is dramatically different from that of small molecules. Polymers diffuse very slowly, with diffusivities normally below 10^{-11} m^2/s, which are multiple orders of magnitude smaller than those of small molecules.[9] In addition, the diffusive behavior of polymers is often complicated by the polymer chain configuration[10-12], the non-Gaussian shape/structure[13-17], and the length scale of interest[10, 18]. Moreover, the length-scale-dependent chain characteristics are affected by the physical environments in which polymers are present.[10, 18] Up to now, many experimental methods have been developed to measure the mobility of polymers under different conditions. These methods include but are not limited to forced Rayleigh scattering (FRS)[8, 14, 16, 19], fluorescence recovery after photobleaching (FRAP)[20-22], fluorescence correlation spectroscopy (FCS)[23, 24], pulse-field gradient nuclear magnetic resonance (PFG-NMR)[25, 26] and secondary ion mass spectroscopy (SIMS)[27]. All of these techniques first generate a concentration gradient over a short length scale and then monitor the evolution of the gradient over time. Chain diffusivities are calculated in the Fickian regime where the square of the length dimension scales linearly with time.

Recently, emergent physical phenomena pertinent to the diffusion of associating polymers have been discovered. The presence of the associating groups (often referred to as stickers) imparts localized, transient connectivity between segments from the same or different polymer chains, which causes the diffusive motion of associating polymers to depart significantly from that of simple linear chains. The self-diffusion of associative linear coiled-coil proteins[8] and terpyridine functionalized star-shaped poly(ethylene glycol) polymers complexed to Zn^{2+} exhibits phenomenological super-diffusion on small length scales and shows Fickian scaling at sufficiently large length scales above 100-1000 R_g (radius of gyration) when observed by FRS. Despite the substantial differences in polymer backbone, sticker chemistry, sticker position and solvent environment, the diffusion of both types of associating polymers can be quantitatively captured by a simple two-state model. The model hypothesizes that associating polymers exist at two different states with two distinct diffusivities, and it also allows for interconversion to take place between the two states.

In order to observe phenomenological super-diffusion, the experimental techniques used to probe diffusion must be able to access the relevant length scales. In FRS, the characteristic length scale is the diffractive spacing, which is determined by the wavelength of the laser used in the experiment and the angle at which the two coherent laser beams intersect. Typically, the diffractive spacing ranges from the several hundreds of nanometers at the small end up to the several microns. For FRAP, the smallest length scale is determined by the pixel size, and the largest length scale may go to the tens of microns or even larger. Previously, phenomenological super-diffusion has only been observed by FRS but not by FRAP. This is probably because FRAP experiments were not performed under the condition that phenomenological super-diffusion could be recognized.

In principle, FRAP may also access information of polymer diffusion at micrometer length scales by using high-magnification objective lenses. Compared to FRS measurements that require a custom-built apparatus, FRAP can be performed on a commercially available confocal fluorescence microscope. Moreover, the development of user-friendly, efficient, and accurate algorithms for interpreting FRAP data has been very active. These two features make FRAP an attractive, popular tool for studying diffusion of macromolecules in materials, cell biology and medicine.[28-31] However, existing FRAP data analysis methods have only been developed for single component Fickian diffusion[32-34] or multicomponent Fickian diffusion[35, 36], a single component Fickian diffusion with a finite probability of binding to a non-mobile species[37-39], or anisotropic diffusion[40]. Therefore, there is a need to develop a method of analyzing FRAP data in experimentally settings described by the two-state model. In addition, it remains to be seen if FRAP can definitively discriminate the two-state model from other models under the relevant conditions where phenomenological super-diffusion is observed.

Herein, a method is established to analyze FRAP data based on the previously developed two-state model. Preliminary experimental efforts are made to compare the observed diffusive behavior probed by FRAP and FRS. Finally, future directions are suggested to quantitatively compare these two measurement techniques.

6.2. Mathematical background

The governing equations for the two-state model in the real space are:

$$\begin{aligned}\frac{\partial C_M}{\partial t} &= D_M \frac{1}{r}\frac{\partial}{\partial r}\left(r\frac{\partial C_M}{\partial r}\right) - k_{on}C_M + k_{off}C_A \\ \frac{\partial C_A}{\partial t} &= D_A \frac{1}{r}\frac{\partial}{\partial r}\left(r\frac{\partial C_A}{\partial r}\right) + k_{on}C_M - k_{off}C_A\end{aligned}, \quad 0 \le r \le w, \quad \text{and} \quad 0 < t, \tag{6-1}$$

subject to the boundary conditions (i = M or A),

$$\frac{\partial C_i}{\partial r}(0,t) = 0, \quad C_i(r \to w, t) = C_{i,eq}, \tag{6-2}$$

and the initial condition of the concentration,

$$C_i(r,0) = f_i(r). \tag{6-3}$$

Here, the governing equations are written in polar coordinates to analyze axisymmetric patterns. In addition, it should be emphasized that the variation of concentration in the z-direction is neglected. This can be achieved by using an objective lens with a low numerical aperture (NA) and by reducing the sample thickness. The boundary w is defined as the radius over which polymer diffusion is analyzed. The first boundary condition is given due to the axisymmetric nature of the FRAP pattern. The second boundary condition applies when w is sufficiently large compared to the radius of the bleached spot such that the dye concentration far away from the spot remains constant throughout the experiment. The initial condition is given by the initial profile created by photobleaching.

By changing the variables,

$$u_i = C_{i,eq} - C_i, \tag{6-4}$$

The governing equations become,

$$\begin{aligned}\frac{\partial u_M}{\partial t} &= D_M \frac{1}{r}\frac{\partial}{\partial r}\left(r\frac{\partial u_M}{\partial r}\right) - k_{on}u_M + k_{off}u_A \\ \frac{\partial u_A}{\partial t} &= D_A \frac{1}{r}\frac{\partial}{\partial r}\left(r\frac{\partial u_A}{\partial r}\right) + k_{on}u_M - k_{off}u_A\end{aligned}, \quad 0 \le r \le w, \quad \text{and} \quad 0 < t, \tag{6-5}$$

subject to the boundary conditions (i = M or A),

$$\frac{\partial u_i}{\partial r}(0,t) = 0\,, \quad u_i(r \to w, t) = 0\,, \tag{6-6}$$

and the initial condition of the relative concentration (normalized by the equilibrium concentration),

$$u_i(r,0) = C_{i,eq} - f_i(r)\,, \tag{6-7}$$

which are identical to the ones before changing the variables. The physical meaning is that the problem of recovery after bleaching is equivalent to the problem in which some amount of substance is added and then spread in the space.

The partial differential equations in eq 6-5 are analytically tractable by applying Fourier transforms to eliminate the spatial dependence of variable u_i and yield ordinary differential equations that are easier to solve. In this particular example, another integral transform method–Hankel transform–is used. Hankel transform, in principle, is similar to Fourier transform, but it is preferable for systems with circular or cylindrical symmetry because of a reduced number of variables.

The concentration u_i (i = M or A) after Hankel transform is defined as,

$$\hat{u}_i(k,t) = \int_0^\infty u_i(r,t) J_0(kr) r dr\,, \tag{6-8}$$

where J_0 is the zeroth order Bessel function of the first kind. The variable transformation in eq 6-7 is necessary in order to make the Hankel transform (eq 6-8) converge.

After multiplying by $J_0(kr)rdr$ and integrating from 0 to w, the governing equations become,

$$\frac{\partial \hat{u}_i}{\partial t} = D_i \int_0^w \frac{\partial}{\partial r}\left(r \frac{\partial u_i}{\partial r}\right) J_0(kr) dr \mp k_{on}\hat{u}_M \pm k_{off}\hat{u}_A\,. \tag{6-9}$$

The second term on the RHS of the equation can be simplified as,

$$
\begin{aligned}
D_i\int_0^w \frac{\partial}{\partial r}\left(r\frac{\partial u_i}{\partial r}\right)J_0(kr)\,dr &= D_i\int_0^w J_0(kr)\,d\left(r\frac{\partial u_i}{\partial r}\right)\\
&= D_i J_0(kr)\left(r\frac{\partial u_i}{\partial r}\right)\Bigg|_0^w - D_i\int_0^w\left(r\frac{\partial u_i}{\partial r}\right)(-k)J_1(kr)\,dr\\
&= D_i J_0(kw)w\left(\frac{\partial u_i}{\partial r}\right)\Bigg|_w + kD_i\int_0^w\left(r\frac{\partial u_i}{\partial r}\right)J_1(kr)\,dr\\
&= D_i J_0(kw)w\left(\frac{\partial u_i}{\partial r}\right)\Bigg|_w + kD_i\int_0^w rJ_1(kr)\,du_i\\
&= D_i J_0(kw)w\left(\frac{\partial u_i}{\partial r}\right)\Bigg|_w + kD_i u_i rJ_1(kr)\Big|_0^w - kD_i\int_0^w u_i krJ_0(kr)\,dr\\
&= D_i J_0(kw)w\left(\frac{\partial u_i}{\partial r}\right)\Bigg|_w + kD_i u_i wJ_1(kw) - k^2 D_i\hat{u}_i
\end{aligned}
\tag{6-10}
$$

The first term vanishes because of the boundary condition at $r = w$, since the concentration is constant and there is no flux. The second term vanishes because $u_i = 0$ at $r = w$. Therefore, the governing equations in the polar coordinates after Hankel transform are the same as in the Cartesian coordinates after transformation.

$$
\begin{aligned}
\frac{\partial\hat{u}_M}{\partial t} &= -k^2 D_M\hat{u}_M - k_{on}\hat{u}_M + k_{off}\hat{u}_A\\
\frac{\partial\hat{u}_A}{\partial t} &= -k^2 D_A\hat{u}_A + k_{on}\hat{u}_M - k_{off}\hat{u}_A
\end{aligned}
\tag{6-11}
$$

The equations can be represented in a vector-matrix form:

$$
\frac{\partial}{\partial t}\begin{bmatrix}\hat{u}_M\\ \hat{u}_A\end{bmatrix} = \begin{bmatrix}-k^2 D_M - k_{on} & k_{off}\\ k_{on} & -k^2 D_A - k_{off}\end{bmatrix}\begin{bmatrix}\hat{u}_M\\ \hat{u}_A\end{bmatrix} = \mathbf{A}\begin{bmatrix}\hat{u}_M\\ \hat{u}_A\end{bmatrix},
\tag{6-12}
$$

with the initial condition,

$$
\hat{u}_i(k,0) = \int_0^w\left[C_{i,eq} - f_i(r,0)\right]J_0(kr)\,r\,dr\,.
\tag{6-13}
$$

Previously, it has been shown that the eigenvalues of matrix **A** are:

$$\lambda_1, \lambda_2 = -\frac{1}{2}\left(k_{on} + k_{off} + k^2 D_M + k^2 D_A\right) \pm \frac{1}{2}\sqrt{\left(k_{on} + k_{off} + k^2 D_M + k^2 D_A\right)^2 - 4\left(k_{on} k^2 D_A + k_{off} k^2 D_M + k^4 D_M D_A\right)}, \tag{6-14}$$

which suggests that the matrix **A** is diagonalizable,

$$\mathbf{A} = \mathbf{V}\Lambda\mathbf{V}^{-1}. \tag{6-15}$$

The columns in the matrix **V** are the corresponding right eigenvectors,

$$\mathbf{V} = \begin{bmatrix} \lambda_1 + k^2 D_A + k_{off} & \lambda_2 + k^2 D_A + k_{off} \\ k_{on} & k_{on} \end{bmatrix}. \tag{6-16}$$

For simplicity, the matrix **A** is denoted as

$$\mathbf{A} = \begin{bmatrix} a & b \\ c & d \end{bmatrix}, \tag{6-17}$$

where

$$\begin{aligned} a &= -k^2 D_M - k_{on} \\ b &= k_{off} \\ c &= k_{on} \\ d &= -k^2 D_A - k_{off} \end{aligned}. \tag{6-18}$$

Therefore, the analytical solution to the linear ODE,

$$\dot{\mathbf{u}}(t) = \mathbf{A}\mathbf{u}(t), \tag{6-19}$$

is given by,

$$
\begin{aligned}
\mathbf{u}(t) &= \mathbf{V}e^{\Lambda t}\mathbf{V}^{-1}\mathbf{u}_0 \\
&= \begin{bmatrix} \lambda_1 - d & \lambda_2 - d \\ c & c \end{bmatrix} \begin{bmatrix} e^{\lambda_1 t} & \\ & e^{\lambda_2 t} \end{bmatrix} \frac{1}{c(\lambda_1 - d) - c(\lambda_2 - d)} \begin{bmatrix} c & -(\lambda_2 - d) \\ -c & \lambda_1 - d \end{bmatrix} \mathbf{u}_0 \\
&= \frac{1}{c(\lambda_1 - \lambda_2)} \begin{bmatrix} (\lambda_1 - d)e^{\lambda_1 t} & (\lambda_2 - d)e^{\lambda_2 t} \\ ce^{\lambda_1 t} & ce^{\lambda_2 t} \end{bmatrix} \begin{bmatrix} c & -(\lambda_2 - d) \\ -c & \lambda_1 - d \end{bmatrix} \mathbf{u}_0 \\
&= \frac{1}{c(\lambda_1 - \lambda_2)} \begin{bmatrix} c(\lambda_1 - d)e^{\lambda_1 t} - c(\lambda_2 - d)e^{\lambda_2 t} & -(\lambda_1 - d)(\lambda_2 - d)e^{\lambda_1 t} + (\lambda_1 - d)(\lambda_2 - d)e^{\lambda_2 t} \\ c^2\left(e^{\lambda_1 t} - e^{\lambda_2 t}\right) & -c(\lambda_2 - d)e^{\lambda_1 t} + c(\lambda_1 - d)e^{\lambda_2 t} \end{bmatrix} \mathbf{u}_0
\end{aligned}
\tag{6-20}
$$

This leads to a solution to the governing equation,

$$
\begin{bmatrix} \hat{u}_M(k,t) \\ \hat{u}_A(k,t) \end{bmatrix} = \frac{1}{c(\lambda_1 - \lambda_2)} \begin{bmatrix} \left[c(\lambda_1 - d)e^{\lambda_1 t} - c(\lambda_2 - d)e^{\lambda_2 t}\right]\hat{u}_M(k,0) + (\lambda_1 - d)(\lambda_2 - d)\left(e^{\lambda_2 t} - e^{\lambda_1 t}\right)\hat{u}_A(k,0) \\ c^2\left(e^{\lambda_1 t} - e^{\lambda_2 t}\right)\hat{u}_M(k,0) + \left[-c(\lambda_2 - d)e^{\lambda_1 t} + c(\lambda_1 - d)e^{\lambda_2 t}\right]\hat{u}_A(k,0) \end{bmatrix}
\tag{6-21}
$$

In Fourier space, the intensity of the fluorescence emission is proportional to the total concentration of the fluorescent species. Therefore, the normalized intensity is,

$$
\begin{aligned}
\frac{\hat{I}(k,t)}{\hat{I}(k,0)} &= \frac{\hat{u}(k,t)}{\hat{u}(k,0)} \\
&= \frac{\hat{u}_M(k,0)\left[c(\lambda_1 - d + c)e^{\lambda_1 t} - c(\lambda_2 - d + c)e^{\lambda_2 t}\right]}{\left[\hat{u}_M(k,0) + \hat{u}_A(k,0)\right]c(\lambda_1 - \lambda_2)} + \\
&\quad \frac{\hat{u}_A(k,0)\left[(\lambda_1 - d)(\lambda_2 - d + c)e^{\lambda_2 t} - (\lambda_2 - d)(\lambda_1 - d + c)e^{\lambda_1 t}\right]}{\left[\hat{u}_M(k,0) + \hat{u}_A(k,0)\right]c(\lambda_1 - \lambda_2)}
\end{aligned}
\tag{6-22}
$$

Because species M and A are in equilibrium at the initial condition, be it in the Fourier space or in the real space,

$$
\frac{\hat{u}_M(k,0)}{\hat{u}_A(k,0)} = \frac{k_{off}}{k_{on}} = \frac{b}{c}.
\tag{6-23}
$$

Thus,

$$\frac{\hat{I}(k,t)}{\hat{I}(k,0)} = \frac{(\lambda_1 - d + c)(\lambda_2 - b - d)e^{\lambda_1 t} + (b + d - \lambda_1)(\lambda_2 - d + c)e^{\lambda_2 t}}{(b+c)(\lambda_2 - \lambda_1)}. \tag{6-24}$$

Therefore, the final solution is,

$$\frac{\hat{I}(k,t)}{\hat{I}(k,0)} = \frac{(\lambda_1 + k^2 D_A + k_{on} + k_{off})(\lambda_2 + k^2 D_A)e^{\lambda_1 t} - (\lambda_1 + k^2 D_A)(\lambda_2 + k^2 D_A + k_{on} + k_{off})e^{\lambda_2 t}}{(k_{on} + k_{off})(\lambda_2 - \lambda_1)}. \tag{6-25}$$

This solution provides the basis for data fitting. There are two main advantages:

(1) Because the intensity ratio does not contain any terms dependent on the initial condition, this proposed analysis method does not require control over the initial pattern (be it a cylindrical or a Gaussian profile) in the FRAP experiment.

(2) Compared to fitting methods using integrated intensity over the radial position of the pattern, this method exploits all the spatial information at a given time point t, which may give more information about the length-scale-dependent diffusion. Specifically, although the initial feature size of the FRAP image is fixed, the spatially resolved concentration profile probes many length scales. If the analysis is done within several pixels, it is equivalent to the case where a small spot is burned in the FRAP experiment.

6.3. Experimental Section

Synthesis of fluorescein-labeled proteins P_4. As shown in Figure 6-1A, fluorescein-labeled associative proteins P_4 were synthesized by coupling fluorescein-5-maleimide to Cys-P_4, a cysteine-flanked protein with four internal coiled-coils connected by polyelectrolyte linkers[8]. First, proteins Cys-P_4 (200 mg, 3.2 μmol) were dissolved in 200 mL of 10 mM phosphate buffer (pH 7.5), and a 20-fold excess of tris(2-carboxyethyl)phosphine (18.2 mg, 64 μmol) was added as

solid to the protein solution. After the mixture was incubated at room temperature for 30 min., 2.71 mL of fluorescein-5-maleimide in DMSO at a concentration of 10 mg/mL (20-fold excess relative to the cysteine content) was added. The reaction was stirred at room temperature overnight. Purification of the fluorescein-labeled proteins Cys-P_4 was achieved by anion exchange and size exclusion chromatography following a previously published procedure[8]. The degree of dye labeling was determined to be 85% by UV-vis spectroscopy (Figure 6-1B) using the extinction coefficient of fluorescein of 68,000 M^{-1} cm^{-1} at 496 nm (specified by Thermo Scientific).

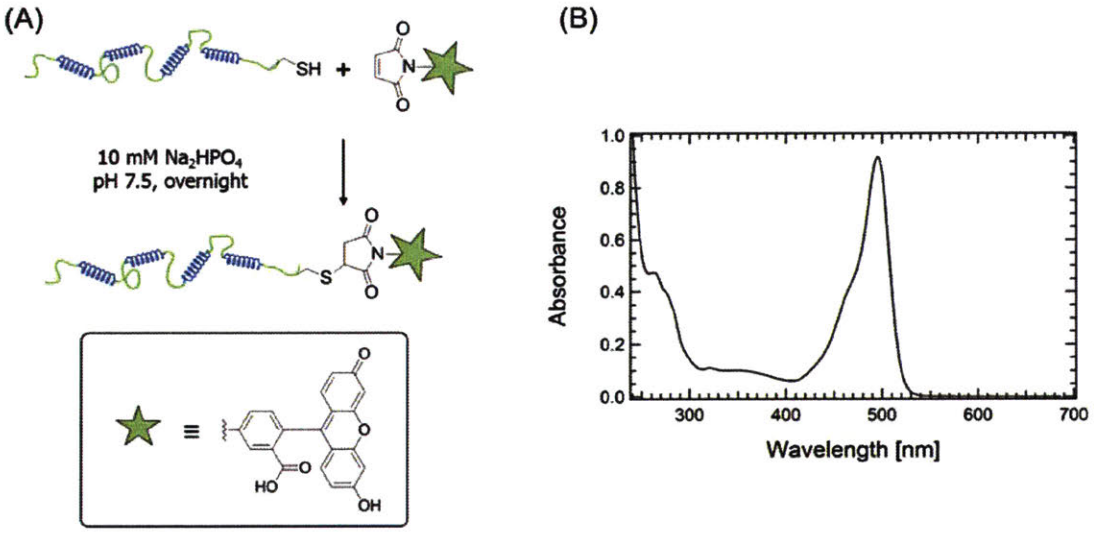

Figure 6-1. Synthesis of fluorescein-labeled proteins P_4 via thiol-maleimide coupling. (A) Reaction scheme. (B) UV-vis spectrum of fluorescein-labeled proteins P_4 at 1 mg/mL in 6 M urea and 20 mM Tris at pH 8.0.

Preparation of hydrogels with labeled proteins. The matrix proteins P_4 and the fluorescein-labeled protein P_4 were hydrated in 100 mM phosphate buffer (pH 7.6, filtered through a 0.2 μm filter) at 4 °C for 2 days. The total protein concentration was 6.5% (w/v), and the dye-labeled protein was approximately 25 μM. The gels were periodically mixed with a micro spatula

to ensure complete mixing of proteins. Before loading into the molds for diffusion measurements, gels were centrifuged at 21,000 ×g for 5 min to remove bubbles.

Diffusion Measurement by Forced Rayleigh Scattering (FRS). Self-diffusion of fluorescein-labeled P_4 proteins was first measured by forced Rayleigh scattering (FRS). The hydrogel specimen was sandwiched between two quartz disks (17 mm in diameter) with a 0.5 mm thick Teflon spacer. The gels were equilibrated at 25 °C for 1 h before further experiments were done. FRS experiments were performed following the previously established procedure.[8] The laser beam from a SpectraPhysics Cyan 100 mW laser at 488 nm (operating at a single longitudinal mode) was split, refocused, and recombined at a beam angle of 0.88 degrees. A holographic grating was generated by exposing the sample for 500 ms, during which a fraction of fluorescein was irreversibly photobleached. The grating spacing d was determined as

$$d = \frac{\lambda}{2\sin(\theta/2)} = \frac{0.488}{2\sin(0.88/2)} = 31.8[\mu m]. \quad (6\text{-}26)$$

The diffusive decay was then monitored by diffraction of a single reading beam at the same wavelength by a factor of 10^{-4}.

Diffusion Measurement by Fluorescence Recovery after Photobleaching (FRAP). Self-diffusion of associative proteins P_4 in hydrogels was also measured by fluorescence recovery after photobleaching (FRAP) on a Zeiss 700 inverted laser scanning confocal fluorescence microscope equipped with a Plan-Apochromat 63× oil immersion objective (NA = 1.40) at room temperature 25 ± 1 °C. The gels were pressed into a glass bottom microwell dish (MatTek, P35G-1.5-10-C) with a sample thickness of approximately 0.5 mm and sealed with a glass cover slide. Before bleaching, 3 images were acquired as background. Then a circular area with a dimeter of

10 μm was bleached by 25 iterated scans using a full power laser at 488 nm. The total bleaching time was 1.2 s. The detector gain was then greatly reduced by a factor of 10^2–10^3 to monitor the recovery process over 250 s and to minimize bleaching. During the recovery process, the data acquisition speed was set to be 2.6 s per image. However, it should be noted all the parameters above were not fully optimized.

6.4. Results and Discussion

Diffusion measurement by forced Rayleigh scattering. Self-diffusion of associative proteins P_4 in hydrogels at 6.5% (w/v) was first measured by forced Rayleigh scattering. The raw diffractive intensity decay vs. time shows a decay-growth-decay profile (Figure 6-2). This phenomenon has been previously observed by many others and explained by the existence of two complementary gratings that are 180 degrees out of phase from each other. However, the exact physical reasons that cause the complementary grating phenomenon is not yet well understood. The raw data is fit to the following equation

$$I = \left[A_1 \exp\left(-t/\tau_1\right) + A_2 \exp\left(-t/\tau_2\right) + B \right]^2 + C, \tag{6-27}$$

where the ratio of the pre-exponential factors A_1/A_2 is always negative, τ_1 and τ_2 are the relaxation time constants of the two gratings, B characterizes the coherent scattering (usually negligible as confirmed by fitting), and C characterizes the incoherent baseline. The corresponding fit for the decay profile is also shown in Figure 6-2. The fit is somewhat satisfactory, and noticeable differences between the fit and the data are observed. Stretched exponential functions are not used due to concerns that introducing too many variables might lead to unpredictable local minima, which makes it difficult to compare the extracted time constants across different experiments.

However, future effort to systematically investigate the function forms for fitting should be undertaken to yield more accurate results. Using the current approach, the time large and small constants are 473.1 ± 7.8 and 75.9 ± 0.8, respectively (error bars are 95% confidence intervals).

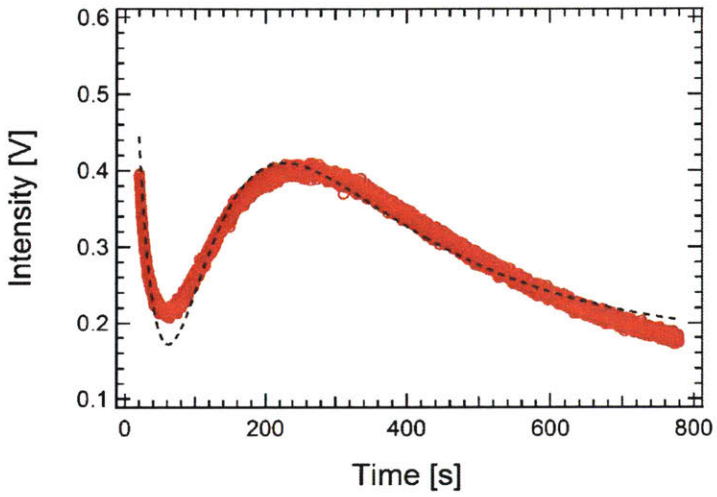

Figure 6-2. Diffractive intensity vs. time showing the decay-growth-decay profile. Red circles: raw data; black dashed line: fit.

The large time constant might be related to the actual diffusion process of the associative proteins, from which a diffusion coefficient is calculated. Self-diffusion of proteins P_4 was previously measured under the same condition by FRS but using *ortho*-nitrostilbene as the photochromic dye. The average grating decay time was 710.7 ± 55.1 s at a beam angle of 0.88 degrees at 25 °C. Through this comparison, it is thus concluded that the large time constant could be the actual time constant responsible for grating relaxation due to diffusion. The differences between the large time constant and previously measured results could be attributed to the batch-to-batch variations of protein purity, experimental errors in preparing the gels at exactly the same concentration, challenges in decoupling the two relaxation time constants or the combination

thereof. The claim that the large time constant provides the diffusion time scale is also supported by experimental observation from others.[19] The small time constant was found to be independent of the length scale, and the physical origin was not diffusive.

Diffusion measurement by fluorescence recovery after photobleaching (FRAP). FRAP measurements on associative proteins were performed on a confocal laser scanning microscope (CLSM). The photobleaching time was two orders of magnitude smaller than the diffusion time scale. Therefore, changes in the concentration of the dye labeled proteins during the bleaching step can be neglected. As shown in Figure 6-3, an initial circular pattern is bleached in the hydrogel throughout the entire sample thickness. Over the time period of 250 s, a substantial recovery of the fluorescence intensity is observed, which is exclusively due to the diffusion of associative proteins. Future experiments can be done at a longer time period to examine the later stage of the recovery process. However, it should be kept in mind that fluorescein is prone to photobleaching. An extended period of recovery monitoring might cause a substantial decrease in the background fluorescence intensity.

The proposed analysis follows the work by Jönsson et al.[36] As described in section 6.2, the intensity profile at different radial positions (the origin is at the center of the bleached spot) and at different time points, I(r,t), is Hankel transformed and then renormalized by the transformed initial intensity, which provides an analytical solution to the two-state model. There are three important steps to be noted in their numerical procedure. First, the intensities in the original image $I(x, y, t)$ are radially averaged to give I(r,t), where the radial positions r are chosen such that they can be directly evaluated by numerical Hankel transform. Second, the numerical Hankel transform

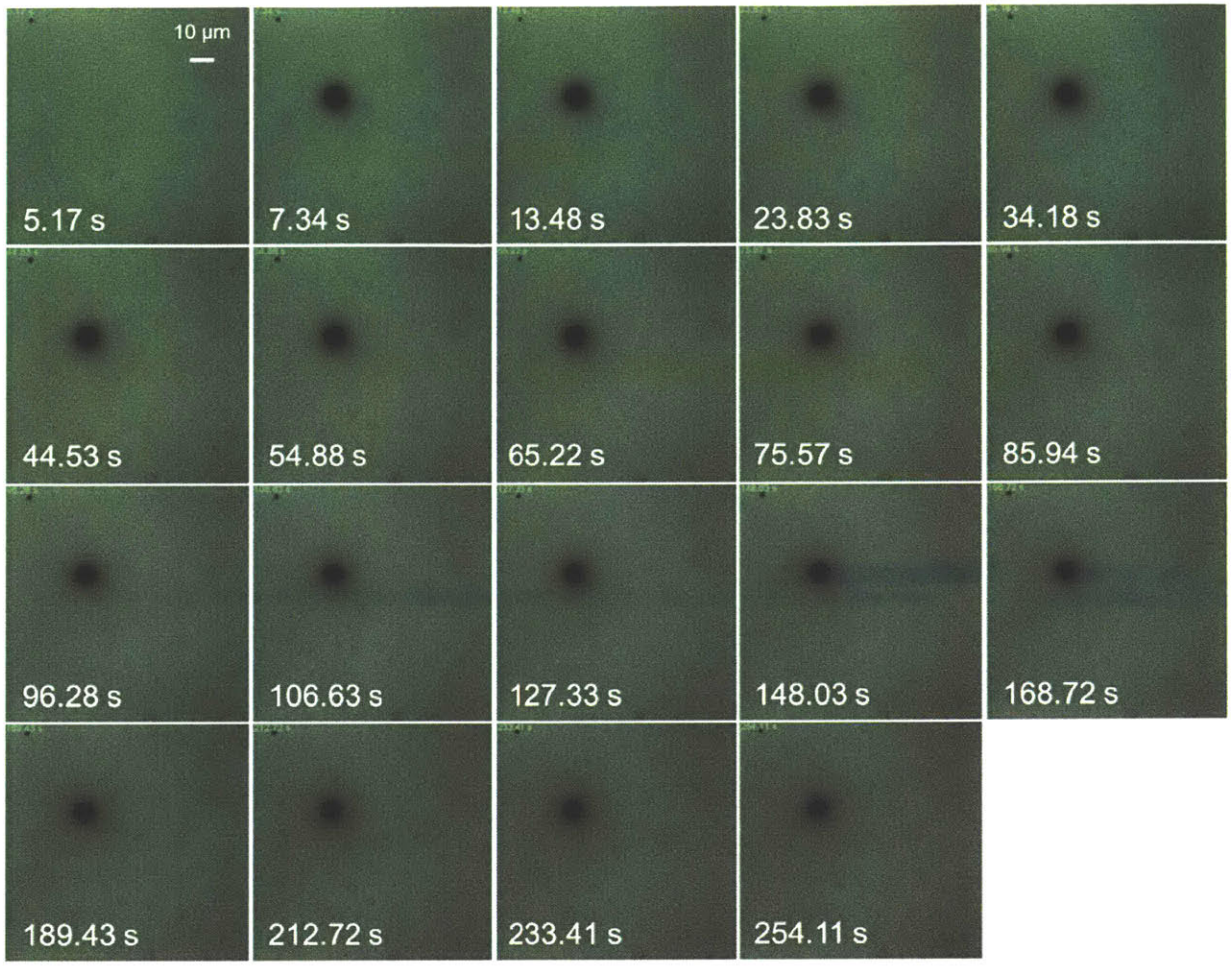

Figure 6-3. Snapshots of FRAP experiments at different time points shown at the bottom left of the images. Scale bar: 10 µm.

is truncated at a selected value of radius *R*. Beyond this radial cutoff, the spatial intensity profile *I*(r,t) is approximated by a Gaussian function that matches the analytical boundary condition. These two steps help reduce the effect of transformation from the noise in the intensity profile. Finally, the numerical Hankel transform is evaluated by a quasi-discretization integration method. The intensity profile is multiplied by a symmetric transformation matrix, and the matrix entities are computed from the roots of the Bessel functions at varying pre-selected *r* values. The

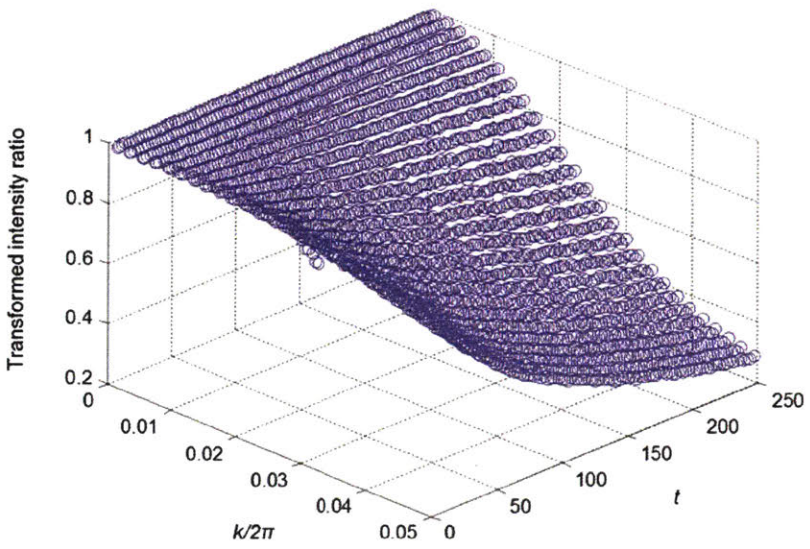

Figure 6-4. Transformed intensity ratio from experiments.

transformed intensity ratio from our experiment is plotted against k and t (Figure 6-4).

By fitting the two-state model solution (eq. 6-25) to the experiment data, it is then possible to extract the model parameters D_M, D_A, k_{on} and k_{off}. One approach is to execute a surface fit, with the two independent variables being k and t. However, this approach demands tight bounds on the initial estimates of model parameters. Unfortunately, the function used to fit the experiment data (eq. 6-25) does not show any characteristics that can give hints on the parameter range (see Figure 6-5). In addition, it is very difficult to discriminate models, for example, the effective diffusion model capturing hindered diffusion of a single component system vs. the two-state model (Figure 6-5).

An alternative approach is to do a series of line fits. At a given point k (inverse of the length scale, or the wave vector), the function reduces to a sum of two exponential functions (see

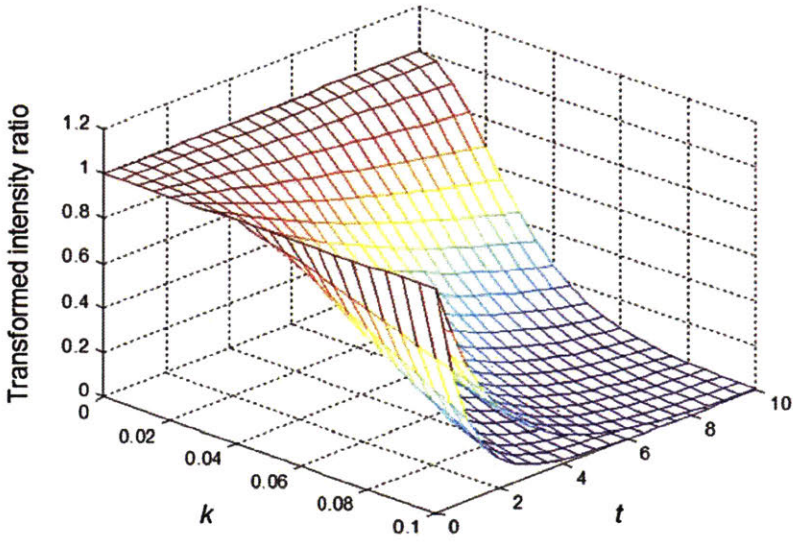

Figure 6-5. Simulated transformed intensity ratio. The upper surface is from the two-state model, and the lower surface is the effective diffusion model. Parameters used in these plots are $D_M = 10^4$, $D_A = 1$, $k_{on} = 100$, and $k_{off} = 1$.

eq 6-25). However, the fast decay process is not obvious in our experiments (Figure 6-4 and 6-6).

The function used to fit the experimental data is chosen to be following:

$$\frac{\hat{I}(k,t)}{\hat{I}(k,0)} = C_1 e^{\lambda_1 t} + C_2 e^{\lambda_2 t} = C_1 e^{-t/\tau_1} + C_2 e^{-t/\tau_2}, \tag{6-28}$$

where λ_1 and λ_2 are related to the small and the large time constant τ_1 and τ_2, respectively, and C_1 and C_2 are parameters that vary at different values of k. In this way, the analysis is essentially the same as what was done for FRS when ONS was used as the photochromic dye. Compared to the surface fitting approach, this 1D data analysis approach may offer an advantage of differentiating

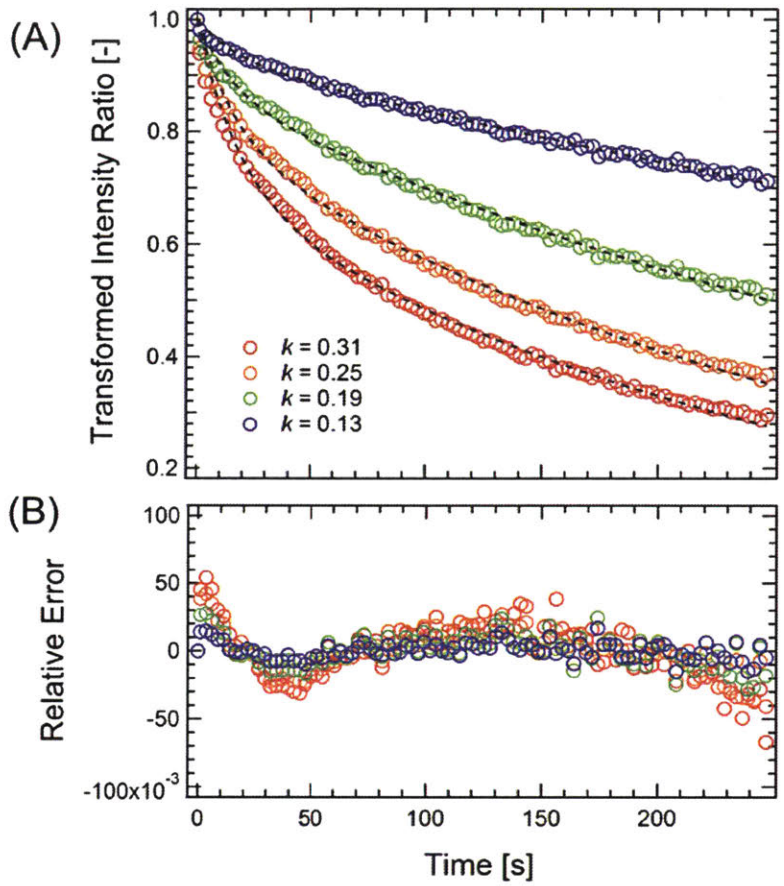

Figure 6-6. Representative time-dependent decay profiles of the transformed intensity ratio (A) and corresponding residuals (B) at various k values (unit: μm^{-1}). The line are fits to the experimental data described by eq 6-28.

models by examining the characteristics of the decay profiles. Specifically, the effective diffusion model should only result in a single exponential decay whereas the two-state model leads to a sum of two exponentials as described by eq 6-28. As shown in Figure 6-6, the function can adequately describe the experimental data, but there are noticeable difference between the fits and the data, especially in the short time regime. Future effort should explore new functional forms for fitting, such as using stretched exponential functions. In addition, the acquisition time setting in FRAP experiments can be optimized to increase the data point density at short times to better quantify

the fast decay. It should also be mentioned that only data with a k value larger than 0.12 μm^{-1} is decision is mainly motivated by the fact that the decay profiles are not obvious at smaller k values. analyzed, where the normalized intensity decay from 1.0 down to a value of 0.75 or below. This decision is mainly motivated by the fact that the decay profiles are not obvious at smaller k values.

Experimental results using the proposed method for FRAP data analysis are shown in Figure 6-7. Since estimation of the small time constants might not be reliable due to the existing systematic errors, here only the large time constants are compared. There are several key observations. First, the relation $<\tau>$ vs. d^2 shows a Fickian scaling, in good agreement with the previous measurement results enabled by FRS using ONS as the photochromic dye. Second, comparison the FRAP measurement with the FRS results where proteins are labeled by fluorescein in both cases, the relaxation time constants are nearly identical at $d^2 = 1009\ \mu m^2$. Third, using the proposed FRAP data analysis method on one FRAP experiment, the relation $<\tau>$ vs. d^2 can be revealed in a d^2 range spanning nearly one order of magnitude. This suggests that the FRAP might be used as an efficient method to probe diffusion on large length scales.

6.5. Conclusions

In summary, self-diffusion of associative coiled-coil proteins was separately measured by forced Rayleigh scattering (FRS) and fluorescence recovery after photobleaching (FRAP) using fluorescein as the photochromic/fluorescent dye. A new method is proposed to analyze FRAP data using the two-state model. A direct comparison of the diffusion measurements by FRS and FRAP suggests consistency between the two experimental efforts.

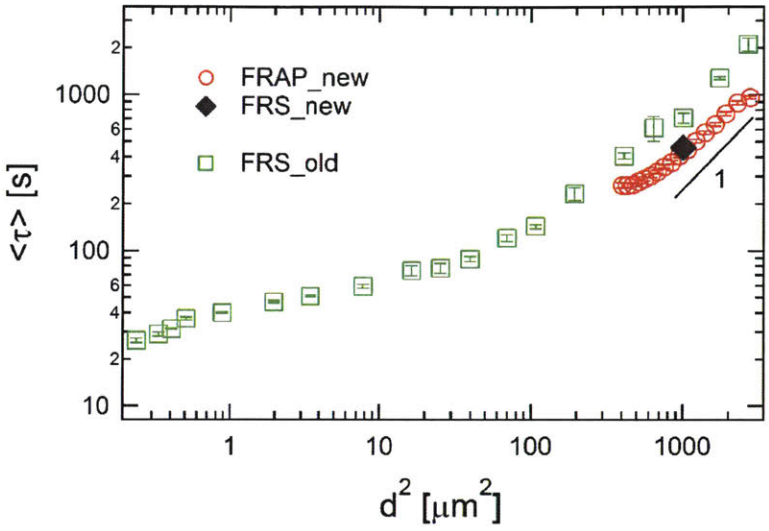

Figure 6-7. Comparison of the relation $<\tau>$ vs. d^2 in different measurements.

6.6. References

1. Campoy-Quiles, M.; Ferenczi, T.; Agostinelli, T.; Etchegoin, P. G.; Kim, Y.; Anthopoulos, T. D.; Stavrinou, P. N.; Bradley, D. D. C.; Nelson, J. Morphology Evolution Via Self-Organization and Lateral and Vertical Diffusion in Polymer:Fullerene Solar Cell Blends. *Nat Mater* 2008, 7, 158-164.

2. Keith, H. D.; Padden, F. J. Influence of Reptation on Localized Diffusion in Crystallizing Polymers. *Journal of Polymer Science Part B: Polymer Physics* 1987, 25, 229-242.

3. Gilbert, J. B.; Rubner, M. F.; Cohen, R. E. Depth-Profiling X-Ray Photoelectron Spectroscopy (Xps) Analysis of Interlayer Diffusion in Polyelectrolyte Multilayers. *Proceedings of the National Academy of Sciences* 2013, 110, 6651-6656.

4. Xu, L.; Selin, V.; Zhuk, A.; Ankner, J. F.; Sukhishvili, S. A. Molecular Weight Dependence of Polymer Chain Mobility within Multilayer Films. *ACS Macro Letters* 2013, 2, 865-868.

5. Schlögl, S.; Trutschel, M.-L.; Chassé, W.; Riess, G.; Saalwächter, K. Entanglement Effects in Elastomers: Macroscopic Vs Microscopic Properties. *Macromolecules* 2014, 47, 2759-2773.

6. Tang, S.; Glassman, M. J.; Li, S.; Socrate, S.; Olsen, B. D. Oxidatively Responsive Chain Extension to Entangle Engineered Protein Hydrogels. *Macromolecules* 2014, 47, 791-799.

7. Tang, S.; Olsen, B. Controlling Topological Entanglement in Engineered Protein Hydrogels with a Variety of Thiol Coupling Chemistries. *Frontiers in Chemistry* 2014, 2.

8. Tang, S.; Wang, M.; Olsen, B. D. Anomalous Self-Diffusion and Sticky Rouse Dynamics in Associative Protein Hydrogels. *Journal of the American Chemical Society* 2015, 137, 3946-3957.

9. Masaro, L.; Zhu, X. X. Physical Models of Diffusion for Polymer Solutions, Gels and Solids. *Progress in Polymer Science* 1999, 24, 731-775.

10. Rubinstein, M.; Colby, R. H. *Polymer Physics*. Oxford University Press: Oxford ; New York, 2003; p xi, 440 p.

11. Watanabe, H. Viscoelasticity and Dynamics of Entangled Polymers. *Progress in Polymer Science* 1999, 24, 1253-1403.

12. McLeish, T. C. B. Tube Theory of Entangled Polymer Dynamics. *Advances in Physics* 2002, 51, 1379-1527.

13. Habuchi, S.; Fujiwara, S.; Yamamoto, T.; Vacha, M.; Tezuka, Y. Single-Molecule Study on Polymer Diffusion in a Melt State: Effect of Chain Topology. *Analytical Chemistry* 2013, 85, 7369-7376.

14. Wang, M.; Timachova, K.; Olsen, B. D. Experimental Measurement of Coil–Rod–Coil Block Copolymer Tracer Diffusion through Entangled Coil Homopolymers. *Macromolecules* 2013, 46, 1651-1658.

15. Wang, M.; Alexander-Katz, A.; Olsen, B. D. Diffusion of Entangled Rod–Coil Block Copolymers. *ACS Macro Letters* 2012, 1, 676-680.

16. Wang, M.; Timachova, K.; Olsen, B. D. Self-Diffusion and Constraint Release in Isotropic Entangled Rod–Coil Block Copolymers. *Macromolecules* 2015, 48, 3121-3129.

17. Odijk, T. The Statistics and Dynamics of Confined or Entangled Stiff Polymers. *Macromolecules* 1983, 16, 1340-1344.

18. Doi, M.; Edwards, S. F. *The Theory of Polymer Dynamics*. Clarendon Press ; Oxford University Press: Oxford Oxfordshire New York, 1986; p xiii, 391 p.

19. Cavicchi, K. A.; Lodge, T. P. Self-Diffusion and Tracer Diffusion in Sphere-Forming Block Copolymers. *Macromolecules* 2003, 36, 7158-7164.

20. Hackelbusch, S.; Rossow, T.; van Assenbergh, P.; Seiffert, S. Chain Dynamics in Supramolecular Polymer Networks. *Macromolecules* 2013, 46, 6273-6286.

21. Rossow, T.; Habicht, A.; Seiffert, S. Relaxation and Dynamics in Transient Polymer Model Networks. *Macromolecules* 2014, 47, 6473-6482.

22. Katzenstein, J. M.; Janes, D. W.; Hocker, H. E.; Chandler, J. K.; Ellison, C. J. Nanoconfined Self-Diffusion of Poly(Isobutyl Methacrylate) in Films with a Thickness-Independent Glass Transition. *Macromolecules* 2012, 45, 1544-1552.

23. Sukhishvili, S. A.; Chen, Y.; Muller, J. D.; Gratton, E.; Schweizer, K. S.; Granick, S. Materials Science: Diffusion of a Polymer /`Pancake/'. *Nature* 2000, 406, 146-146.

24. King, J. T.; Yu, C.; Wilson, W. L.; Granick, S. Super-Resolution Study of Polymer Mobility Fluctuations near C*. *ACS Nano* 2014, 8, 8802-8809.

25. Rittig, F.; Fleischer, G.; Kärger, J.; Papadakis, C. M.; Almdal, K.; Štěpánek, P. Anisotropic Self-Diffusion in a Hexagonally Ordered Asymmetric Pep−Pdms Diblock Copolymer Studied by Pulsed Field Gradient Nmr. *Macromolecules* 1999, 32, 5872-5877.

26. Bachus, R.; Kimmich, R. Molecular Weight and Temperature Dependence of Self-Diffusion Coefficients in Polyethylene and Polystyrene Melts Investigated Using a Modified N.M.R. Field-Gradient Technique. *Polymer* 1983, 24, 964-970.

27. Segalman, R. A.; Jacobson, A.; Kramer, E. J.; Lustig, S. R. Polymer Diffusion in Semicrystalline Polymers Using Secondary Ion Mass Spectroscopy. *Macromolecules* 2004, 37, 2613-2617.

28. Ott, A.; Bouchaud, J. P.; Langevin, D.; Urbach, W. Anomalous Diffusion in ``Living Polymers'': A Genuine Levy Flight? *Physical Review Letters* 1990, 65, 2201-2204.

29. Meyvis, T. K. L.; De Smedt, S. C.; Van Oostveldt, P.; Demeester, J. Fluorescence Recovery after Photobleaching: A Versatile Tool for Mobility and Interaction Measurements in Pharmaceutical Research. *Pharmaceutical Research* 16, 1153-1162.

30. Klonis, N.; Rug, M.; Harper, I.; Wickham, M.; Cowman, A.; Tilley, L. Fluorescence Photobleaching Analysis for the Study of Cellular Dynamics. *European Biophysics Journal* 2014, 31, 36-51.

31. Lorén, N.; Hagman, J.; Jonasson, J. K.; Deschout, H.; Bernin, D.; Cella-Zanacchi, F.; Diaspro, A.; McNally, J. G.; Ameloot, M.; Smisdom, N., *et al.* Fluorescence Recovery after Photobleaching in Material and Life Sciences: Putting Theory into Practice. *Quarterly Reviews of Biophysics* 2015, 48, 323-387.

32. Seiffert, S.; Oppermann, W. Systematic Evaluation of Frap Experiments Performed in a Confocal Laser Scanning Microscope. *Journal of Microscopy* 2005, 220, 20-30.

33. Berk, D. A.; Yuan, F.; Leunig, M.; Jain, R. K. Fluorescence Photobleaching with Spatial Fourier Analysis: Measurement of Diffusion in Light-Scattering Media. *Biophysical Journal* 1993, 65, 2428-2436.

34. Braeckmans, K.; Peeters, L.; Sanders, N. N.; De Smedt, S. C.; Demeester, J. Three-Dimensional Fluorescence Recovery after Photobleaching with the Confocal Scanning Laser Microscope. *Biophysical Journal* 2003, 85, 2240-2252.

35. Hauser, G. I.; Seiffert, S.; Oppermann, W. Systematic Evaluation of Frap Experiments Performed in a Confocal Laser Scanning Microscope – Part Ii: Multiple Diffusion Processes. *Journal of Microscopy* 2008, 230, 353-362.

36. Jönsson, P.; Jonsson, M. P.; Tegenfeldt, J. O.; Höök, F. A Method Improving the Accuracy of Fluorescence Recovery after Photobleaching Analysis. *Biophysical Journal* 2008, 95, 5334-5348.

37. Sprague, B. L.; Pego, R. L.; Stavreva, D. A.; McNally, J. G. Analysis of Binding Reactions by Fluorescence Recovery after Photobleaching. *Biophysical Journal* 2004, 86, 3473-3495.

38. Sprague, B. L.; Müller, F.; Pego, R. L.; Bungay, P. M.; Stavreva, D. A.; McNally, J. G. Analysis of Binding at a Single Spatially Localized Cluster of Binding Sites by Fluorescence Recovery after Photobleaching. *Biophysical Journal* 2006, 91, 1169-1191.

39. Kang, M.; Kenworthy, A. K. A Closed-Form Analytic Expression for Frap Formula for the Binding Diffusion Model. *Biophysical Journal* 2008, 95, L13-L15.

40. Travascio, F.; Zhao, W.; Gu, W. Y. Characterization of Anisotropic Diffusion Tensor of Solute in Tissue by Video-Frap Imaging Technique. *Annals of Biomedical Engineering* 2009, 37, 813-823.

Chapter 7 Oxidatively Responsive Chain Extension to Entangle Engineered Protein Hydrogels

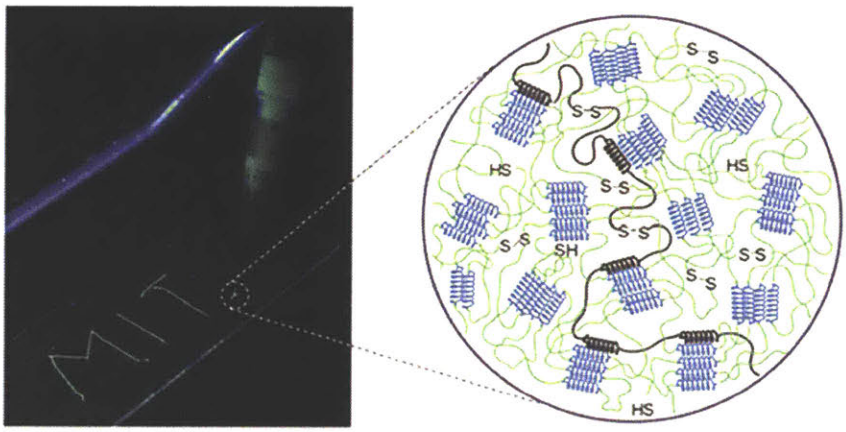

Engineering artificial protein hydrogels for medical applications requires precise control over their mechanical properties, including stiffness, toughness, extensibility and stability in the physiological environment. Here we demonstrate topological entanglement as an effective strategy to robustly increase the mechanical tunability of a transient hydrogel network based on coiled-coil interactions. Chain extension and entanglement are achieved by coupling the cysteine residues near the N- and C- termini, and the resulting chain distribution is found to agree with the Jacobson-Stockmayer theory. By exploiting the reversible nature of the disulfide bonds, the entanglement effect can be switched on and off by redox stimuli. With the presence of entanglements, hydrogels exhibit a 7.2-fold enhanced creep resistance and a suppressed erosion rate by a factor of 5.8, making the gels more mechanically stable in a physiologically relevant open

system. While hardly affecting material stiffness (only resulting in a 1.5-fold increase in the plateau modulus), the entanglements remarkably lead to hydrogels with a toughness of 65,000 J/m^3 and extensibility to approximately 3,000% engineering strain, which enables the preparation of tough yet soft tissue simulants. This improvement in mechanical properties resembles that from double-network hydrogels, but is achieved with the use of a single associating network and topological entanglement. Therefore, redox-triggered chain entanglement offers an effective approach for constructing mechanically enhanced and responsive injectable hydrogels.

7.1. Introduction

Artificially engineered protein hydrogels have been widely investigated for regenerative medicine, tissue engineering and other biomedical applications.[1-3] Advances in molecular biology and protein biosyntheses allow precise control of the protein structure, enabling bottom-up design of the gel mechanical properties. These mechanical properties play an important role in controlling cell-material interactions. For example, the differentiation of stem cells is greatly influenced by matrix elasticity,[4, 5] and an abnormal stiffness of the matrix can alter the biological responses of cells.[6] By incorporating different modular building blocks such as coiled-coils or elastin-like domains, engineered protein hydrogels can achieve a variety of mechanical properties, including elasticity, toughness and resilience.[7-9] In particular, physical hydrogels with coiled-coil associating domains show shear-banding flow followed by remarkably rapid self-healing, which enables their use as injectable cell-encapsulated materials with high cell viability post-injection.[10] Moreover, the binding affinity of coiled-coils can be changed by pH, ionic strength and temperature, allowing the mechanical properties of hydrogels to be tuned by external stimuli.[9, 11, 12]

Coiled-coil proteins have well-defined molecular structures, including monodisperse primary chains and sequence-defined coiled-coil domains that make them interesting model

systems where the structure-property relationships, including thermodynamics (such as equilibrium modulus) and kinetics (such as stress relaxation) of gels can be compared with a broad spectrum of polymer physics theories.[13-18] The physics of transient networks has attracted great interest since 1946, when Green and Tobolsky first proposed a kinetic model to capture the relaxation dynamics of transient networks.[15] Tanaka and Edwards generalized the Green-Tobolsky theory by realizing that the deconstruction and recreation rates of the network junctions can be different, depending on the end-to-end distance of the network strand.[16, 19-21] Annable et al. examined the rheology of hydrophobic ethoxylated urethane associative thickeners (HEUR-AT) in aqueous solution, further demonstrating that the complex network topologies (such as superbridges) impart the concentration dependence of the rheological behaviors to associating polymers.[17] Leibler, Rubinstein, Colby and Semenov proposed the sticky Rouse and sticky reptation theories to describe the relaxation dynamics of polymers with pendent associating groups.[22-24] They find that many material properties, such as the relaxation time and the zero-shear-rate viscosity, have a strong dependence on the concentration. The sticky Rouse and sticky reptation models have found the success in explaining some of the viscoelastic behaviors of many supramolecular polymer networks.[25-27] In addition to these studies of polymers with associating groups covalently bonded along the main chain, several authors have investigated polymers with dimeric associating groups localized only at the chain ends, capable of chain extension but not network formation. Cates proposed a living polymer model to study polymers with end-functionalized dimeric associating domains.[28] The model reveals several relaxation mechanisms, depending on the ratio of the lifetime of the associating groups to the reptation time, and ratio of the entanglement length to the average length of polymers. Many experimental studies confirm

Cates' theory, especially those investigating polymers with self-complementary H-bonding motifs.[29, 30]

Understanding the structure-property relationship of associating polymers as well as reversible transient networks enables preparation of physical hydrogels with versatile mechanical properties; however, there are several drawbacks of physically crosslinked injectable hydrogels that limit their practical applications. These gels generally undergo rapid erosion (dominated by surface erosion) when physical interactions governing the transient network relax due to thermal fluctuations.[7, 31] In addition, a relatively low yield stress makes these hydrogels susceptible to both creep and mechanical failure if they are stressed during use.[10] Finally, physically crosslinked hydrogels are usually brittle, exhibiting low toughness and extensibility. Although in certain cases, many of these shortcomings can be addressed by chemically crosslinking the protein strands,[32-34] the injectable flow behavior is lost.

While polymer hydrogels are traditionally brittle, high molecular weight polymer melts are tough due to the presence of physical entanglements between polymer chains. These entanglements impart elastic recoil[35] and strain hardening behavior[36, 37] to polymer liquids. The low polymer concentration in gels requires a very high polymer molecular weight to achieve chain entanglements, and a few authors have reported chain entanglement in chemically crosslinked synthetic polymer gels, where the molecular weight of network strand exceeds the entanglement molecular weight.[38, 39] However, it has not been realized in biocompatible and mechanically tunable engineered protein hydrogels. The molecular weight of engineered proteins achievable in high yield by biosyntheses is limited; therefore, an alternative relies on efficient coupling reactions to link protein molecules to produce long chains.[40-43] Disulfide formation *via* thiol oxidation is a protein conjugation strategy that takes advantages of natural cysteine residues, does not require

additional (potentially toxic) chemical modifiers, and can be driven to high yield with simple synthetic procedures. In addition, the disulfide bonds can break down in a reducing environment, providing an opportunity to control the molecular architecture with redox stimuli, and producing oxidatively responsive materials. Recently, responsive disulfide formation has been used to stabilize self-assembled nanofibers from peptide amphiphiles[44] and to chemically crosslink coiled-coil domains in artificially engineered protein hydrogels.[45] Although high molecular weight synthetic copolymers have been prepared by oxidation of thiols on the polymer chain ends,[46] to the best of our knowledge, this strategy has not been applied to synthesize high molecular weight protein gels.

Herein, we demonstrate oxidatively-triggered disulfide bond formation as a method to prepare high molecular weight artificially engineered protein hydrogels containing coiled-coil associations. Under appropriate processing conditions these gels may be prepared in a physically entangled state. The physical entanglements lead to enhanced toughness, similar to that of double network hydrogels, with a single network. Unlike other approaches to gel toughening, large improvements in toughness and extensibility are demonstrated with only a small change in the hydrogel stiffness. Finally, it is shown that the oxidative trigger may be used to turn the entanglements on and off, leading to responsive transitions between a brittle and tough state that enable entanglements and the resulting mechanical property improvements to be incorporated into injectable biomaterials.

7.2. Experimental Section

Protein Synthesis and Purification. The genes encoding for Cys-P_4-Cys and P_4 were prepared and transformed into the SG13009 strain of *Escherichia coli* for protein expression by

Glassman *et al.*[47]. Proteins were expressed at 37 °C in 1 L TB culture in a shaker flask. The expression was induced by 1.0 mM isopropyl β-D-1-thiogalactopyranoside (IPTG) at an optical density of 0.9–1.0. Six hours after induction, the cells were harvested by centrifugation at 4 °C and 6,000 RPM for 10 min, and the cell pellets were stored at -80 °C overnight. The cells were resuspended in lysis buffer (10 mM Tris, 1 mM EDTA, 100 mM NaCl, 5 mM $MgCl_2$, pH 7.5). Lysozyme (100 mg) was added and the mixture was incubated at 4 °C for 2 h, followed by sonication for 30 min. The lysate was centrifuged at 4 °C and 9,000 RPM for 30 min. DNAse I and RNAse A (2 mg each) were added to the clarified lysate and the mixture was incubated at 37 °C for 2 h. The lysate was further denatured by 8 M urea, buffered with 100 mM phosphate, and 20 mM β-mercaptoethanol. Protein was first purified by precipitation in 20% – 30% ammonium sulfate and was further purified by anionic exchange using QAE-Sephadex A-50 resin (GE Healthcare) in 6 M urea, 20 mM Tris and 20 mM β-mercaptoethanol as wash buffer. Impurities were eluted using up to 100 mM NaCl and protein was eluted at 1 M NaCl. The purity was assessed by SDS-PAGE (Figure D-1). A typical expression yield was 150 mg/L.

Oxidation of Cysteine Residues to Trigger Chain Extension. Protein was dissolved in a buffer with 6 M urea, 20 mM Tris and pH 8.0 to a final concentration of 10 (w/v)%. To reduce the existing disulfide bonds during protein purification, a two-fold excess TCEP was added. The mixture was allowed to stir for a week at 4 °C. Oxidized protein was dialyzed and lyophilized. Oxidation can also be triggered by other methods (Figure D-2): (1) Small amount of hydrogen peroxide was added to the reduced hydrogel, followed by mechanical mixing to ensure homogeneous distribution of hydrogen peroxide; (2) Chain extended protein can be reduced by the addition of a five-fold excess of DTT, following by periodic mechanical mixing to allow air oxidation.

Sodium Dodecyl Sulfate-Polyacrylamide Gel Electrophoresis (SDS-PAGE) Analysis of Chain Extension Reaction. The molecular weight distribution of the product mixture after chain extension reaction was analyzed by SDS-PAGE (Mini-PROTEAN® TGX™ gels, 4-15%, BioRad) under non-reducing condition at 150 V. The linear and ring species were assumed to have the same electrophoretic mobility. The weight fraction of species was estimated using densitometry with BioRad Image Lab software.

Circular Dichroism (CD). Proteins were dissolved in phosphate buffer to a final concentration of 20 μM. Protein solutions were further filtered through 0.2 μm PES filters. The protein concentrations after filtering were determined spectrophotometrically. CD spectra were recorded on an Aviv Model 202 Circular Dichroism Spectrometer (Figure D-3). Experiments were performed in a rectangular cell with a path length of 1 mm. Measurement was taken from 260 nm to 195 nm with 1 nm resolution and an averaging time of 10 s.

Phosphate Buffer Preparation. The phosphate buffer was prepared by dissolving 13 mmol $NaH_2PO_4 \cdot H_2O$, 87 mmol $Na_2HPO_4 \cdot 7H_2O$ in 1L MilliQ water to reach a final pH of 7.6, and was further filtered through 0.2 μm PES filters for sterilization.

Rheology. Frequency sweep and creep experiments were performed on an Anton Paar MCR 301 rheometer. A cone-plate geometry (25 mm and 1° cone) was used with TruGap® accessories. Protein samples were hydrated in phosphate buffer to a desired concentration for two days before the experiment. Samples were centrifuged to remove bubbles before loading onto the rheometer, and the edge of hydrogel sample was coated with mineral oil to minimize water evaporation. To eliminate thermal and shear history, samples were heated to 90 °C and cooled to 25 °C at 5 °C/min. This brief thermal treatment unfolds the coiled-coil domains upon heating above 52 °C,[9] enabling rapid stress relaxation in the protein network. Frequency sweep

experiments were performed from 100 rad/s to 0.001 rad/s at 1% strain, which was confirmed to be in the linear viscoelastic regime (LVE) using strain sweep experiments. In creep experiments, samples were subjected to a constant load for 2 h, after which the load was subsequently removed to examine the recovery behavior for 2 h. Four different loading conditions (25 Pa, 50 Pa, 75 Pa and 100 Pa) were tested to ensure that the test was in the linear regime.

Surface Erosion. Protein hydrogel samples were hydrated in phosphate buffer to a final concentration of 15% (w/v) for two days before the erosion experiment. Approximately 50 μL of protein hydrogel samples were loaded into a cylinder well with 6.4 mm in diameter and 8.5 mm in height in a 96-well plate. Hydrogels were centrifuged for 2 h at 4,000 g to flatten the hydrogel surface and the thickness of each gel sample was 1.50 ± 0.12 mm. Extra phosphate buffer (250 μL) was added into each well. The erosion experiment was performed at 35 °C without mechanical agitation. The protein concentration in the supernatant was measured spectrophotometrically, with each measurement performed in triplicate.

Uniaxial Compression. Hydrogel specimens were pressed into cylindrical Teflon molds of 8 mm diameter and 8 mm height. Samples were annealed in a humidified chamber at 37 °C for 3 h and stored in fridge at 4 °C for 2 days to allow stress relaxation. No visible defects were observed within the samples. Uniaxial compression experiments were performed on a Zwick/Roell Z2.5/TS1S materials testing machine and TestXpert V10.1 master software (Ulm, Germany) with a 20 N load cell. All tests were performed at room temperature, 24 ± 1 °C. A layer of soapy water was used to provide lubrication during compression. A preload of approximately 0.005 – 0.01 N was applied to samples to initiate contact. Two test procedures were used in this study. (A) Compression experiments were performed at three different nominal strain rates (0.1%/s, 1%/s and 10%/s) to a final true strain of 160%, followed by unloading to 0% strain at a

nominal strain rate of 10%/s. (B) Interval loading at 1% s^{-1} nominal strain rate to 160% true strain, with partial unloading (10%/s nominal strain rate) segments at 40%, 80%, 120% to probe the relaxation behavior.

Uniaxial Tension. For better visualization, hydrogels were hydrated in phosphate buffer supplemented with 0.1 mg/mL fluoresceinamine (isomer I, Sigma). Hydrogel specimens were prepared in rectangular Teflon molds 20 mm in width, 28 mm in length and 2 mm in thickness. Samples were annealed in a humidified chamber at 37 °C for 3 h and stored in fridge at 4 °C for 2 days to allow stress relaxation. A custom designed cutter was used to obtain a dogbone shaped tensile specimen with a neck width of 4 mm (Figure D-4). No visible defects were observed after cutting. Uniaxial tension experiments were performed on a Zwick/Roell Z2.5/TS1S materials testing machine and TestXpert V10.1 master software (Ulm, Germany) with a 20 N load cell. All tests were performed at room temperature, 24 ± 1 °C. Sandpaper was glued to the grips to provide friction and to ensure that the sample did not slip. The ramp-relaxation testing protocol consisted of loading ramps alternated with relaxation intervals of 600 seconds, until specimen failure. During the loading ramps the specimens were stretched at an average true strain rate at 0.06 1/s to increasing levels of engineering strain (625%, 1,250% and 2,500%, 3,750%) until mechanical failure. Three independent experiments were performed and the error bars reported in the text are the standard deviations of the measurement. To study the effect of the wait period on the mechanical performance of gels, a one minute wait time was used as control (Figure D-7).

7.3. Results and Discussion

Oxidatively Responsive Topological Entanglements for Mechanical Reinforcement. Chain extension by thiol coupling in concentrated protein hydrogels leads to topological

entanglement as the molecular weight is increased during macromolecular polycondensation, providing a basis for oxidatively responsive changes in gel mechanics. The artificial proteins Cys-P_4-Cys and P_4 (Figure D-1) are chosen as model systems to study the chain extension effect: both proteins contain four coiled-coil domains (P) separated by flexible polyelectrolyte blocks (C_{10}) (Figure 7-1A), but cysteine residues are engineered into Cys-P_4-Cys near the N- and C- termini. Hydrophobic interactions and salt bridging drive the coiled-coil domains to form pentameric bundles, providing physical crosslinks in the hydrogel. The chain extension reaction by disulfide bond formation leads to the formation of high molecular weight products. Densitometry analysis using SDS-PAGE of the oxidation reaction mixture provides an estimation of the molecular weight distribution, which is expected to follow the Jacobson-Stockmayer distribution.[48] This theory assumes that the chain distribution of the linear species obeys the Flory-Schulz distribution, and it additionally accounts for the effect of intramolecular polycondensation (ring formation). A nonlinear regression fit to this model gives an overall end-group conversion of $p = 0.712 \pm 0.061$ and a ring weight fraction of $w_r = 0.262 \pm 0.148$. The weight average degrees of polymerization of the chain fraction, the ring fraction, and the system are $\bar{X}_{cw} = 4.13 \pm 1.17$, $\bar{X}_{rw} = 1.42 \pm 0.13$, and $\bar{X}_w = 3.43 \pm 0.95$, corresponding to weight average molar mass of $\bar{M}_{cw} = 261.0 \pm 73.9$ kDa, $\bar{M}_{rw} = 89.7 \pm 8.2$ kDa, and $\bar{M}_w = 216.8 \pm 60.0$ kDa (Figure 1B, see Appendix D for calculation details). Despite the difficulty inherent in achieving high conversion by coupling high molar mass proteins, a significant fraction of high molecular weight chain entangled products was formed. Compared to the theoretical distribution, the monomeric protein has a smaller fraction of loops. This discrepancy may be due in part to approximations in the Jacobson-Stockmayer theory (Gaussian chain statistics and equal reactivity of endgroups) or also due to a fraction of cysteine residues that are unreactive (i.e. due to oxidation to sulfones). Circular dichroism (CD)

experiments reveal that chain extension does not affect the folded structure of coiled-coils (Figure D-3), suggesting that the folded coiled-coil junctions are unperturbed by chain extension.

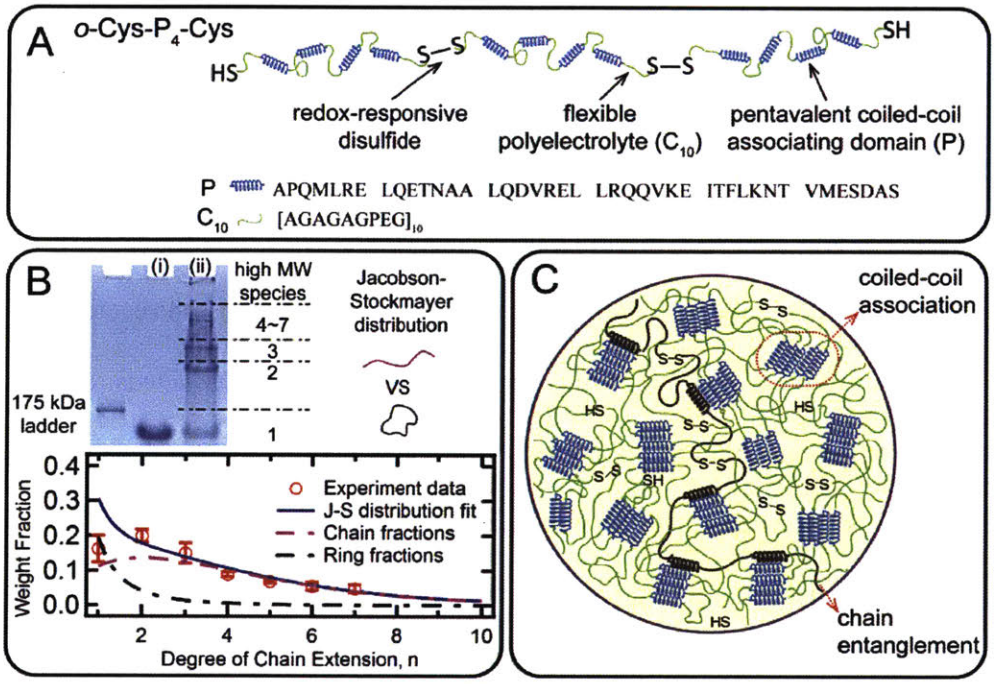

Figure 7-1. Illustration of the hydrogel design. (A) Molecular design of oxidatively-responsive chain extended artificially engineered proteins. (B) SDS-PAGE characterizing the molecular weight and its distribution of extended chains: (i) Cys-P_4-Cys before oxidation reaction, and (ii) chain extended protein mixture. The molecular weight distribution is analyzed by densitometry and further fit to the Jacobson-Stockmayer distribution that accounts for the intramolecular looping. Error bars represent the standard deviations of three separate experiments. (C) Schematic illustration of networks combining coiled-coil association and chain entanglement in protein hydrogels.

Chain entanglements manifest in the linear viscoelastic response of the protein gels through a small increase in the high frequency plateau of the storage modulus and the appearance of a second plateau at low frequency (Figure 7-2A). At frequencies from 10 rad/s to 100 rad/s in small amplitude oscillatory shear (SAOS), both P_4 and *o*-Cys-P_4-Cys (oxidized, chain extended Cys-P_4-

Cys) display a plateau storage modulus (G'_∞), at 10,500 ± 120 Pa and 15,300 ± 650 Pa, respectively. However, for P_4, a crossover in G' and G'' is observed at approximately 0.35 rad/s; below this frequency, G' and G'' approach to the terminal relaxation behavior ($G' \sim \omega^2$ and $G'' \sim \omega$). This qualitative behavior is typical for physical gels.[10, 49] A noticeable deviation from the Rouse-like behavior in this low frequency regime (starting from 0.01 rad/s) might be due to the effect of coiled-coil association on the Rouse relaxation, resembling unentangled transient polymer networks with blocky H-bonding domains.[27] In contrast, the simple oxidative chain extension of Cys-P_4-Cys yields a gel where G' is larger than G'' over the entire frequency window, and a second plateau modulus (~ 900 Pa) is observed at low frequencies down to 10^{-3} rad/s. This behavior is qualitatively similar to entangled polymer solutions and melts.[50]

To prove that this low frequency plateau modulus results from the formation of topological chain entanglements due to an increase in the molecular weight of *o*-Cys-P_4-Cys, two simple tests are performed. First, chain extension is shown to be reversible, which provides the opportunity to turn entanglement on and off by redox stimuli. The addition of mild reducing agents such as TCEP to *o*-Cys-P_4-Cys chain extended hydrogels causes the entanglement effects on mechanical properties to disappear as the molecular weight of the protein is reduced (Figure D-2A). The term "mild" indicates that the added reagents do not chemically alter amino acid functional groups (except cysteines) or the protein structure. The robustness of thiol oxidation as a method to introduce entanglements via chain extension is also demonstrated by the use of other oxidation

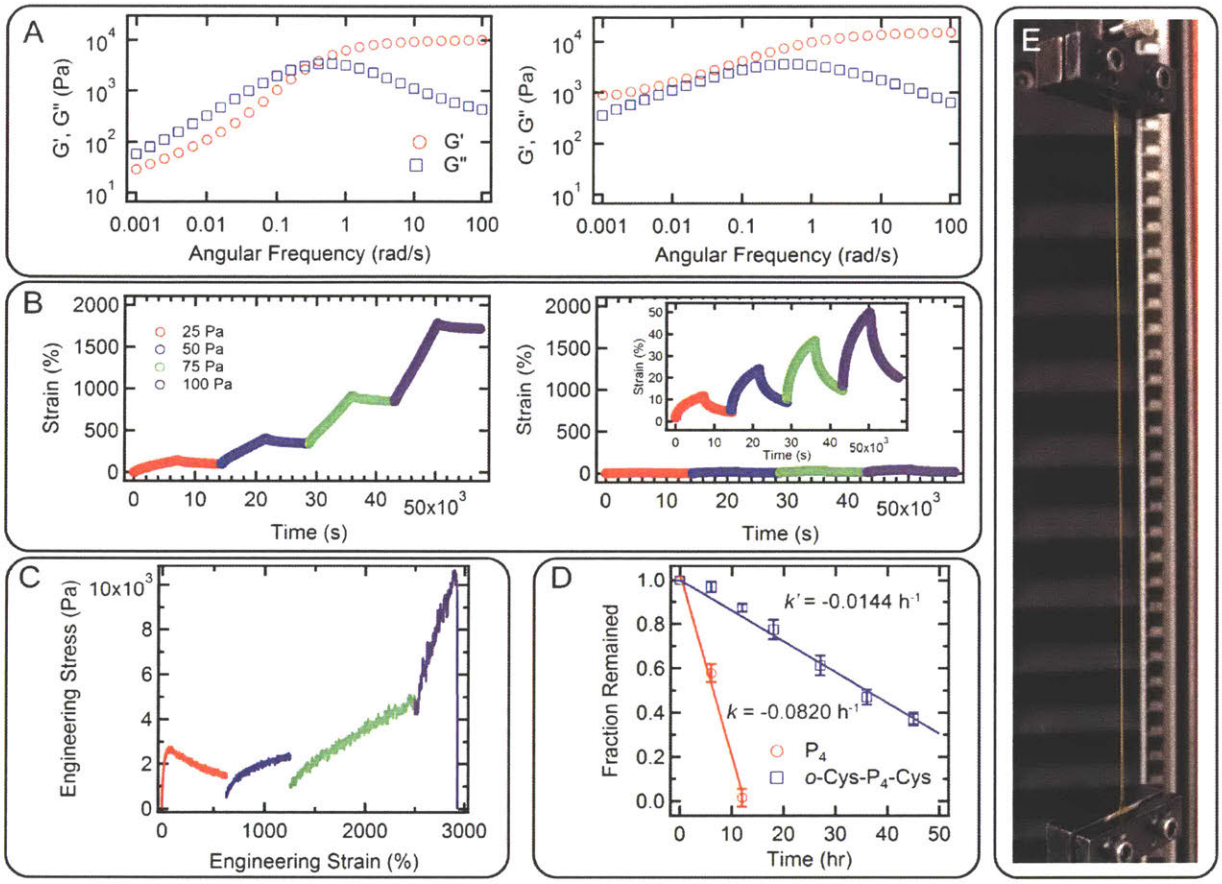

Figure 7-2. Comparison of the mechanical response of unextended gels and chain extended gels. (A) The effect of chain entanglement is demonstrated in the linear viscoelastic domain: frequency sweeps of hydrogel P_4 (left) and *o*-Cys-P_4-Cys (right) at 15% (w/v) at 25 °C. (B) Compared to P_4 (left), the entangled *o*-Cys-P_4-Cys hydrogel (right) shows significant creep resistance and elastic recovery. The inset in the right panel shows the same data magnified to enhance detail. Measurements were performed on 15% (w/v) samples at 25 °C. (C) Uniaxial tensile experiment (25 °C) on *o*-Cys-P4-Cys at 15% (w/v) showing remarkable improvement on the hydrogel's toughness and extensibility upon introducing entanglement. (D) Surface erosion of hydrogel P_4 and *o*-Cys-P_4-Cys at 15% (w/v) at 35 °C. The erosion rate was estimated from a linear fit of the data. Error bars represent the standard deviations of three separate experiments. (E) A stretched dogbone gel specimen *o*-Cys-P_4-Cys at 15% (w/v) during tensile loading at 3,100% engineering strain.

methods (Figure D-2B). It is shown that the entanglement forms by adding a mild oxidant H_2O_2 to the reduced Cys-P_4-Cys hydrogel, as evidenced by the similar properties observed in SAOS experiment. Second, the low frequency plateau modulus is shown to weakly depend on temperature. The entanglement plateau becomes more obvious as the frequency sweep spectrum shifts to the high frequency regime at elevated temperature (Figure D-5); however, the physical associations among coiled-coils show a strongly temperature-dependent relaxation (Figure D-6). The coiled-coil relaxation time is estimated from the frequency where a maximum in G'' occurs in the high frequency regime, $\tau_c = 2\pi/\omega_h$.[22, 51] In general, the coiled-coil relaxation time decreases with increasing temperature according to the Arrhenius law, $\tau_c \sim \exp(1/T)$, suggesting that the hydrogel properties are predominantly governed by association-disassociation dynamics in the high frequency regime.[52]

The presence of chain entanglements in these protein gels creates many of the same enhancements observed in double network hydrogels,[47, 53-55] but with the use of a single network with topological entanglement. While hydrogel P_4 is so brittle that its toughness and extensibility could not be measured in tensile loading, the entangled gels show enhanced toughness of 65,000 ± 24,500 J/m due to their dramatic increase in extensibility under a designed test profile, with failure engineering strain of 2,970 ± 860% (Figure 7-2C, the relationship between the engineering stress and strain and the true stress and strain can be found in Appendix D). It is also particularly noteworthy that the presence of these topological entanglements leads to large increases in toughness and extensibility without a large increase in the small-strain modulus, which provides an effective approach to prepare tough yet soft hydrogels. Chain entanglements also lead to a decrease in the irrecoverable creep compliance by a factor of 7.2, from 0.227 1/Pa for P_4 to 1.63 1/Pa for *o*-Cys-P_4-Cys (Figure 7-2B), as well as a decrease in the surface erosion rate by a factor

of 5.8 (Figure 7-2D), making the gels significantly more robust under sustained load and in open systems, where physical hydrogels have traditionally had a performance disadvantage relative to other materials.[31, 45, 56]

While the P_4 hydrogel creeps readily under all examined loads (from 25 Pa to 100 Pa) and reaches a final strain of ~ 1,700% after four steps of loading-unloading, hydrogel *o*-Cys-P_4-Cys only strains to 20% under the same conditions, almost two orders of magnitudes lower than that of P_4. Elastic recovery after loading in the linear regime is 80% ~ 90%, comparable to some synthetic shape-memory elastomers[57, 58] due to the elastic recoil of the entangled chains. Interestingly, unlike many double network hydrogels with chemical crosslinks, the chain extended hydrogel is still hand-injectable through a 26-gauge needle even with the presence of chain entanglements (Figure 7-3). To investigate the flow behavior during injection, the gel is subjected to steady shear for 50 strain units at 1 1/s strain rate. The rupture of the transient network occurs within less than 10 s, with its shear modulus dropping from 11,200 Pa to 380 Pa. Further shear leads to a continuous slow decrease in the modulus. The recovery behavior after shear is monitored under SAOS at 1 rad/s for 1,000 s. It is found that the mechanical strength of gels rapidly recovers to more than 99% of its original modulus within several seconds. Such nearly-instantaneous recovery kinetics is consistent with observation in other protein hydrogels with the same associating coiled-coil domains.[10]

From Chain Extension to Topological Chain Entanglement. Chain extension leads to topological entanglement when the protein concentration is above the critical entanglement concentration, as is the case for entangled polymer solutions and melts. The contribution of chain extension/entanglement to the network modulus is examined by comparing the frequency spectra

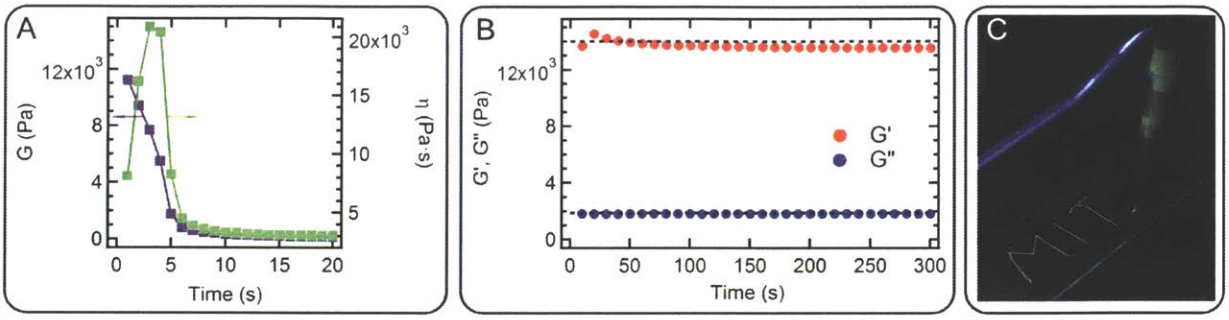

Figure 7-3. Rapid shear and recovery behavior of the hydrogel o-Cys-P_4-Cys at 15% (w/v). (A) Fast drop in shear modulus and viscosity at the start-up of steady shear at 1 1/s strain rate for 50 s. (For clarity, only data from the first 20 s is shown.) (B) Nearly instantaneous recovery of the mechanical properties of gels after shear, examined under SAOS at 1 rad/s and 1 % stain for 1,000 s. (For clarity, only data from the first 300 s is shown.) Dash lines in black showing the original values of G' and G''. (C) Demonstration of the hand-injectability of the chain extended hydrogel through a 26-gauge needle. The concentration of fluorescein is at 0.1 mg/mL in the gels.

of both *o*-Cys-P_4-Cys and P_4 hydrogels at different protein concentrations and temperatures (Figure D-5 and Figure D-6, respectively). At 10.0 and 12.5% (w/v), the entanglement plateau signature is absent in the low-frequency regime, while the entanglement plateau is observed for concentrations of 15.0% (w/v) and above. The observed critical entanglement concentration is close to that estimated using the sticky reptation theory (see calculation in Appendix D). The quantitative relationship between the entanglement plateau modulus and the protein concentration is shown in Figure 7-4A. For entangled polymer solutions,[51] the plateau modulus scales as $G_e \sim \varphi^{\alpha}$, where φ is the volume fraction of the protein in gels. For the *o*-Cys-P_4-Cys gels linear regression yields a concentration scaling exponent of $\alpha = 7.0$. Compared to synthetic polymers that have a typical value of α in the range of 2.0 ~ 2.3, the entanglement plateau modulus of *o*-Cys-P_4-Cys hydrogels depends strongly on the concentration. Two effects may contribute to this

stronger than expected concentration dependence. First, interchain coiled-coil interactions may enhance the long range topological constraints between entangled chains, effectively decreasing the entanglement molecular weight (M_e). M_e in gels at different concentrations can be estimated from the entanglement plateau modulus (Figure 7-4A).[59] According to the tube theory,[60] the dynamic topological interaction can only be observed when the system has a molecular weight larger than M_e. For hydrogels at low protein concentrations, the predicted M_e is larger than 500 kg mol^{-1}. The lack of entanglement comes from the fact that M_e is much larger than the experimentally measured molecular weight for chain extended proteins. Second, topological rearrangement of the coiled-coil network at increasing concentration leads to an increased degree of entanglement in hydrogels. This effect is evidenced by changes in the plateau modulus of the gels. The modulus contributed by the coiled-coil associations is obtained by subtracting the entanglement plateau modulus from the high frequency modulus (Figure 7-4B), and the corresponding number density of the elastically effective chains is calculated based on the affine network theory (Figure 7-4C). It is found that chain extension and entanglement results in an increase in the plateau modulus at high frequency by a factor of 1.32 to 1.69, higher than the theoretical prediction of 1.23 (see Appendix D for calculation details). Although a relatively high ratio is observed at low protein volume fractions, this measurement is in the vicinity of the critical gelation concentration where a small shift in gelation concentration due to chain extension effectively shifts the phase separation boundary, causing the ratio in moduli to increase. At higher concentrations, the increase in the number density of elastically effective chains suggests that chain extension and entanglement restructure the associative protein network. The transformation from intramolecular coiled-coil association to intermolecular association gives the strong concentration dependence of the entanglement plateau, consistent with the sticky reptation theory.[24]

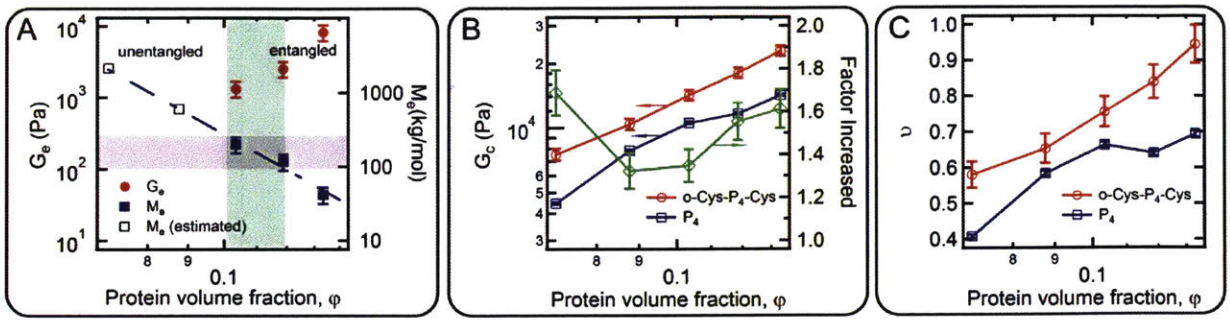

Figure 7-4. The contribution of chain entanglement and coiled-coil association to network mechanics. (A) Entanglement plateau modulus and the entanglement molecular weight as a function of protein concentration. The purple shaded area highlights the estimated molecular weight (from the lowest M_n to the highest M_w) from the analysis based on the Jacobson-Stockmayer theory. The green shaded area marks the experimentally observed onset of chain entanglement. (B) Comparison of plateau modulus contributed by coiled-coil association as a function of protein concentration at 25 °C (red for hydrogel *o*-Cys-P_4-Cys, and blue for hydrogel P_4). Data in green showing the ratio of the two moduli at the same concentration. (C) Comparison of the fractions of elastically effective chains in *o*-Cys-P_4-Cys and P_4. Error bars represent the standard deviations of the measurement. ($N = 3$)

Interactions between Topological Entanglement and Coiled-coil Association. The presence of chain entanglements in the protein gel significantly slows the relaxation of coiled-coil associations, as seen in frequency sweep in SAOS (Figure 7-5A, Figure D-5 and Figure D-6). At low protein concentration (10.0 and 12.5% (w/v)), the relaxation times of coiled-coils in both P_4 and *o*-Cys-P_4-Cys hydrogels are very similar, as determined by $\tau_c = 2\pi/\omega_h$. On the contrary, when the protein concentration exceeds the critical entanglement concentration, the coiled-coil relaxation time in the chain extended hydrogel is two to three times higher than that in the lower molecular weight gel. Although the association-disassociation dynamics of the coiled-coil domain

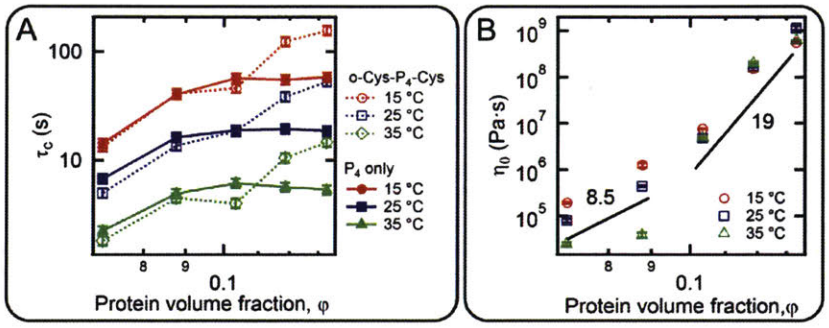

Figure 7-5. The interplay between the coiled-coil association and chain entanglement. (A) Coiled-coil relaxation time as a function of concentration and temperature, determined from the frequency where G" reaches its maximum at the high frequency regime in SAOS. Lines connecting data points are used to guide the eye. (B) Zero-shear rate viscosity of o-Cys-P4-Cys as a function of temperature and concentration, showing that coiled-coil association introduces a very strong concentration dependence of viscosity. Error bars represent the standard deviations of the measurement ($N = 3$).

localizes on a small length scale (the length scale of an alpha helix, ~5 nm), we hypothesize that entanglements on a larger length scale (the length scale of an entangled segment) slow diffusion of the extended protein chains and effectively constrain thermal fluctuation of the coiled-coils, as is predicted by the sticky reptation theory.[22] While the microscopic coiled-coil association and dissociation rates may remain unchanged, the slowed diffusion reduces the ability of the coiled-coil to exchange binding partners. According to sticky reptation theory, it is reasoned that a coiled-coil typically returns to its original cluster after an unsuccessful search to bind to a new cluster, effectively coupling stress relaxation due to coiled-coil strand exchange to the slower reptation dynamics.[24] In addition to entanglements, the slowing of coiled-coil dynamics is likely responsible for some of the observed decrease in creep compliance and erosion rate (Figure 7-2B and Figure 7-2C).

The associating coiled-coil domains, in turn, have effects on reptation. The zero-shear-rate viscosities (η_0) of *o*-Cys-P4-Cys at different temperatures and concentrations, obtained from the inverse of the slope in creep at steady-state,[51] are compared in Figure 7-5B. Below the entanglement concentration, η_0 shows strong dependence on temperature, following Arrhenius law, consistent with the previous argument that coiled-coil association is the exclusive contribution to the network properties in this unentangled regime.[52] On the contrary, in the entangled regime, η_0 shows a stronger dependence on concentration and a weak dependence on temperature (the zero-shear-rate viscosity should be linearly proportional to the temperature in this regime[24]). Over the narrow range of concentration investigated, a power law fit to $\eta_0 \sim \varphi^\beta$ gives an average exponent $\beta = 19$, which is a significantly larger value than the exponent of 3.4 predicted by the tube theory of reptation.[60] In addition, the sticky reptation theory predicts the exponents in the regimes $\varphi_e < \varphi < \varphi_{ren}$, $\varphi_{ren} < \varphi < \varphi_s$ and $\varphi_s < \varphi < \varphi_{le}$ are 6.8, 8.5 and 3.75, respectively.[24] Although the range of concentration studied is not large enough to clearly establish a power law regime, and the average exponent is significantly larger than the ones predicted by the sticky reptation theory, both the experiment and theory demonstrate the strong concentration dependence upon chain entanglement. Furthermore, a key difference between our experimental result and the sticky reptation theory is that coiled-coils form pentameric bundles instead of the dimeric associating domains treated in the theory. The relaxation dynamics of these systems is in contrast to end-associating polymers[28] where bond relaxation leads to changes in the effective chain molecular weight and can relax entanglements.

Mechanical Enhancement in Axial Loading. Topological entanglement significantly affects the rate-dependence and nonlinearity of the large-strain mechanical response of protein gels. The tensile responses of hydrogels *o*-Cys-P4-Cys and P4 cannot be directly compared, as P4

is extremely fragile and the tensile specimens immediately fail at the grips. The mechanical properties of two hydrogels are therefore compared in uniaxial compression at 0.1, 1 and 10%/s nominal strain rates (Figure 7-6A and 7-6B, the definition of the true stress and true strain can be found in Appendix D). The use of true stress-strain enables direct comparison between compression and tension data, and it also reveals the strain hardening behavior at large strains under stretching. The entangled gels display higher initial moduli and flow stress, as well as enhanced entropic stiffening at larger strains. The differences are more significant at low strain rates, consistent with the observations in shear rheology. At the highest strain rate of 10%/s, the fragility of the P_4 gel leads to partial failure/splitting around the periphery of the specimen at larger strains, as reflected in the stress-strain response. Conversely, at the 10%/s strain rate, the *o*-Cys-P_4-Cys gel does not fail and exhibits enhanced elastic recovery during unloading due to the entropic recoil of the entangled molecular network. This finding again suggests the presence of chain entanglement with a characteristically long relaxation time associated with chain reptation. At low strain rates, both gels show similar unloading behaviors, as the imposed time scale is larger than the longest network relaxation time. Indeed, the unloading slopes of the stress-strain response during interval loading/partial unloading cycles at 1%/s cannot be readily distinguished (Figure 7-6C). In summary, the main effects of entanglements at these intermediate levels of deformation (up to a true strain of 1.6) are increasing the (small strain) modulus through the increase in the number of elastically effective chains and increasing the resistance to viscous flow, especially at low strain rates.

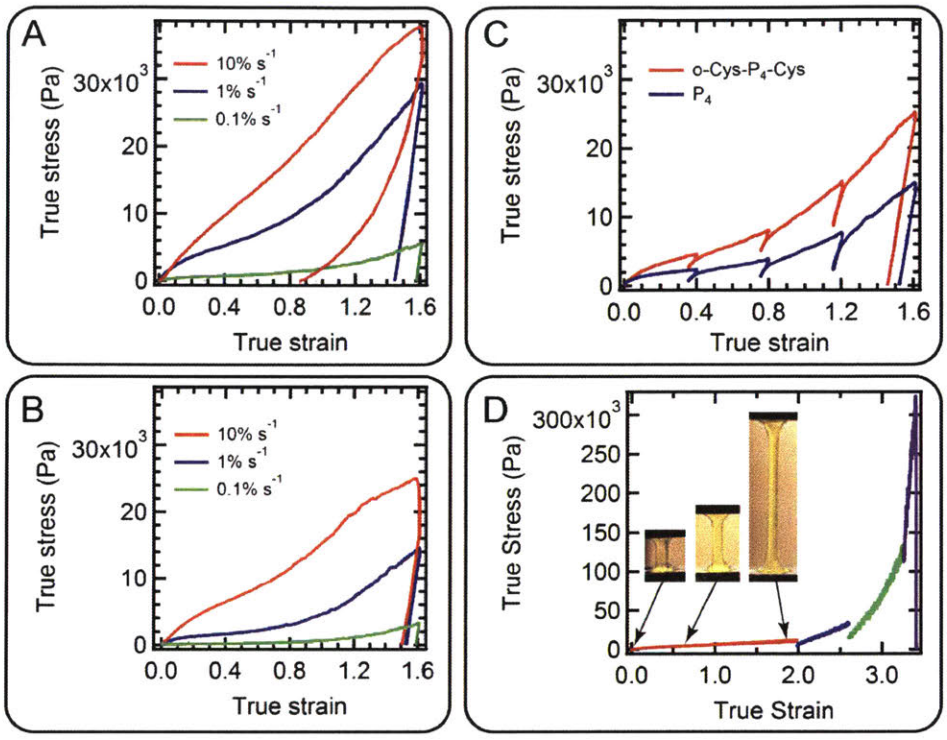

Figure 7-6. Mechanical enhancement in axial loading. Uniaxial compression of *o*-Cys-P_4-Cys (A) and P_4 (B) showing the rate-dependence and nonlinearity of the stress response of gels to 80% nominal strain. (C) Uniaxial compression at 1% 1/s nominal strain rate showing that chain entanglement does not affect the relaxation behavior at small deformation. (D) True stress-strain curve of topologically entangled gel reveals the strain hardening behavior during tensile loading. The photographs in the inset illustrate the neck stabilization and propagation, and the stable drawing of the specimen. All hydrogels are prepared at 15% (w/v) concentration.

The entanglement effect becomes more pronounced at very large strain that is well characterized under tensile loading. Dramatic stiffening of the true stress-strain response is found to occur at true strains over 200%. Although less apparent, the early stiffening associated with stretch of the entangled network is sufficient to stabilize the tensile response of the *o*-Cys-P_4-Cys gel specimen. This leads to neck propagation and drawing, with engineering strains at failure

reaching approximately 3,000% (Figures 6-2C, 6-2E and 6-6D). The selected ramp-relaxation tensile protocol also demonstrates significant load relaxation at intermediate deformations, possibly owing to the fast coiled-coil association-disassociation dynamics, in agreement with the compression experiment results. Interestingly, at large deformations, the stress level is maintained even during relaxation. This effect might be ascribed to the strain-induced alignment of the molecular network, with entangled protein chains undergoing a coil-stretch transition that leads to remarkable resistance to strain localization and mechanical failure. Sufficient relaxation time intervals in the ramp-relaxation loading protocol are found to be critical to reach this extremely high extensibility. If the relaxation interval is shortened from ten minutes to one minute, the ultimate tensile strain is reduced to 1,250% engineering strain (Figure D-7). Further studies are underway to study the structural transformation during tensile loading.

7.4. Conclusions

Topological entanglements are introduced into a coiled-coil protein hydrogel, achieving a dramatic enhancement in many mechanical properties. The interplay between reptation and coiled-coil association significantly suppresses the network relaxation, making hydrogels more resistant to creep and erosion in an open system. Chain entanglement promotes a mechanical transition from a highly brittle state to a tough and highly extensible state, enabling artificial protein hydrogels to be stretched up to approximately 3,000% engineering strain. Based on the reversible nature of the disulfide linkages, the improvement in network properties can be triggered by different redox stimuli. This network enhancement strategy can potentially be generalized to other hydrogel systems, and the presented redox responsive network toughening approach shows

promise of synthetizing hydrogels that can mimic the high toughness of native tissues such as tendon and cartilage.

7.5. References

1. Shen, W. Engineered Polypeptides for Tissue Engineering. In *Biomaterials for Tissue Engineering Applications*, Burdick, J.; Mauck, R., Eds. Springer Vienna: 2011; pp 243-275.
2. Gomes, S.; Leonor, I. B.; Mano, J. F.; Reis, R. L.; Kaplan, D. L. Natural and Genetically Engineered Proteins for Tissue Engineering. *Progress in Polymer Science* 2012, 37, 1-17.
3. DiMarco, R. L.; Heilshorn, S. C. Multifunctional Materials through Modular Protein Engineering. *Adv Mater* 2012, 24, 3923-3940.
4. Engler, A. J.; Sen, S.; Sweeney, H. L.; Discher, D. E. Matrix Elasticity Directs Stem Cell Lineage Specification. *Cell* 2006, 126, 677-689.
5. Mammoto, A.; Ingber, D. E. Cytoskeletal Control of Growth and Cell Fate Switching. *Current Opinion in Cell Biology* 2009, 21, 864-870.
6. Erickson, I. E.; Huang, A. H.; Sengupta, S.; Kestle, S.; Burdick, J. A.; Mauck, R. L. Macromer Density Influences Mesenchymal Stem Cell Chondrogenesis and Maturation in Photocrosslinked Hyaluronic Acid Hydrogels. *Osteoarthritis and Cartilage* 2009, 17, 1639-1648.
7. Kim, M.; Tang, S.; Olsen, B. D. Physics of Engineered Protein Hydrogels. *Journal of Polymer Science Part B: Polymer Physics* 2013, 51, 587-601.
8. Urry, D. W. Molecular Machines: How Motion and Other Functions of Living Organisms Can Result from Reversible Chemical Changes. *Angewandte Chemie International Edition in English* 1993, 32, 819-841.
9. Petka, W. A.; Harden, J. L.; McGrath, K. P.; Wirtz, D.; Tirrell, D. A. Reversible Hydrogels from Self-Assembling Artificial Proteins. *Science* 1998, 281, 389-392.
10. Olsen, B. D.; Kornfield, J. A.; Tirrell, D. A. Yielding Behavior in Injectable Hydrogels from Telechelic Proteins. *Macromolecules* 2010, 43, 9094-9099.
11. Banta, S.; Wheeldon, I. R.; Blenner, M. Protein Engineering in the Development of Functional Hydrogels. *Annual Review of Biomedical Engineering* 2010, 12, 167-186.

12. Kopeček, J.; Yang, J. Smart Self-Assembled Hybrid Hydrogel Biomaterials. *Angewandte Chemie International Edition* 2012, 51, 7396-7417.

13. Semenov, A. N.; Rubinstein, M. Thermoreversible Gelation in Solutions of Associative Polymers. 1. Statics. *Macromolecules* 1998, 31, 1373-1385.

14. Dobrynin, A. V. Phase Diagram of Solutions of Associative Polymers. *Macromolecules* 2004, 37, 3881-3893.

15. Green, M. S.; Tobolsky, A. V. A New Approach to the Theory of Relaxing Polymeric Media. *The Journal of Chemical Physics* 1946, 14, 80-92.

16. Tanaka, F.; Edwards, S. F. Viscoelastic Properties of Physically Crosslinked Networks. 1. Transient Network Theory. *Macromolecules* 1992, 25, 1516-1523.

17. Annable, T.; Buscall, R.; Ettelaie, R.; Whittlestone, D. The Rheology of Solutions of Associating Polymers: Comparison of Experimental Behavior with Transient Network Theory. *Journal of Rheology* 1993, 37, 695-726.

18. Tripathi, A.; Tam, K. C.; McKinley, G. H. Rheology and Dynamics of Associative Polymers in Shear and Extension: Theory and Experiments. *Macromolecules* 2006, 39, 1981-1999.

19. Tanaka, F.; Edwards, S. F. Viscoelastic Properties of Physically Crosslinked Networks: Part 1. Non-Linear Stationary Viscoelasticity. *Journal of Non-Newtonian Fluid Mechanics* 1992, 43, 247-271.

20. Tanaka, F.; Edwards, S. F. Viscoelastic Properties of Physically Crosslinked Networks: Part 2. Dynamic Mechanical Moduli. *Journal of Non-Newtonian Fluid Mechanics* 1992, 43, 273-288.

21. Tanaka, F.; Edwards, S. F. Viscoelastic Properties of Physically Crosslinked Networks: Part 3. Time-Dependent Phenomena. *Journal of Non-Newtonian Fluid Mechanics* 1992, 43, 289-309.

22. Leibler, L.; Rubinstein, M.; Colby, R. H. Dynamics of Reversible Networks. *Macromolecules* 1991, 24, 4701-4707.

23. Rubinstein, M.; Semenov, A. N. Thermoreversible Gelation in Solutions of Associating Polymers. 2. Linear Dynamics. *Macromolecules* 1998, 31, 1386-1397.

24. Rubinstein, M.; Semenov, A. N. Dynamics of Entangled Solutions of Associating Polymers. *Macromolecules* 2001, 34, 1058-1068.

25. Xu, D.; Craig, S. L. Scaling Laws in Supramolecular Polymer Networks. *Macromolecules* 2011, 44, 5465-5472.

26. Hackelbusch, S.; Rossow, T.; van Assenbergh, P.; Seiffert, S. Chain Dynamics in Supramolecular Polymer Networks. *Macromolecules* 2013, 46, 6273-6286.

27. Feldman, K. E.; Kade, M. J.; Meijer, E. W.; Hawker, C. J.; Kramer, E. J. Model Transient Networks from Strongly Hydrogen-Bonded Polymers. *Macromolecules* 2009, 42, 9072-9081.

28. Cates, M. E. Reptation of Living Polymers: Dynamics of Entangled Polymers in the Presence of Reversible Chain-Scission Reactions. *Macromolecules* 1987, 20, 2289-2296.

29. Sijbesma, R. P.; Beijer, F. H.; Brunsveld, L.; Folmer, B. J. B.; Hirschberg, J. H. K. K.; Lange, R. F. M.; Lowe, J. K. L.; Meijer, E. W. Reversible Polymers Formed from Self-Complementary Monomers Using Quadruple Hydrogen Bonding. *Science* 1997, 278, 1601-1604.

30. Folmer, B. J. B.; Sijbesma, R. P.; Versteegen, R. M.; van der Rijt, J. A. J.; Meijer, E. W. Supramolecular Polymer Materials: Chain Extension of Telechelic Polymers Using a Reactive Hydrogen-Bonding Synthon. *Adv Mater* 2000, 12, 874-878.

31. Shen, W.; Zhang, K.; Kornfield, J. A.; Tirrell, D. A. Tuning the Erosion Rate of Artificial Protein Hydrogels through Control of Network Topology. *Nat Mater* 2006, 5, 153-158.

32. Welsh, E. R.; Tirrell, D. A. Engineering the Extracellular Matrix: A Novel Approach to Polymeric Biomaterials. I. Control of the Physical Properties of Artificial Protein Matrices Designed to Support Adhesion of Vascular Endothelial Cells. *Biomacromolecules* 2000, 1, 23-30.

33. Charati, M. B.; Ifkovits, J. L.; Burdick, J. A.; Linhardt, J. G.; Kiick, K. L. Hydrophilic Elastomeric Biomaterials Based on Resilin-Like Polypeptides. *Soft Matter* 2009, 5, 3412-3416.

34. Asai, D.; Xu, D.; Liu, W.; Garcia Quiroz, F.; Callahan, D. J.; Zalutsky, M. R.; Craig, S. L.; Chilkoti, A. Protein Polymer Hydrogels by in Situ, Rapid and Reversible Self-Gelation. *Biomaterials* 2012, 33, 5451-5458.

35. Edwards, S. F.; Vilgis, T. The Effect of Entanglements in Rubber Elasticity. *Polymer* 1986, 27, 483-492.

36. Liu, G.; Sun, H.; Rangou, S.; Ntetsikas, K.; Avgeropoulos, A.; Wang, S.-Q. Studying the Origin of ``Strain Hardening": Basic Difference between Extension and Shear. *Journal of Rheology* 2013, 57, 89-104.

37. Donald, A. M.; Kramer, E. J. Effect of Molecular Entanglements on Craze Microstructure in Glassy Polymers. *Journal of Polymer Science: Polymer Physics Edition* 1982, 20, 899-909.

38. Yang, J.; Wang, X.-P.; Xie, X.-M. In Situ Synthesis of Poly(Acrylic Acid) Physical Hydrogels from Silica Nanoparticles. *Soft Matter* 2012, 8, 1058-1063.

39. Bose, R. K.; Lau, K. K. S. Mechanical Properties of Ultrahigh Molecular Weight Phema Hydrogels Synthesized Using Initiated Chemical Vapor Deposition. *Biomacromolecules* 2010, 11, 2116-2122.

40. Xiao, J.; Tolbert, T. J. Synthesis of N-Terminally Linked Protein Dimers and Trimers by a Combined Native Chemical Ligation-Cuaac Click Chemistry Strategy. *Organic Letters* 2009, 11, 4144-4147.

41. Fang, G.-M.; Li, Y.-M.; Shen, F.; Huang, Y.-C.; Li, J.-B.; Lin, Y.; Cui, H.-K.; Liu, L. Protein Chemical Synthesis by Ligation of Peptide Hydrazides. *Angewandte Chemie International Edition* 2011, 50, 7645-7649.

42. Sahin, E.; Kiick, K. L. Macromolecule-Induced Assembly of Coiled-Coils in Alternating Multiblock Polymers. *Biomacromolecules* 2009, 10, 2740-2749.

43. Vila-Perelló, M.; Liu, Z.; Shah, N. H.; Willis, J. A.; Idoyaga, J.; Muir, T. W. Streamlined Expressed Protein Ligation Using Split Inteins. *Journal of the American Chemical Society* 2012, 135, 286-292.

44. Hartgerink, J. D.; Beniash, E.; Stupp, S. I. Peptide-Amphiphile Nanofibers: A Versatile Scaffold for the Preparation of Self-Assembling Materials. *Proceedings of the National Academy of Sciences* 2002, 99, 5133-5138.

45. Shen, W.; Lammertink, R. G. H.; Sakata, J. K.; Kornfield, J. A.; Tirrell, D. A. Assembly of an Artificial Protein Hydrogel through Leucine Zipper Aggregation and Disulfide Bond Formation. *Macromolecules* 2005, 38, 3909-3916.

46. Zhang, Q.; Ye, J.; Lu, Y.; Nie, T.; Xie, D.; Song, Q.; Chen, H.; Zhang, G.; Tang, Y.; Wu, C., *et al.* Synthesis, Folding, and Association of Long Multiblock (Peo23-B-Pnipam124)750 Chains in Aqueous Solutions. *Macromolecules* 2008, 41, 2228-2234.

47. Glassman, M. J.; Chan, J.; Olsen, B. D. Reinforcement of Shear Thinning Protein Hydrogels by Responsive Block Copolymer Self-Assembly. *Advanced Functional Materials* 2013, 23, 1182-1193.

48. Jacobson, H.; Stockmayer, W. H. Intramolecular Reaction in Polycondensations. I. The Theory of Linear Systems. *The Journal of Chemical Physics* 1950, 18, 1600-1606.

49. Skrzeszewska, P. J.; de Wolf, F. A.; Werten, M. W. T.; Moers, A. P. H. A.; Cohen Stuart, M. A.; van der Gucht, J. Physical Gels of Telechelic Triblock Copolymers with Precisely Defined Junction Multiplicity. *Soft Matter* 2009, 5, 2057-2062.

50. Ferry, J. *Viscoelastic Properties of Polymers*. 3d ed.; Wiley: New York, 1980; p xxiv, 641 p.

51. Graessley, W. W. *Polymeric Liquids and Networks : Dynamics and Rheology*. Garland Science: London ; New York, 2008; p xix, 801 p.

52. Séréro, Y.; Aznar, R.; Porte, G.; Berret, J. F.; Calvet, D.; Collet, A.; Viguier, M. Associating Polymers: From "Flowers" to Transient Networks. *Physical Review Letters* 1998, 81, 5584-5587.

53. Gong, J. P. Why Are Double Network Hydrogels So Tough? *Soft Matter* 2010, 6, 2583-2590.

54. Sun, J.-Y.; Zhao, X.; Illeperuma, W. R. K.; Chaudhuri, O.; Oh, K. H.; Mooney, D. J.; Vlassak, J. J.; Suo, Z. Highly Stretchable and Tough Hydrogels. *Nature* 2012, 489, 133-136.

55. Glassman, M. J.; Olsen, B. D. Structure and Mechanical Response of Protein Hydrogels Reinforced by Block Copolymer Self-Assembly. *Soft Matter* 2013, 9, 6814-6823.

56. Betre, H.; Setton, L. A.; Meyer, D. E.; Chilkoti, A. Characterization of a Genetically Engineered Elastin-Like Polypeptide for Cartilaginous Tissue Repair. *Biomacromolecules* 2002, 3, 910-916.

57. Li, J.; Viveros, J. A.; Wrue, M. H.; Anthamatten, M. Shape-Memory Effects in Polymer Networks Containing Reversibly Associating Side-Groups. *Adv Mater* 2007, 19, 2851-2855.

58. Chen, Y.; Kushner, A. M.; Williams, G. A.; Guan, Z. Multiphase Design of Autonomic Self-Healing Thermoplastic Elastomers. *Nat Chem* 2012, 4, 467-472.

59. Larson, R. G.; Sridhar, T.; Leal, L. G.; McKinley, G. H.; Likhtman, A. E.; McLeish, T. C. B. Definitions of Entanglement Spacing and Time Constants in the Tube Model. *Journal of Rheology* 2003, 47, 809-818.

60. McLeish, T. C. B. Tube Theory of Entangled Polymer Dynamics. *Advances in Physics* 2002, 51, 1379-1527.

Chapter 8 : Controlling Topological Entanglement in Engineered Protein Hydrogels with a Variety of Thiol Coupling Chemistries

Topological entanglements between polymer chains are achieved in associating protein hydrogels through the synthesis of high molecular weight proteins *via* chain extension using a variety of thiol coupling chemistries, including disulfide formation, thiol-maleimide, thiol-bromomaleimide and thiol-ene. Coupling of cysteines *via* disulfide formation results in the most pronounced entanglement effect in hydrogels, while other chemistries provide versatile means of changing the extent of entanglement, achieving faster chain extension, as well as providing a facile method of controlling the network hierarchy and incorporating stimuli responsivities. The addition of trifunctional coupling agents causes incomplete crosslinking and introduces branching architecture to the protein molecules. The high-frequency plateau modulus and the entanglement plateau modulus can be tuned by changing the ratio of difunctional chain extenders to the trifunctional branching units. Therefore, these chain extension reactions show promise in delicately controlling the relaxation and mechanical properties of engineered protein hydrogels in ways that complement their design through genetic engineering.

8.1. Introduction

Control of advanced mechanical properties of hydrogels is central to their applications. In many situations, such as engineering simulant materials of articular cartilage or blood vessels[1], hydrogels are required to support mechanical load and maintain structural integrity. Multiple approaches have been developed to address this issue, with an emphasis on increasing the network toughness and elastic moduli, such as preparing double-networks[2, 3] and fabricating composite materials[4, 5]. In some scenarios where dynamic properties such as injectability, self-healing, shape memory, and controlled degradation/reinforcement are desirable, non-covalent crosslinks and stimuli-responsive triggers can be incorporated into gels to fulfill the application requirements.[6-9] However, many methods developed in synthetic polymer systems cannot be readily applied to protein hydrogels, and manipulating the mechanical response of the gels presents a new challenge. Because the function of a protein is related to its hierarchical structure and the diversity of amino acid functional groups, site-specific and orthogonal reactions are often required to preserve protein properties in the final gel. In addition, the modification reactions can usually only be performed in aqueous buffers due to the poor solubility of proteins in organic solvents.

Currently there are two main strategies for chemically modifying proteins to manipulate the mechanical properties of protein hydrogels. The first strategy is covalently crosslinking protein polymer chains by adding crosslinking reagents[10-12], catalysts[13, 14] and/or enzymes[15]. As this method only modifies the amino acid residues participating in junction formation, the protein strands can retain most of their function (e.g., elasticity and stimuli responsivity). In addition, many mechanical properties at equilibrium, such as modulus and maximum swelling ratio, can be controlled by varying the dosage of the crosslinking agents according to well-known laws of hydrogel physics and network theories[16-18]. In a typical crosslinking reaction, however, the

formation of network imperfections, such as dangling chains and inelastic loops, is usually uncontrollable and difficult to quantify.[19] The second strategy is coupling synthetic polymers with proteins to prepare chimeric copolymers.[9, 20-23] Interactions leading to self-assembly of the polymer or protein components then create nanostructure within the hydrogel, which in some cases can be triggered by external stimuli. This method allows delicate manipulation of hydrogel mechanics, such as erosion rate, toughness and elasticity. However, preparing hybrid hydrogels adds challenges in materials synthesis and purification.

Recently, we developed a facile method for introducing entanglements into protein hydrogels through simple chain extension reactions, and we exploited this entanglement effect to engineer new mechanical responses into the materials.[24] This strategy minimally modifies the protein molecules, only extending protein chains by establishing disulfide end linkages, yet it creates a drastic enhancement in many mechanical properties, including the low-frequency modulus, resistance to creep, extensibility and toughness. The disulfide linkages are redox responsive, which provides opportunities to regulate network mechanics by redox stimuli.

In addition to disulfide coupling, several other thiol chemistries are promising candidates for coupling high molar mass proteins: thiol-maleimide, thiol-bromomaleimide and thiol-ene coupling. Thiol-maleimide chemistry enables site-specific modification of cysteine residues and has been a popular route for constructing protein-based bioconjugates.[25, 26] Recently, the thiol-maleimide addition has been found to be reversible, offering new opportunities to control the degradation of the conjugates.[27] Thiol-dibromomaleimide conjugation has emerged as another important "click" chemistry,[28-30] but only recently has its potential in the chain extension reaction been appreciated.[31] The thiomaleimide adduct is redox responsive: the addition of reducing reagents such as β-mercaptoethanol (BME) reverses the reaction and recovers the unmodified

proteins. Compared to other coupling chemistries, the thiol-ene reaction is the most rapid coupling method, with extremely high bimolecular rate constants in the thiyl-alkene addition, ranging from 10^5 to 10^7 M^{-1} s^{-1},[32] which is 4-5 orders of magnitude larger than thiol-maleimide addition.[33] Despite potential side reactions,[34] there exist many successful examples demonstrating the use of thiol-ene chemistry in direct protein modification.[35-37]

In this work, thiol-maleimide, thiol-bromomaleimide and thiol-ene coupling chemistries for applications in protein chain extension reactions to produce entangled hydrogels are compared. In addition, the ability to use chain extension points for the modification of proteins with poly(*N*-isopropylacrylamide) (PNIPAM) side chains is established, demonstrating thermally responsive mechanical behavior. By using trifunctional chain coupling agents, branched proteins are also prepared, and the effect of the ratio of di to trifunctional chain coupling agents on entanglements is assessed. These experiments demonstrate sophisticated control of molecular structure and network mechanics in engineered protein hydrogels, yielding the ability to control chain topology, chain entanglement, and chemical functionalization all through thiol-based chain coupling chemistries.

8.2. Materials and Methods

8.2.1 Materials

Bismaleimide diethylene glycol (**1a**) was purchased from Thermo Fischer. Maleimide-PEG(1k)-maleimide (**1b**) was purchased from creative PEGWorks. The average molecular weight of the PEG portion determined by ^{1}H NMR was 1,082 Da. β-cyclodextrin (βCD) and 2,2'-Azobis[2-(2-imidazolin-2-yl)propane]dihydrochloride (VA-044) were purchased from Wako

USA. All other chemical reagents were purchased from commercial sources (Sigma-Aldrich and VWR) and used as received unless otherwise noted.

8.2.2 Characterization

^{1}H NMR spectra were recorded in $CDCl_3$ or DMSO-*d*$_6$ using a Varian Mercury 300 MHz Spectrometer in Department of Chemistry Instrumentation Facilities at MIT. High-resolution mass spectrometry (HRMS) data was obtained on a Bruker Daltonics APEXIV 4.7 Tesla Fourier Transform Ion Cyclotron Resonance Mass Spectrometer. Matrix assisted laser desorption ionization mass spectrometry (MALDI) data was obtained on a Bruker Omniflex MALDI-TOF Mass Spectrometer. α-Cyano-4-hydroxycinnamic acid (CHCA) was used as matrix. Gel permeation chromatography (GPC) was performed on an Agilent 1260 system equipped with a Wyatt Optilab T-rEX refractive index (RI) detector and a Wyatt Mini-DAWN multi-angle light scattering (LS) detector. The mobile phase was DMF supplemented with 0.02 M LiBr and the instrument was operated at 1.0 mL/min at 70 °C.

8.2.3 Protein Cys-P$_4$-Cys expression and purification

Protein expression and purification by ammonium sulfate purification have been described previously[24]. In this study, the proteins were additionally purified by anion exchange chromatography using a HiTrap Q Sepharose HP 5 mL column (GE healthcare, WI), eluting with a gradient of 0-500 mM NaCl in 6 M urea and 20 mM Tris (pH 8.0). A typical isolation yield is 120 mg per liter culture and the protein purity was determined to be >97% by sodium dodecyl sulfate-polyacrylamide gel electrophoresis (SDS-PAGE).

8.2.4 Chemical Compound Synthesis

Dibromomaleimide-alkyne. The synthesis procedure reported elsewhere[29] was slightly modified. Potassium carbonate (0.89 g, 6.50 mmol) was suspended in 20 mL acetone and 2,3-dibromomaleimide (1.5 g, 5.90 mmol) was added to the slurry in one portion and the reaction was left to stir at room temperature for 5 min. Propargyl bromide (80% in toluene, 0.72 mL, 6.50 mmol) was added dropwise to the mixture over 10 min. After 24 h, solvent was removed under vacuum and the mixture was redissolved in DCM. Salts were filtered and the residue was loaded onto a silica gel column. The crude product was purified by flash chromatography, eluted with 0-2% MeOH in DCM (TLC R_f = 0.78, stained with $KMnO_4$ solution) to afford 492 mg **4** as a white powder (yield 28.5%). ^{1}H NMR (300 MHz, $CDCl_3$) δ 4.38 (d, J = 2.4 Hz, 2H), 4.83 (t, J = 2.4 Hz, 1H). DART HRMS (m/z) calcd for $C_7H_4Br_2NO_2$ $[M+H]^+$: 293.8586; found 293.8585.

Dibromomaleimide-β-CD. To a 25 mL Schlenk tube was added **4** (58.5 mg, 0.20 mmol), mono-6-deoxy-6-azido-β-cyclodextrin[38] (116.0 mg, 0.10 mmol), Cu(I)Br (14.3 mg, 0.10 mmol) and 5 mL DMF. The mixture was degassed through 3 freeze-pump-thaw cycles. 2,2'-Bipyridine (15.6 mg, 0.10 mmol) was added to the frozen mixture and the mixture was degassed one more time. The click reaction was performed at 30 °C for 24 h. Catalyst was removed by passing through a short alumina column and the product was obtained by precipitation in acetone twice to get 63 mg **2** as a yellow powder (yield 43.4%). ^{1}H NMR (300 MHz, DMSO-d_6) δ 8.06 (s, 1H), 5.95-5.60 (m, 14H), 5.10-4.67 (m, 9H), 4.65-4.42 (m, 6H), 3.79-3.48 (m, 28H), 3.43-3.21 (m, overlaps with HOD). MALDI-TOF MS (m/z) calcd for $C_{49}H_{72}Br_2N_4O_3Na$ $[M+Na]^+$: 1473.22; found 1473.22.

Bisallyl tetraethylene glycol. Tetraethylene glycol (5.0 g, 25.7 mmol) was dissolved in 30 mL anhydrous DMF. Sodium hydride (3.5 g, 60% in mineral oil, 87.5 mmol) was added to the

mixture in one portion. The mixture was cooled with a water bath and allowed to stir for 30 min at room temperature. After the reaction stopped bubbling, allyl bromide (9.5 g, 78.4 mmol) was added dropwise. After 14 h, excess NaH was quenched by adding 10 mL saturated NH_4Cl aqueous solution. The mixture was diluted with EtOAc, washed with DI water and brine, and dried over $MgSO_4$. Then solvent was removed under reduced pressure. The crude product was purified by silica gel column chromatography, eluted with 50% EtOAc in hexanes (TLC R_f = 0.41, stained with $KMnO_4$ solution) to afford 3.65 g **3** as a slightly yellow liquid (yield 51.8%). ^{1}H NMR (300 MHz, $CDCl_3$) δ 5.91 (ddt, J = 17.1 Hz, J = 10.5 Hz, ^3J = 5.7 Hz, 2H), 5.27 (ddt, J = 17.1 Hz, J = 1.5 Hz, J = 1.5 Hz, 2H), 5.18 (ddt, J = 17.1 Hz, J = 1.8 Hz, J = 1.2 Hz, 2H), 4.02 (dt, J = 5.7 Hz, J = 1.5 Hz, 4H), 3.68-3.58 (m, 16H). DART HRMS (m/z) calcd for $C_{14}H_{27}O_5$ $[M+H]^+$: 275.1853; found 275.1851.

EMP-Adamantane (EMP-Ad). The synthesis of 2-ethylsulfanylthiocarbonylsulfanyl-2-methylpropionic acid (EMP) was performed as previously reported.[39, 40] To a 25 mL round bottom flask was added EMP (179.5 mg, 0.80 mmol), 1-adamantane methanol (159.6 mg, 0.96 mmol), 4-dimethylaminopyridine (DMAP) (19.5 mg, 0.16 mmol) and 5 mL DCM. After all reagents were dissolved, *N,N'*-dicyclohexylcarbodiimide (DCC) (247.6 mg, 1.20 mmol) was added in one portion. The reaction mixture was stirred at room temperature overnight. The precipitate was filtered and the solvent was removed under vacuum. The crude product was purified by silica gel column chromatography, eluted with 30% DCM in hexanes (TLC R_f = 0.30, yellow or stained with $KMnO_4$ solution) to afford 210 mg **5** as a bright yellow solid (yield 70.5%). ^{1}H NMR (300 MHz, $CDCl_3$) δ 3.60 (s, 2H), 3.25 (q, J = 7.5 Hz, 2H), 1.93 (s, 3H), 1.71-1.60 (m, 12H), 1.49 (d, J = 2.4 Hz, 6H), 1.28 (d, J = 7.5 Hz, 3H). ESI HRMS (m/z) calcd for $C_{18}H_{28}O_2S_3$ $[M+H]^+$: 373.1343; found 373.1324.

PNIPAM-Ad. *N*-isopropyl acrylamide (NIPAM) was freshly purified by sublimation and azobisisobutyronitrile (AIBN) was recrystallized twice from ethanol. In polymerization, NIPAM (1.09 g, 9.6 mmol), EMP-Ad (29.8 mg, 0.080 mmol), AIBN (2.63 mg, 0.016 mmol) and 4.8 mL acetonitrile were added to a 25 mL Schlenk tube. The reaction mixture was subjected to 3 cycles of freeze-pump-thaw to degas oxygen. The reaction was heated at 60 °C for 4 h, after which polymers were recovered by precipitation in diethyl ether. The molar mass of the obtained polymer was 7.8 kg/mol (from GPC, dispersity $Đ$ = 1.05), 7.4 kg/mol (from ^{1}H NMR endgroup analysis) and 7.0 kg/mol (from MALDI-TOF MS), respectively.

8.2.5 Extending protein chains using different cysteine coupling chemistries (including branching reactions)

Thiol-Maleimide Coupling. Protein Cys-P_4-Cys was dissolved in denaturing buffer (8 M urea and 100 mM phosphate, pH 8.0) to reach a concentration of 10% (w/v). Tris(2-carboxyethyl)phosphine (TCEP) (20 eq.) was added to the solution and the pH was adjusted to 7.5. Bismaleimide **1a** or **1b** was dissolved in DMF, and was added to the solution (1 eq.). The reaction was stirred at room temperature for 3 days, and it was then dialyzed against MilliQ water and lyophilized. The long reaction time was chosen based on experimental results to maximize endgroup conversion and entanglement in gels.

Thiol-Bromomaleimide Coupling. Protein Cys-P_4-Cys was dissolved in denaturing buffer (8 M urea and 100 mM phosphate, pH 8.0) to reach a concentration of 10% (w/v). TCEP (20 eq.) was added to the solution and the pH was adjusted to 6.2. βCD functionalized dibromomaleimide **2** was dissolved in DMSO, and was added to the solution (1 eq.). The reaction was stirred at 4 °C for 7 days, and it was then dialyzed against MilliQ water and lyophilized.

Thiol-ene Coupling. Protein Cys-P_4-Cys was dissolved in denaturing buffer (8 M urea and 100 mM phosphate, pH 8.0) to reach a concentration of 10% (w/v). TCEP (20 eq.) was added to the solution. The mixture was left to stir at room temperature for 4 h, and it was then dialyzed against MilliQ water and lyophilized. After reduction, >99% of the proteins were in the monomeric state, assessed by SDS-PAGE (Figure E-1). Reduced proteins were hydrated in 100 mM sodium phosphate buffer (pH 7.6), and mixed with **3** (1 eq.) and VA-044 (0.2 eq.). The final concentration was adjusted to 20% (w/v). Hydrogel samples were loaded on the rheometer after hydration for 2 days. The reaction was triggered by heating at 60 °C for 3 h. The moduli were monitored at 25 °C to ensure that the steady state was reached before measurement.

In branching reactions, the trifunctional crosslinker 2,4,6-triallyloxy-1,3,5-triazine **6** was used in place of the bifunctional crosslinker **3**. The total number of alkene groups was kept in 1:1 molar ratio to thiol groups, while the amount of **6** was varied from 0-100% of the total mole fraction of alkene-containing oligomer.

8.2.6 Rheology

Rheology experiments were performed on Anton Paar MCR 301, 501 and 702 rheometers using a cone and plate geometry (25 mm diameter, 1° cone and 50 μm truncation gap) or a parallel plate geometry (10 mm diameter and 300 μm gap, only for measurement with βCD-functionalized protein hydrogels). The quantitative measurement of hydrogel mechanics was not affected by the choice of rheometers. Lyophilized proteins were hydrated in 100 mM sodium phosphate buffer (pH 7.6) to a final concentration of 20% (w/v). Hydrogels were kept at 4 °C for 2 days to allow complete hydration. In order to minimize dehydration during measurement, the edges of hydrogel samples were coated with mineral oil. After loaded on the rheometer, the sample heated from 25 °C to 90 °C and cooled to 25 °C at 5 °C/min. Unfolding the coiled-coil domain at high temperatures

allowed rapid stress relaxation within the gel to eliminate any shear history, but within the swept temperature window no sol-gel transition was observed (see Figure E-1). Frequency sweep measurements were performed at 1% strain in the linear viscoelastic regime (LVE). In creep experiments, a 25 Pa load was exerted on hydrogels for 2 h, and the load was removed to monitor the recovery behavior for 2 h. The creep-recovery experiment was repeated at 50 Pa load to ensure the deformation was independent of the applied load.

8.3. Results and Discussion

8.3.1 Comparison of various chemistries on the chain extension reaction

Chain extension of cysteine end-capped proteins can be achieved by applying thiol-maleimide, thiol-bromomaleimide and thiol-ene coupling chemistries under appropriate reaction conditions (Scheme 8-1 and Figure 8-1). All chemistries require reduction of existing disulfides to recover reactive cysteine residues. In order to achieve significant changes in mechanical properties, the conversion of these macromolecular polycondensation reactions must be relatively high to produce proteins of high molecular weights. In practice, this is achieved by controlling stoichiometry of the reacting species. A theoretical full conversion of endgroups can only be obtained when the ratio of cysteines to alkenes is 1:1. Running the reaction for extended periods is also useful to reach high conversions.

Each chemistry offers its own distinct advantages and disadvantages for chain extension. In the thiol-maleimide reaction, pH control is critical to minimize amine-maleimide coupling while achieving fast conjugation.[41] In addition, dimaleimide reagents are commercially available with a varying distance between the two maleimide groups, and this spacer length may affect the

Scheme 8-1. Cysteine coupling chemistries to extend protein chains. (I) Thiol-maleimide conjugation; (II) thiol-dibromomaleimide conjugation; and (III) thiol-ene chick chemistry.

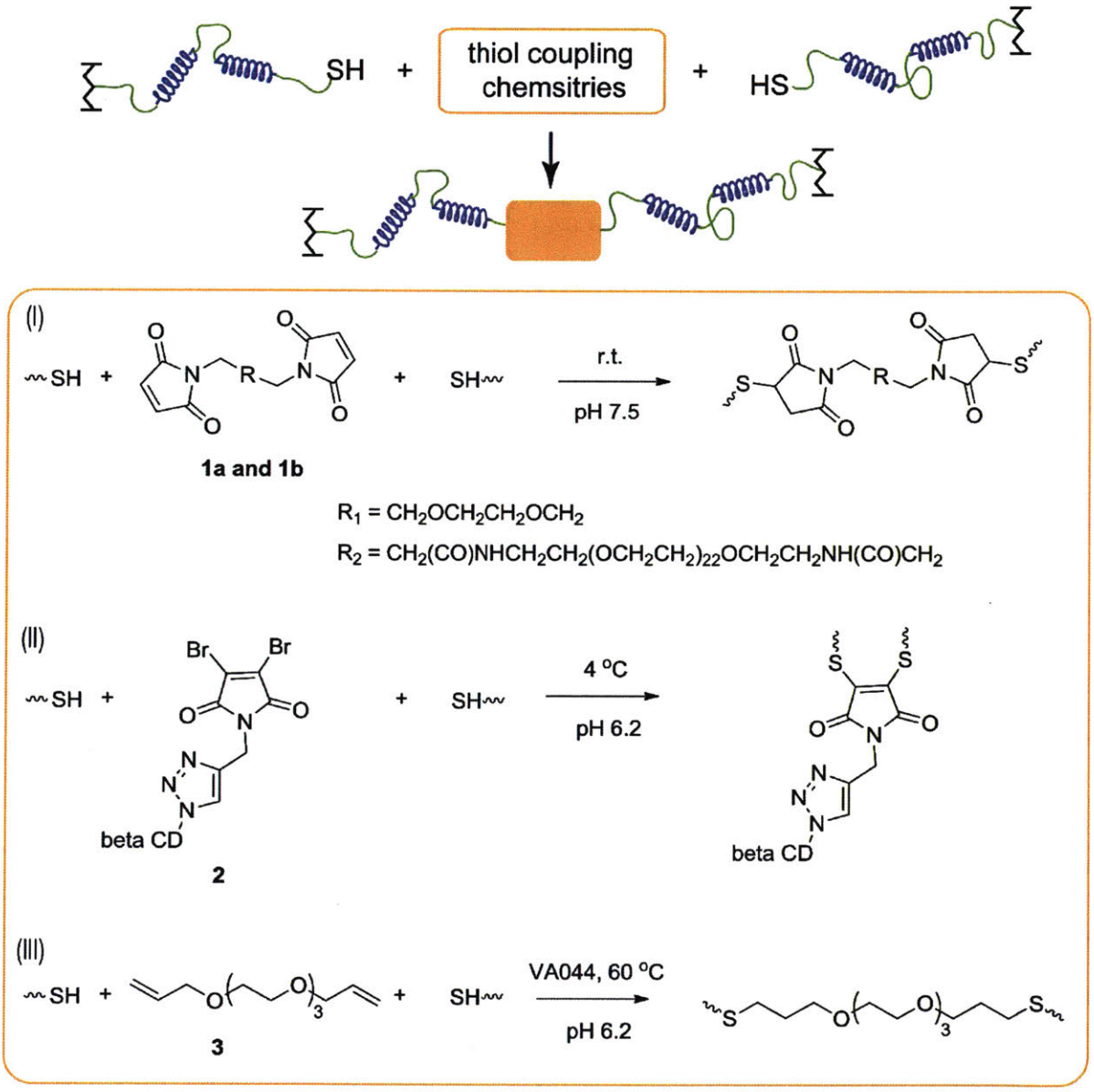

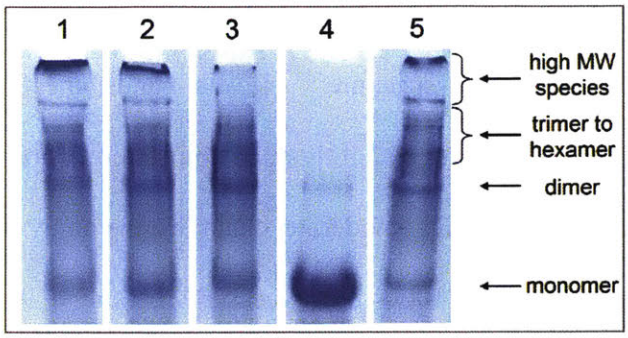

Figure 8-1. Analysis of the chain extension products by SDS-PAGE. Lane 1: thiol-maleimide with 1a; lane 2: thiol-maleimide with 1b; lane 3: thiol-dibromomaleimide; lane 4: reduction of chain-extended proteins by BME; lane 5: thiol-ene. The abundance of high molecular weight species in thiol-ene and thiol-maleimide corresponds to their higher entanglement plateau.

polycondensation reaction due to their subtle differences in solubility or by altering the propensity to form bridges or primary loops.[42] To study the effect of the distance between two conjugation sites, bismaleimide with two different oligo ethylene glycol spacer lengths **1a** and **1b** are used to conduct chain extension. It is found that the spacer length does not greatly affect the chain extension when the coupling reagents can be solubilized and homogeneously dispersed in the reaction.

As for thiol-dibromomaleimide coupling, controlling the hydrolysis of the maleimide ring, especially the monothio adduct, is crucial to attain significant chain extension. If hydrolysis happens on the dithio adduct, transformation from maleimide to maleamic acid does not affect chain extension, and it only results in loss of the reversibility of the thiomaleimide adduct (Scheme E-1). In contrast, hydrolysis of the monothio adduct can potentially limit the conversion, as the number of reactive bromomaleimide functional group decreases (Scheme E-1). Maleimide

hydrolysis can be regulated in many ways, including changing temperature, pH[43] and the electron density distribution in the maleimide structure[44]. In our hands, the first two parameters are optimized: a low temperature (4 °C) and a slightly acidic buffer condition (pH 6.2) are chosen to be the reaction condition, under which moderate chain extension is achieved. After chain extension, the protein is exposed to 1000-fold excess BME, and ~ 98% of the proteins are converted to the monomeric state (Figure 8-1), which demonstrates the reversibility of the dithiomaleimide adduct.

In the thiol-ene coupling strategy, bis allyl compound **3** is chosen as the chain extender to prevent homopolymerization of alkenes that can occur when (meth)acrylate groups are used[45], and water soluble VA-044 is selected as the thermal initiator for its low decomposition temperature. As the thiol-ene reaction is tolerant of oxygen [46], no cumbersome degassing procedure is required, enabling its convenient use in applications. Upon heating at 60 °C for 3 h, a large fraction of high-molecular-weight proteins is formed. While thermally initiated chain extension is used here in order to ensure homogeneous reaction through a concentrated solution, it is also possible to perform photoinitiated chain extension using this chemistry, especially in occasions when spatial and temporal control of gel mechanics is required. TCEP needs to be removed prior to the thiol-ene reaction; otherwise the degree of chain extension is fairly low (Figure E-2). The deleterious effect of TCEP may be due to the desulfurization of cysteines catalyzed by TCEP during free-radical-based reactions, an effect that has been observed under similar reaction conditions.[47]

Cysteine coupling chemistries exhibit different performances in the chain extension reaction, and the differences in the molecular weight distribution of the chain-extended proteins result in varying extents of entanglement in the protein hydrogels. As shown in Figure 8-2, hydrogels prepared *via* different chemistries all show an entanglement plateau modulus in the low-

frequency regime. The chain molar mass distributions extracted from gels in Figure 8-1 do not fit well to the Jacobson-Stockmayer distribution, likely because of challenges in controlling stoichiometry of reagents in small samples and because of difficulty in quantitatively separating the large high molar mass band, which contains a mix of proteins with a molar mass of ca. 380 kg/mol and above (6-mers and above). Therefore, the chain extension and the entanglement effect is quantitatively analyzed by the entanglement plateau moduli in the low frequency regime. The apparent entanglement molecular weight M_e can be estimated as[48]

$$M_e = \frac{5}{4}\frac{\rho\varphi RT}{G_e} \tag{8-1}$$

with ρ being the protein density, φ the protein volume fraction in the gel, R the gas constant, T the absolute temperature and G_e the entanglement plateau modulus. Although the entanglement plateau modulus should not depend on the molecular weight of the protein polymers in the high molecular weight limit, proteins formed *via* macromolecular polycondensation show very broad molecular weight distributions with a certain fraction of the protein chains below the critical entanglement length. These "small" proteins act as macromolecular diluents and lower the effective concentration of the entangled species, consistent with the concentrations investigated being in the transition from the sticky Rouse phase to the sticky reptation regime[24]. Therefore, increasing chain molecular weight, particularly the low molar mass tail, can increase M_e. Consequently, differences in the degree of chain extension will yield differences in the plateau modulus of gels.

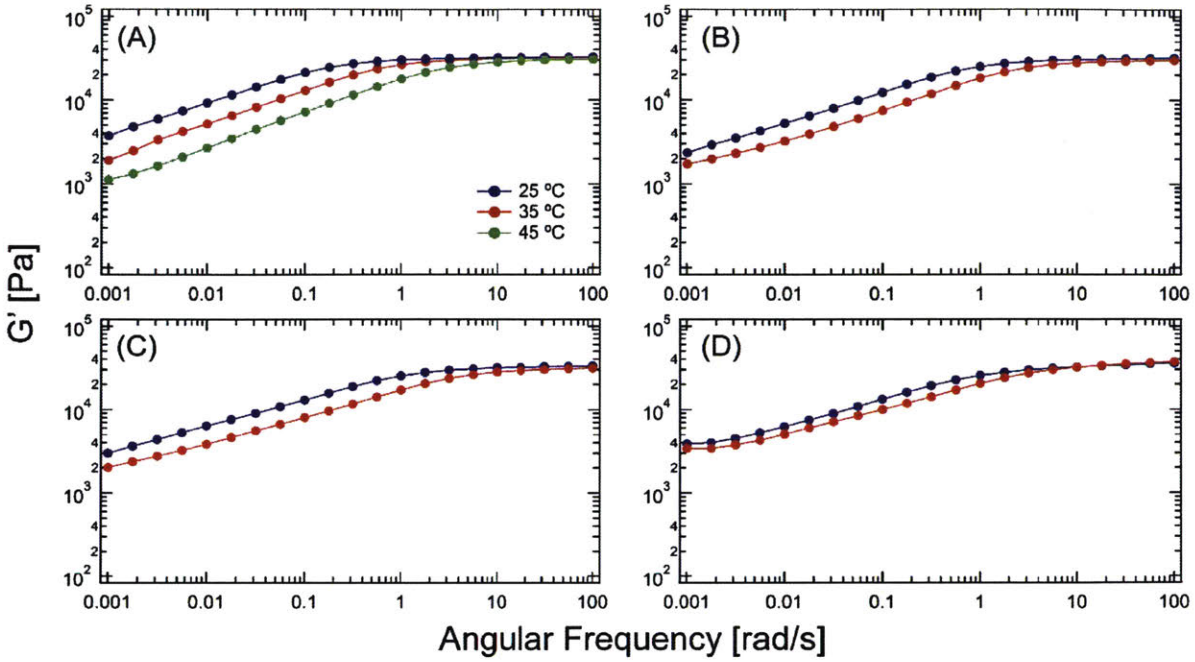

Figure 8-2. Comparison of rheological frequency sweeps of chain extended hydrogels from various chemistries. (A) Thiol-maleimide with 1a; (B) thiol-maleimide with 1b; (C) thiol-dibromomaleimide; and (D) thiol-ene. The plateau modulus in the low frequency regime down to 0.001 rad/s is the entanglement plateau. The frequency spectrum shifts to the high-frequency end at elevated temperatures.

Compared to disulfide bridging investigated previously[24], the three chemistries examined here show lower degrees of chain extension. G_e and M_e are compared in Figure 8-3(A) and (B). For 20% (w/v) hydrogels, disulfide coupling leads to a G_e of around 8800 Pa, approximately 2-8 times larger than the G_e's from other chemistries. As a result, M_e is only 55 kg/mol in the disulfide coupling, even smaller than the molecular weight of a monomeric protein. The reasons for the lower entanglement molar masses in disulfide coupling are two-fold. First and most importantly, the stoichiometric imbalance between alkenes and thiols, due to inevitable experimental errors, set a practical limit of the functional group conversion in the A-A + B-B type macromolecular

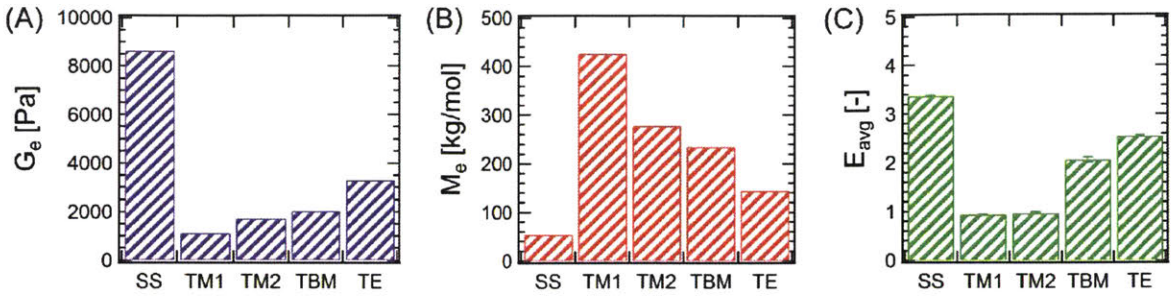

Figure 8-3. Comparison of (A) the entanglement plateau moduli, (B) the apparent entanglement molecular weights and (C) the average entanglement densities. SS: disulfide, data from (Tang et al., 2014); TM1: thiol-maleimide with 1a; TM2: thiol-maleimide with 1b; TBM: thiol-dibromomaleimide; TE: thiol-ene. Error bars represent a 95% confidence interval.

polycondensation that becomes more acute for chemistry performed on small samples. On the contrary, the disulfide bridging chemistry has no theoretical limit in the degree of chain extension due to stoichiometry since it is an A-A type polycondensation. Second, there are various side reactions in thiol-maleimide, thiol-bromomaleimide and thiol-ene coupling, which limit their ability to reach full conversion. As mentioned previously, the primary concern is that the occurrence of side reactions may reduce the availability of the reactive functional groups (e.g., maleimide hydrolysis) or cause uncontrolled chain coupling (e.g., amine-maleimide coupling). These side reactions further exacerbate challenges in controlling the stoichiometry of A and B reactive groups in the macromolecular polycondensation. G_e not only provides clues to analyze the extent of entanglement, but also provides information on the effect of side reactions. The difference in G_e might indicate that fewer side reactions occur in the thiol-ene coupling in the three chemistries examined in the study. Interestingly, although coupling with **2** only reaches moderate chain extension and side reactions might have the most detrimental effect, G_e from thiol-

bromomaleimde coupling is larger those from thiol-maleimide chemistries. It is hypothesized that the supramolecular association between βCD and amino acid residues forms weak and dynamic crosslink junctions (with equilibrium constant log$K$ around 2-3) [49], thus increasing the modulus in the low-frequency regime.

Creep experiments also provide information to compare the entanglement effects in gels prepared by different chemistries. Here, entanglement density E is used to quantify the entanglement effect, a quantity defined as the number of entanglements per molecule, namely, $E = M/M_e$.[50] Strictly speaking, the definition above is used to describe the extent of entanglement of monodisperse polymers. Here the concept is borrowed to provide an estimate of the number-averaged entanglement density. In the low E limit (when $E < 6$), the average entanglement density in the chain extended protein mixtures can be calculated as

$$E_{avg} = 2.5 J_e^0 G_e \tag{8-2}$$

where J_e^0 is the recoverable compliance, calculated as the extrapolated intercept from a linear fit in steady state of the J-t data (Figure E-3); G_e is the entanglement plateau modulus, as defined by Graessley[50] differently than the definition by Larson *et al.* shown above by a factor of 4/5. As shown in Figure 8-3(C), the low E values confirm the previous assumption that the entanglement density is not large. It is also found that the average entanglement densities of the chain-extended proteins gives the same trend as the entanglement plateau moduli in gels, namely, disulfide > thiol-ene > thiol-bromomaleimide > thiol-maleimide. For entangled gels prepared *via* thiol-maleimide coupling, E_{avg} is only approximately unity. On the contrary, E_{avg} is larger than 3 for gels prepared *via* disulfide bridging.

Because dibromomaleimide can be readily functionalized, dibromomaleimide coupling provides a facile method of incorporating biological niches into the hydrogel network and embedding additional stimuli triggers to manipulate network structure. To illustrate this concept, dibromomaleimide is first derivatized with alkyne, and is further functionalized with βCD through copper-catalyzed azide-alkyne cycloaddition (CuAAC) to obtain **2** (Scheme 8-2). βCD is chosen because its internal cavity can host many small guest molecules, such as drugs, *via* hydrogen bonding and hydrophobic interactions[51]. The most widely used complexation pair is βCD-adamantane with an association constant K_a of about 5×10^4 M^{-1}.[52] This supramolecular association may offer modification sites to attach functionalities to the protein backbone. Here, the βCD-adamantane host-guest interaction is used to demonstrate the ability to add thermoreversible association to hydrogels. Adamantane end-capped monodisperse PNIPAM is synthesized by reversible addition-fragmentation chain transfer (RAFT) polymerization using trithiocarbonate **5** as the RAFT agent (Figure E-4), and the polymer's endgroup structure is confirmed by MALDI-TOF and NMR (Figures E-5 and E-6, respectively). Upon complexation, the hybrid structure is hypothesized to adopt a graft-like structure: the chain-extended protein serves as backbone while the thermoresponsive polymers PNIPAM graft as side chains (Figure 4). Under the experimental conditions, approximately 91.8% of the PNIPAM can be attached to the proteins (see calculation details in Appendix E and Figure E-8). The high-frequency plateau modulus (G' at 100 rad/s) of the hybrid gel is 10 kPa larger than the unmodified gel, and it increases moderately with increasing temperature, with a peak value at around 28 °C. The entanglement modulus also increases from 2030 Pa to 3670 Pa. The enhancement in the both moduli might originate from changes of protein architecture, and the formation of nanostructure within the gel due to segregation between the PNIPAM domain and the protein domain. Such microphase

separation may even exist at low temperature, as enhancement in moduli is observed as low as 5 °C. This observation is consistent with the previous finding that PNIPAM segregation takes place even when the polymers are highly solvated.[22]

Scheme 8-2. Synthesis of (A) dibromomaleimide functionalized βCD and (B) adamantane functionalized trithiocarbonate RAFT agent.

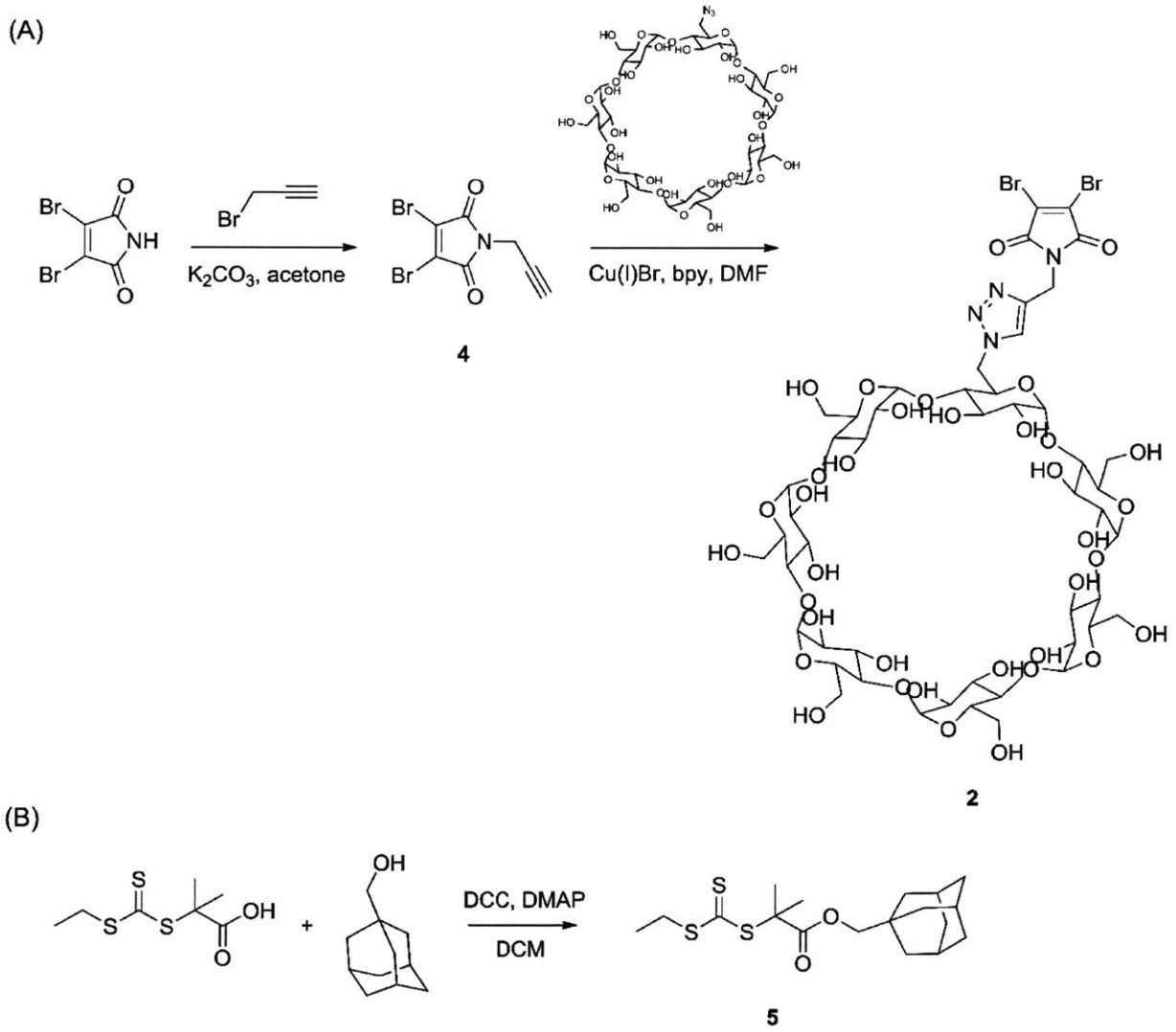

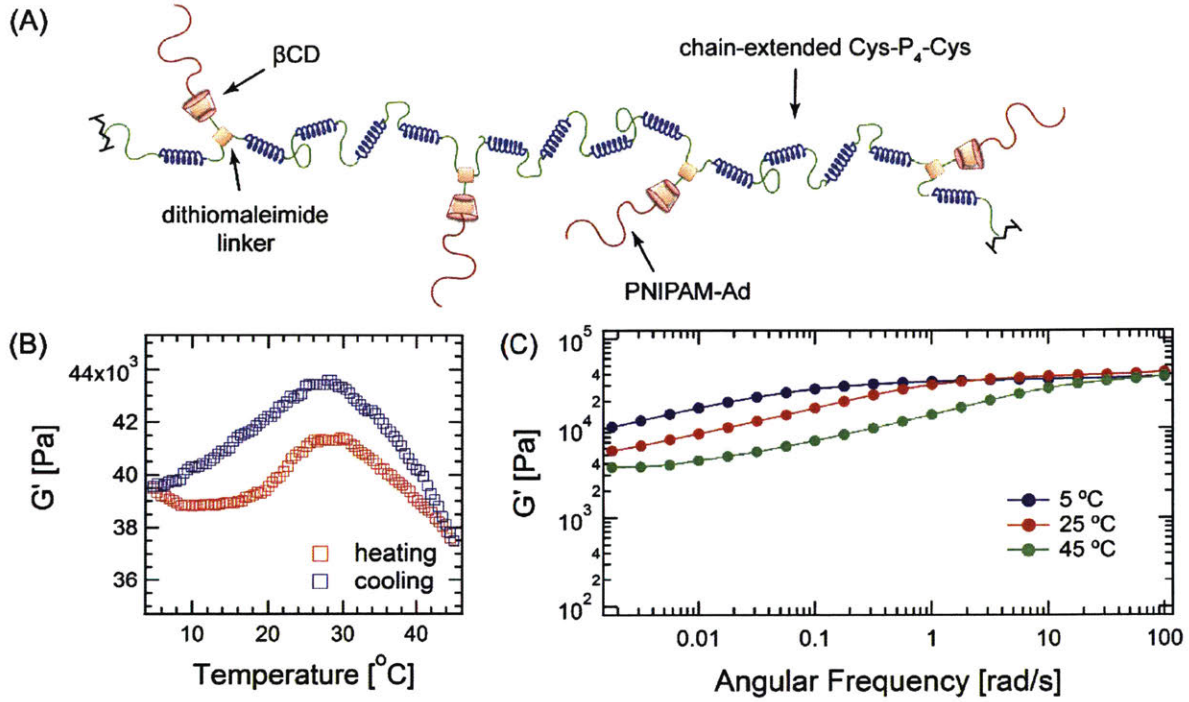

Figure 8-4. Structure and mechanics of hybrid protein-polymer hydrogels. (A) Illustration of the brush-like structure of PNIPAM-extended-P4 chimeric molecule formed via βCD-adamantane complexation; (B) Temperature sweep at 1 °C/min heating/cooling rate; (C) Frequency sweep spectra.

8.3.2 Influence of branched architecture on the mechanical properties

Branched polymers have attracted much interest for fundamental studies and industrial applications due to their distinct flow behaviors compared to their linear analogs.[50, 53-57] However, few reports characterize the synthesis or properties of branched proteins, using either chemical methods or cellular machinery.[58] Here, branched proteins are synthesized with the use of multifunctional crosslinkers in the chain extension reaction, demonstrating an important means to control the mechanical properties of protein gels by modulating the chain structure. The effect of branching is examined by varying the fraction of the trifunctional crosslinker (2,4,6-triallyloxy-

1,3,5-triazine, **6**) from 0 to 100% in the total alkenes (note that the ratio of total alkenes to thiols is kept 1:1). The hydrogels are prepared by thiol-ene click chemistry *via* thermal initiation. Similar to chain extension, all branching reactions are found to reach high endgroup conversion, yielding significant fractions of high molar mass proteins from SDS-PAGE (Figure 8-5). Significant differences in molecular weight distribution of proteins among the 6 reactions examined cannot be measured by gel electrophoresis. An exception occurs at 100% triene, where a larger fraction of low molar mass protein is present, suggesting that the endgroup conversion might be lower than those in other cases. All protein hydrogels are able to be dissolved in 6 M urea buffer post reaction, confirming the hypothesis that addition of **6** only results in branching and not crosslinking, even with 100% triene crosslinker. The gel point under each reaction condition can be calculated using the Carothers equation or the Flory-Stockmayer theory (see calculation details in Appendix and Figure E-8), which shows great dependence on the triene composition. The solubility of gels in urea suggests that the conversion of the endgroups is below the gel point in all cases.

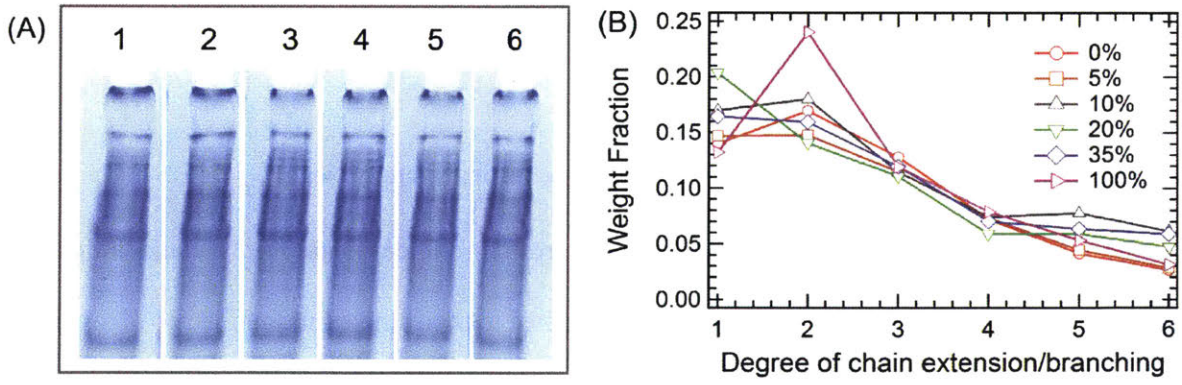

Figure 8-5. Molecular weight distribution of proteins in the branching reaction. (A) SDS-PAGE: The molar fractions of triene 6 in lanes 1-6 is 0, 5, 10, 20, 35, and 100%, respectively; (B) Weight fraction extracted by densitometry.

The mechanical properties of hydrogels are influenced by the branched structure of the proteins. To better compare the entire relaxation spectra with different fractions of **6**, rheology data from creep experiments are converted to the dynamic compliance *J'* and *J"* using a Fourier transform,[59]

$$J'(\omega) = J_e^0 - \omega\int_0^\infty \left[J_e^0 - J(t) + t/\eta_0\right]\sin\omega t dt \tag{8-3}$$

$$J"(\omega) = 1/\omega\eta_0 + \omega\int_0^\infty \left[J_e^0 - J(t) + t/\eta_0\right]\cos\omega t dt \tag{8-4}$$

where J_e^0 is the recoverable compliance, ω the angular frequency, η_0 the zero-shear-rate viscosity, t the experiment time. J_e^0 and η_0 are the intercept and the inverse of the slope, respectively, from a linear fit in steady-state phase of creep. The dynamic compliances are further translated into dynamic moduli *G'* and *G"*,

$$G' = J'/\left(J'^2 + J"^2\right) \tag{8-5}$$

$$G" = J"/\left(J'^2 + J"^2\right) \tag{8-6}$$

The combined master curves are shown in Figure 8-6, which can be divided into three different regimes according to the relaxations present in the gels (from fast to slow): the coiled-coil regime, the entanglement regime and the terminal regime. With addition of a small amount of **6** (5% and 10%), both the high-frequency modulus (G'_∞) and the entanglement modulus (G_e) decrease. This suggests that adding a small amount of crosslinker only causes short chain branching and small drops in the backbone length of the chain-extended proteins, since this would result in a decrease in the total number of entanglements. However, at 20% triene, both G'_∞ and G_e reach their peak values, where the number density of the branch points and the branch length reach an optimal combination. In this case, the backbone length of the protein is likely to be comparable to the

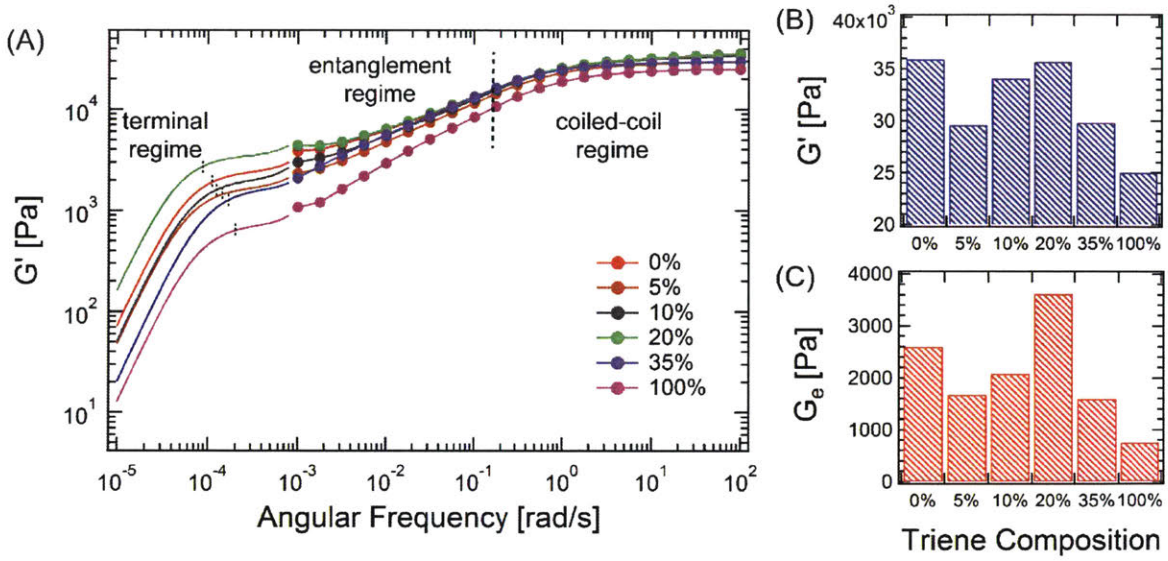

Figure 8-6. Comparison of the mechanical properties of branched hydrogels at different triene compositions. (A) Master curves at 25 °C from oscillatory shear and creep experiments; (B) comparison of the high-frequency moduli; (C) comparison of the entanglement moduli, determined from the converted low-frequency plateau.

linear case, as the molecular weight distributions from SDS-PAGE of these two cases are not distinguishable, but the branched structure provides extra topological interactions. The introduced branches retard the reptation of the entire molecule, as it is only after arm retraction that the reptation of the chain-extended backbone is allowed to happen.[60] Although the coiled-coil relaxation is only slightly affected by the molecule topology (see Figures E-9 and E-10), the reptation regime broadens in the frequency spectrum and extends towards the low frequency regime. This is consistent with the observation of randomly branched polymers in the melt state.[60] Further increase of the triene composition leads to decreases in both G'_∞ and G_e. This is hypothesized to originate from the decreased endgroup conversion and the formation of hyperbranched molecular structures. The densely packed branches impose permanent topological

barriers for different chains to entangle, which leads to much lower solution viscosities.[61] Recently, the viscoelasticity and the dynamic relaxation of the synthetic hydrogels is found to be essential to mimic the complex biological tissues.[62] The presented branching reaction in this study establishes a facile approach of tuning the network mechanics over the entire frequency window, especially in the long time relaxation, which can be useful in mimicking the properties of natural tissues.

8.4. Conclusions

Under appropriate conditions, thiol-maleimide, thiol-bromomaleimide and thiol-ene coupling can all result in significant chain extension. The differences in chemistries' reactivity and side reactions may cause variations in the molecular weight and its distribution of chain-extended proteins and the topological entanglement effect in gels. While thiol-maleimide conjugation is the most common and the easiest to implement, thiol-ene click chemistry can achieve high endgroup conversion fairly rapidly. Thiol-bromomaleimide shows its potential in reversibly modifying proteins, and using functionalized dibromomaleimide as a chain extender allows further control of hydrogels' properties by incorporating side chain functionalities into the protein architecture. Here, thermoresponsive changes in mechanical properties of gels are demonstrated with PNIPAM grafts. Lastly, branched proteins are prepared in $A_2 + B_2/B_3$ mixed type reactions. The entanglement plateau modulus is increased when branches are long enough to enhance topological constraints yet the added branches do not sacrifice the backbone length. In conclusion, the structure of engineered proteins and their assembly behaviors can be easily modified with the use of different chemistries, which presents a rich toolbox to tailor the structure-properties of protein materials in various applications.

8.5. References

1. Drury, J. L.; Mooney, D. J. Hydrogels for Tissue Engineering: Scaffold Design Variables and Applications. *Biomaterials* 2003, 24, 4337-4351.

2. Gong, J. P.; Katsuyama, Y.; Kurokawa, T.; Osada, Y. Double-Network Hydrogels with Extremely High Mechanical Strength. *Advanced Materials* 2003, 15, 1155-1158.

3. Sun, J.-Y.; Zhao, X.; Illeperuma, W. R. K.; Chaudhuri, O.; Oh, K. H.; Mooney, D. J.; Vlassak, J. J.; Suo, Z. Highly Stretchable and Tough Hydrogels. *Nature* 2012, 489, 133-136.

4. Haraguchi, K.; Takehisa, T. Nanocomposite Hydrogels: A Unique Organic–Inorganic Network Structure with Extraordinary Mechanical, Optical, and Swelling/De-Swelling Properties. *Advanced Materials* 2002, 14, 1120-1124.

5. Wang, Q.; Mynar, J. L.; Yoshida, M.; Lee, E.; Lee, M.; Okuro, K.; Kinbara, K.; Aida, T. High-Water-Content Mouldable Hydrogels by Mixing Clay and a Dendritic Molecular Binder. *Nature* 2010, 463, 339-343.

6. Kloxin, A. M.; Kasko, A. M.; Salinas, C. N.; Anseth, K. S. Photodegradable Hydrogels for Dynamic Tuning of Physical and Chemical Properties. *Science* 2009, 324, 59-63.

7. Guvendiren, M.; Lu, H. D.; Burdick, J. A. Shear-Thinning Hydrogels for Biomedical Applications. *Soft Matter* 2012, 8, 260-272.

8. Holten-Andersen, N.; Harrington, M. J.; Birkedal, H.; Lee, B. P.; Messersmith, P. B.; Lee, K. Y. C.; Waite, J. H. Ph-Induced Metal-Ligand Cross-Links Inspired by Mussel Yield Self-Healing Polymer Networks with near-Covalent Elastic Moduli. *Proceedings of the National Academy of Sciences* 2011, 108, 2651-2655.

9. Glassman, M. J.; Chan, J.; Olsen, B. D. Reinforcement of Shear Thinning Protein Hydrogels by Responsive Block Copolymer Self-Assembly. *Advanced Functional Materials* 2013, 23, 1182-1193.

10. Li, L.; Teller, S.; Clifton, R. J.; Jia, X.; Kiick, K. L. Tunable Mechanical Stability and Deformation Response of a Resilin-Based Elastomer. *Biomacromolecules* 2011, 12, 2302-2310.

11. Trabbic-Carlson, K.; Setton, L. A.; Chilkoti, A. Swelling and Mechanical Behaviors of Chemically Cross-Linked Hydrogels of Elastin-Like Polypeptides. *Biomacromolecules* 2003, 4, 572-580.

12. Chung, C.; Lampe, K. J.; Heilshorn, S. C. Tetrakis(Hydroxymethyl) Phosphonium Chloride as a Covalent Cross-Linking Agent for Cell Encapsulation within Protein-Based Hydrogels. *Biomacromolecules* 2012, 13, 3912-3916.

13. Lv, S.; Dudek, D. M.; Cao, Y.; Balamurali, M. M.; Gosline, J.; Li, H. Designed Biomaterials to Mimic the Mechanical Properties of Muscles. *Nature* 2010, 465, 69-73.

14. Shen, W.; Lammertink, R. G. H.; Sakata, J. K.; Kornfield, J. A.; Tirrell, D. A. Assembly of an Artificial Protein Hydrogel through Leucine Zipper Aggregation and Disulfide Bond Formation. *Macromolecules* 2005, 38, 3909-3916.

15. Davis, N. E.; Ding, S.; Forster, R. E.; Pinkas, D. M.; Barron, A. E. Modular Enzymatically Crosslinked Protein Polymer Hydrogels for in Situ Gelation. *Biomaterials* 2010, 31, 7288-7297.

16. Graessley, W. W. *Polymeric Liquids and Networks : Structure and Properties*. Garland Science: New York, 2004; p xv, 559 p.

17. Tanaka, F. *Polymer Physics : Applications to Molecular Association and Thermoreversible Gelation*. Cambridge University Press: Cambridge, 2011; p xv, 387 pages.

18. Kim, M.; Tang, S.; Olsen, B. D. Physics of Engineered Protein Hydrogels. *Journal of Polymer Science Part B: Polymer Physics* 2013, 51, 587-601.

19. Zhou, H.; Woo, J.; Cok, A. M.; Wang, M.; Olsen, B. D.; Johnson, J. A. Counting Primary Loops in Polymer Gels. *Proceedings of the National Academy of Sciences* 2012.

20. Sahin, E.; Kiick, K. L. Macromolecule-Induced Assembly of Coiled-Coils in Alternating Multiblock Polymers. *Biomacromolecules* 2009, 10, 2740-2749.

21. Jing, P.; Rudra, J. S.; Herr, A. B.; Collier, J. H. Self-Assembling Peptide-Polymer Hydrogels Designed from the Coiled Coil Region of Fibrin. *Biomacromolecules* 2008, 9, 2438-2446.

22. Glassman, M. J.; Olsen, B. D. Structure and Mechanical Response of Protein Hydrogels Reinforced by Block Copolymer Self-Assembly. *Soft Matter* 2013, 9, 6814-6823.

23. Wu, L. C.; Yang, J.; Kopeček, J. Hybrid Hydrogels Self-Assembled from Graft Copolymers Containing Complementary B-Sheets as Hydroxyapatite Nucleation Scaffolds. *Biomaterials* 2011, 32, 5341-5353.

24. Tang, S.; Glassman, M. J.; Li, S.; Socrate, S.; Olsen, B. D. Oxidatively Responsive Chain Extension to Entangle Engineered Protein Hydrogels. *Macromolecules* 2014, 47, 791-799.

25. Canalle, L. A.; Lowik, D. W. P. M.; van Hest, J. C. M. Polypeptide-Polymer Bioconjugates. *Chemical Society Reviews* 2010, 39, 329-353.

26. Stephanopoulos, N.; Francis, M. B. Choosing an Effective Protein Bioconjugation Strategy. *Nat Chem Biol* 2011, 7, 876-884.

27. Baldwin, A. D.; Kiick, K. L. Tunable Degradation of Maleimide–Thiol Adducts in Reducing Environments. *Bioconjugate Chemistry* 2011, 22, 1946-1953.

28. Smith, M. E. B.; Schumacher, F. F.; Ryan, C. P.; Tedaldi, L. M.; Papaioannou, D.; Waksman, G.; Caddick, S.; Baker, J. R. Protein Modification, Bioconjugation, and Disulfide Bridging Using Bromomaleimides. *Journal of the American Chemical Society* 2010, 132, 1960-1965.

29. Jones, M. W.; Strickland, R. A.; Schumacher, F. F.; Caddick, S.; Baker, J. R.; Gibson, M. I.; Haddleton, D. M. Polymeric Dibromomaleimides as Extremely Efficient Disulfide Bridging Bioconjugation and Pegylation Agents. *Journal of the American Chemical Society* 2011, 134, 1847-1852.

30. Robin, M. P.; Wilson, P.; Mabire, A. B.; Kiviaho, J. K.; Raymond, J. E.; Haddleton, D. M.; O'Reilly, R. K. Conjugation-Induced Fluorescent Labeling of Proteins and Polymers Using Dithiomaleimides. *Journal of the American Chemical Society* 2013, 135, 2875-2878.

31. Cui, Y.; Yan, Y.; Chen, Y.; Wang, Z. Dibromomaleimide Derivative as an Efficient Polymer Coupling Agent for Building Topological Polymers. *Macromolecular Chemistry and Physics* 2013, 214, 470-477.

32. Northrop, B. H.; Coffey, R. N. Thiol–Ene Click Chemistry: Computational and Kinetic Analysis of the Influence of Alkene Functionality. *Journal of the American Chemical Society* 2012, 134, 13804-13817.

33. Schelté, P.; Boeckler, C.; Frisch, B.; Schuber, F. Differential Reactivity of Maleimide and Bromoacetyl Functions with Thiols: Application to the Preparation of Liposomal Diepitope Constructs. *Bioconjugate Chemistry* 1999, 11, 118-123.

34. Schöneich, C. Mechanisms of Protein Damage Induced by Cysteine Thiyl Radical Formation. *Chemical Research in Toxicology* 2008, 21, 1175-1179.

35. Valkevich, E. M.; Guenette, R. G.; Sanchez, N. A.; Chen, Y.-c.; Ge, Y.; Strieter, E. R. Forging Isopeptide Bonds Using Thiol–Ene Chemistry: Site-Specific Coupling of Ubiquitin

Molecules for Studying the Activity of Isopeptidases. *Journal of the American Chemical Society* 2012, 134, 6916-6919.

36. Weinrich, D.; Lin, P.-C.; Jonkheijm, P.; Nguyen, U. T. T.; Schröder, H.; Niemeyer, C. M.; Alexandrov, K.; Goody, R.; Waldmann, H. Oriented Immobilization of Farnesylated Proteins by the Thiol-Ene Reaction. *Angewandte Chemie International Edition* 2010, 49, 1252-1257.

37. Dondoni, A.; Massi, A.; Nanni, P.; Roda, A. A New Ligation Strategy for Peptide and Protein Glycosylation: Photoinduced Thiol–Ene Coupling. *Chemistry – A European Journal* 2009, 15, 11444-11449.

38. Petter, R. C.; Salek, J. S.; Sikorski, C. T.; Kumaravel, G.; Lin, F. T. Cooperative Binding by Aggregated Mono-6-(Alkylamino)-.Beta.-Cyclodextrins. *Journal of the American Chemical Society* 1990, 112, 3860-3868.

39. Lai, J. T.; Filla, D.; Shea, R. Functional Polymers from Novel Carboxyl-Terminated Trithiocarbonates as Highly Efficient Raft Agents. *Macromolecules* 2002, 35, 6754-6756.

40. Convertine, A. J.; Lokitz, B. S.; Vasileva, Y.; Myrick, L. J.; Scales, C. W.; Lowe, A. B.; McCormick, C. L. Direct Synthesis of Thermally Responsive Dma/Nipam Diblock and Dma/Nipam/Dma Triblock Copolymers Via Aqueous, Room Temperature Raft Polymerization†. *Macromolecules* 2006, 39, 1724-1730.

41. Hermanson, G. T. Bioconjugate Techniques, 2nd Edition. *Bioconjugate Techniques, 2nd Edition* 2008, 1-1202.

42. Dutton, S.; Rolfes, H.; Stepto, R. F. T. Comparison of Ahmad-Rolfes-Stepto Theory, Rate Theory and Monte-Carlo Modelling of Gel Point and Network Modulus. *Polymer* 1994, 35, 4521-4526.

43. Ryan, C. P.; Smith, M. E. B.; Schumacher, F. F.; Grohmann, D.; Papaioannou, D.; Waksman, G.; Werner, F.; Baker, J. R.; Caddick, S. Tunable Reagents for Multi-Functional Bioconjugation: Reversible or Permanent Chemical Modification of Proteins and Peptides by Control of Maleimide Hydrolysis. *Chemical Communications* 2011, 47, 5452-5454.

44. Nathani, R. I.; Chudasama, V.; Ryan, C. P.; Moody, P. R.; Morgan, R. E.; Fitzmaurice, R. J.; Smith, M. E. B.; Baker, J. R.; Caddick, S. Reversible Protein Affinity-Labelling Using Bromomaleimide-Based Reagents. *Organic & Biomolecular Chemistry* 2013, 11, 2408-2411.

45. Hoyle, C. E.; Bowman, C. N. Thiol–Ene Click Chemistry. *Angewandte Chemie International Edition* 2010, 49, 1540-1573.

46. Hoyle, C. E.; Lowe, A. B.; Bowman, C. N. Thiol-Click Chemistry: A Multifaceted Toolbox for Small Molecule and Polymer Synthesis. *Chemical Society Reviews* 2010, 39, 1355-1387.

47. Wan, Q.; Danishefsky, S. J. Free-Radical-Based, Specific Desulfurization of Cysteine: A Powerful Advance in the Synthesis of Polypeptides and Glycopolypeptides. *Angewandte Chemie International Edition* 2007, 46, 9248-9252.

48. Larson, R. G.; Sridhar, T.; Leal, L. G.; McKinley, G. H.; Likhtman, A. E.; McLeish, T. C. B. Definitions of Entanglement Spacing and Time Constants in the Tube Model. *Journal of Rheology* 2003, 47, 809-818.

49. Rekharsky, M. V.; Inoue, Y. Complexation Thermodynamics of Cyclodextrins. *Chemical Reviews* 1998, 98, 1875-1918.

50. Graessley, W. W. *Polymeric Liquids and Networks : Dynamics and Rheology*. Garland Science: London ; New York, 2008; p xix, 801 p.

51. Davis, M. E.; Brewster, M. E. Cyclodextrin-Based Pharmaceutics: Past, Present and Future. *Nat Rev Drug Discov* 2004, 3, 1023-1035.

52. Harries, D.; Rau, D. C.; Parsegian, V. A. Solutes Probe Hydration in Specific Association of Cyclodextrin and Adamantane. *Journal of the American Chemical Society* 2005, 127, 2184-2190.

53. Dealy, J. M.; Wissbrun, K. F. *Melt Rheology and Its Role in Plastics Processing : Theory and Applications*. Van Nostrand Reinhold: New York, 1990; p xix, 665 p.

54. Lohse, D. J.; Milner, S. T.; Fetters, L. J.; Xenidou, M.; Hadjichristidis, N.; Mendelson, R. A.; García-Franco, C. A.; Lyon, M. K. Well-Defined, Model Long Chain Branched Polyethylene. 2. Melt Rheological Behavior. *Macromolecules* 2002, 35, 3066-3075.

55. Wood-Adams, P.; Costeux, S. Thermorheological Behavior of Polyethylene: Effects of Microstructure and Long Chain Branching. *Macromolecules* 2001, 34, 6281-6290.

56. Wang, Z.; Chen, X.; Larson, R. G. Comparing Tube Models for Predicting the Linear Rheology of Branched Polymer Melts. *Journal of Rheology (1978-present)* 2010, 54, 223-260.

57. Janzen, J.; Colby, R. H. Diagnosing Long-Chain Branching in Polyethylenes. *Journal of Molecular Structure* 1999, 485–486, 569-584.

58. Zhang, W.-B.; Sun, F.; Tirrell, D. A.; Arnold, F. H. Controlling Macromolecular Topology with Genetically Encoded Spytag–Spycatcher Chemistry. *Journal of the American Chemical Society* 2013, 135, 13988-13997.

59. Ferry, J. *Viscoelastic Properties of Polymers*. 3d ed.; Wiley: New York, 1980; p xxiv, 641 p.

60. McLeish, T. C. B. Tube Theory of Entangled Polymer Dynamics. *Advances in Physics* 2002, 51, 1379-1527.

61. Voit, B. I.; Lederer, A. Hyperbranched and Highly Branched Polymer Architectures—Synthetic Strategies and Major Characterization Aspects. *Chemical Reviews* 2009, 109, 5924-5973.

62. McKinnon, D. D.; Domaille, D. W.; Cha, J. N.; Anseth, K. S. Biophysically Defined and Cytocompatible Covalently Adaptable Networks as Viscoelastic 3d Cell Culture Systems. *Advanced Materials* 2013, n/a-n/a.

Chapter 9 Conclusions

9.1. Summary

Associating polymers have been widely used in different applications such as self-healing materials, conductive electrolytes, rheological modifiers, and devices for cell/protein delivery. Despite these successful examples, there are still many significant challenges in fully understanding the physics of associating networks. This is due largely to the interplay of polymer topologies and association chemistries that exhibits complex behavior highly dependent on the time and length scales of interest. This thesis first examined the diffusive motions of associating polymers, a problem that has not received much attention in the past two decades. Surprising "super-diffusion" was discovered for the first time, and the experimental results were explained by a simple two-state model considering the dynamic equilibrium of association and dissociation. The fundamental insights gained from these studies illustrate how dynamics translates from associating functional groups to molecules up to the entire network. In the second part, this thesis presented a new strategy of modulating the network mechanics specifically on long time scales while inducing minimal changes in the chemical composition of the associating polymers. By tuning the entanglement dynamics of macromolecules from their molecular structure, this thesis demonstrates an ability to produce hydrogels that are soft but tough and highly extensible.

The first part of this thesis experimentally measured self-diffusion of unentangled associating polymers with a variety of molecular structures and sticker chemistries at the gel state. The first model system investigated was hydrogels formed by linear proteins with four coiled-coils along the backbone. By using forced Rayleigh scattering (FRS), it was observed for the first time that the self-diffusion of these associative proteins in the hydrogels transitioned from Fickian

diffusion scaling to phenomenological super-diffusion at the length scales that were nearly 100-1000 times the radius gyration of the chains. Interestingly, the scaling of grating relaxation time vs. squared grating spacing seemed to recover Fickian diffusion behavior when the diffusion length scale decreased to hundreds of nm. Such anomalous diffusion phenomenon was observed at varying temperature and gel concentrations. A two-state model was proposed to explain the experimental results. The model hypothesized that the associating polymers appear at a fast-diffusing state and a slow-diffusing state, and the two states can exchange at appreciable rates. The simplicity of this phenomenological model provided an analytical solution to capture the two Fickian regimes and described the physical origin of the phenomenological super-diffusion by a transition between the two Fickian limits. Oscillatory shear rheology was used to probe the macroscopic network relaxation. The presence of a sticky-Rouse-like relaxation was seen in these coiled-coil protein gels, which suggested collective mobility of the associating polymers. Furthermore, a phenomenological dissociation rate was extracted from the two-state model, which yielded a time-temperature-concentration superposition of the rheological data in a concentration regime where intermolecular association was dominant. Finally, the concentration scalings of the chain diffusivity, the zero-shear-rate viscosity and the phenomenological dissociation rate all qualitatively agreed with the sticky Rouse theory.

The generality of the observed anomalous diffusion was then demonstrated by exploring associating networks with a very distinct molecular structure and sticker chemistry. The second model system used in the thesis was four-arm polyethylene glycol (PEG) polymers with chain ends decorated with terpyridine moieties, which formed transient linkages with zinc ions. The diffusion behavior of these polymers was again probed by FRS. Similar to the experimental findings in the coiled-coil protein hydrogels, self-diffusion of these star-shaped associating polymers also showed

two Fickian diffusion regimes and one phenomenological super-diffusion regime. In addition, diffusion of the same star-shaped tracers containing only three associating arms was explored. Compared to the cases of self-diffusion, the grating relaxation time was smaller in all tracer diffusion measurements. Experimental data of both self- and tracer diffusion were analyzed by the two-state model. It was found that a reduction in the number of associating group caused an increase in the apparent polymer mobility and a faster transition from the associative to the molecular state. The sticky Rouse theory also found success in describing the concentration dependence of the apparent chain diffusion coefficients and the phenomenological sticker lifetime.

The third model network was linear poly(*N*,*N*-dimethylacrylamide) polymers with many pendant histidine side groups transiently linked to nickel ions. The sticker density of this model system was dramatically higher than the ones in the other two cases. Only Fickian diffusion was observed within the experimentally accessible window. In addition, this study demonstrated a method termed diffusion spectrometry to study the dissociation rate of stickers in the gels, which distinguished from previous measurements that were performed in dilute solution and on isolated junctions where the effect of polymer backbone was neglected. The sticker dissociation rate was found faster than the sticker exchange rate determined by linear rheology, demonstrating that sticker dissociation was a prerequisite step for exchange.

This thesis also explored the use of fluorescence recovery after photobleaching (FRAP) to measure diffusion of associating polymers in the gels. A mathematical framework was developed to analyze the FRAP data in situations where the two-state model applies. Preliminary results suggested that the proposed FRAP-based method allowed more efficient characterization of the diffusive behavior of associating polymers and also had the potential to discriminate different models.

The second part of the thesis explored new strategies to control the mechanical properties of associating networks, especially from a polymer physics perspective. Using the multi-block coiled-coil proteins as a model system, linearly extended proteins were prepared via disulfide linkages connecting the chain ends. The molecular weight and molecular weight distribution in the reaction mixtures prepared *via* macromolecular condensation agreed well with the theoretical Stockmayer-Jacobson distribution. When the gels were prepared at the entanglement state, it was observed that the low-frequency modulus, creep resistance, extensibility and toughness of the network all increased substantially. Notably, all of these enhancements in the network mechanics only resulted in a small increase in the high-frequency modulus. The network relaxation time (or the exchange time of the network junctions) and the zero-shear-rate viscosity were extracted from shear rheology measurements. The concentration dependence of these two dynamic properties qualitatively matched the prediction of the sticky reptation theory. Furthermore, by taking advantage of the redox responsiveness of the disulfide groups, it was shown that the entanglement effect as well as the resulting mechanical enhancement could be reversibly switched on and off by small-molecule redox modulators.

Since the entanglement effect is governed by the molar mass and the molecular architecture of the chain-extended proteins, it was then hypothesized that by employing various thiol-coupling chemistries in the chain-extension reactions, one can easily control the degree of chain extension, the extent of entanglement and thus the corresponding mechanical properties. To this end, four different chemistries were systematically explored and compared, which were disulfide formation, thiol-maleimide conjugation, thiol-bromomaleimide conjugation, and thiol-ene coupling. The last three chemistries were A_2+ B_2 type polycondensation reactions, whereas the first one was self-polycondensation reaction. It was found that the reaction *via* disulfide formation provided the

highest degree of chain extension, while the other three chemistries suffered from side reactions and/or possessed limitation due to an experimental imbalance of the stoichiometry of the two reactive functional groups. Additionally, this thesis explored the use of trifunctional crosslinkers in the thiol-coupling reactions while keeping the extent of reaction below the chemical gel point to yield branched proteins that were capable of chain entanglement. The entanglement network modulus and the longest relaxation time could be tuned by varying the amount of trifunctional crosslinkers in the reactions.

In summary, this thesis has made important contributions to advance our understanding of the dynamics and mechanics of associating networks. A series of studies in the first part has provided new experimental evidence of the anomalous diffusion of associating polymers. We believe this knowledge will provide important guidance for future theoretical efforts to further understand the complex behavior of diffusion. The efforts in the second part of the thesis have provided a new perspective in guiding the design of and control over the mechanical properties of associative networks. It is demonstrated that the macroscopic mechanical properties of networks can be effectively tailored by engineering the structure or architecture of the network forming macromolecular constituents without altering their chemical composition.

9.2. Outlook

There are many opportunities and challenges to further explore the dynamics of associating polymer networks. First, there is a need to develop new techniques to enable diffusion measurement on length scales below the diffraction limit and approaching 100 nm. Current measurements on diffusion of associating polymers use forced Rayleigh scattering (FRS) or fluorescence recovery after photobleaching (FRAP), which are inherently constrained by the

diffraction limit of light because both techniques reply on changes of optical signals (fluorescence or absorbance) in the specimen for creating the concentration gradient and detecting the gradient evolution over time. However, information of diffusion on length scales around 100 nm is very important for understanding the slow mode diffusion. Therefore, development of new techniques is necessary to examine the slow diffusive behavior on the relevant small length scales.

Second, future research should identify the physical details of the two diffusive states hypothesized in the phenomenological two-state model. Although the current model provides satisfactory descriptions of the experimental diffusion data and yields estimations of the model parameters that allow quantitative comparisons between different experimental systems and comparisons between experiment and theory, current explanation remains on a phenomenological level. For the simplest associative polymer explored in the thesis, there are more than two true molecular states, where each molecular state is unambiguously defined by a combination of the sticker states (closed or open) on the polymers. Future work needs to carefully address how multiple molecular states collapse into two simple phenomenological diffusive states. In addition, complementary efforts in simulation and theory are also indispensable to yield insights into the physics of diffusion of associating polymers.

Third, with deeper understanding of the physical origin of anomalous diffusion of associating polymers, it will be very interesting to probe the structural basis for the phenomenological super-diffusion from an experiment perspective. The two model systems that have shown phenomenological super-diffusion have four stickers per chain. In contrast, the system that has many (nearly twenty) stickers per polymer chain does not exhibit super-diffusion within the narrow experimentally accessible parameter space. Identifying the criteria for observing super-diffusion, especially on the molecular level, is a challenging topic. In addition, it should be

mentioned that the systems explored in this thesis all have well-defined molecular structure. Future investigations can be extended to more complex systems, for example, naturally derived biopolymers that have a much larger degree of structural heterogeneity such as molecular weight and distribution, sticker position and sticker bond type. It will be interesting to see how the two-state model might be modified to describe these systems.

On the mechanics side, there are also several exciting research directions to pursue. First, stain-included alignment of polymer chains is a well-known phenomenon that contributes to the mechanical stiffening or rise of viscosity. In this thesis, it is concluded that entanglement leads to substantial improvement in the network stretchability and toughness when the gels are under uniaxial tension. The physical origin is hypothesized to be the alignment of entangled chains causing stabilization or even strengthening of the associative bonds between protein molecules. To validate the hypothesis, *in situ* structural characterization methods such as scattering or microscopy can be employed to quantify the extent of alignment. Very recently, a similar chain-extension strategy was applied on linear polydimethylsiloxane (PDMS) polymers with pendant 2,6-pyridinedicarboxamide side groups that were capable of complexing with metal ions to form coordinate bonds, and similar mechanical enhancement in network stretchability and toughness was observed.[1] Therefore, it is expected that studies of the entangled protein gels should yield generalizable physical insights into the toughening mechanism induced by chain entanglement. Furthermore, studying chain alignment under shear comparing to elongation may yield new knowledge.

The mechanical properties under high-rate deformation will be another interesting topic for future exploration. By combining information from creep and small amplitude oscillatory shear, this thesis has carefully characterized the mechanical response of gels in a frequency range

of 10^{-5} to 10^{2} rad/s, where network relaxation is attributed to the exchange of stickers between network junctions and the diffusive motions of chains. However, there is a still lack of fundamental knowledge regarding the relaxation mechanisms of associative networks at larger deformation rates, especially in the kHz range that is relevant to blast or ballistic deformation. Existing techniques for studying the mechanical properties of polymer networks under such high-rate deformation include split Hopkinson pressure bar[2, 3] (strain-rate up to 10^{3} s^{-1}), drop weight tests[3, 4] (strain-rate up to 10^{3} s^{-1}), and high-bandwidth AFM rheology[5] (frequency range: 1 Hz to 10 kHz), to name a few. However, these methods cannot be easily applied for studying associative networks that are often softer and are more prone to fracture compared to their covalent counterparts. Therefore, a major challenge will be developing new experimental tools for high-rate mechanical characterizations.

9.3. References

1. Li, C.-H.; Wang, C.; Keplinger, C.; Zuo, J.-L.; Jin, L.; Sun, Y.; Zheng, P.; Cao, Y.; Lissel, F.; Linder, C., *et al.* A Highly Stretchable Autonomous Self-Healing Elastomer. *Nat Chem* 2016, advance online publication.
2. Ferreira, F.; Vaz, M. A.; Simões, J. A. Mechanical Properties of Bovine Cortical Bone at High Strain Rate. *Materials Characterization* 2006, 57, 71-79.
3. Field, J. E.; Walley, S. M.; Proud, W. G.; Goldrein, H. T.; Siviour, C. R. Review of Experimental Techniques for High Rate Deformation and Shock Studies. *International Journal of Impact Engineering* 2004, 30, 725-775.
4. Roland, C. M.; Twigg, J. N.; Vu, Y.; Mott, P. H. High Strain Rate Mechanical Behavior of Polyurea. *Polymer* 2007, 48, 574-578.
5. Nia, Hadi T.; Bozchalooi, Iman S.; Li, Y.; Han, L.; Hung, H.-H.; Frank, E.; Youcef-Toumi, K.; Ortiz, C.; Grodzinsky, A. High-Bandwidth Afm-Based Rheology Reveals That

Cartilage Is Most Sensitive to High Loading Rates at Early Stages of Impairment. *Biophysical Journal* 2013, 104, 1529-1537.

Appendix A: Supporting Information for Chapter 3

1. Estimation of the radius of gyration (R_g) of protein P_4.

It is assumed that the protein P_4 is in good solvent condition where the scaling $R_g \sim M^{0.6}$ applies.[1, 2] The R_g of protein P_4 is estimated by comparing its molecular weight to a single C_{10} domain,

$$R_{g,P_4} \approx \left(\frac{M_{P_4}}{M_{C_{10}}}\right)^{0.6} R_{g,C_{10}} \approx \left(\frac{62.8}{7.9}\right)^{0.6} \times 5 = 17.3(\text{nm}) \tag{1}$$

In the calculation above, the R_g value of C_{10} measured by quasi-elastic light scattering (ca. 5 nm) from Shen *et al.*,[3] is used.

2. Derivation of the analytical solutions of the decay time constants from the two-state model.

The governing equations in the real space are

$$\begin{aligned} \frac{\partial C_M}{\partial t} &= D_M \frac{\partial^2 C_M}{\partial x^2} - k_{on} C_M + k_{off} C_A \\ \frac{\partial C_A}{\partial t} &= D_A \frac{\partial^2 C_A}{\partial x^2} + k_{on} C_M - k_{off} C_A \end{aligned} \tag{2}$$

After Fourier transform, the equations become

$$\begin{aligned} \frac{\partial \hat{C}_M}{\partial t} &= -q^2 D_M \hat{C}_M - k_{on} \hat{C}_M + k_{off} \hat{C}_A \\ \frac{\partial \hat{C}_A}{\partial t} &= -q^2 D_A \hat{C}_A + k_{on} \hat{C}_M - k_{off} \hat{C}_A \end{aligned} \tag{3}$$

where $q = 2\pi/d$ and the concentration $\hat{C}_i$ (i = M or A) in Fourier space is defined as

$$\hat{C}_i(q,t) = \int_{-\infty}^{\infty} C_i(x,t) e^{-iq \cdot x} dx \tag{4}$$

The equations can be represented in a vector-matrix form.

$$\frac{\partial}{\partial t}\begin{bmatrix}\hat{C}_M\\ \hat{C}_A\end{bmatrix}=\begin{bmatrix}-q^2D_M-k_{on} & k_{off}\\ k_{on} & -q^2D_A-k_{off}\end{bmatrix}\begin{bmatrix}\hat{C}_M\\ \hat{C}_A\end{bmatrix} \tag{5}$$

A general solution to the equations above is

$$\hat{C}_i = m_{i,1}\exp(r_1 t)+m_{i,2}\exp(r_2 t) \tag{6}$$

where r_1 and r_2 are the eigenvalues of the matrix:

$$r_1, r_2 = \frac{-\left(k_{on}+k_{off}+q^2D_M+q^2D_A\right)\pm\sqrt{\left(k_{on}+k_{off}+q^2D_M+q^2D_A\right)^2-4\left(k_{on}q^2D_A+k_{off}q^2D_M+q^4D_MD_A\right)}}{2} \tag{7}$$

And they can be related to the time constants in the FRS decay by

$$\tau = -\frac{1}{r} \tag{8}$$

The dimensional time constants are

$$\tau_1, \tau_2 = \frac{2}{\left(k_{on}+k_{off}+q^2D_M+q^2D_A\right)\mp\sqrt{\left(k_{on}+k_{off}+q^2D_M+q^2D_A\right)^2-4\left(k_{on}q^2D_A+k_{off}q^2D_M+q^4D_MD_A\right)}} \tag{9}$$

By defining the following dimensionless constants,

$$\tilde{d}^2 \equiv \frac{k_{off}}{q^2D_A}\gamma K_{eq}, \qquad K_{eq} \equiv \frac{k_{on}}{k_{off}}, \qquad \gamma \equiv \frac{D_A}{D_M}, \qquad \tilde{\tau} = k_{off}\tau \tag{10}$$

the dimensionless time constants become

$$\tilde{\tau}_1, \tilde{\tau}_2 = 2\Bigg/\left[\left(1+K_{eq}+\frac{\gamma K_{eq}}{\tilde{d}^2}+\frac{\gamma^2 K_{eq}}{\tilde{d}^2}\right)\mp\sqrt{\left(1+K_{eq}+\frac{\gamma K_{eq}}{\tilde{d}^2}+\frac{\gamma^2 K_{eq}}{\tilde{d}^2}\right)^2-4\left(\frac{\gamma^2 K_{eq}}{\tilde{d}^2}+\frac{\gamma K_{eq}^2}{\tilde{d}^2}+\frac{\gamma^3 K_{eq}^2}{\tilde{d}^4}\right)}\right] \tag{11}$$

Note that the time constant τ_2 is at least two orders of magnitude smaller than τ_1 (Figure A-1). In FRS experiment, the small time constant is always less than 1 s, even for gels at high concentrations. When analyzing the FRS results and performing the fitting, the first few data points

were discarded to eliminate the effect from the small time constant. This practice should minimally affect the extraction of the large time constant. In the following, the time constant τ refers to the large time constant.

3. Asymptotically matched solutions to the Fickian regimes.

(1) For the Fickian regime at large d^2,

$$\tau = \frac{2}{k_{on} + k_{off} + q^2 D_M - \sqrt{\left(k_{on} + k_{off} + q^2 D_M\right)^2 - 4q^2 D_M k_{off}}} \tag{12}$$

In the limit of infinitely large d^2, or vanishingly small q^2, the solution becomes

$$\tau = \frac{d^2}{4\pi^2 D_A}\left(\frac{K_{eq}+1}{K_{eq}+1/\gamma}\right) = \frac{d^2}{4\pi^2 D_M}\left(\frac{K_{eq}+1}{\gamma K_{eq}+1}\right) \tag{13}$$

(2) For the Fickian regime at small d^2,

$$\tau = \frac{1}{k_{off} + q^2 D_A} \tag{14}$$

In the limit of very small d^2, or infinitely large q^2, the solution becomes

$$\tau = \frac{d^2}{4\pi^2 D_A} \tag{15}$$

The solutions (13) and (15) are plotted in Figure 3, and the solutions (12) and (14) are plotted in Figure A-2.

4. Prediction from the two-state model.

(1) *A limiting case in the two-state model.*

As shown in Figure A-3, the two-state model loses its sensitivity to the parameters K_{eq} and γ, when $K_{eq} >> 1$ and $\gamma K_{eq} << 1$ (the relevant condition in experiment). It can be seen that the shape of the

curve is completely determined by $w = (K_{eq}+1)/(K_{eq}+1/\gamma)$ where K_{eq} is large and γ is small for typical hydrogel materials. The position of the curve is determined by k_{off} and D_B, which are useful values for non-dimensionalization. The solution of the non-dimensionalized time constant in the limiting case (the bold curve) can be expressed as

$$\tilde{\tau} = \frac{w\tilde{d}^4 + (1-w)\tilde{d}^2}{\tilde{d}^2 + 1 - w} \tag{16}$$

where in the limit of $K_{eq} >> 1$ and $\gamma K_{eq} << 1$.

$$w = \frac{K_{eq}+1}{K_{eq}+1/\gamma} \approx \frac{1}{\gamma K_{eq}} \tag{17}$$

(2) *Slope of the power-law regime.*

By differentiating the equation (13), the slope in the power-law regime can be obtained,

$$\frac{d\log\tau}{d\log d^2} = \frac{\frac{\tilde{d}^4}{w} + 2\left(1-\frac{1}{w}\right)\frac{\tilde{d}^2}{w} + \left(1-\frac{1}{w}\right)^2}{\frac{\tilde{d}^4}{w} + \left(1-\frac{1}{w^2}\right)\tilde{d}^2 + \left(1-\frac{1}{w}\right)^2} \tag{18}$$

The solution is plotted in Figure A-4. The minimum of the slope is located at the inflection point,

$$\left.\frac{d\log\tau}{d\log d^2}\right|_{\text{inflection}} = \frac{2\left(\frac{1}{\sqrt{w}} - \frac{1}{w}\right)}{1-\frac{1}{w}} = \frac{2}{1+\sqrt{w}} \tag{19}$$

The solution is shown in Figure A-5.

5. Construction of the shear rheology master curves.

In order to obtain the dynamic moduli in the low frequency regime (below 0.001 rad/s), time dependent creep compliance was first transformed into dynamic moduli using the methods described by Ferry.[4]

$$J'(\omega) = J_e^0 - \omega\int_0^\infty \left[J_e^0 - J(t) + t/\eta_0\right]\sin\omega t dt \tag{20}$$

$$J''(\omega) = 1/\omega\eta_0 + \omega\int_0^\infty \left[J_e^0 - J(t) + t/\eta_0\right]\cos\omega t dt \tag{21}$$

where J_e^0 is the recoverable compliance, and η_0 the zero-shear-rate viscosity. They are the intercept and the inverse of the slope from a linear fit in the steady-state of creep, respectively. The dynamic moduli were thus calculated as

$$G' = J'/\left(J'^2 + J''^2\right) \tag{22}$$

$$G'' = J''/\left(J'^2 + J''^2\right) \tag{23}$$

The data obtained by SAOS and by transformation from the creep data overlap for at least one decade in the frequency domain, confirming the efficacy of the method describe here.

6. Fitting the rheology data to different models.

The Maxwell model is one of the simplest models to capture the viscoelastic behaviors of hydrogels, combining one elastic element and one viscous element in series to describe the viscoelasticity of the polymeric materials.[1] The time dependent stress relaxation modulus is

$$G(t) = G_0 \exp\left(-t/\tau_M\right) \tag{24}$$

where τ_M is the characteristic relaxation time of the materials, and G_0 is the quiescent modulus. The Maxwell model can be derived from the Green-Tobolsky transient network theory.[5] Maxwell elements can be combined in parallel to characterize the multiple relaxation modes typically found in the technologically relevant materials.

The stretched exponential model or Kohlrausch-Williams-Watts (KWW) model, is an empirical adaption of the Maxwell model, where the mathematical form of the stress relaxation modulus is

$$G(t) = G_0 \exp\left[-(t/\tau_{KWW})^{\beta}\right] \tag{25}$$

where τ_{KWW} is the KWW time constant, and β is the stretched exponent ranging from 0 to 1. The stretched exponent is used to describe a distribution of relaxation times centered about the mean relaxation, as shown in eqn (19) in the main text. The KWW model has been used to describe the relaxation process of disordered materials, such as glasses.[6] The stretched exponential function has proven to be mathematically consistent with the terminal relaxation behavior where $G' \sim \omega^2$ and $G'' \sim \omega$.[7]

To fit the different models to the experimental results, a continuous relaxation spectrum $H(\tau)$ is constructed based on the combined dynamic moduli. The method used here is followed by the algorithm proposed by Honerkamp and Weese,[8, 9] and recently modified and implemented in MATLAB by Arsia *et al.*[10]. Briefly, it uses a regularization term weighed by the parameter λ in the objective function $V(\lambda)$ to balance the accuracy of the fit and the smoothness of the desired function considering possible noise in the experimental data.

$$\begin{aligned} V(\lambda) = & \sum_{i=1}^{n}\left(\frac{G_e'(\omega_i) - G'(\omega_i; H(\tau))}{G_e'(\omega_i)}\right)^2 \\ & + \sum_{i=1}^{n}\left(\frac{G_e''(\omega_i) - G''(\omega_i; H(\tau))}{G_e''(\omega_i)}\right)^2 \\ & + \lambda\int_{-\infty}^{\infty}\left(\frac{d^2 \ln(H)}{d\tau^2}\right) d(\ln\tau) \end{aligned} \tag{26}$$

where the subscript e denotes the data from experiment. The accuracy of the computed spectrum is evaluated by comparing the dynamic moduli converted from the relaxation spectrum to the

experiment results. Subsequently, the relaxation modulus is calculated from the relaxation spectrum using the equation:[4]

$$G(t) = \int_{-\infty}^{\infty} H \exp(-t/\tau) d \ln \tau \tag{27}$$

Next, the relaxation spectrum was fit separately in the low and high frequency regimes to the three models and the fitting results were compared. Fitting the relaxation modulus to the models mathematically reduces the variables in the manipulations. Finally, the dynamic moduli were computed with a Fourier Transform:[4]

$$G'(\omega) = \omega \int_0^{\omega} G(t) \sin \omega t dt \tag{28}$$

$$G''(\omega) = \omega \int_0^{\omega} G(t) \cos \omega t dt \tag{29}$$

7. Analysis of the concentration regime in the work from Craig and coworkers[11].

According to the sticky Rouse model,[12] the concentration at which strands between two stickers overlap is calculated as

$$\varphi_s = N_s^{1-3\nu}$$

where N_s is the number of monomers in a sticky Rouse segment and ν is the Flory exponent. DMSO is treated as a Θ-solvent for poly(4-vinyl pyridine), thus $\nu = 0.5$.[13] For a sticker concentration of 5 mol% in polymers, $N_s = 19$. Therefore,

$$\varphi_s = N_s^{1-3\nu} = 19^{-0.5} = 0.23$$

It is greater than the polymer concentration in gels (100 mg/mL).

Because there exists only one scaling law in the relation $\eta_0 \sim c^p$, and the concentration of 100 mg/mL is within the concentration investigated,[13] it is reasoned that the concentration of 100 mg/mL is above φ_{ren}. Otherwise it should exhibit two different scaling laws.

Supplementary Figures

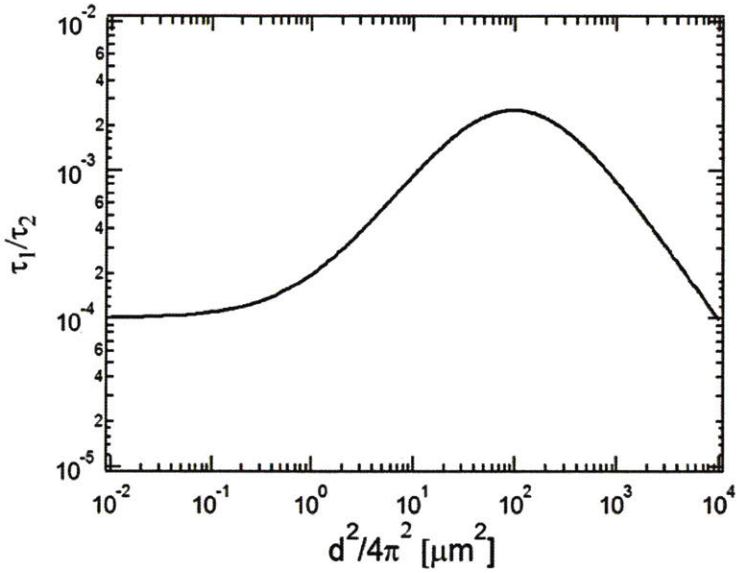

Figure A-1. The ratio of two time constants as a function of d^2. The parameter values are $D_M = 10^{-8}$ m^2/s, $D_A = 10^{-12}$ m^2/s, $k_{on} = 100$ s^{-1}, and $k_{off} = 1$ s^{-1}.

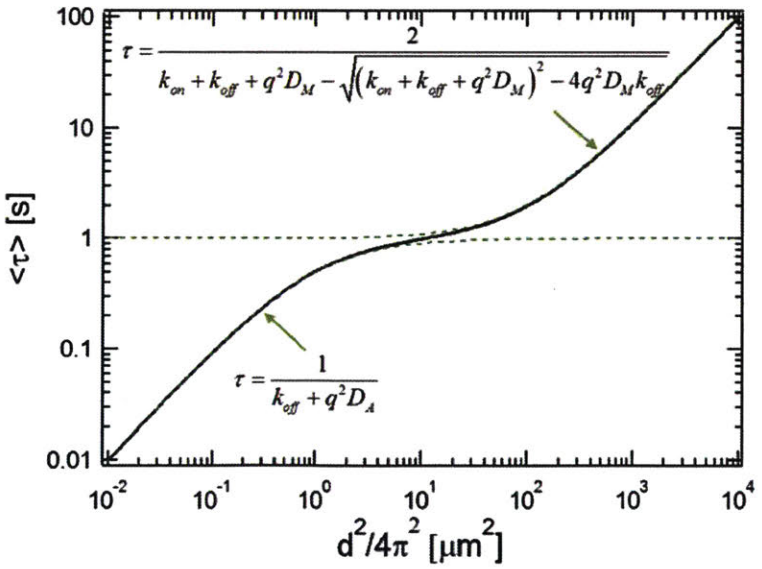

Figure A-2. Modified asymptotically matched solutions including the reaction terms. Parameter values $D_M = 10^{-8}$ m^2/s, $D_A = 10^{-12}$ m^2/s, $k_{on} = 100$ s^{-1}, and $k_{off} = 1$ s^{-1}.

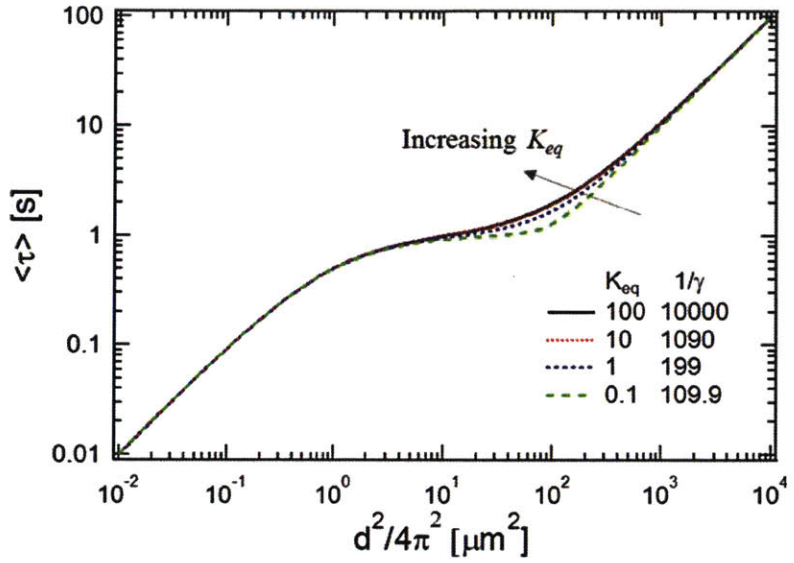

Figure A-3. Behavior of the two-state model when approaching the limit where $K_{eq} >> 1$ and $\gamma K_{eq} << 1$. All the curves has the same value of $(K_{eq}+1)/(K_{eq}+1/\gamma) = 0.01$. The values of K_{eq} and γ are noted in the legend, and other parameters are $D_A = 10^{-12}$ m^2/s, and $k_{off} = 1$ s^{-1}.

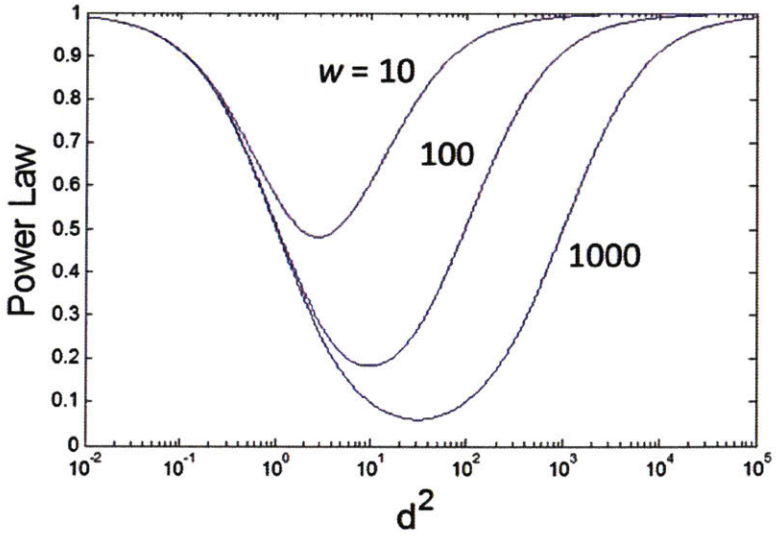

Figure A-4. The instantaneous slope in the two-state model. The range of d^2 with a slope below 1 indicates the super diffusive region.

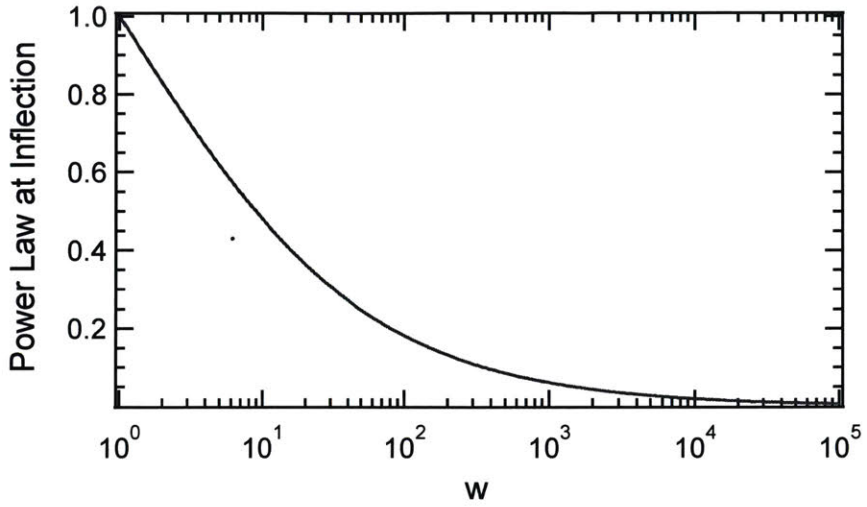

Figure A-5. The power law exponent at the inflection point as a function of the width of the power law regime.

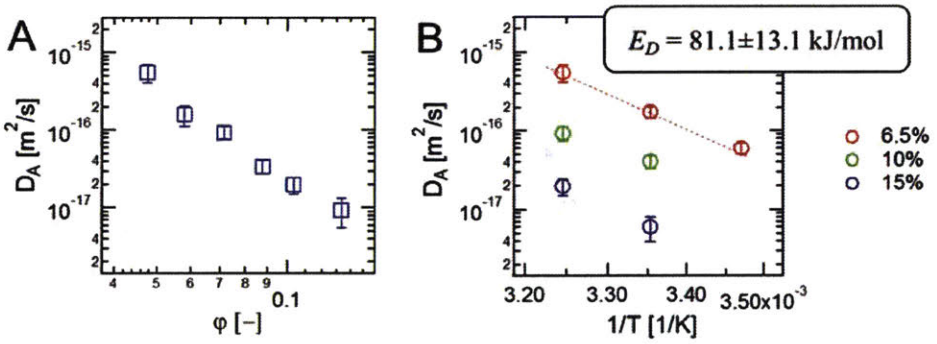

Figure A-6. Concentration (A) and temperature (B) dependence of the diffusivity of the associated species. Error bars represent 95% confidence interval from fit to the two-state model.

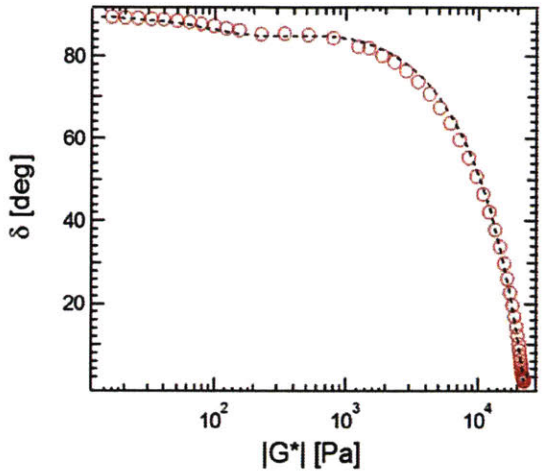

Figure A-7. Van Gurp-Palmen plot of protein gels showing a local minimum that represents a second relaxtion mode. Data points are shown in red open circles, and the black dashed line is from fit to eqn (14) in the main text.

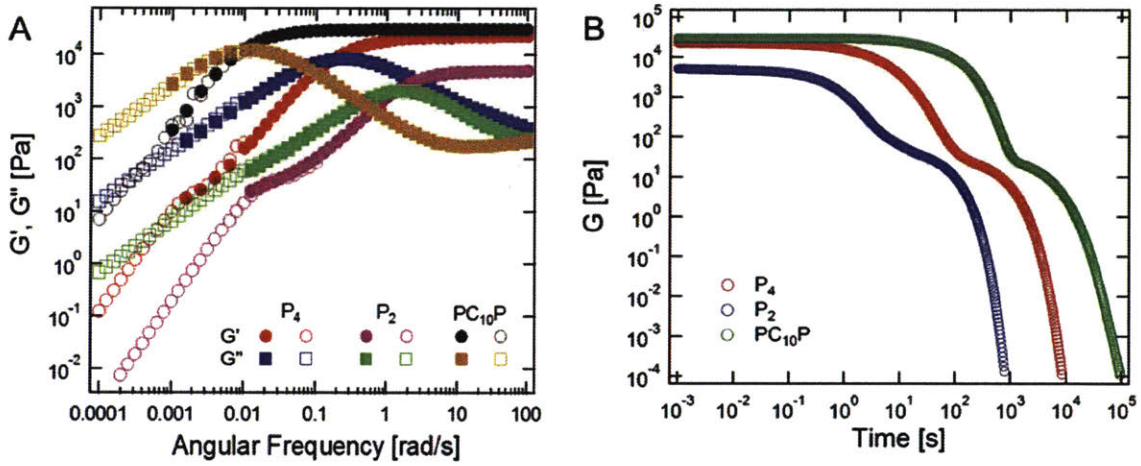

Figure A-8. Comparison of the (A) dynamic moduli master curves and (B) relaxation moduli master curves from various protein constructs. Data transformed from creep experiments is noted by symbols with a dot inside. The multiblock proteins P_4 (62.8 kDa) and P_2 (63.2 kDa) have nearly identical molar masses but a different number of coiled-coil domains; the protein $PC_{10}P$ (20.5 kDa) has the same length of C_{10} linkers but has a triblock architecture.

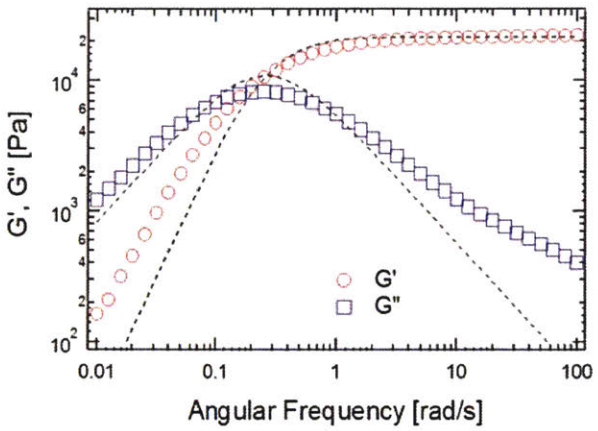

Figure A-9. Fitting the dynamic moduli from frequency sweep measurement with the Maxwell model (black dashed line). Data from P_4 hydrogels at 25% (w/v) measured at 25 °C.

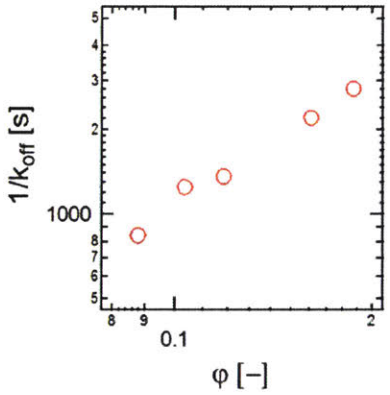

Figure A-10. Molecular dissociation time for proteins from diffusion measurements. Rate constants k_{off} not measured at the reference temperature (25 °C) are calculated from the concentration scaling $k_{off} \sim \varphi^{-1.57}$ and the Arrhenius law $\ln k \sim E/RT$.

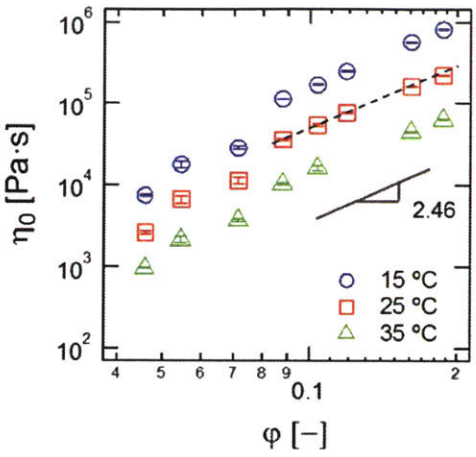

Figure A-11. Concentration dependence of zero-shear-rate viscosity (determined as the inverse of the slope in the creep compliance – time curve at steady state). Error bars represent standard deviations from measurements performed in triplicate.

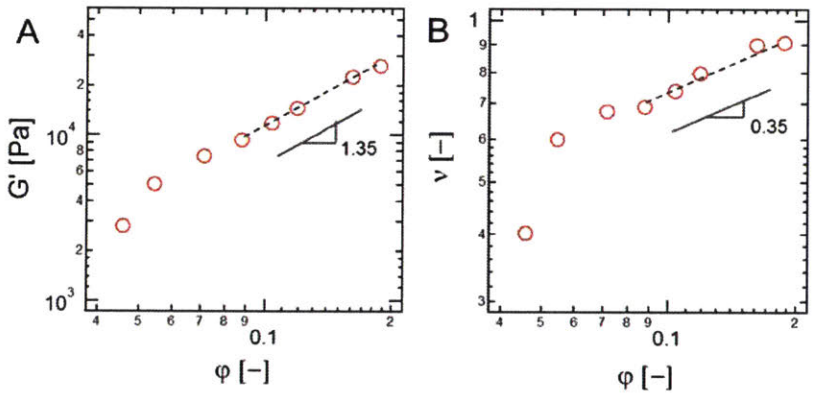

Figure A-12. Concentration dependence of (A) high-frequency plateau modulus and (B) number fraction of elastically effective chains.

References:

1. Rubinstein, M.; Colby, R. H. *Polymer Physics*. Oxford University Press: Oxford ; New York, 2003; p xi, 440 p.
2. Fetters, L. J.; Hadjichristidis, N.; Lindner, J. S.; Mays, J. W. Molecular Weight Dependence of Hydrodynamic and Thermodynamic Properties for Well - Defined Linear Polymers in Solution. *Journal of Physical and Chemical Reference Data* 1994, 23, 619-640.
3. Shen, W.; Kornfield, J. A.; Tirrell, D. A. Structure and Mechanical Properties of Artificial Protein Hydrogels Assembled through Aggregation of Leucine Zipper Peptide Domains. *Soft Matter* 2007, 3, 99-107.
4. Ferry, J. *Viscoelastic Properties of Polymers*. 3d ed.; Wiley: New York, 1980; p xxiv, 641 p.
5. Green, M. S.; Tobolsky, A. V. A New Approach to the Theory of Relaxing Polymeric Media. *The Journal of Chemical Physics* 1946, 14, 80-92.
6. Welch, R. C.; Smith, J. R.; Potuzak, M.; Guo, X.; Bowden, B. F.; Kiczenski, T. J.; Allan, D. C.; King, E. A.; Ellison, A. J.; Mauro, J. C. Dynamics of Glass Relaxation at Room Temperature. *Physical Review Letters* 2013, 110, 265901.
7. Kawasaki, Y.; Watanabe, H.; Uneyama, T. A Note for Kohlrausch-Williams-Watts Relaxation Function. *Nihon Reoroji Gakkaishi* 2011, 39, 127-131.
8. Honerkamp, J.; Weese, J. Determination of the Relaxation Spectrum by a Regularization Method. *Macromolecules* 1989, 22, 4372-4377.
9. Honerkamp, J.; Weese, J. A Nonlinear Regularization Method for the Calculation of Relaxation Spectra. *Rheologica Acta* 1993, 32, 65-73.
10. Takeh, A.; Shanbhag, S. A Computer Program to Extract the Continuous and Discrete Relaxation Spectra from Dynamic Viscoelastic Measurements. *Appl Rheol* 2013, 23.
11. Yount, W. C.; Loveless, D. M.; Craig, S. L. Small-Molecule Dynamics and Mechanisms Underlying the Macroscopic Mechanical Properties of Coordinatively Cross-Linked Polymer Networks. *Journal of the American Chemical Society* 2005, 127, 14488-14496.
12. Rubinstein, M.; Semenov, A. N. Dynamics of Entangled Solutions of Associating Polymers. *Macromolecules* 2001, 34, 1058-1068.
13. Xu, D.; Craig, S. L. Scaling Laws in Supramolecular Polymer Networks. *Macromolecules* 2011, 44, 5465-5472.

Appendix B: Supporting Information for Chapter 4

Supporting Figures

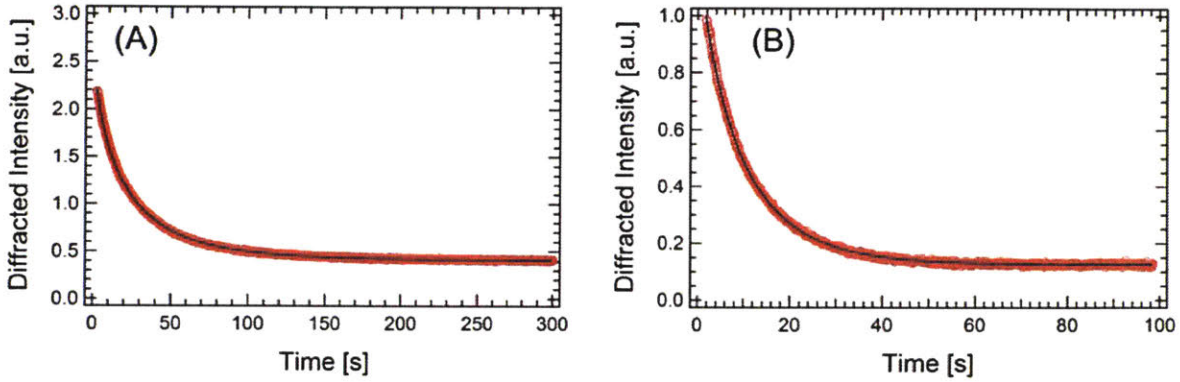

Figure B-1. Representative decays of the diffracted scattering intensity over time as probed by FRS for the diffusion of associating star-shaped PEG polymers in model transient networks. The red open circles are experimental data, and the black lines are fits to a stretched exponential function. (A) Self-diffusion, gel concentration 15% (w/v), measurement at a beam angle of 6.88 degrees. (B) Tracer diffusion, gel concentration 20% (w/v), measurement at a beam angle of 6.88 degrees. Both measurements were performed at 25 °C.

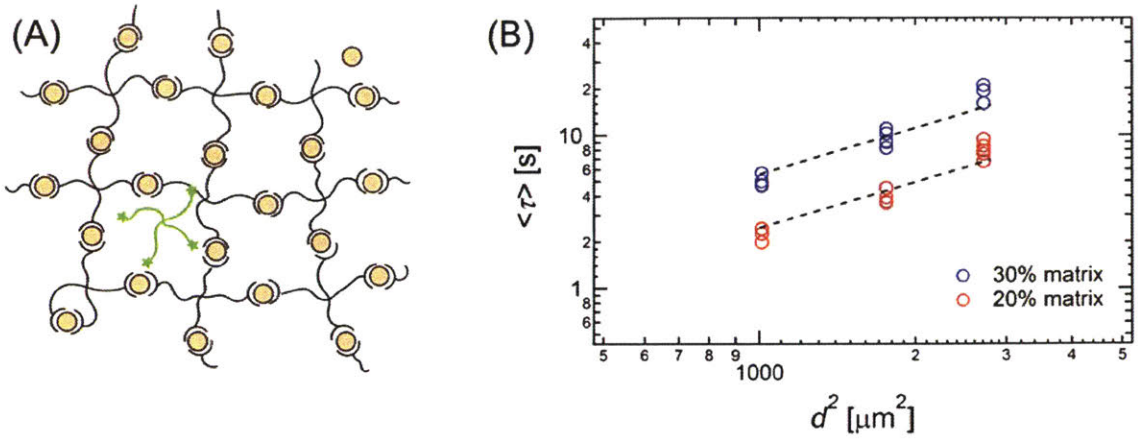

Figure S2. (A) Schematic presentation of an unassociating four-arm PEG polymer (labeled in green) diffusing in a model transient network formed by terpyridine-capped four-arm PEG complexed with Zn^{2+} in DMF. (B) Corresponding $<\tau>$ vs. d^2 relation. The matrix concentrations are 20 and 30% (w/v), respectively. Dashed lines are linear regressions of slope 1 that determine the tracer diffusion coefficients. While only Fickian diffusion is observed within a narrow window of length and time scales accessible by FRS experiments, anomalous diffusion should not be expected since there is a lack of associative interactions between the labeled, non-sticky polymers and the surrounding matrix. Diffusion at lower concentrations, 10 and 15% (w/v), is too fast to be accurately measured.

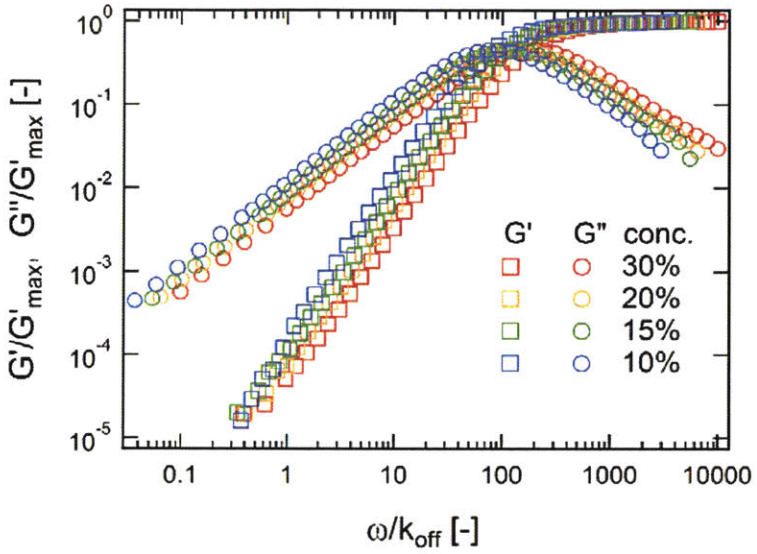

Figure S3. Rheology data plotted in a reduced parameter space. As seen in the figure, however, renormalization by the molecular dissociation rate k_{off} does not yield perfect collapse of the data. The reference temperature is 25 °C.

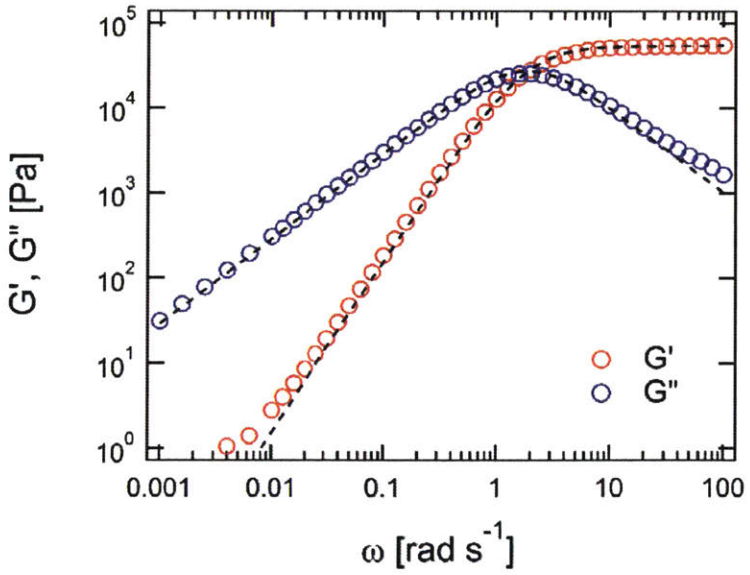

Figure S4. Fitting the single Maxwell model to the dynamic moduli of gels at 30% (w/v) at 25 °C. There are noticeable differences between the fit (black dashed line) and the experimental data (open circles)

Additional Experimental Details

1. Synthesis of four-arm PEG polymers with all chain ends capped by nitrobenzofurazan (NBD)

Commercial tetra-arm PEG-OH (Creative PEGWorks, M_n = 10 kg mol^{-1}, M_w/M_n = 1.03, 4.57 g, 0.46 mmol) was end-labeled with NBD in two steps (Scheme S1). In the first step, the polymer was dissolved in dry dichloromethane (80 mL), dry pyridine (0.48 mL, 5.4 mmol) was added to the solution, followed by addition of *p*-nitrophenyl chloroformate (0.58 g, 2.8 mmol). The resulting suspension was stirred at room temperature overnight, the precipitate was filtered off, and brine (250 mL) was added to the filtrate. The mixture was extracted with dichloromethane (2 × 400 mL), the organic layer was dried over $MgSO_4$ and then concentrated *in vacuo*. The product, tetra-arm PEG-*p*-nitrophenylcarbonate, was precipitated by pouring the concentrate into cold diethyl ether, yielding a slightly violet solid **1** (4.14 g, 86%). ^{1}H NMR (700 MHz, DMSO-d_6, δ): 8.32 (d, J = 9.1 Hz, 8H), 7.57 (d, J = 9.1 Hz, 8H), 3.31 (m, 902H) ppm.; IR (ATR, cm^{-1}): v = 2880 (m), 2360 (w), 2342 (w), 1965 (w), 1769 (w), 1524 (w), 1466 (m), 1359 (w), 1342 (m), 1279 (m), 1240 (w), 1216 (w), 1146 (m), 1101 (s), 1059 (s), 961 (s), 841 (s). 668 (w), 658 (w).

In the second step, triethylamine (42 μL, 0.30 mmol) was added to a solution of tetra-arm PEG-*p*-nitrophenylcarbonate as just formed (0.5 g, 0.025 mmol) in dimethylformamide (5 mL, HPLC grade), followed by addition of (S)-(+)-4-(3-aminopyrrolidino)-7-nitrobenzofurazan (NBD) **2** (0.037 g, 0.15 mmol). The orange mixture was stirred for 1 d at room temperature, purified by dialysis in water, and lyophilized to obtain **3** as an orange solid (0.45 g, 85%). The degree of substitution of the chain-end pendant *p*-nitrophenylcarbonate groups by NBD tags was determined to be 92% by UV absorption spectroscopy; in addition, in ^{1}H NMR, the peaks addressable to *p*-nitrophenylcarbonate have disappeared after this conversion. ^{1}H NMR (400 MHz, DMSO-d_6, δ):

8.24 (d, J = 10.0 Hz, 4H), 5.75 (d, J = 10.4 Hz, 4H), 4.55 (s, 16H), 3.53–3.47 (m, 902H, PEG-backbone) ppm.

Scheme B-1. Synthesis of four-arm PEG polymers with all chain ends capped by NBD.

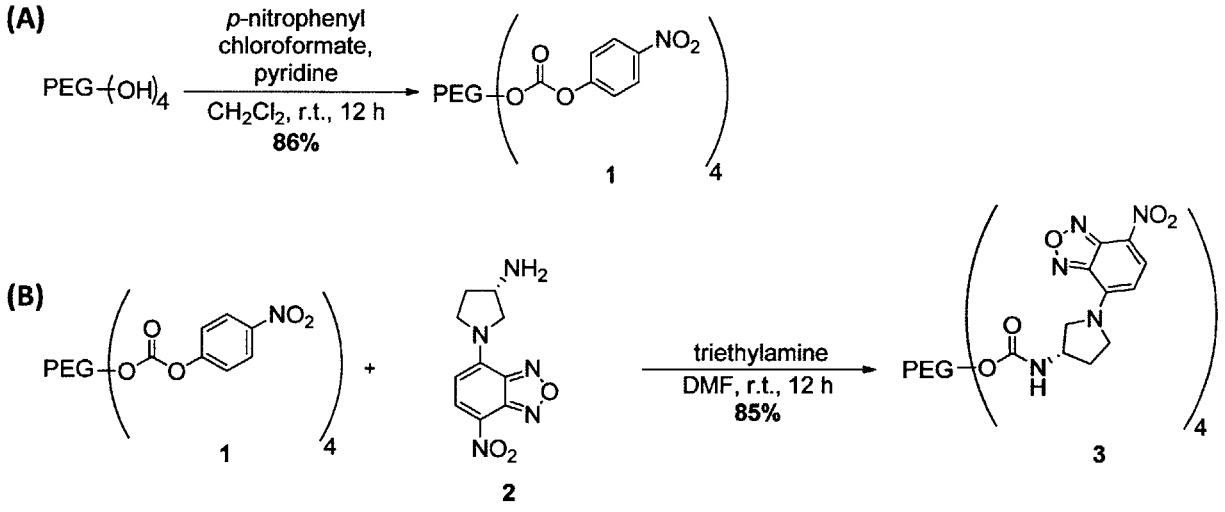

2. Sample preparation for diffusion measurement

1 mol% of the NBD-labeled non-associative four-arm PEG was mixed with the gel-forming matrix polymers and was dissolved in 500 μL of DMF. Separately, $Zn(NO_3)_2 \cdot 6H_2O$ in a 2:1 stoichiometric concentration to the PEG polymer was dissolved in 500 μL of DMF and vortexed to reach complete dissolution of solids. Equal volumes of the two solutions were then combined in an Eppendorf tube and mixed rigorously with a micro spatula to ensure homogenous mixing. The sample was centrifuged at 21,100 ×g for 10 min to remove bubbles. The sample was sealed between two quartz disks (17 mm in diameter) separated by a 0.5 mm thick Teflon spacer. Specimens were equilibrated at 25 °C for at least 30 min before further experiments were conducted.

Additional Calculation Details

1. Definition of the volume fraction

The volume fraction of polymers in the transient network is calculated based on the assumption that the total volume of the gels is the sum of the polymer volume and the solvent volume. In addition, the density of tetra-arm PEG is taken as 1.128×10^3 kg m^{-3}. Therefore, the volume fraction is given by

$$\varphi = \frac{m_p/\rho_p}{m_p/\rho_p + V_s}$$

where the subscripts p and s represent polymer and solvent, respectively, m is the mass, ρ is the density, and V is the volume. In this study, the volume fractions of gels are 0.081, 0.117, 0.151, and 0.210 for concentrations 10, 15, 20, and 30% (w/v), respectively.

2. Estimation of the overlap volume fraction of the segment between two stickers (φ_s)

The overlap concentration, c^*, for the four-arm PEG polymers is 94 g L^{-1}, as estimated previously.[1] Since the stickers are located at the end of the arms in each star polymer, the overlap volume fraction of the segment between two stickers (φ_s) is approximated as the overlap volume fraction of the star-shaped polymers:

$$\varphi_s = \frac{c^*}{\rho} = \frac{1.7 \times 94\left[\text{g L}^{-1}\right]}{1.06 \times 10^3\left[\text{g L}^{-1}\right]} = 0.089$$

This calculation suggests that the most of the gel concentrations investigated in this work are above φ_s.

3. Estimation of the entanglement volume fraction of the segment between two stickers (φ_e)

Following the classic reptation theory,[2] the entanglement volume fraction φ_e is estimated to be

$$\varphi_e = \left(\frac{N_{e0}}{N}\right)^{3\nu-1}$$

where N_{e0} is the number of monomers between entanglements in a melt, N is the degree of polymerization of the polymer, and υ is the Flory exponent. The entanglement molecular weight[3] for PEO is 1,730 g mol^{-1}, and the molecular weight of the segment between two stickers is 5,000 g mol^{-1}. Therefore,

$$\varphi_e = \left(\frac{N_{e0}}{N}\right)^{3\nu-1} = \left(\frac{M_{e0}}{M}\right)^{3\nu-1} = \left(\frac{1730}{5000}\right)^{3\times 0.588-1} = 0.44$$

All the gel samples investigated in this study are below φ_e. This estimation is consistent with the fact that no entanglement plateau is observed in the low-frequency limit in frequency sweep experiments.

References

1. Rossow, T.; Habicht, A.; Seiffert, S. Relaxation and Dynamics in Transient Polymer Model Networks. Macromolecules 2014, 47, 6473-6482.
2. Rubinstein, M.; Semenov, A. N. Dynamics of Entangled Solutions of Associating Polymers. Macromolecules 2001, 34, 1058-1068.
3. Fetters, L. J.; Lohse, D. J.; Colby, R. H. Chain Dimensions and Entanglement Spacings. In Physical Properties of Polymers Handbook, Mark, J. E., Ed. Springer New York: New York, NY, 2007; pp 447-454.

Appendix C: Supporting Information for Chapter 5

Supplementary Figures Cited in the Main Text

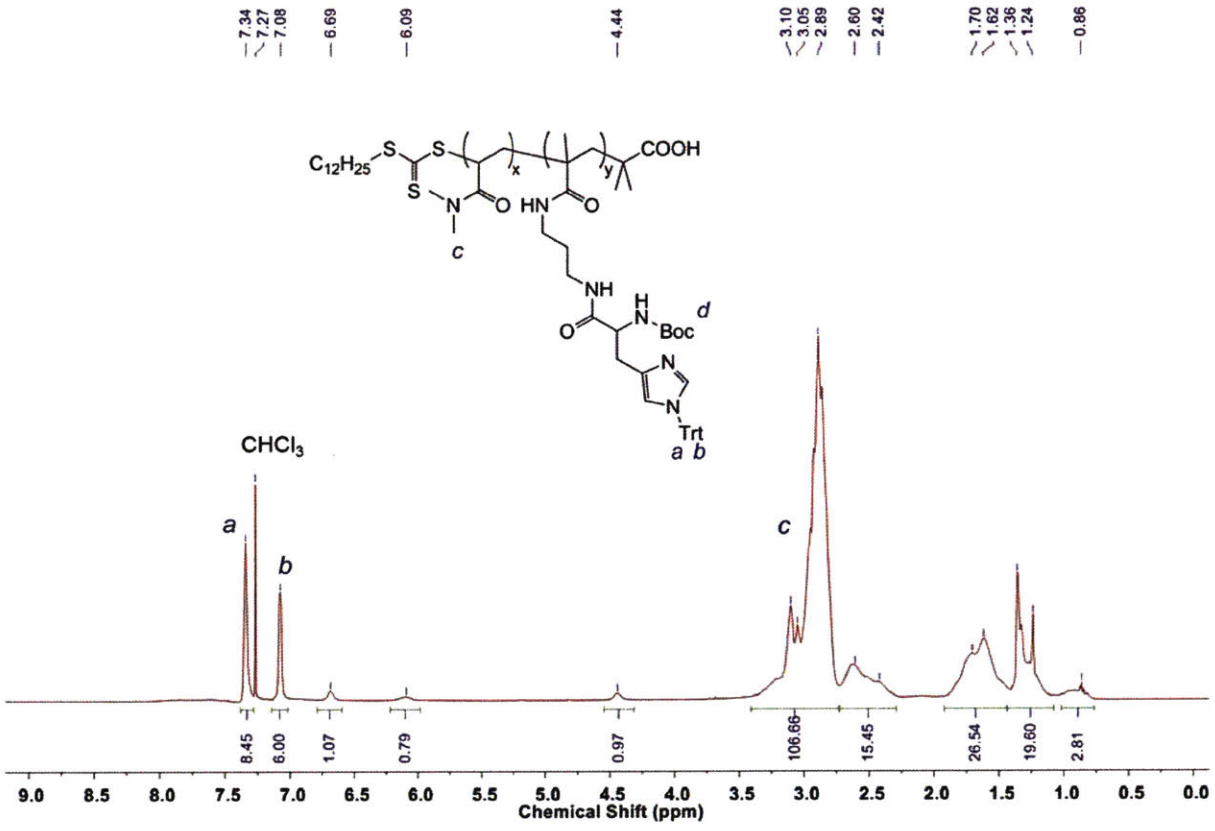

Figure C-1. ^{1}H NMR characterization of PDMA polymers with protected histidine side groups ($CDCl_3$, 500 MHz). Peaks assigned in the spectrum are used for calculating the monomer ratio in the polymers.

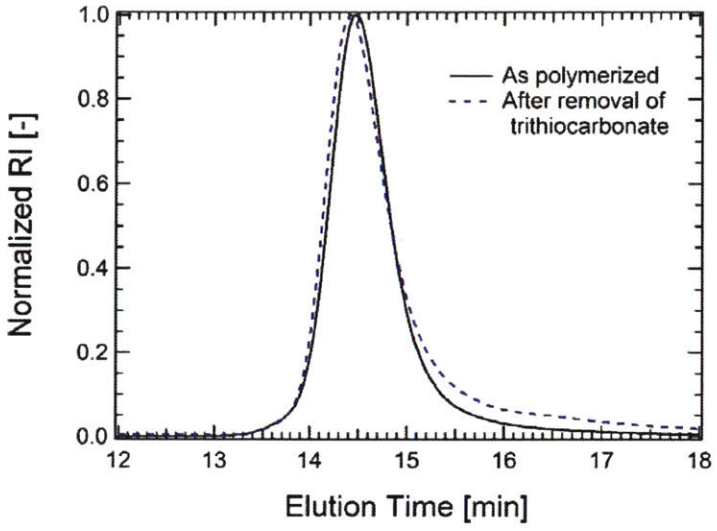

Figure C-2. GPC characterization of copolymers (a) as polymerized and (b) after removal of trithiocarbonate.

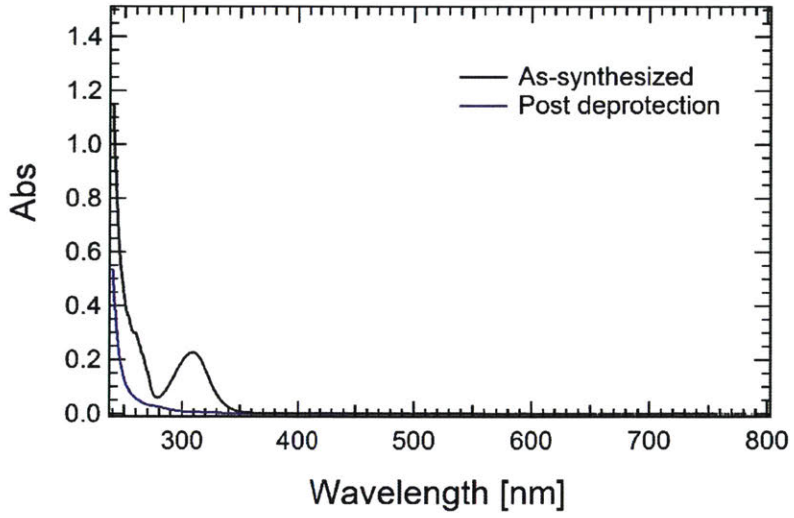

Figure C-3. UV-vis spectroscopy confirming the removal of trithiocarbonate chain ends. Both polymers were prepared in MeOH at 0.5 mg mL^{-1}.

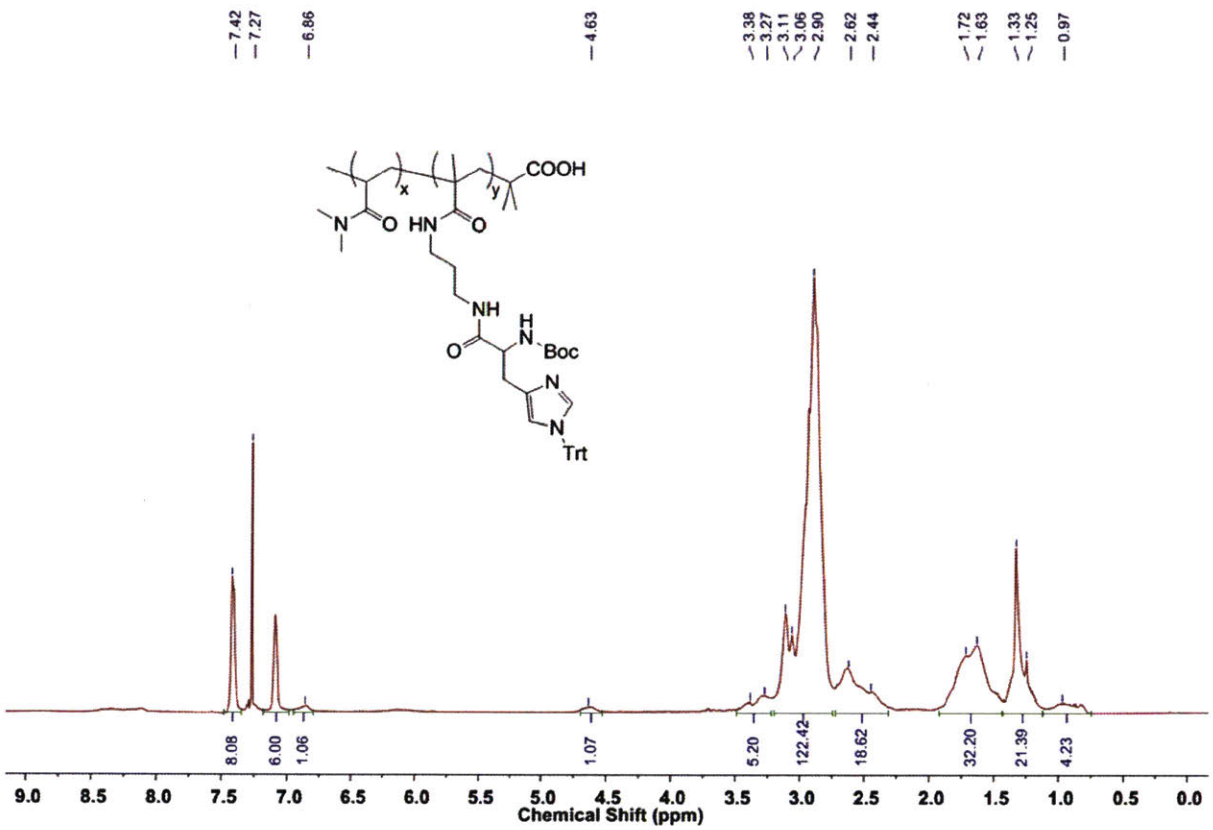

Figure C-4. ^{1}H NMR characterization of PDMA polymers with protected histidine side groups after the removal of trithiocarbonate ($CDCl_3$, 500 MHz).

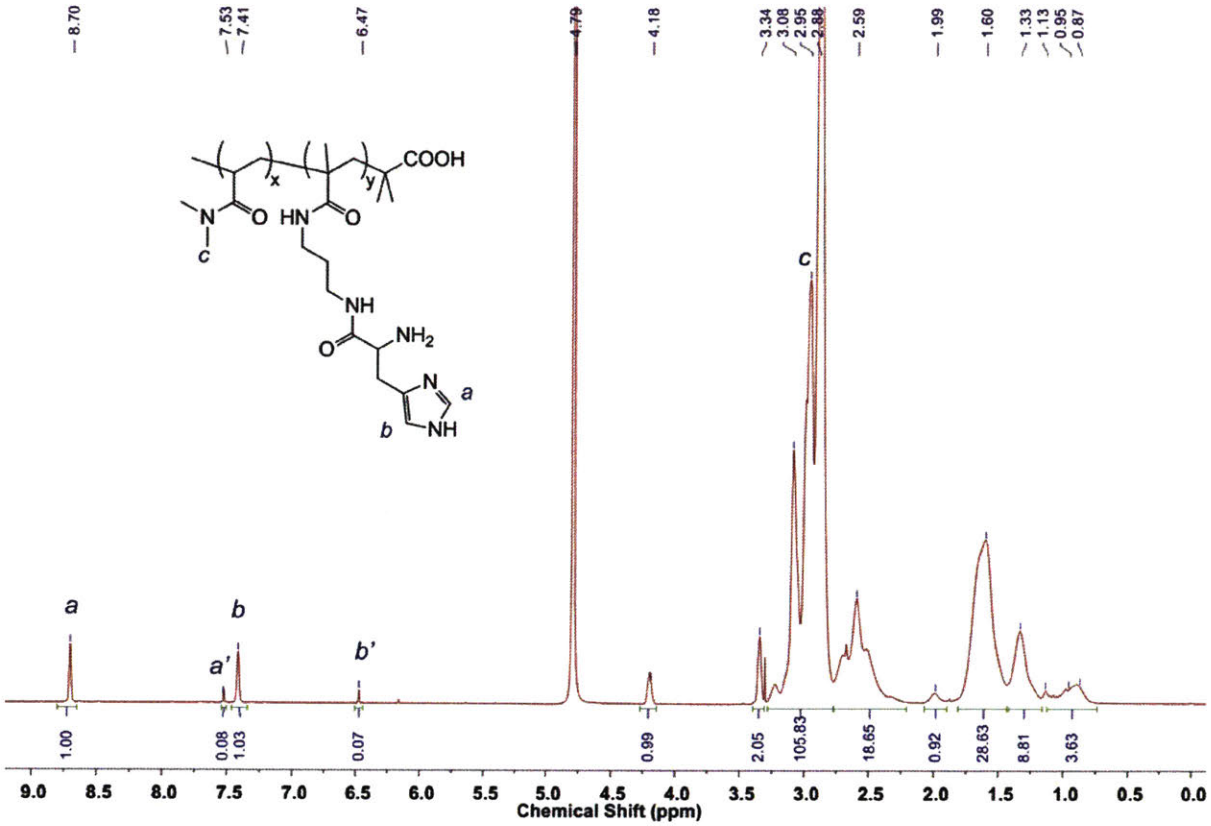

Figure C-5. ^{1}H NMR characterization of copolymers after removal of trithiocarbonate chain end and the protecting groups (Boc and Trt) (D_2O, 500 MHz). The proton peaks *a* and *b* correspond to the histidine-TFA salt, and the peaks *a'* and *b'* correspond to the free histidine.

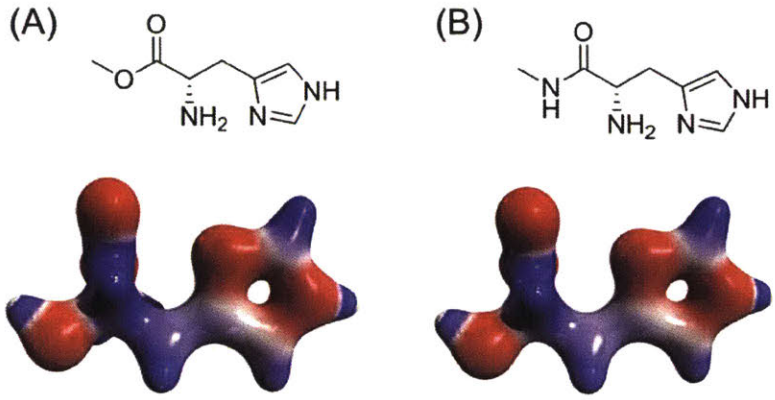

Figure C-6. Comparison of the electron density map of (A) histidine methyl ester and (B) histidine methyl amide (an analogue to the polymer-conjugated histidine moieties). Calculation was performed in Gaussian 03 using the basis set B3LYP/6-31G(d).

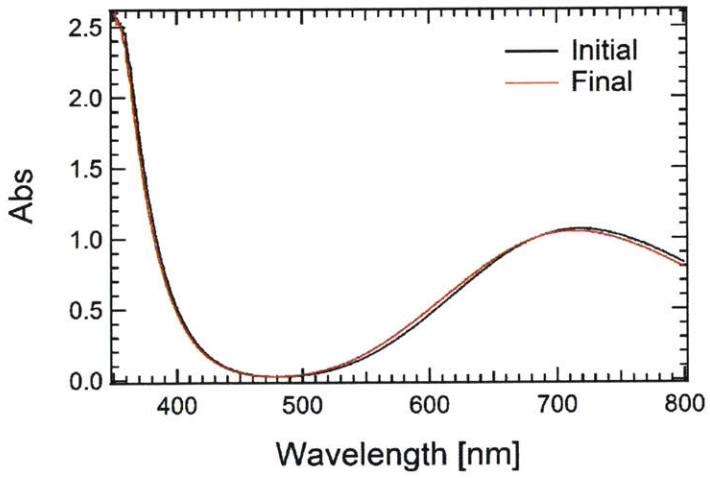

Figure C-7. Comparison of the UV-vis spectrum at the initial and final stage of the metal exchange experiment. The spectrum at the initial state is calculated by adding the separately measured absorbance of 20 mM $CuCl_2$ in 100 mM Bis-Tris (pH 7.0) and absorbance of 1 mM $NiCl_2$ and 2 mM histidine methyl ester in 100 mM Bis-Tris (pH 7.0).

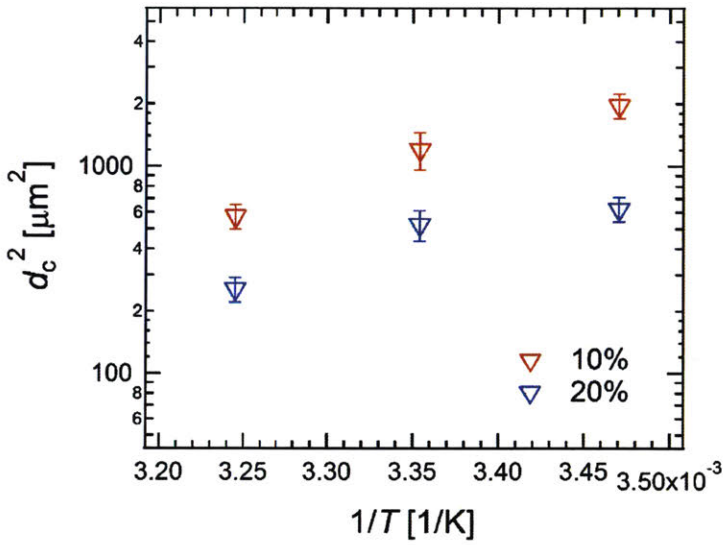

Figure C-8. Transition d_c^2 at varying temperatures and gel concentrations.

Supplementary Tables Cited in the Main Text

Table C-1. Comparison of the experimentally measured molar extinction coefficient of metal-ligand complexes at 598 nm at 25 °C. Unit: M^{-1} cm^{-1}.

Species	Molar Extinction Coefficient
BisTrisCu	22.2
HisCu	54.5
His_2Cu	95.9
BisTrisNi	2.68
HisNi	3.82
His_2Ni	6.29

Calculation Details

1) The mole fraction of monomer 1 in polymers

The ratio of DMA:**1** in the as-synthesized polymers **P1** was estimated from ^{1}H NMR (Figure S1):

$$\frac{f_{DMA}}{f_1} = \frac{106.7/6}{6/6} = 17.8. \quad (1)$$

Therefore, the mole fraction of monomer **1** is

$$f_1 = \frac{1}{17.8+1} = 0.053. \quad (2)$$

2) The molecular weight of the final polymers

The molecular weight of the as-synthesized polymers **P1** was 42.5 kg mol^{-1}. In addition, it was known that the ratio of monomer DMA and **1** was 17.8:1. Assuming the each polymer had x number of the **1**, and hence 17.8x number of DMA, the unknown x can be solved from,

$$99.1 \times 17.8x + 621.3 \times x + 364.6 = 42.5 \times 10^3 \quad (3)$$

where the molecular weight of 364.6 g mol^{-1} corresponds to DMP end group. The solution is x = 17.7.

After removal of the RAFT chain end and deprotection of Boc and Trt groups, the polymer molecular weight is,

$$99.1 \times 17.8 \times 17.7 + 279.3 \times 17.7 = 36.2 \times 10^3 \left(\text{kg mol}^{-1}\right). \quad (4)$$

3) The entanglement and overlap volume fraction of polymers

According to the reptation theory, the entanglement volume fraction is

$$\varphi_e = \left(\frac{N_{e0}}{N}\right)^{3\nu-1}, \tag{5}$$

where N_{e0} is the number of monomers between entanglements in a melt, N is the degree of polymerization of the polymer, and υ is the Flory exponent. Since N_{e0} of PDMA has not been reported in the literature to the author's knowledge, the entanglement concentration for the histidine modified PDMA polymers in this study is estimated by comparison to literature data. The entanglement concentration of PDMA at a molecular weight of 3.4×10^3 kg mol^{-1} is 0.81% (w/w), or equivalently $\varphi_e \approx 0.0062$, determined from the transition of zero-shear-rate viscosity of PDMA aqueous solution.[1] From eq 5, it can be shown that:

$$\varphi_{e,2} = \left(\frac{N_1}{N_2}\right)^{3\nu-1} \varphi_{e,1}, \tag{6}$$

where the subscripts 1 and 2 denote the case from the literature and from the current study, respectively. Therefore, the entanglement volume fraction for the polymer synthesized in this study is (assuming good solvent condition)

$$\varphi_{e,2} = \left(\frac{3400/0.09913}{(17.7+1)\times 17.8}\right)^{3\times 0.588-1} 0.0062 = 0.22. \tag{7}$$

The concentrations of gels in this work are 10 and 20% (w/v), which correspond to volume fractions of 0.071 and 0.13, respectively, assuming that the polymer density is 1.3×10^3 kg m^{-3}. Both are below the entanglement limit.

Similarly, the overlap concentration can be estimated as

$$\varphi_2^* = \left(\frac{N_1}{N_2}\right)^{3\nu-1} \varphi_1^* = \left(\frac{3400/0.09913}{(17.7+1)\times 17.8}\right)^{3\times 0.588-1} \frac{0.0007}{1.3} = 0.019, \quad (8)$$

which uses the overlap concentration[1] of PDMA at a molecular weight of 3.4×10^3 kg mol^{-1}, 0.07% (w/w). Both gel concentrations are above the overlap threshold.

For comparison, the overlap volume fraction[2] for four-arm poly(ethylene glycol) of 10 kg mol^{-1} is 0.062.

4) The sticker density in this work and in the work by Fullenkamp[3]

As shown in eq 2, the number density of stickers in this work is 0.053.

For the work by Fullenkamp using four-arm poly(ethylene glycol) of 10 kg mol^{-1}, the number density of stickers is

$$f_s = \frac{4}{10/0.044} = 0.018, \quad (9)$$

which is approximately 1/3 of that in this work.

5) Solution composition in metal exchange experiments

Logarithms of the equilibrium constants for histidine-metal complexes (metal = Ni^{II} and Cu^{II}) and logarithms of the acid dissociation constants for histidine are taken from a publication[4] and summarized in Table S2.

Table C-2. Summary of equilibrium constants for histidine methyl ester at 25 °C. The unit of K_i is M^{-1}.

Metal ions	$\log(K_1)$	$\log(K_2)$
Cu^{2+}	8.48 ± 0.04	5.90 ± 0.04
Ni^{2+}	6.19 ± 0.04	4.91 ± 0.04
H^+	5.35 (pK_{a1})	7.30 (pK_{a2})

In addition, it is realized that the buffering agent Bis-Tris also forms complexes with Cu^{2+} and Ni^{2+}. Related equilibrium constants are documented in the work[5] by Scheller *et al.* Note that the complexation between Bis-Tris and divalent metal ions is not considered in the work[3] by Fullenkamp *et al.* In fact, the appearance of the metal-ligand change transfer band in the UV-vis spectrum at the initial state of the experiment (Figure C-6) is mainly due to complexation between Cu^{2+} and Bis-Tris.

Table C-3. Summary of equilibrium constants for Bis-Tris at 25 °C.

Metal ions	$\log(K)$
Ni^{2+}	3.59 ± 0.02
Cu^{2+}	5.27 ± 0.01
H^+	6.56 ± 0.04 (pK_a)

It is assumed that the total concentrations of histidine groups, Ni^{II}, Cu^{II} and Bis-Tris are conserved throughout the experiment, which gives the following four mass balance equations:

$$[His]_T = [His] + [HisH] + [HisH_2] + [HisNi] + 2[His_2Ni] + [HisCu] + 2[His_2Cu] \quad (10)$$

$$[Ni]_T = [Ni] + [HisNi] + [His_2Ni] + [BisTrisNi] \quad (11)$$

$$[Cu]_T = [Cu] + [HisCu] + [His_2Cu] + [BisTrisCu] \quad (12)$$

$$[BisTris]_T = [BisTris] + [BisTrisH] + [BisTrisNi] + [BisTrisCu] \quad (13)$$

The four independent variables are chosen to be the concentrations of free histidine groups, Ni^{2+}, Cu^{2+} and Bis-Tris. The concentration of other species can be expressed as functions of these four variables based on equilibrium relations. Under the experiment condition that $[His]_T$ = 2 mM, $[Ni]_T$ = 1 mM, $[Cu]_T$ = 20 mM, and $[BisTris]_T$ = 100 mM, the concentration of all species at the start and the end of the metal exchange experiment are calculated using the fsolve routine in MATLAB, and the results are shown in Table C-4.

Table C-4. Concentration of major species before and after the metal exchange experiments. Unit: mM.

Species	Start	End
BisTris	80.0	80.3
BisTrisCu	20.0	18.7
His_2Ni	9.86×10^{-1}	--
HisNi	1.10×10^{-2}	--
His_2Cu	--	7.04×10^{-1}
HisCu	--	5.79×10^{-1}
BisTrisNi	--	9.88×10^{-1}

Note that the calculation shown above neglects the influences of water and Cl^- ions that might participate into the formation of complexes of Ni^{II} and Cu^{II} with the ligands.

At a constant pH of 7.0, the maximum concentration of free Cu^{2+} is only ca. 23 μM, calculated from the solubility product constant[6] of $Cu(OH)_2$. This solubility limit is obviously too low to drive the metal exchange process. Therefore, the presence of the buffering agent Bis-Tris is necessary not only for maintaining a constant pH environment but also for supplying a sufficient amount of Cu^{2+} through complexation. Nonetheless, since the equilibrium constant of Bis-Tris-copper complexes is smaller than the one of histidine-copper complexes, metal exchange still takes place under this condition.

6) Derivation of the time-dependent absorbance of solution mixture in metal exchange experiment

Based on the calculation results listed in Table S4, the key reaction steps are hypothesized to be

$$(1)\ \mathrm{His_2Ni} \xrightarrow{k_1} \mathrm{HisNi} + \mathrm{His}; \tag{14}$$

$$(2)\ \mathrm{HisNi} \xrightarrow{k_2} \mathrm{His} + \mathrm{Ni}; \tag{15}$$

$$(3)\ \mathrm{BisTrisCu} \xrightarrow{k_3} \mathrm{BisTris} + \mathrm{Cu}; \tag{16}$$

$$(4)\ \mathrm{BisTris} + \mathrm{Ni} \xrightarrow{k_4} \mathrm{BisTrisNi}; \tag{17}$$

$$(5)\ \mathrm{Cu} + \mathrm{His} \xrightarrow{k_5} \mathrm{CuHis}; \tag{18}$$

$$(6)\ \mathrm{HisCu} + \mathrm{HisCu} \underset{k_{-6}}{\overset{k_6}{\rightleftarrows}} \mathrm{His_2Cu} + \mathrm{Cu}. \tag{19}$$

The depletion rate for the bis-histidine-nickel complexes is given by

$$\frac{d[\mathrm{His_2Ni}]}{dt} = -k_1[\mathrm{His_2Ni}], \tag{20}$$

and the solution is

$$[\mathrm{His_2Ni}] = [\mathrm{His_2Ni}]_0 \exp(-k_1 t). \tag{21}$$

The mass balance for the histidine groups by eq 10 is then simplified based on the following rationales. First, the concentrations of HisH and $HisH_2$ are negligible under the experimental condition. Second, in the presence of large excess of Cu^{2+} and Ni^{2+}, the free histidine ligand can be treated as an active specie. By applying pseudo steady-state approximation (PSSA) on His, it is reasoned that the concentration of His remains nearly constant and fairly low (on the order of μM), which can be neglected compared to other major species (in the mM range). Third, PSSA is also applied to HisNi based on similar reasons. Equilibrium calculation informs that the concentration of HisNi is in the μM range, and it is neglected as well. These arguments together give a simplified mass balance for the histidine:

$$[\mathrm{His}]_T = 2[\mathrm{His_2Ni}] + [\mathrm{HisCu}] + 2[\mathrm{His_2Cu}] \approx 2[\mathrm{His_2Ni}]_0. \tag{22}$$

Substitute eq 21 into eq 22 yields

$$[\mathrm{HisCu}] + 2[\mathrm{His_2Cu}] \approx 2[\mathrm{His_2Ni}]_0 [1 - \exp(-k_1 t)]. \tag{23}$$

Since HisCu and His_2Cu are in equilibrium,

$$[\mathrm{His_2Cu}] = [\mathrm{HisCu}][\mathrm{His}] K_2, \tag{24}$$

where $K_2 = 10^{5.90}$ given in Table S2. By combining eqs 23 and 24, the concentrations of HisCu and His_2Cu can be obtained:

$$[\mathrm{HisCu}] = \frac{2}{1 + 2K_2[\mathrm{His}]} [\mathrm{His_2Ni}]_0 [1 - \exp(-k_1 t)], \tag{25}$$

and

$$[\mathrm{His_2Cu}] = \frac{2K_2[\mathrm{His}]}{1+2K_2[\mathrm{His}]}[\mathrm{His_2Ni}]_0\left[1-\exp(-k_1 t)\right]. \tag{26}$$

From the mass balance of Cu (eq 12), the concentration of BisTrisCu at a given time t is

$$[\mathrm{BisTrisCu}] = [\mathrm{BisTrisCu}]_0 - [\mathrm{HisCu}] - [\mathrm{His_2Cu}]. \tag{27}$$

Based on the results shown in Tables C-1 and C-4, Ni complexes have negligible contribution to the total absorbance of the solution mixture due to their much lower concentrations and order-of-magnitude smaller molar extinction coefficients. Therefore, the absorbance of the mixture at the wavelength of 598 nm as a function of time can be calculated as:

$$A = \varepsilon_{\mathrm{HisCu}} b[\mathrm{HisCu}] + \varepsilon_{\mathrm{His_2Cu}} b[\mathrm{His_2Cu}] + \varepsilon_{\mathrm{BisTrisCu}} b[\mathrm{BisTrisCu}], \tag{28}$$

where the Beer-Lambert law is used and b is the path length (1 cm).

Combining eqs 25–28 gives,

$$\begin{aligned} A = {} & (\varepsilon_{\mathrm{HisCu}} - \varepsilon_{\mathrm{BisTrisCu}}) b \frac{2}{1+2K_2[\mathrm{His}]}[\mathrm{His_2Ni}]_0\left[1-\exp(-k_1 t)\right] + \\ & (\varepsilon_{\mathrm{His_2Cu}} - \varepsilon_{\mathrm{BisTrisCu}}) b \frac{2K_2[\mathrm{His}]}{1+2K_2[\mathrm{His}]}[\mathrm{His_2Ni}]_0\left[1-\exp(-k_1 t)\right] + \\ & \varepsilon_{\mathrm{BisTrisCu}} b[\mathrm{BisTrisCu}]_0 \end{aligned} \tag{29}$$

Eq 29 provides the basis for using metal exchange experiments to extract the dissociation rate of the His_2Ni complexes under the specified experimental condition. Note that the product K_2[His] is of order one and cannot be eliminated. However, based on the PSSA on His, K_2[His] can be treated as a constant throughout the experiment. Therefore, the total absorbance of the mixture has the following function form,

$$A = C_1 - C_2 \exp(-k_1 t). \tag{30}$$

In eq 30, C_1 and C_2 are two fitting parameters (constants), and k_1 is the dissociation rate of interest. However, noticeable deviation from the exponential function is observed, and similar phenomenon has been reported in experiments on other metal-ligand complexes[7, 8]. Therefore, the time-dependent mixture absorbance is fit to a stretched exponential function instead to better describe the experimental data.

$$A = C_1 - C_2 \exp\left(-\left(\frac{t}{\tau}\right)^{\beta}\right). \tag{31}$$

where β is the stretched exponent ranging from 0 to 1. The dissociation time is assigned to be first-moment average:

$$\langle \tau_d \rangle = \frac{\tau}{\beta}\Gamma\left(\frac{1}{\beta}\right). \tag{32}$$

7) Notes on the modified two-state model

The following modified two-state model is used to describe the concentration changes of dye-labeled stickers in the forced Rayleigh scattering experiment:

$$\begin{aligned} \frac{\partial C_S}{\partial t} &= D_S \frac{\partial^2 C_S}{\partial x^2} - k_{on}{}^* C_S + k_{off} C_A \\ \frac{\partial C_A}{\partial t} &= D_A \frac{\partial^2 C_A}{\partial x^2} + k_{on}{}^* C_S - k_{off} C_A \end{aligned}, \tag{33}$$

where C_S and C_A are the concentration of the free stickers and the bounded stickers, D_S and D_A are the corresponding diffusivities, k_{on}* and k_{off} are the rate constants for the apparent association and dissociation reactions, respectively. In the limit when $\gamma = D_A/D_S$ is vanishingly small, the time constants predicted by the modified two-state model are given as:

$$\tau_1, \tau_2 = \frac{2}{\left(k_{on}^* + k_{off} + q^2 D_S\right) \mp \sqrt{\left(k_{on}^* + k_{off} + q^2 D_S\right)^2 - 4 k_{off} q^2 D_S}}, \tag{34}$$

where q is the reciprocal variable to the grating spacing d, i.e., $q = 2\pi/d$. The solutions are obtained *via* a Fourier transform method, as described elsewhere[9]. The following discussion will only focus on the large time constant τ_1, which can be reliably extracted from experiments.

Using perturbation analysis, it can be shown that the asymptotic solution for τ_1 in the large length scale limit ($d^2 \rightarrow \infty$) is

$$\tau_1 = \frac{d^2}{4\pi^2 D_S}\left(K_{eq} + 1\right)\left[1 + \frac{4\pi^2 D_S}{k_{on}^* d^2}\frac{K_{eq}^2}{\left(K_{eq} + 1\right)^2}\right]. \tag{35}$$

Therefore, the value of the K_{eq} only slightly changes the curvature transitioning from the pure dissociation-controlled regime to the pure diffusion-controlled regime (the second term in the square bracket).

When $K_{eq} >> 1$, the equation above becomes,

$$\tau_1 \approx \frac{d^2}{4\pi^2 D_S}\left(K_{eq} + 1\right)\left(1 + \frac{4\pi^2 D_S}{k_{on}^* d^2}\right) \approx \frac{d^2\left(K_{eq} + 1\right)}{4\pi^2 D_S}, \tag{36}$$

where the effective/apparent diffusion coefficient for the stickers is $D_{S,eff} = D_S/(1+K_{eq})$.

In the small length scale limit ($d^2 \rightarrow 0$),

$$\tau_1 \approx \frac{1}{k_{off}}, \tag{37}$$

which allows the dissociation rate/time to be obtained.

8) Estimation of the equilibrium constant K_{eq} and the fraction of dangling stickers f

The diffusion coefficient of non-associative fluorescein molecules in gels is estimated from the Mackie–Meares model:

$$\frac{D_S(\varphi)}{D_0} = \left(\frac{1-\varphi}{1+\varphi}\right)^2, \tag{38}$$

where D_0 is the viscosity in pure aqueous solution, approximately 4.0×10^{-10} m^2 s^{-1} at ambient temperature,[10] and φ is the polymer volume fraction (calculated based on the density of PDMA polymers 1.30×10^3 kg m^{-3}). The values of D_S in gels are shown in Table S5, and a 10% relative error is given to account for the uncertainty.

The equilibrium constant K_{eq} defined in the modified two-state model is calculated as

$$K_{eq} = \frac{D_S}{D_{S,eff}}, \tag{39}$$

where $D_{S,eff}$ is the effective diffusivity for the dye-labeled small-molecule stickers in the gels.

Since the apparent association rate is defined as $k_{on}^* = k_{on}C_{F,eq}$, the equilibrium constant K_{eq} can be related to the junction binding constant $K_{eq,j}$ through $K_{eq} = K_{eq,j}C_{F,eq}$. Therefore, the fraction of dangling stickers f is calculated as

$$f = \frac{C_{F,eq}}{C_{total}} = \frac{K_{eq}}{K_{eq,j} C_{total}}, \tag{40}$$

where C_{total} is the total concentration of stickers in the gels. The value of $K_{eq,j}$ was estimated to be $10^{5.24}$ from Fullenkamp *et al.*[3]

Table C-5. Summary of estimated parameters: the diffusion coefficient of non-associative fluorescein molecules in gels D_S, the equilibrium constant K_{eq}, and the fraction of dangling stickers f.

Gel conc. (%)	φ	$10^{10} \times D_S$ [$m^2 s^{-1}$]	$10^{-2} \times K_{eq}$	$10^2 \times f$
10	0.0714	3.0 ± 0.3	2.5 ± 0.5	3.3 ± 0.7
20	0.133	2.3 ± 0.2	4.2 ± 0.7	3.0 ± 0.5

9) Estimation of diffusivity ratio γ

The diffusivity D_{self} gives the upper bound for D_A, the diffusivity of the polymer-conjugated associative junctions defined in the modified two-state model. Therefore, the diffusivity ratio can be estimated,

$$\gamma = \frac{D_{self}}{D_S} = \frac{D_{self}}{D_{S,eff} K_{eq}} = \frac{2.1 \times 10^{-5}}{1.7} \frac{1}{K_{eq}} \sim 10^{-7}, \tag{41}$$

where K_{eq} is assumed to be on the order of 100 based on previous calculation.

Additional NMR Spectra

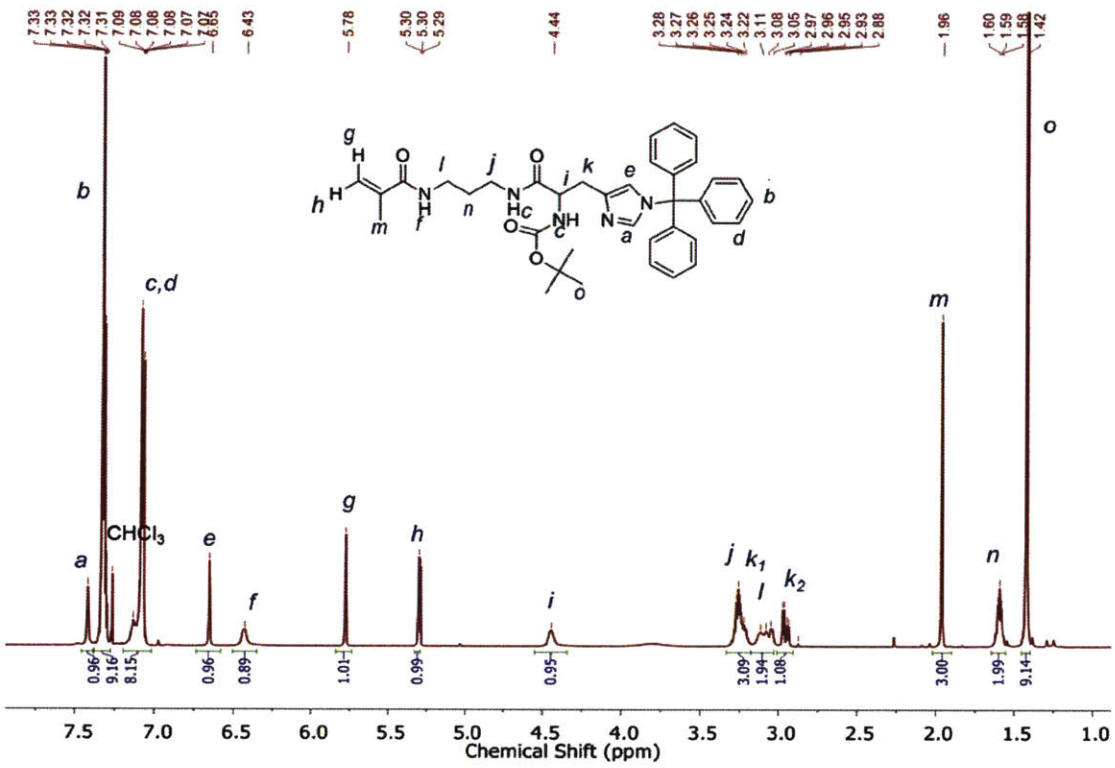

Figure C-9. ^{1}H NMR spectrum of **2** in $CDCl_3$ (300 MHz).

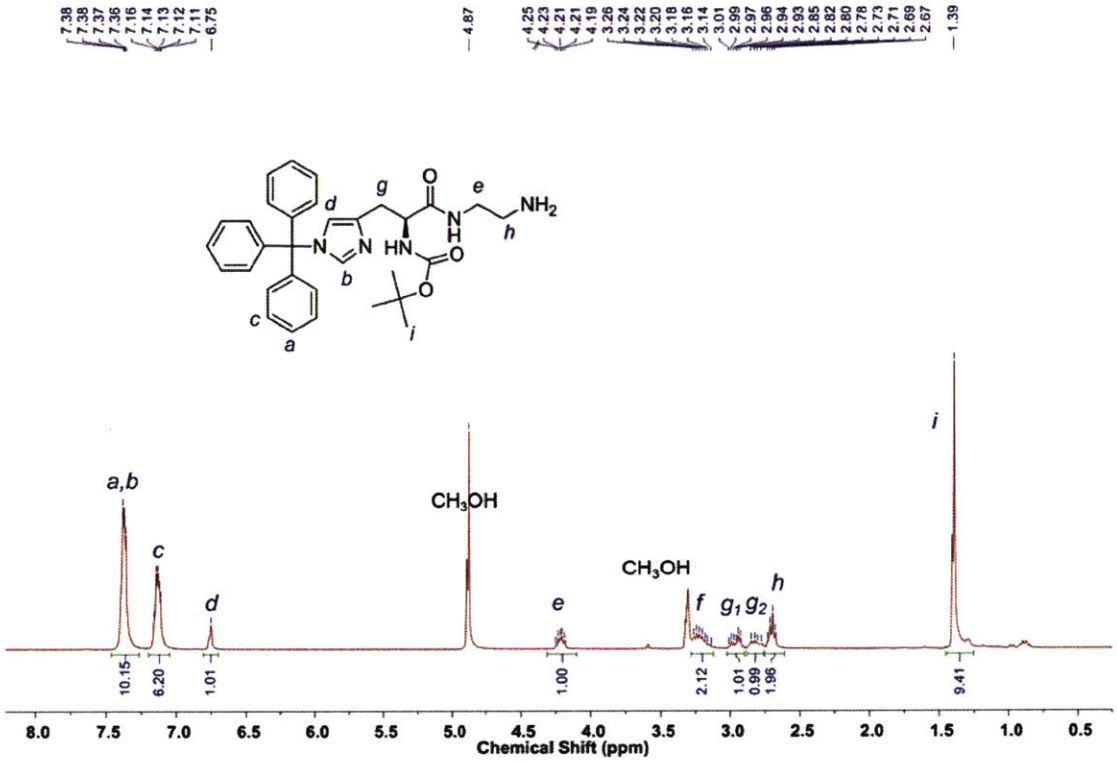

Figure C-10. ^{1}H NMR spectrum of **3** in CD_3OD (300 MHz).

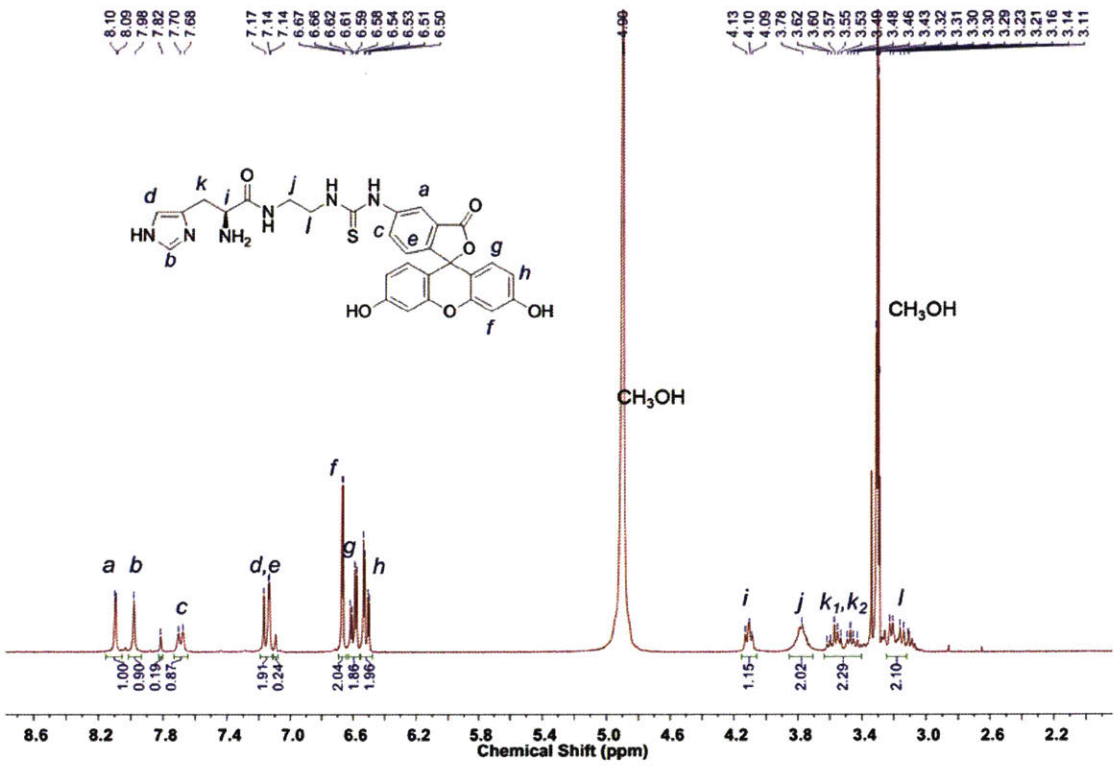

Figure S11. ^{1}H NMR spectrum of **5** in CD_3OD (300 MHz).

References:

1. Fredlake, C. P.; Hert, D. G.; Kan, C.-W.; Chiesl, T. N.; Root, B. E.; Forster, R. E.; Barron, A. E. Ultrafast DNA Sequencing on a Microchip by a Hybrid Separation Mechanism That Gives 600 Bases in 6.5 Minutes. *Proceedings of the National Academy of Sciences* 2008, 105, 476-481.
2. Kondo, S.; Chung, U.-i.; Sakai, T. Effect of Prepolymer Architecture on the Network Structure Formed by Ab-Type Crosslink-Coupling. *Polym J* 2014, 46, 14-20.
3. Fullenkamp, D. E.; He, L.; Barrett, D. G.; Burghardt, W. R.; Messersmith, P. B. Mussel-Inspired Histidine-Based Transient Network Metal Coordination Hydrogels. *Macromolecules* 2013, 46, 1167-1174.
4. Conley, H. L.; Martin, R. B. Transition Metal Ion Promoted Hydrolyses of Amino Acid Esters1. *The Journal of Physical Chemistry* 1965, 69, 2923-2935.
5. Scheller, K. H.; Abel, T. H. J.; Polanyi, P. E.; Wenk, P. K.; Fischer, B. E.; Sigel, H. Metal Ion/Buffer Interactions. *European Journal of Biochemistry* 1980, 107, 455-466.
6. Hidmi, L.; Edwards, M. Role of Temperature and Ph in Cu(Oh)2 Solubility. *Environmental Science & Technology* 1999, 33, 2607-2610.
7. Henderson, I. M.; Hayward, R. C. Substituent Effects on the Stabilities of Polymeric and Small Molecule Bis-Terpyridine Complexes. *Polymer Chemistry* 2012, 3, 1221-1230.
8. Wang, R.; Geven, M.; Dijkstra, P. J.; Martens, P.; Karperien, M. Hydrogels by Supramolecular Crosslinking of Terpyridine End Group Functionalized 8-Arm Poly(Ethylene Glycol). *Soft Matter* 2014, 10, 7328-7336.
9. Tang, S.; Wang, M.; Olsen, B. D. Anomalous Self-Diffusion and Sticky Rouse Dynamics in Associative Protein Hydrogels. *Journal of the American Chemical Society* 2015, 137, 3946-3957.
10. Dursch, T. J.; Taylor, N. O.; Liu, D. E.; Wu, R. Y.; Prausnitz, J. M.; Radke, C. J. Water-Soluble Drug Partitioning and Adsorption in Hema/Maa Hydrogels. *Biomaterials* 2014, 35, 620-629.

Appendix D: Supporting Information for Chapter 7

Calculation Details

1) The protein volume fraction in the hydrogel (φ) is calculated based on the following assumptions:

- The density of protein ρ is 1.3 g cm^{-3}.[1]
- The volume of the hydrogel is the sum of the solvent volume and the protein volume.

2) Averaged molecular weight (MW) and molecular weight distribution (MWD)

The weight fraction of each species is estimated using densitometry analysis. Due to the resolution limitation of SDS-PAGE, the high molecular weight species cannot be well separated. Therefore, only weight fractions (from three different SDS-PAGEs) of unimer to heptamer are used in the calculation. By using the MATLAB built-in lsqcurvefit algorithm, the MWD is fit to the theoretical Jacobson-Stockmayer distribution.[2] Briefly, assuming that the molecular size distribution for the chain fraction of the same form as the distribution in the ring-free case, namely, the Flory-Schulz distribution, the number of n-mer linear chains in the mixture is

$$C_n = Ax^n$$

where A is a normalization constant and x is the fraction of reacted endgroups in the chain fraction.

The number of n-mer rings in the mixture is assumed to be

$$R_n = Bx^n n^{-5/2}$$

where B is a constant.

Therefore, the weight fraction of n-mer, including chains and rings, is

$$w_n = \frac{n(C_n + R_n)}{\sum n(C_n + R_n)} = \frac{\frac{A}{B} n x^n + x^n n^{-3/2}}{\frac{A}{B}\frac{x}{(1-x)^2} + \sum x^n n^{-3/2}} = \frac{anx^n + x^n n^{-3/2}}{\frac{ax}{(1-x)^2} + \sum x^n n^{-3/2}}$$

The fitting parameters are a (the ratio of A to B) and x. Their values from nonlinear regression are 0.574 ± 0.378, and 0.610 ± 0.089, respectively. By using the values of a and x, other quantities can be calculated as follows.

The number and weight fractions of rings in the system is

$$n_r = \frac{\sum R_n}{\sum (C_n + R_n)} = \frac{\sum x^n n^{-5/2}}{\frac{ax}{(1-x)} + \sum x^n n^{-5/2}}$$

$$w_r = \frac{\sum n R_n}{\sum n(C_n + R_n)} = \frac{\sum x^n n^{-3/2}}{\frac{ax}{(1-x)^2} + \sum x^n n^{-3/2}}$$

The fraction of reacted functional groups in the system is

$$p = x + (1-x) w_r$$

The number and weight average degrees of polymerization of the chain fraction are

$$\bar{X}_{cn} = \frac{1}{1-x}, \quad \bar{X}_{cw} = \frac{1+x}{1-x}$$

The number and weight average degrees of polymerization of the ring fraction are

$$\bar{X}_{rn} = \frac{\sum x^n n^{-3/2}}{\sum x^n n^{-5/2}}, \qquad \bar{X}_{rw} = \frac{\sum x^n n^{-1/2}}{\sum x^n n^{-3/2}}$$

The number and weight average degrees of polymerization of the system are

$$\bar{X}_n = n_r \bar{X}_{rn} + (1 - n_r)\bar{X}_{cn}, \qquad \bar{X}_w = w_r \bar{X}_{rw} + (1 - w_r)\bar{X}_{cw}$$

The values above are listed in Table S1. The error bars in the calculation represent the 95 % confidence interval of the fitting parameter, calculated based on built-in nlparci algorithm.

Table S1. Summary of the average degrees of polymerization and molecular weights calculated from the Jacobson-Stockmayer theory.

	Chain fraction	Ring fraction	Total
$\bar{X}_n$	2.57 ± 0.58	1.17 ± 0.04	1.96 ± 0.40
$\bar{M}_n$ (kDa)	162.4 ± 36.6	73.9 ± 2.5	123.9 ± 25.3
$\bar{X}_w$	4.13 ± 1.17	1.42 ± 0.13	3.43 ± 0.95
$\bar{M}_w$ (kDa)	261.0 ± 73.9	89.7 ± 8.2	216.8 ± 60.0

3) Stress-strain curve and toughness in tensile experiments

The stress-strain curve is obtained from the force-displacement relation. The engineering stress is calculated using the initial cross sectional area 2 mm × 4 mm in the dog bone. The engineering strain is calculated using the 8 mm as the initial length for approximation. We choose this value instead of the 10 mm gauge length accounting for non-uniform deformation within the specimen. Use of a video extensometer at early deformation enabled accurate calculation of the strain field in the specimen. It was verified that the calculated strain based on 8 mm initial length was within the range of the strain values calculated from video extensometer. True stress and strain are calculated via the following relations:

$$\varepsilon_T = \ln(1+\varepsilon_E)$$

$$\sigma_T = \sigma_E(1+\varepsilon_E)$$

where ε_E is the engineering strain, ε_T is the true strain, σ_E is the engineering stress and σ_T is the true stress.

The toughness of topologically entangled gels is calculated as the area under the engineering stress-strain curve. Three independent experiments were performed and the error bars reported in the text are the standard deviation of the measurement.

4) Entanglement molecular weight in gels

The entanglement molecular weight is calculated as[3]

$$M_e = \frac{4}{5}\frac{\rho\varphi RT}{G_e}$$

where R is the universal constant 8.314 J K^{-1} mol^{-1}, T is the absolute temperature, G_e is the entanglement plateau modulus. Three independent experiments for hydrogel *o*-Cys-P_4-Cys at 15 (w/v)% were performed and the error bars reported in the text are standard deviation of the measurement. This relative standard deviation is used for estimating the error bars for the entanglement plateau modulus at 17.5 (w/v)% and 20 (w/v)%.

5) The number of elastically effective chains after chain extension

For protein Cys-P_4-Cys (monomer) in the reduced state, there are 3 elastically effective chains per molecule. The theoretical maximum number of elastically effective chains per protein monomer for a linear n-mer extended protein is given by 4 - 1/n, whereas it is a constant of 4 for

all the looping species. The theoretical molecular weight distributions of the linear and ring molecules are calculated from the Jacobson-Stockmayer theory mentioned previously. Therefore, the total number of elastically effective chains per monomer is

$$\upsilon = \frac{(4-1/n)C_n}{\sum(C_n+R_n)} + \frac{4R_n}{\sum(C_n+R_n)} = 4 - \frac{\sum C_n/n}{\sum(C_n+R_n)} = 4 - \frac{\sum \frac{ax^n}{n}}{\frac{ax}{(1-x)} + \sum x^n n^{-5/2}}$$

$$= 4 + \frac{a\ln(1-x)}{\frac{ax}{(1-x)} + \sum x^n n^{-5/2}}$$

Substituting the numerical values from the fit gives $\upsilon = 3.68$.

6) The fraction of elastically effective chains in the protein hydrogel

$$v_{\text{eff}} = \frac{G'_\infty(\text{expt})}{G'_\infty(\text{theo})} = \frac{G'_\infty(\text{expt})}{\upsilon RT}$$

where υ is the molar density of elastically effective chains. For P_4, $\upsilon = 3c$, c being the protein molar concentration in the unit of mol m^{-3}; for *o*-Cys-P_4-Cys, $\upsilon = 3.68c$. As a result, the theoretical prediction of the increase in the fraction of elastically effective chains should be 1.23.

7) The entanglement volume fraction (φ_e)

The sticky reptation theory[4] predicts that the entanglement volume fraction follows the equation

$$\varphi_e = \left(\frac{N_{e0}}{N}\right)^{3\nu-1}$$

where N_{e0} is the number of monomers between entanglements in a melt, N is the degree of polymerization of the polymer, and υ is the Flory exponent.

After chain extension, the total number of monomers in the polymer is

$$N = 2.57 \times 714 = 1835$$

A good solvent quality is assumed, giving the Flory exponent υ as 0.588.

Due to the difficulty of obtaining the entanglement segment length in a melt for a protein, N_{e0} is estimated to be 100, bounded between 37~40 (for flexible PEO) to 128~130 (for rigid PS). [5]

Thus the entanglement volume fraction is estimated as

$$\varphi_e = \left(\frac{N_{e0}}{N}\right)^{3\nu-1} = \left(\frac{100}{1835}\right)^{3\times 0.588-1} = 0.1083$$

From linear rheology, the entanglement effect is observed in gels at concentration 15 (w/v)% and above. Therefore the entanglement volume fraction should be somewhere between 0.0877 and 0.1034. The prediction from sticky reptation is close to the experimental result.

8) Estimation of overlap concentration of strands between stickers

The overlap concentration between stickers, namely the C_{10} domain, can be estimated using the radius of gyration (measured by quasi-elastic light scattering from Shen *et al.*)[6]

$$c^* = \frac{3M}{4\pi N_A R_g^3} = \frac{3\times 7870.17\times 10^{-3}}{4\pi \times 6.023\times 10^{23}\times\left(5\times 10^{-9}\right)^3} = 25.0\left(\frac{\text{kg}}{\text{m}^3}\right) = 25\left(\frac{\text{mg}}{\text{mL}}\right)$$

which gives the overlap volume fraction

$$\varphi_s = \frac{c^*}{\rho} = \frac{25}{1300} = 0.019$$

An alternative is to use the result given by the sticky Rouse and sticky reptation to estimate the overlap volume fraction

$$\varphi_s = N_s^{1-3\nu} = 90^{1-3\times 0.588} = 0.032$$

where N_s is the number of monomers in the C_{10} domain. The two results calculated above are close to each other.

Considering the fact that the C_{10} domain only takes up ca. 62% of the total molecular weight of Cys-P_4-Cys, the corrected overlap volume fraction of C_{10} becomes 0.031 ~ 0.052. All the hydrogels investigated here are above the overlap concentration of the C_{10} domain. At low concentrations, with $\varphi_s < \varphi < \varphi_e$, the protein dynamics can be modeled by the sticky Rouse theory. Once the protein volume fraction exceeds φ_e, the dynamics should be explained by sticky reptation. At all concentrations, the strands between stickers are below the entanglement molecular weight. In experiments, no entanglement signature was observed when $PC_{10}P$ gels are prepared at high concentration, even up to 30 (w/w)%, corresponding to a protein volume fraction of 0.248.[7] Therefore, in the entangled state, the chain extended hydrogels are in the regime $\varphi_e < \varphi < \varphi_{ren}$ and $\varphi_{ren} < \varphi < \varphi_{le}$ according to the sticky reptation theory.

Supplemental Figures

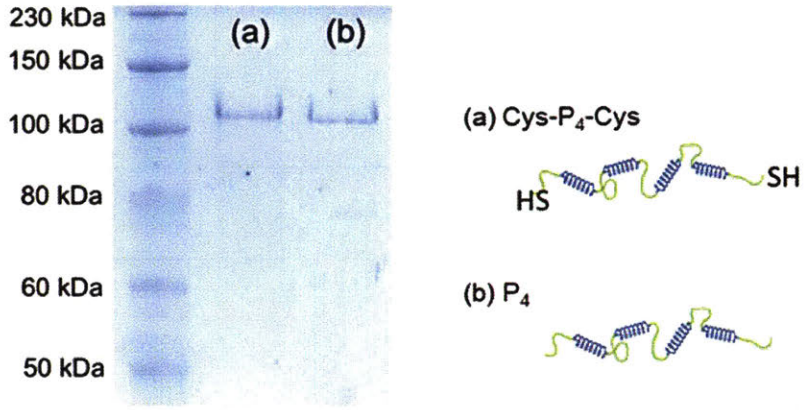

Figure D-1. SDS-PAGE showing the purity of proteins (a) Cys-P_4-Cys and (b) P_4. The proteins run on the gel with an apparent molecular weight equal to approximately twice the true molecular weight. The weak binding affinity to the C_{10} domains results in reduced effective charge and electrophoretic mobility, an effect which has been previously observed for structurally similar proteins. [8]

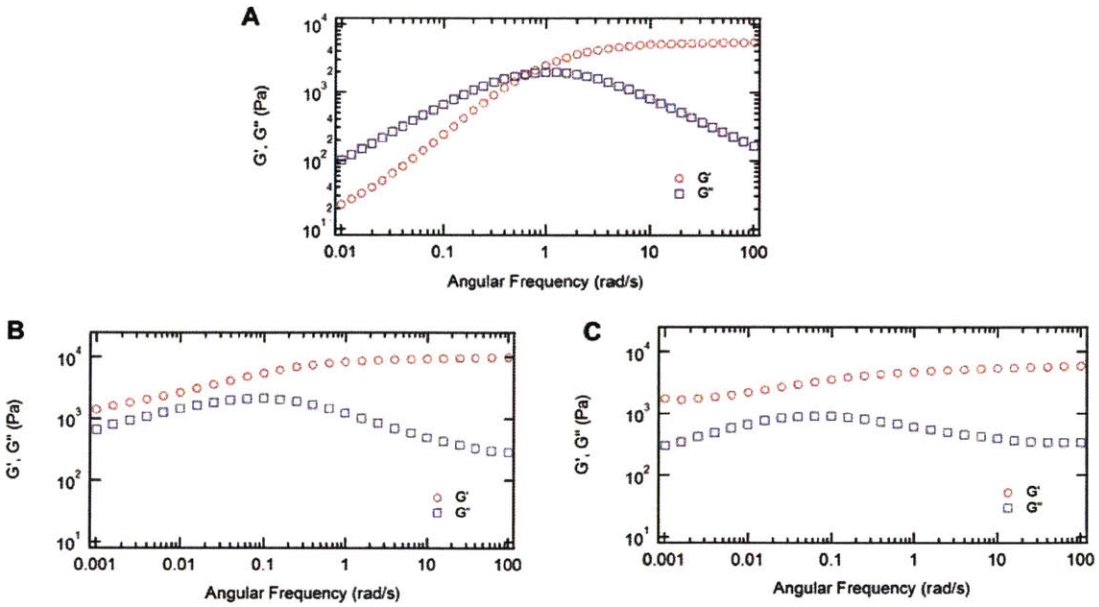

Figure D-2. The entanglement plateau modulus is oxidatively-responsive. (A) Adding TCEP to a chain extended protein hydrogel can eliminate the chain entanglement effect. A five-fold excess TCEP was added to reduce the as-formed disulfide. The drop in the high frequency plateau is believed to come from the pH change.[9] (B) Upon mixing with 0.5 μL 30 wt% hydrogen peroxide, the entanglement feature is recovered. (C) Hydrogel *o*-Cys-P4-Cys processed by another oxidation method: DTT (5× excess) was used to reduce the disulfide, and the hydrogel was then mechanically mixed periodically before loading on the rheometer. Again the drop in high frequency plateau is possibly due to the pH environment change, while the entanglement plateau remains unaffected.

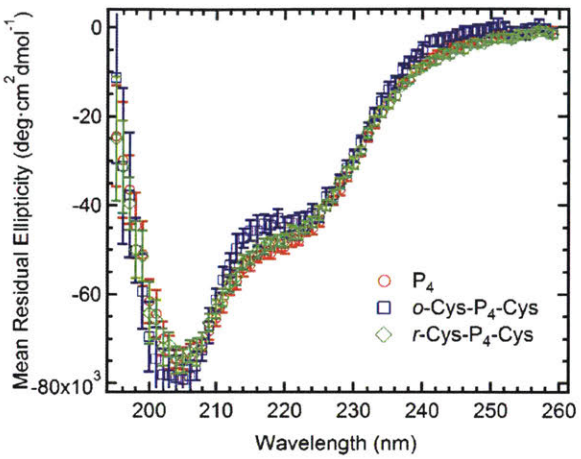

Figure D-3. Circular dichroism (CD) experiment showing that the secondary structure of the coiled-coils remains unchanged among proteins. The CD data is analyzed using the CONTINLL algorithm (providing good estimates of the α-helices content in the protein) in the CDPro package with a basis set of 43 soluble and 13 membrane proteins.[10, 11] Estimated α-helices contents in P_4, *o*-Cys-P_4-Cys (oxidized, chain extended Cys-P_4-Cys) and *r*-Cys-P_4-Cys (reduced Cys-P_4-Cys) are 67.0 %, 74.0 % and 65.9%, respectively.

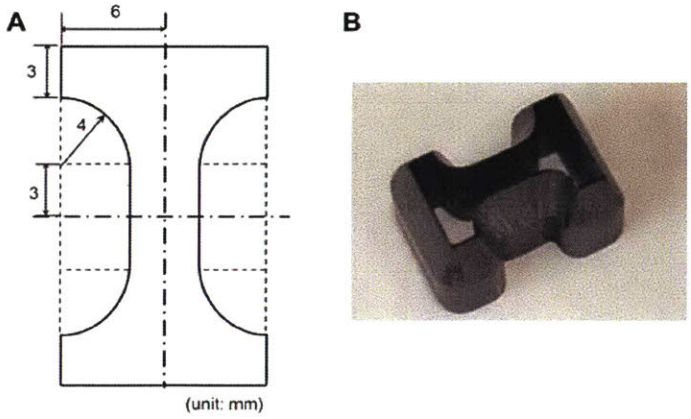

Figure D-4. (A) An engineering drawing of the dog bone dimension; (B) A photograph of the dog bone cutter.

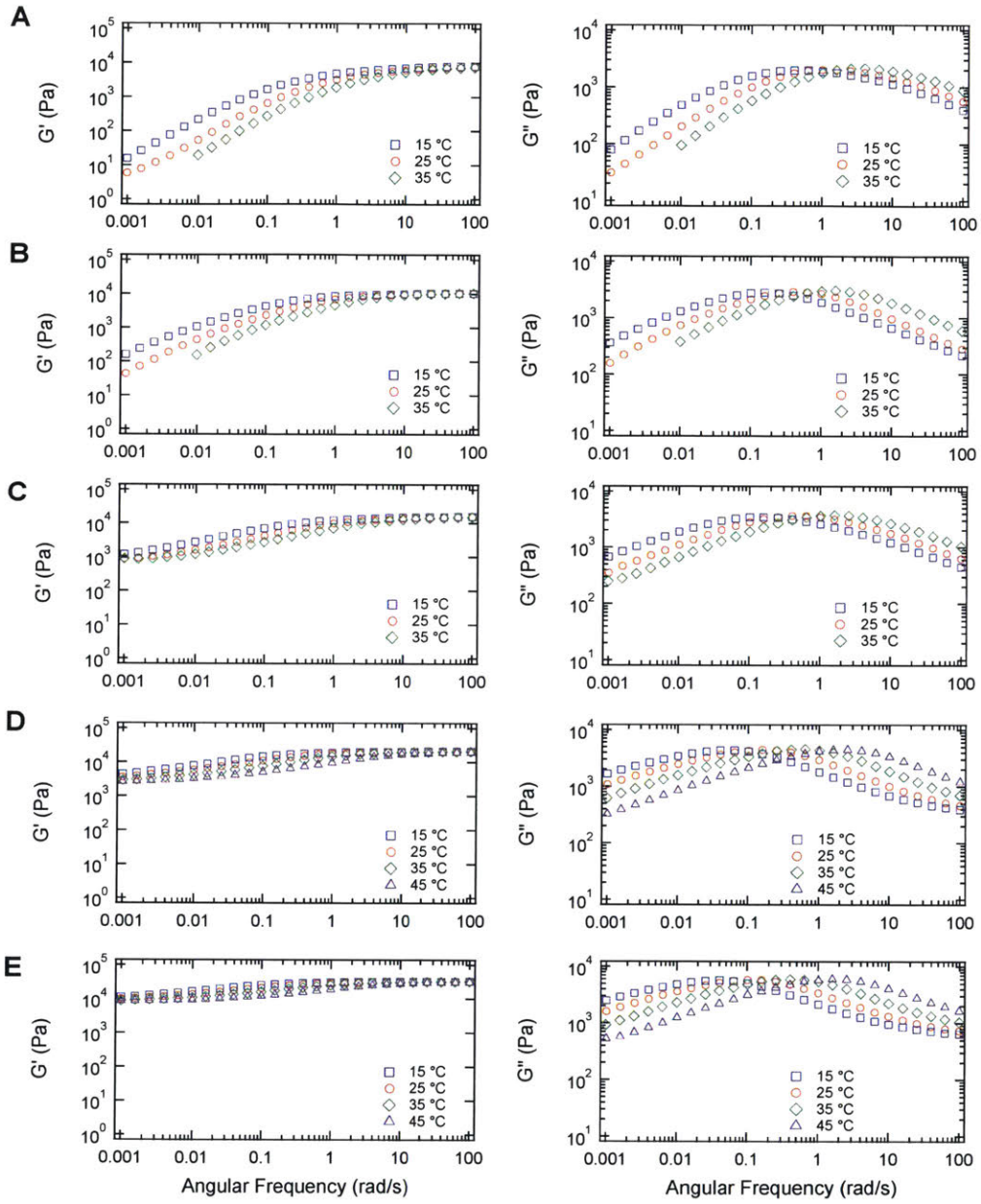

Figure D-5. Frequency sweeps of hydrogel *o*-Cys-P4-Cys as a function of temperature (at 15, 25 and 35 °C, some at 45 °C) at different concentrations (A) 10.0, (B) 12.5, (C) 15.0, (D) 17.5 and (E) 20.0 (w/v)%.

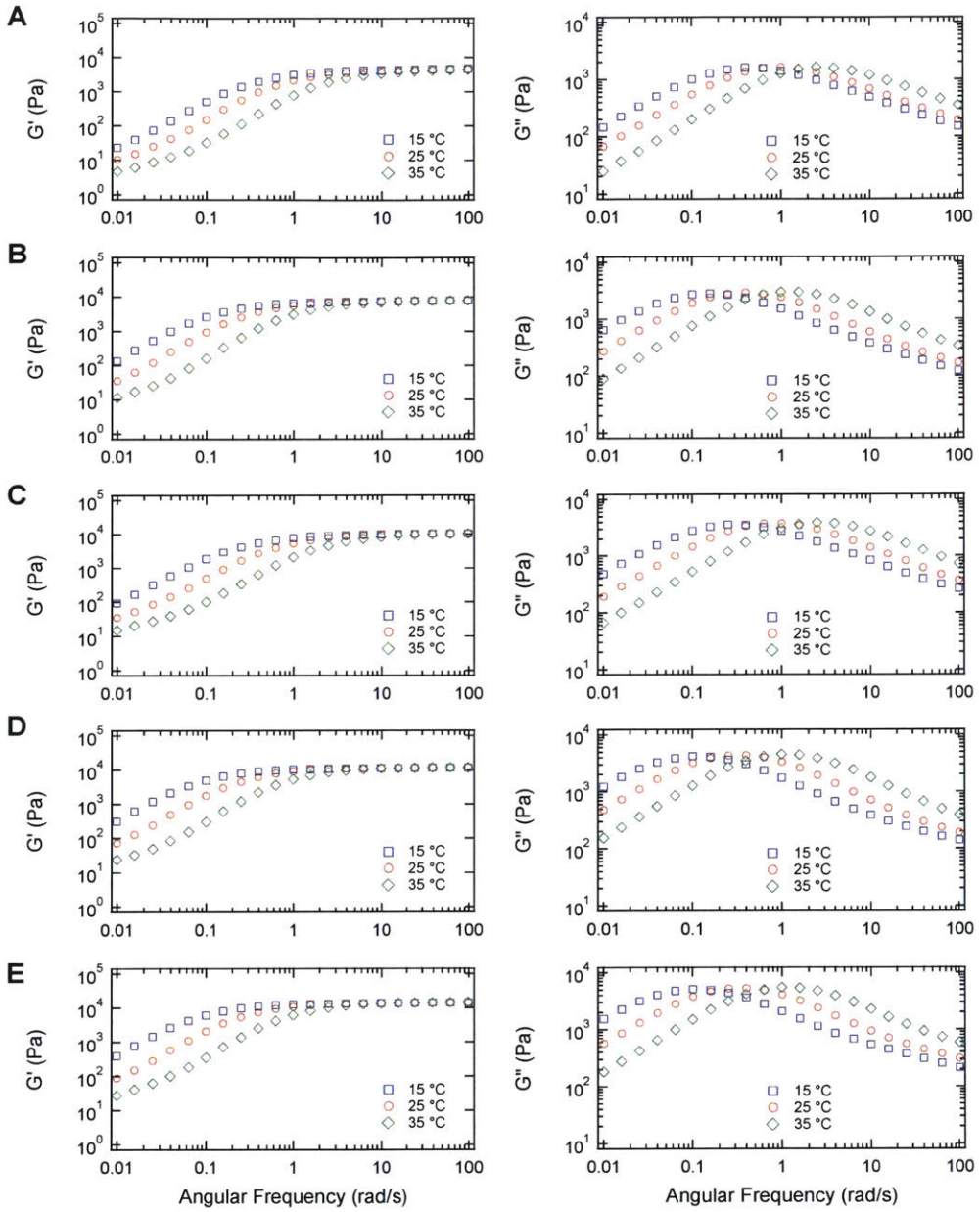

Figure D-6. Frequency sweeps of hydrogel P_4 as a function of temperature (at 15, 25 and 35 °C) at different concentrations (A) 10.0, (B) 12.5, (C) 15.0, (D) 17.5 and (E) 20.0 (w/v)%).

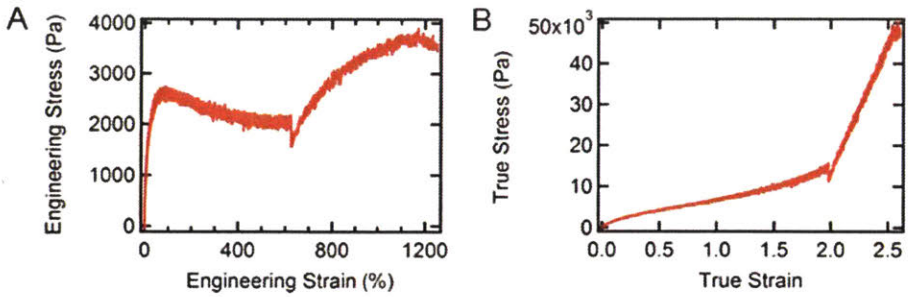

Figure D-7. Stress-Strain curve of hydrogel o-Cys-P4-Cys under tensile loading with a shortened relaxation period of 1 min. (A) Engineering stress-strain; and (B) True stress-strain.

References:

1. Welsh, E. R.; Tirrell, D. A. Engineering the Extracellular Matrix: A Novel Approach to Polymeric Biomaterials. I. Control of the Physical Properties of Artificial Protein Matrices Designed to Support Adhesion of Vascular Endothelial Cells. *Biomacromolecules* 2000, 1, 23-30.
2. Jacobson, H.; Stockmayer, W. H. Intramolecular Reaction in Polycondensations. I. The Theory of Linear Systems. *The Journal of Chemical Physics* 1950, 18, 1600-1606.
3. Larson, R. G.; Sridhar, T.; Leal, L. G.; McKinley, G. H.; Likhtman, A. E.; McLeish, T. C. B. Definitions of Entanglement Spacing and Time Constants in the Tube Model. *Journal of Rheology (1978-present)* 2003, 47, 809-818.
4. Rubinstein, M.; Semenov, A. N. Dynamics of Entangled Solutions of Associating Polymers. *Macromolecules* 2001, 34, 1058-1068.
5. Fetters, L. J.; Lohse, D. J.; Richter, D.; Witten, T. A.; Zirkel, A. Connection between Polymer Molecular Weight, Density, Chain Dimensions, and Melt Viscoelastic Properties. *Macromolecules* 1994, 27, 4639-4647.
6. Shen, W.; Kornfield, J. A.; Tirrell, D. A. Structure and Mechanical Properties of Artificial Protein Hydrogels Assembled through Aggregation of Leucine Zipper Peptide Domains. *Soft Matter* 2007, 3, 99-107.
7. Glassman, M. J.; Chan, J.; Olsen, B. D. Reinforcement of Shear Thinning Protein Hydrogels by Responsive Block Copolymer Self-Assembly. *Advanced Functional Materials* 2013, 23, 1182-1193.
8. McGrath, K. P.; Fournier, M. J.; Mason, T. L.; Tirrell, D. A. Genetically Directed Syntheses of New Polymeric Materials. Expression of Artificial Genes Encoding Proteins with Repeating -(Alagly)3proglugly- Elements. *Journal of the American Chemical Society* 1992, 114, 727-733.
9. Shen, W. Structure, Dynamics, and Properties of Artificial Protein Hydrogels Assembled through Coiled-Coil Domains. Dissertation/Thesis, California Institute of Technology, Pasadena, 2005.
10. Greenfield, N. J. Using Circular Dichroism Spectra to Estimate Protein Secondary Structure. *Nat. Protocols* 2007, 1, 2876-2890.
11. Johnson, W. C. Analyzing Protein Circular Dichroism Spectra for Accurate Secondary Structures. *Proteins: Structure, Function, and Bioinformatics* 1999, 35, 307-312.

Appendix E: Supporting Information for Chapter 8

Calculation details

1) Estimation of the theoretical fraction of PNIPAM associated with chain-extended proteins

Assuming βCD is all attached to the proteins, the concentration of βCD in the chain-extended protein hydrogel can be calculated as

$$c = \frac{n}{V} = \frac{\frac{200\ (mg)}{63000\ (g/mol)}}{1000 + \frac{200}{1.3}\ (\mu L)} = 2.75(mM)$$

And 1 eq. of adamantane functionalized PNIPAM is used to mix with the chain-extended proteins. The association constant can be expressed as

$$K_a = \frac{[Complex]}{[CD][PNIPAM - Ad]} = \frac{1-x}{cx^2} = 5 \times 10^4\ (M^{-1})$$

where x is the fraction of the unassociated βCD and adamantane. The positive root to the equation gives the physical fraction of free βCD and adamantane, that is, 0.082. Therefore, about 91.8% of the PNIPAM is expected to participate in associations with proteins.

The calculation above assumes that the chemical modification does not result in great changes in association constant, which has been shown in literature.[1-5] Even if the association constant decreases by an order of magnitude, the complexation remains to be strong and more than 76% of the βCD and adamantane participate into the formation of inclusion complex (see Figure E-7).

2) Calculation of the gel points using the Carothers Equation and the Flory-Stockmayer theory.

From the Carothers equation:

Assuming the molar fraction of triene **6** in the total alkenes is α, the average functionality of the reaction mixture is

$$f_{avg} = \frac{1 \times 2 + (1-\alpha) \times 2 + \alpha \times 3}{1 + (1-\alpha) + \alpha} = \frac{4+\alpha}{2}$$

Thus the gel point is calculated to be

$$p_c = \frac{2}{f_{avg}} = \frac{4}{4+\alpha}$$

From the Flory-Stockmayer theory:

The gel point p_c approaching the limit $\bar{X}_w \to \infty$ is predicted to be

$$p_C = \frac{1}{[(f_{w,A}-1)(f_{w,B}-1)]^{1/2}}$$

where $f_{w,A}$ and $f_{w,B}$ are the weight average functionalities of groups A (thiols) and B (alkenes). In the branching reactions,

$$f_{w,A} = 2$$

$$f_{w,B} = \frac{2^2(1-\alpha) + 3^2\alpha}{2(1-\alpha) + 3\alpha} = \frac{4+5\alpha}{2+\alpha}$$

The gel point is

$$p_C = \frac{1}{[(f_{w,A}-1)(f_{w,B}-1)]^{1/2}} = \frac{1}{\left(\frac{4+5\alpha}{2+\alpha}-1\right)^{1/2}} = \left(\frac{2+\alpha}{2+4\alpha}\right)^{1/2}$$

The results are plotted in Figure E-8.

Supplementary Figures

Scheme E-1. Hydrolysis of maleimide during the chain extension reaction via thiol-dibromomaleimide coupling.

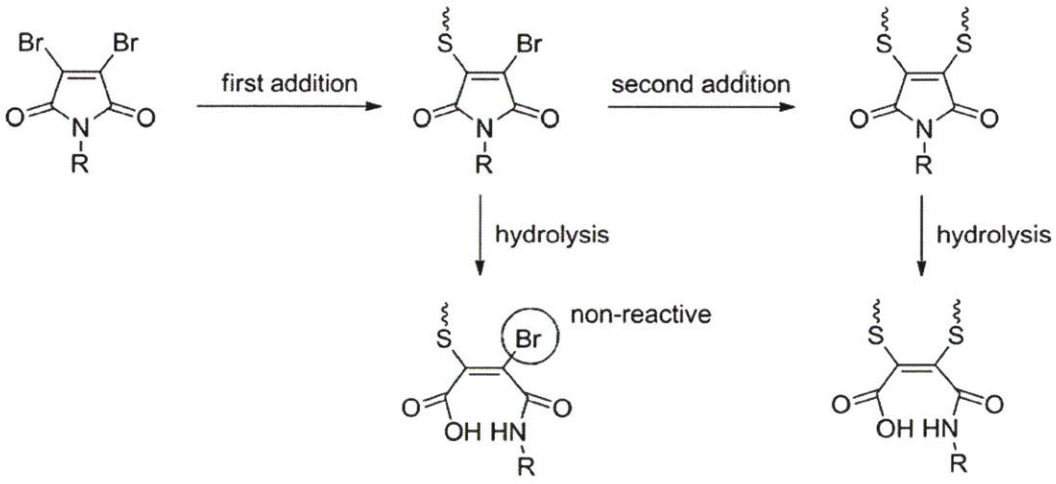

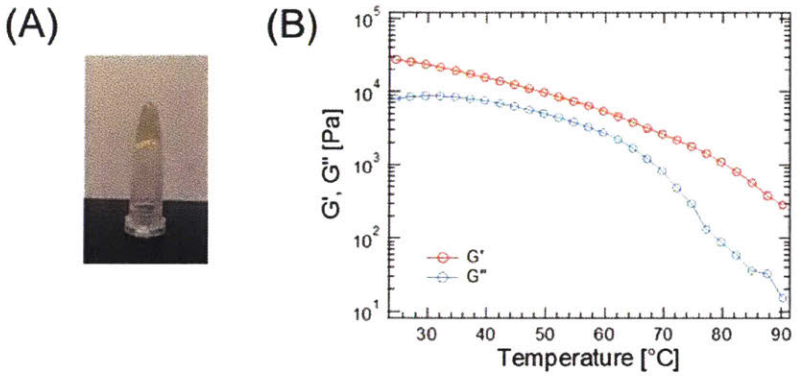

Figure E-1. (A) Inversion test showing the entangled hydrogel remains to be in the gel phase after holding at 100 °C for 1 min. (B) Representative temperature sweep of entangled protein hydrogels at 20% (w/v) concentration, measured at 1 rad/s and 1% strain. Both of the tests show that no sol-gel transition is observed in the experiment temperature window in the entangled hydrogel.

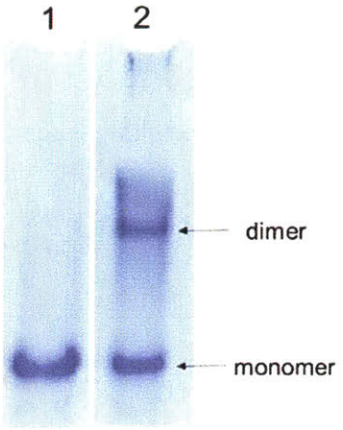

Figure E-2. Lane 1: SDS-PAGE of proteins after reduction by TCEP. More than 99% of the proteins are in monomeric state determined from densitometry. Lane 2: SDS-PAGE of thiol-ene chain extension with the presence of TCEP. Only a low degree of chain extension is reached.

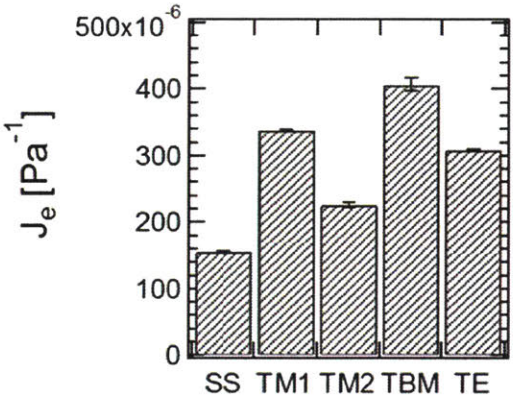

Figure E-3. Comparison of recoverable compliances in entangled hydrogels. SS: disulfide; TM1: thiol-maleimide with 1a; TM2: thiol-maleimide with 1b; TBM: thiol-dibromomaleimide; TE: thiol-ene.

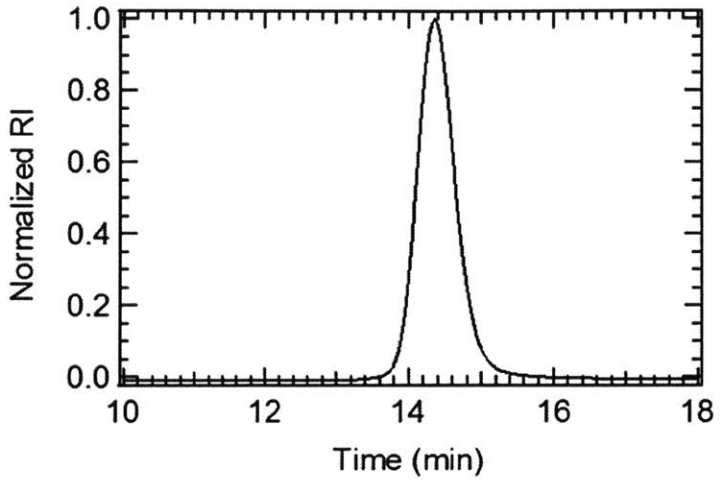

Figure E-4. GPC trace of PNIPAM-Ad. The number average molecular weight M_n = 7.8k and dispersity $Đ$ = 1.05.

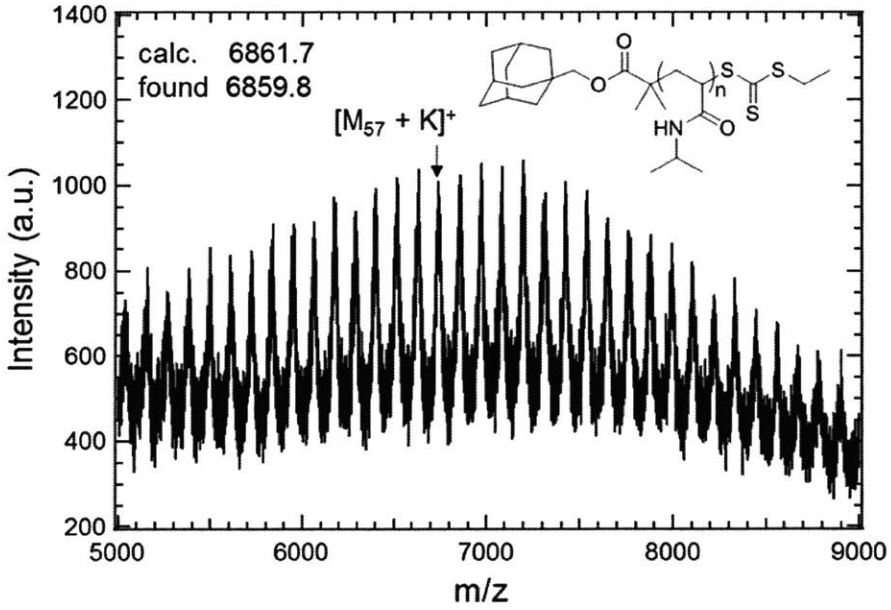

Figure E-5. MALDI-TOF spectrum of PNIPAM-Ad confirming the endgroup structure after polymerization.

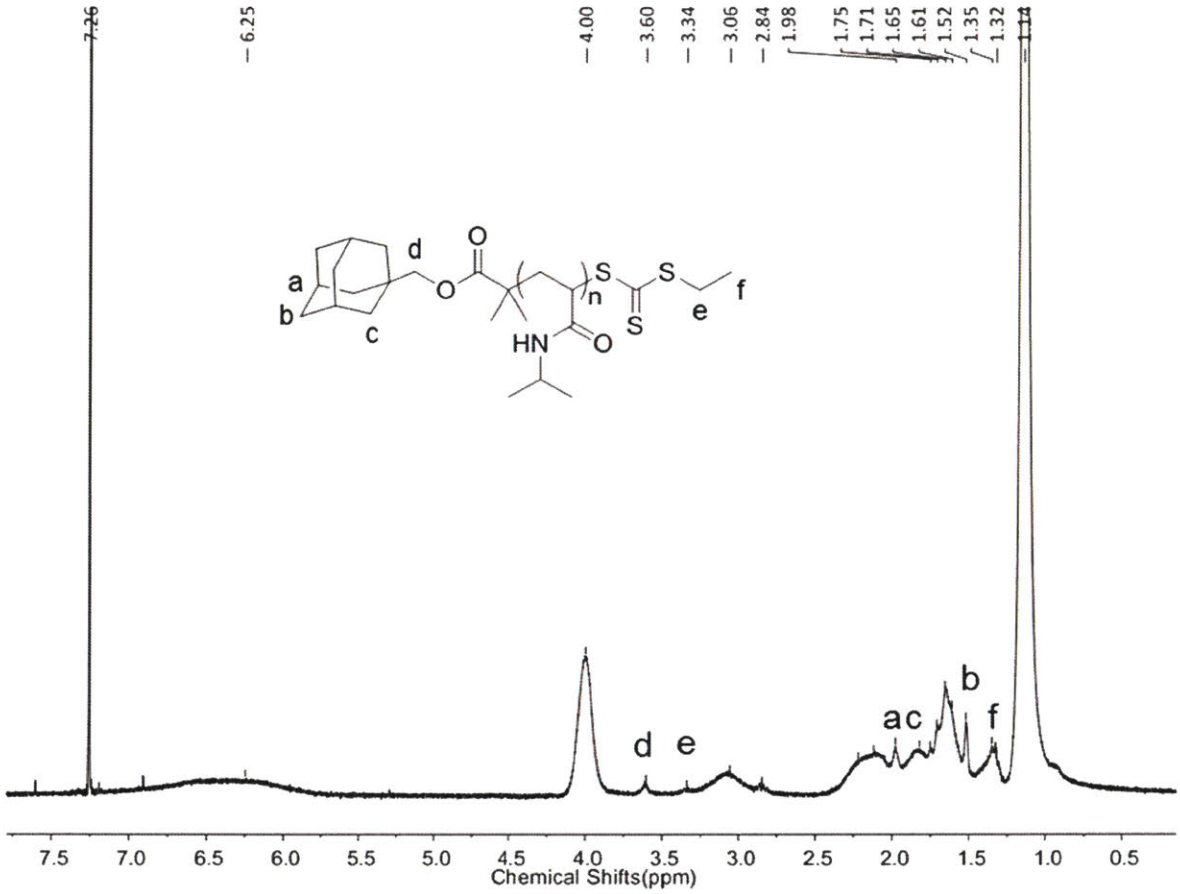

Figure E-6. ^{1}H-NMR spectrum of PNIPAM-Ad confirm the presence of the endgroup post polymerization.

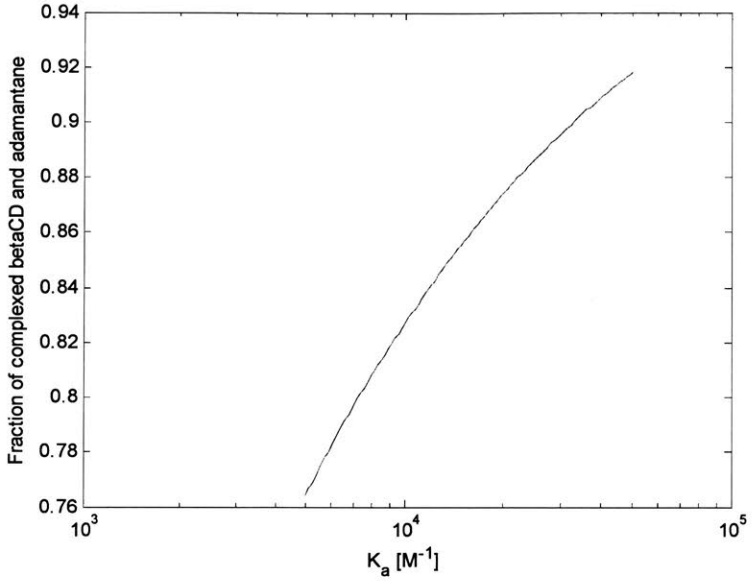

Figure E-7. Effect of K_a on the concentration of associating β-CD and adamantane.

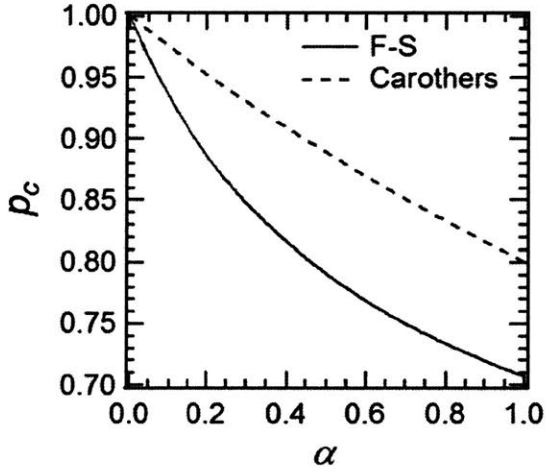

Figure E-8. The theoretical gel points from the Carothers and Flory-Stockmayer theories versus fraction of trifunctional crosslinker **6**.

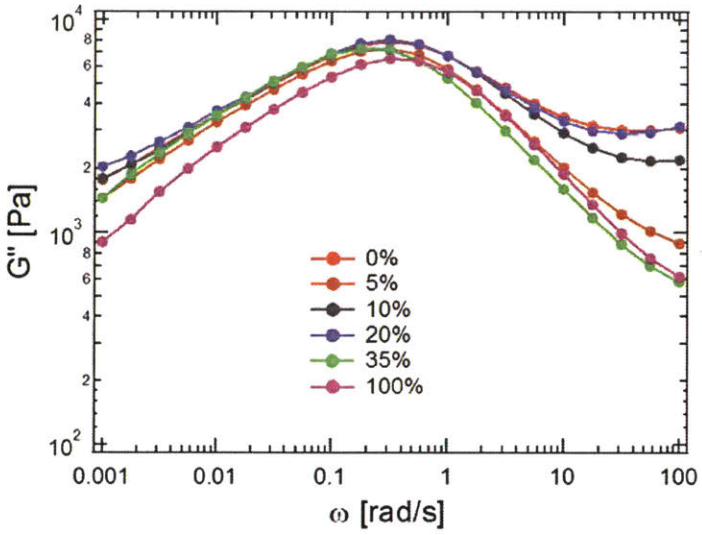

Figure E-9. Frequency spectra G" vs. ω at different triene compositions.

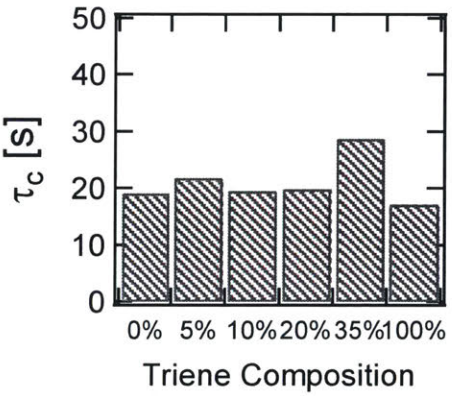

Figure E-10. The relaxation times of the coiled-coil domain in branched protein hydrogels at different triene compositions. The coiled-coil relaxation time is estimated as the inverse of the frequency where G" reach its maximum in the high-frequency regime, namely, $\tau_c = 2\pi/\omega$.

References:

1. Moers, C.; Nuhn, L.; Wissel, M.; Stangenberg, R.; Mondeshki, M.; Berger-Nicoletti, E.; Thomas, A.; Schaeffel, D.; Koynov, K.; Klapper, M., *et al.* Supramolecular Linear-G-Hyperbranched Graft Polymers: Topology and Binding Strength of Hyperbranched Side Chains. *Macromolecules* 2013, 46, 9544-9553.
2. Osman, S. K.; Brandl, F. P.; Zayed, G. M.; Teßmar, J. K.; Göpferich, A. M. Cyclodextrin Based Hydrogels: Inclusion Complex Formation and Micellization of Adamantane and Cholesterol Grafted Polymers. *Polymer* 2011, 52, 4806-4812.
3. Auzély-Velty, R.; Rinaudo, M. New Supramolecular Assemblies of a Cyclodextrin-Grafted Chitosan through Specific Complexation. *Macromolecules* 2002, 35, 7955-7962.
4. Chiba, J.; Sakai, A.; Yamada, S.; Fujimoto, K.; Inouye, M. A Supramolecular DNA Self-Assembly Based on [Small Beta]-Cyclodextrin-Adamantane Complexation as a Bioorthogonal Sticky End Motif. *Chemical Communications* 2013, 49, 6454-6456.
5. Weickenmeier, M.; Wenz, G. Cyclodextrin Sidechain Polyesters — Synthesis and Inclusion of Adamantan Derivatives. *Macromolecular Rapid Communications* 1996, 17, 731-736.